

Engineering of the photonic environment of single nitrogen-vacancy centers in diamond

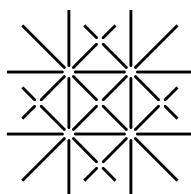
Inauguraldissertation

zur
Erlangung der Würde eines Doktors der Philosophie
vorgelegt der
Philosophisch-Naturwissenschaftlichen Fakultät
der Universität Basel

von

Daniel Riedel

aus Deutschland



U N I
B A S E L

Basel, 2017

The original document is saved on the university of Basel document server
<http://edoc.unibas.ch>



This work is licensed under a Creative Commons Attribution-NonCommercial-NoDerivatives 4.0
International License.

Genehmigt von der Philosophisch-Naturwissenschaftlichen Fakultät auf Antrag von

Prof. Dr. Richard J. Warburton

Prof. Dr. Patrick Maletinsky

Prof. Dr. David Hunger

Basel, den 12.12.2017

Prof. Dr. Martin Spiess
Dekan



Creative Commons License Deed

Attribution-NonCommercial-NoDerivatives 4.0 International

This is a human-readable summary of (and not a substitute for) the license.

You are free to:



Share — copy and redistribute the material in any medium or format

The licensor cannot revoke these freedoms as long as you follow the license terms.

Under the following terms:



Attribution — You must give appropriate credit, provide a link to the license, and indicate if changes were made. You may do so in any reasonable manner, but not in any way that suggests the licensor endorses you or your use.



NonCommercial — You may not use the material for commercial purposes.



NoDerivatives — If you remix, transform, or build upon the material, you may not distribute the modified material.

No additional restrictions — You may not apply legal terms or technological measures that legally restrict others from doing anything the license permits.

Notices:

You do not have to comply with the license for elements of the material in the public domain or where your use is permitted by an applicable exception or limitation.

No warranties are given. The license may not give you all of the permissions necessary for your intended use. For example, other rights such as publicity, privacy, or moral rights may limit how you use the material.

Abstract

The nitrogen-vacancy (NV) center in diamond has an optically addressable, highly coherent spin. However, an NV center even in high quality single-crystalline material is a very poor source of single photons: extraction out of the high-index diamond is inefficient, the emission of coherent photons represents just a few per cent of the total emission, and the decay time is large. In principle, all three problems can be addressed with a resonant microcavity, which significantly boosts the emission rate of coherent photons into the cavity mode based on the Purcell effect. In practice though, it has proved difficult to implement this concept: photonic engineering hinges on nano-fabrication yet it is notoriously difficult to process diamond without degrading the NV centers.

In this thesis, we present a microcavity scheme which employs minimally processed diamond membranes, thereby preserving the high quality of the starting material. The miniaturized plano-concave Fabry-Pérot microcavity platform features full *in situ* spatial and spectral tunability. We demonstrate a clear change in the lifetime for multiple individual NV centers on tuning both the cavity frequency and anti-node position. The overall Purcell factor for the zero-phonon line (ZPL) of $F_P^{\text{ZPL}} \sim 30$ translates to an increase in the ZPL emission probability from $\sim 3\%$ to $\sim 46\%$.

Furthermore, we report the creation of a low-loss, broadband optical antenna giving highly directed output from a coherent single spin in the solid state. The device, the first crystalline solid-state realization of a dielectric antenna, is engineered for individual NV electronic spins in diamond. The photonic structure preserves the high spin coherence of single-crystalline diamond ($T_2 \gtrsim 100\ \mu\text{s}$). We demonstrate a directionality of close to 10 and single photon count rates approaching one MHz. The analysis of the angular emission pattern of our device suggests that 95% of the broadband NV fluorescence is channeled into a solid angle corresponding to a numerical aperture of 0.8.

The abovementioned approaches feature complementary benefits. The narrowband enhancement of the ZPL emission rate provided by the microcavity benefits applications in quantum information processing relying on coherent photons. With the prospect of integrating lifetime-limited emitters and achieving a high ZPL collection efficiency our results pave the way for much enhanced spin-photon and spin-spin entanglement rates.

On the other hand, by channeling the major fraction of the broadband NV fluorescence into a narrow solid angle the dielectric optical antenna facilitates efficient spin read-out. Our approach enables a near-unity collection efficiency which, upon mitigation of the known photon losses, renders it a potential key technology for quantum sensing applications.

Contents

Abstract

1	Introduction	1
2	Theory	7
2.1	Nitrogen-vacancy center in diamond	7
2.1.1	Formation of NV centers	7
2.1.2	Electronic level structure	9
2.1.3	Vibronic structure	13
2.1.4	Temperature effects	16
2.1.5	Optical spin pumping and readout	16
2.1.6	Optically detected magnetic resonance	18
2.1.7	Spin readout	19
2.1.8	Coherent spin manipulation	20
2.1.9	Spin-photon and spin-spin entanglement	27
2.2	Cavity quantum electrodynamics	29
2.2.1	Jaynes-Cummings model	29
2.2.2	Emitter-cavity coupling including system losses	33
2.2.3	Spontaneous emission and Purcell enhancement	34
2.3	Plano-concave Fabry-Pérot cavities	37
2.3.1	Effective cavity length	42
2.3.2	Coupled diamond-air cavity	44
3	Deterministic enhancement of coherent photon generation from a nitrogen-vacancy center in ultrapure diamond	46
3.1	Fully tunable open-access Fabry-Pérot microcavity	47
3.1.1	Concave micromirror template fabrication	49
3.1.2	Diamond fabrication	53
3.2	Linewidth measurements	58

3.3	Cavity coupling experiment	62
3.3.1	Cavity coupling of single NV centers	65
3.3.2	Observation of lifetime modification	67
3.3.3	Analysis of the Purcell enhancement	67
3.3.4	Theoretical description	70
3.3.5	Estimation of the outcoupling efficiency	74
3.4	Conclusions and potential improvements	76
4	A low-loss, broadband antenna for efficient photon collection from a coherent spin in diamond	83
4.1	Antenna design and implementation	86
4.2	Diamond fabrication	87
4.3	Experimental setup	93
4.4	Results and discussion	95
4.4.1	Angular emission pattern	95
4.4.2	Coupling of single NV centers	98
4.4.3	Optically detected magnetic resonance and coherent spin manipulation	100
4.5	Conclusions and outlook	102
5	Summary and future directions	104
	Appendices	109
A	Transfer-matrix calculations	109
B	Dynamics of an emitter-cavity system in the one-excitation limit	115
C	Characterization of absorption losses in the employed GaP material	121
D	Calculations of the emission pattern of the dielectric optical antenna structure and estimation of collection efficiency	123
	References	148
	Acknowledgements	149
	Curriculum Vitae	150
	List of Publications	151

Chapter 1

Introduction

More than a hundred years ago the advent of quantum theory radically changed the view of our world. Since then, there has been the persistent quest to transfer the laws of quantum physics into novel technology.

Within the last decades there has been tremendous progress on precisely manipulating single and a few interconnected quantum systems. In seminal experiments fundamental quantum phenomena have been employed for high-precision measurements approaching the Heisenberg limit [1, 2], the teleportation of quantum states of matter [3, 4, 5] and the loophole-free entanglement of remote quantum systems [6, 7, 8, 9]. Quantum-based technologies are poised to revolutionize the fields of metrology [10, 11], computation [12, 13] and communication [14, 15, 16].

In particular for quantum information processing, where the use of quantum networks comprising several interconnected nodes constitutes the most promising approach, scalability is an important factor. The main challenge for suitable real-world applications is to create robust quantum technology platforms in solid state which have the prospect to integrate many quantum bits (qubits) in a single device. In addition, solid-state based approaches have the advantage that, unlike experiments with isolated atoms, complex laser cooling and trapping techniques are not required. The individual solid-state nodes acting as fast quantum processors or quantum memories are interconnected via a photonic channel. Therefore, creating an efficient interface between the solid-state nodes and this photonic channel is an essential task.

Individual optically active electron spins in semiconductors, confined by nanoscale potentials, constitute promising solid-state qubit candidates. Similar to atoms, these systems feature the possibility of exquisite optical control of their electron spin state when cooled down to cryogenic temperatures. The spins can be initialized, manipulated and read out using laser excitation due to spin-selective optical transitions.

It has been shown that these spins can be entangled with coherent photons [17, 18, 19, 20], which exhibit linewidths approaching the transform limit [21, 22, 23, 24, 25] resulting

in a high degree of indistinguishability. Due to this spin-photon entanglement, the emitted photons carry information about the spin state which allows them to mediate a connection among remote spins. Upon interference of indistinguishable photons from two different systems on a beamsplitter the two remote spins are projected into an entangled state. This process is known as entanglement swapping, which has the advantage that the exact nature of the resulting entangled state is heralded by the detection pattern of the photons at the two output ports [26, 6, 27, 28].

Ideally, systems employed in quantum networks need to exhibit a high flux of photons to establish the remote entanglement at a fast rate and a long spin coherence time to efficiently harness the established entanglement. Several different systems are being considered, which typically only fulfill one of the aforementioned criteria. Most recent achievements have been obtained using optically active quantum dots and nitrogen-vacancy (NV) centers in diamond [19].

Single spins in self-assembled quantum dots [29] possess outstanding photonic properties due to the relatively short radiative lifetime of their excited state where the major fraction of photon emission is coherent and indistinguishable [23, 24, 25]. The coherence properties of the electron spins of these quantum dots, however, are strongly impaired by the fluctuating environment of nuclear spins [30], which limits the number of qubit operations before the spin dephases.

NV color centers in diamond [31] exhibit highly coherent spins, but suffer from poor photonic properties. Facilitated by a nuclear spin free environment, free-induction decay spin coherence times $T_2^* \sim 200 \mu\text{s}$ even at room temperature have been shown for NV centers in high-quality isotopically purified diamond hosts [32]. In addition, it is possible to map the spin state of the NV to nearby nuclear spins [33], which have proven to be an excellent quantum memory with storage times exceeding one second [34]. For NV centers at cryogenic temperatures both quantum teleportation [5] and remote entanglement [26, 6] have been demonstrated.

However, the rate of establishing an interconnection between different quantum nodes is severely hampered by the low probability ($\sim 3\%$) of coherent photon emission into the zero-phonon line (ZPL). The majority of the photons is emitted into the spectrally broad red-shifted phonon sideband, where photon emission is accompanied by the creation of a phonon. Only ZPL photons show the high degree of indistinguishability required for the application in entanglement protocols. Furthermore, due to the non-directional emission of photons and total internal reflection at the interface of the high-index diamond with air, only a small fraction of these ZPL photons can be collected and hence exploited in applications. Additionally, NV centers exhibit long radiative lifetimes compared to

other solid-state emitters [35] (~ 12 ns), which limits the flux of photons.

Coupling the ZPL of the NV center to a high quality-factor, low mode volume optical microcavity offers a potential remedy for these deficiencies. The emission rate of ZPL photons into the cavity mode is strongly enhanced due to the Purcell effect [36]. Fermi's golden rule [37] describes the rate of spontaneous decay of an emitter as being proportional to the density of final states and the interaction strength of the emitter with the vacuum electric field. In a microcavity, both quantities are significantly increased due to the strong spectral and spatial confinement of the resonant electromagnetic mode.

In recent years several different approaches to couple single NV centers to cavities have been employed, including ring-resonators [38] and photonic crystal cavities [39, 40], where Purcell enhancement factors of up to 70 have been reported. Diamond-nanophotonics, however, is still in its infancy and suffers from the severe drawback that the fabrication of nanostructures strongly deteriorates the quality of the optical transitions. The fabrication process introduces a randomly fluctuating charge environment in the vicinity of the NV center leading to strong spectral fluctuations. The resulting inhomogeneous broadening of the ZPL transition renders the photons emitted from these devices unsuitable for the creation of remote entanglement, which relies strongly on indistinguishability. So far, close to transform-limited linewidths have only been demonstrated in high-purity single-crystalline diamond bulk material [41].

Unlike other quantum systems NV centers have the important advantage that even at ambient conditions they are photostable [42] and exhibit a highly coherent spin [32]. Furthermore, the spin state of the NV center can be readily initialized via optical pumping. An important consequence of the optical pumping cycle is that the brightness of the NV photoluminescence is spin-state dependent. This feature can be harnessed for reading out the spin state of NV center. Driving resonant spin transitions with external microwave fields combined with optical initialization and readout of the spin state enabled the demonstration of coherent spin manipulation [43].

The NV center can be employed as an atomic sized sensor because the energetic separation of the different spin sublevels is susceptible to various external influences such as strain [44, 45], temperature [46, 47], electric [48] and magnetic fields [49, 50]. The use of various coherent spin manipulation techniques yields a quantitative measure of the external perturbation. For the sensitivity of these sensing schemes the detection rate of the broadband NV photoluminescence (PL) is an essential figure of merit [50]. Several monolithic approaches have been pursued to enhance the collection efficiency of the NV PL by either overcoming total internal reflection [51, 52, 53] or harnessing it to guide the light towards the detection optics [54, 55, 56, 57, 58].

The goal of this thesis is to engineer the photonic environment of single NV centers in order to increase the PL photon detection rates. Nearly all NV-based applications rely on an efficient readout of the PL as a function of various experimental parameters. As mentioned before, the collection efficiencies, however, are intrinsically limited by the non-directional emission of NV PL and total internal reflection. Typically, only $\sim 3\%$ of the NV photons can be collected using conventional microscope optics due to the non-directional PL emission and total internal reflection at the diamond-air interface [55]. In addition, applications in quantum information processing relying on coherent photons suffer from the low probability ($\sim 3\%$) of coherent photon emission into ZPL.

In order to circumvent these limitations, high-quality single-crystalline diamond membranes are integrated with low-loss photonic structures based on layered dielectric materials. Two complementary approaches are presented which both rely on the engineering of the NV's photonic environment. On one hand, by embedding single NV centers into a dielectric optical antenna the main fraction ($> 95\%$) of the broadband NV PL emission is extracted from the diamond and channeled into a narrow solid angle. On the other hand, by coupling single NV centers to a miniaturized Fabry-Pérot microcavity the generation rate of coherent ZPL photons is significantly boosted which results in a twofold reduction of the NV radiative lifetime and an increase of the fraction of ZPL emission by more than an order of magnitude from $\sim 3\%$ to almost 50% .

In Ch. 2 the general properties of NV centers are introduced and it is explored what gives rise to the rich physics of this color center. Different techniques to create NV centers are discussed and it is described what is required to obtain favorable optical and spin properties. Next, the most important aspects of the electronic structure of the NV center are reviewed including how coupling to phonons affects the NV's optical emission spectrum. Then, the mechanism for polarization of the spin state under continuous illumination is explained. This polarization mechanism gives rise to a spin-state dependent NV PL intensity, which can be harnessed for optical spin readout. Furthermore, the manipulation of the spin using microwave fields is described, which allows for the creation of coherent spin superpositions. These spin superpositions can be entangled with the temporal mode of resonantly emitted ZPL photons, which in turn can be used to mediate an entanglement between two remote NV centers. Next, the interaction of light with an NV center in the framework of the Jaynes-Cummings model is reviewed and it is presented how coupling of the ZPL to a cavity results in an acceleration of the emission rate and why this enhancement is increased for high quality-factors (Q -factors) and small mode volumes V . Finally, the concept of a plano-concave Fabry-Pérot microcavity is introduced, which is a versatile platform and features a high Q/V ratio.

The open-access geometry of this cavity scheme readily allows for the integration of a diamond membrane containing NV centers.

In Ch. 3 the experimental results on the deterministic coupling of single NV centers to the plano-concave microcavity at cryogenic temperatures are presented. First, the fabrication scheme for the creation of atomically smooth concave micromirror templates by CO₂ laser ablation is introduced. These mirror templates are successively coated with high-reflectivity low-loss distributed Bragg reflectors (DBRs) resulting in high Q -factors. Next, the fabrication of thin diamond micromembranes exhibiting low surface roughness is presented. The ZPL linewidths of NV centers in these micromembranes are measured using resonant excitation in order to verify that the minimal processing of the diamond layers mitigates the detrimental effects of plasma etching. The micromembranes are then transferred onto a planar mirror and integrated into the microcavity. In a cryogenic experiment the ZPLs of several NV centers are coupled to the cavity. The effect of this cavity coupling on the radiative decay rate of the NV centers is deterministically probed for spectral and spatial detuning of the cavity mode. The results are in good quantitative agreement with theoretical predictions which indicate an increase in the ZPL emission probability η_{ZPL} by more than an order of magnitude from $\sim 3\%$ to almost 50% . Finally, it is analyzed how the transmission of the two cavity mirrors needs to be adapted in order to maximize the photon collection efficiency. Upon improving the geometry and mitigating losses the model suggests that η_{ZPL} would approach unity.

In Ch. 4, the first experimental realization of a dielectric optical antenna devised for single NV centers in diamond is presented. First, the device formed by a thin single-crystalline diamond micromembrane bonded to a gallium phosphide solid immersion lens (GaP SIL) is introduced and it is explained how the interfaces air-diamond-GaP give rise to the antenna effect. Analytical calculations of the antenna emission pattern are performed which predict that $> 95\%$ of the NV PL is channeled into a narrow solid angle ($\text{NA} > 0.8$) within the GaP. Efficient light extraction from the GaP is facilitated by the hemispherical shape of the SIL resulting in an orthogonal incidence of the light onto the GaP-air interface. The angular radiation pattern of the dielectric antenna for different diamond thicknesses is measured and an excellent agreement with the calculations is found. For single NV centers in a thin diamond membrane a directionality of the PL emission of ~ 10 and a photon count rate approaching one MHz are experimentally determined. Finally, it is verified that the fabrication of the micromembrane does not compromise the NV spin properties by measuring the coherence of the NV centers within the micromembrane.

In Ch. 5 the main results of the thesis are summarized and future directions for the

experiments are suggested. It is highlighted in particular that the design of the photonic devices presented in this thesis is generic. Coupling other color centers in diamond or other materials is an immediate possibility given that high-quality micromembranes with smooth surfaces can be fabricated. Furthermore, it is pointed out that the microcavity can be harnessed to enhance the Raman process within diamond. It is predicted that, if both the Raman pump laser and the Raman transition itself are resonant with the microcavity, Raman lasing would emerge at relatively low-pump powers.

Chapter 2

Theory

2.1 Nitrogen-vacancy center in diamond

The nitrogen-vacancy (NV) center in diamond is a naturally occurring atom-sized color center. An NV center is formed if two neighboring carbon atoms within the diamond crystal lattice are substituted by a nitrogen atom and an adjacent vacant lattice site (Fig. 2.1(a)). The three electrons of the carbon dangling bonds and two electrons of the nitrogen atom are confined at the NV center and form a quantum system often referred to as an artificial molecule.

Similarly to molecules the electronic orbitals of the NV center can be well described using the linear combination of atomic orbitals (LCAO) approach. The energetic position of the Fermi level within the diamond bandgap determines which of the charge states the NV center most stable [59]. The Fermi level can be adjusted by applying a voltage [60, 61], by controlling the density of nitrogen donors or, for near surface NVs, by controlling the surface termination of the diamond [62].

In the negatively charged state NV^- an additional electron is added to the quantum system, which originates for example from a nearby nitrogen donor. For experiments typically NV^- is considered, which stand out for its optically addressable highly coherent spin. For the remainder of this thesis the negative charge state of the NV center is considered, if not denoted otherwise explicitly.

2.1.1 Formation of NV centers

NVs are the second most abundant defect centers of the diamond lattice, after the substitutional nitrogen atom, which is often referred to as P_1 center [63]. One way to create NV centers is to irradiate the diamond with high energy particles like electrons, neutrons or protons which have enough energy to remove a carbon atom from its lattice site and hence create vacancies. If the diamond is heated up to temperatures $T \gtrsim 800^\circ\text{C}$

the vacancies become mobile. During this annealing process it is thermodynamically favorable for the vacancies to combine with nitrogen atoms to form NV centers. With this technique it is possible to create very high concentrations of NVs in nitrogen-rich diamonds.

For many applications, however, it is required to isolate individual NV centers. Natural diamonds that exhibit a low enough number of impurity atoms lack the desired control in NV densities and locations. Advances in high-pressure high-temperature growth, however, allow for the creation of 1b-diamonds with a low nitrogen concentration, $[N] \sim 100$ ppm. Using this material it was possible for the first time to report on the optical detection of a single isolated NV center [64]. Nevertheless, the nitrogen content of these diamonds is still relatively high. Interactions with the electron spins of nearby nitrogen strongly influence the spin dynamics of the NV center and limit coherent spin manipulation.

Chemical vapor deposition (CVD) growth of diamond has enabled the artificial creation of 2a-type diamonds with an ultralow level of impurity atoms ($[N] < 1$ ppb and $[B] < 1$ ppb), which electrically outperform the purest natural diamonds [65, 66]. The defect concentration in these diamonds is so low that lifetime-limited emission linewidths of single emitters could be observed [41]. The NV spin coherence time is also strongly increased, where now the decoherence is mainly limited by fluctuating nuclear spins of the ^{13}C isotope, with a natural abundance of 1.1 %. It has been shown that by the creation of a nearly nuclear-spin free diamond lattice of ^{12}C isotopes, using isotopically purified precursors during the growth process, record-high spin free-induction decay times $\sim 200 \mu\text{s}$ at room temperature can be obtained [32].

The native NV density in these materials is very low and the NV distribution is random. For applications it is thus preferable to introduce additional NV centers into the diamond. Nitrogen within the diamond can be converted into an NV by the aforementioned highly energetic radiation and successive annealing. Alternatively, proton beam [67] and laser [68] writing techniques have been reported recently which enable the localized creation of vacancies with a high lateral resolution. If these techniques are combined with delta-doping, where a thin nitrogen-rich layer is introduced into the diamond during the CVD growth [69], in principle precise three dimensional positioning is possible.

The implantation of nitrogen ions constitutes another method to deterministically create NV centers with high efficiency [70]. Upon implantation into the diamond crystal, the ions leave a trace of vacancies which can be harnessed for the creation of NV centers during the annealing process. By adjusting the energy of the ions the depth at which

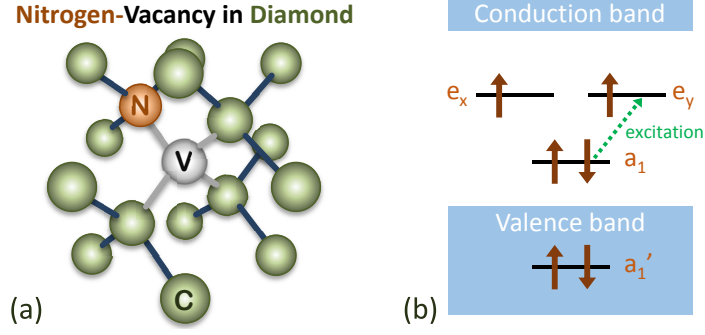


Fig. 2.1. (a) Schematic of the nitrogen-vacancy (NV) center in diamond. Two carbon atoms are replaced by a substitutional nitrogen atom and a void lattice site. The NV exhibits C_{3v} symmetry where the T_d symmetry inherited from the host lattice is broken due to the nitrogen atom. (b) The electron occupation of the NV orbitals for the negative charge state exemplarily shown for the $m_s = +1$ ground state. In accordance with Hund's rule the electrons first occupy the lower lying a_1' and a_1 orbitals with opposite spins before filling the e orbitals. Occupation of e_x and e_y with $|\uparrow\uparrow\rangle$ corresponds to the $m_s = +1$ ground state. If the NV is excited on electron from the a_1 orbital is promoted in one of the e orbitals (dashed green arrow).

the NV centers are created can be controlled. Conversely, a high lateral accuracy of the implantation process can be attained via focused ion beam implantation [71] and implantation through nanoapertures [72] or pierced AFM tips [73].

2.1.2 Electronic level structure

The electronic level structure of the NV center can be described by first principle numeric calculations, where a supercell of carbon atoms comprising the NV center is defined and the electronic states are calculated via density functional theory [74]. This method, however, is limited due to the complexity of solid-state systems and exponential scaling of the computation time with the problem size. Using a group theoretical approach, which harnesses the symmetry properties of the NV center, on the other hand, constitutes a simpler way to describe the electronic structure and allows the prediction of interactions qualitatively [75, 76].

The NV center exhibits C_{3v} symmetry with its axis orientated along the crystallographic [111] axis of the diamond lattice (Fig. 2.1(a)). For the C_{3v} symmetry group the irreducible representations of rotational symmetry are given by A_1 , A_2 and E . The electrons of the NV^- center occupy the four symmetrized LCAO orbitals a_1' , a_1 , e_x and e_y comprising superpositions of the dangling orbitals of the adjacent nitrogen and carbon atoms. In its ground state the orbital occupation of the NV center is given by $a_1'^2 a_1^2 e^2$. In accordance with the paramagnetic filling rule of orbitals (Hund's rule) first the two

lower-lying orbitals a'_1 and a_1 are occupied with two electrons of opposite spin each.

Depending on the orbital configuration of the e orbitals and the arrangement of the spins the ground state can take several different overall configurations. The lowest energy configuration is given if the two electrons of highest energy occupy the e_x and e_y orbitals in an antisymmetric combination which minimizes the Coulomb energy. As the electrons occupy an antisymmetric orbital singlet state $|e_x e_y - e_y e_x\rangle$ their spin configuration must be in a triplet state in accordance with Pauli's exclusion principle. The energetic groundstate is hence given by 3A_2 , where A_2 denotes the orbital symmetry of the state and the "3" indicates the spin triplet.

Fig. 2.1(b) illustrates which orbitals the electrons of the NV^- occupy in the 3A_2 ground state with triplet spin orientation $|\uparrow\uparrow\rangle$ ($m_s = +1$). The other spin orientations are given by $|\downarrow\downarrow\rangle$ ($m_s = -1$) and $|\uparrow\downarrow\rangle + |\downarrow\uparrow\rangle$ ($m_s = 0$), respectively. The $m_s = 0$ and $m_s = \pm 1$ spin states are separated energetically by the zero-field splitting $D \approx 2.88$ GHz. The fact that the spins are aligned parallel in the $m_s = \pm 1$ states leads to an effective inter-electron repulsion due to spin-spin interaction resulting in an energy shift D with respect to the $m_s = 0$ state.

If the NV^- center is optically excited one electron is promoted from the a_1 orbital to one of the e orbitals [77]. The orbital occupation of the excited state is then given by $a_1'^2 a_1^1 e^3$. The additional electron in one of the e orbitals results in a change of Coulomb interaction, which leads to an energetic splitting between ground and excited state of 1.945 eV (637 nm). Due to their weak oscillator strength the excited state lifetime is typically 12 – 13 ns for NV centers located in bulk diamond [78].

The relevant energy levels of the excited state are described by an orbital doublet spin triplet state 3E (Fig. 2.2(a)). The doublet structure results from the fact that the electron from the a_1 orbital can be either excited to the e_x or e_y orbital. The resulting six states are labeled according to their symmetry. Here, $E_{x,y}$ correspond to the $m_s = 0$ state of the spin triplet, while $A_{1,2}$ and $E_{1,2}$ comprise superpositions of the $m_s = \pm 1$ spin triplet states.

According to selection rules only certain transitions between sublevels of ground excited state are allowed: $m_s = 0 \Rightarrow E_{x,y}$ are connected via a linearly polarized transition, while the $m_s = \pm 1 \Rightarrow A_{1,2}/E_{1,2}$ -transitions involve circularly polarized light [79] (Fig. 2.2(a)). For NV centers in high-purity bulk diamond these optical transitions are highly coherent. As displayed in Fig. 2.2(b), nearly lifetime-limited optical Rabi oscillation can be driven between the ground and excited state populations on the $m_s = 0 \Rightarrow E_x$ -transition [80] (compare Sec. 2.1.8).

The energetic spacing between the different excited state levels is governed by spin-

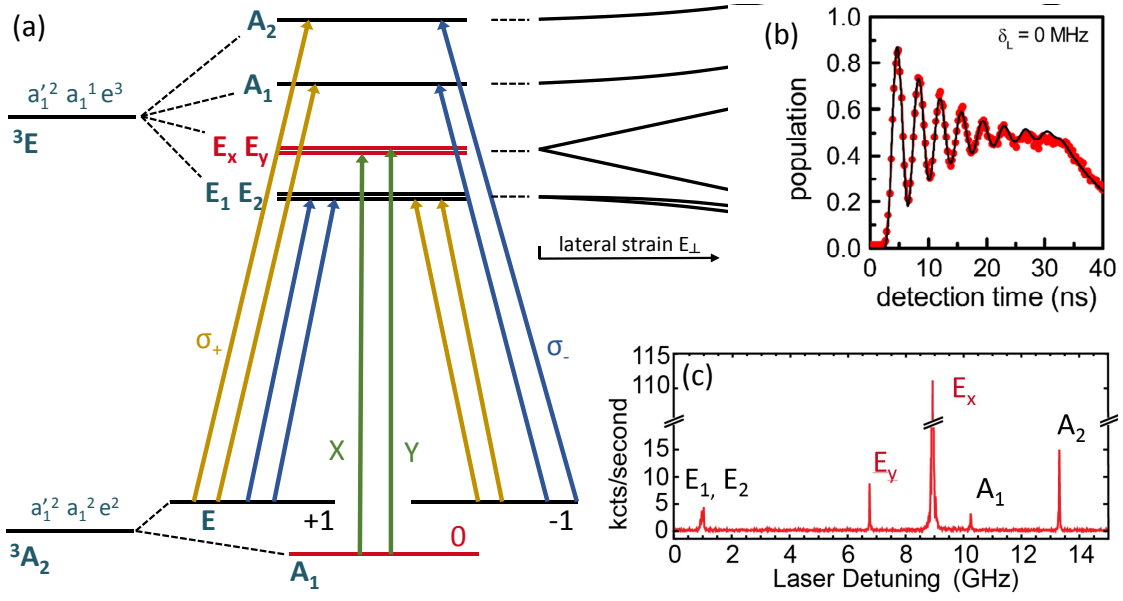


Fig. 2.2. (a) Electronic level structure of the NV center ground ($a_1'^2 a_1^2 e^2$) and excited state ($a_1'^2 a_1^1 e^3$). The ground state spin triplet of 3A_2 comprises two E -symmetric states and one A_1 -symmetric state corresponding to the $m_s = \pm 1$ and $m_s = 0$ spin orientations, respectively. The excited state is an orbital doublet spin triplet state 3E with six different individual levels E_1, E_2, E_x, E_y, A_1 and A_2 . According to optical selection rules transitions from the ground to excited state are allowed from $m_s = 0$ to $E_{x,y}$ with linearly polarized and from $m_s = \pm 1$ to $A_{1,2}$ and $E_{1,2}$ with circularly polarized light. The relative energetic spacings of the excited state levels are depending on how much lateral strain E_{\perp} is exerted on the NV. (b) Resonant optical Rabi oscillations at zero laser detuning δ_L for the $m_s = 0 \Rightarrow E_x$ -transition. Adapted from Ref. [80]. (c) Photoluminescence excitation spectrum of an NV center under additional microwave excitation; frequency is given relative to 470.443 THz. Adapted from Ref. [82].

orbit and spin-spin interaction. A deformation of the lattice due to strain leads to an additional energetic shift of the levels as the C_{3V} symmetry is broken. Strain parallel to the NV axis shifts all the excited state levels by the same amount while lateral strain splits the levels and lifts the initial degeneracy of the $E_{1,2}$ and $E_{x,y}$ levels [81] (Fig. 2.2(a)). Fig. 2.2(c) illustrates that all different transitions of NV^- can be addressed by resonant excitation. Here, the NV center is in a low strain environment, where the energetic splitting between the different excited states is on the order of GHz [82].

External electric fields couple to the excited state levels via the DC Stark effect in a similar manner as strain. Hence, using electric gates the energy shift induced by a strained environment can be compensated [83]. Time-varying external electric fields within the diamond caused by fluctuations of the charge environment of the NV, however, lead to an inhomogeneous broadening of the resonant transitions [84].

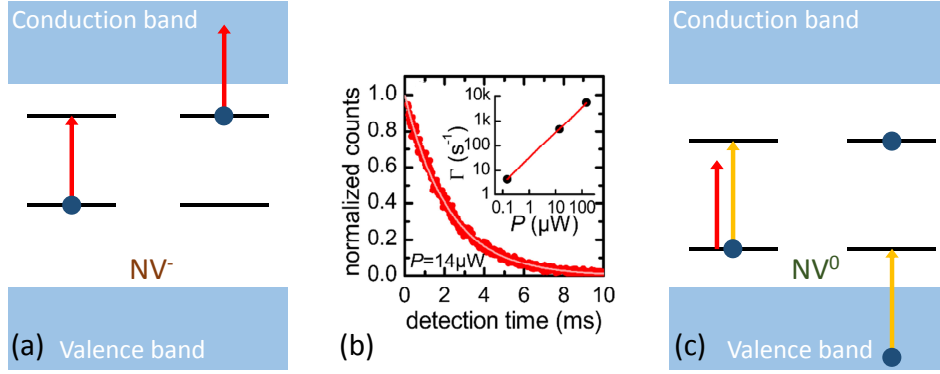


Fig. 2.3. (a) Illustration of the ionization of NV^- under resonant optical excitation (red arrow). While the NV^- is in the excited state the absorption of an additional photon transfers the excited electron to the conduction band. (b) Resonant excitation of NV^- leads to exponential decay of fluorescence due to photoionization. Inset: Ionization rate Γ as function of power of the resonant excitation laser. Adapted from Ref. [80]. (c) Illustration of the reversion from the neutral charge state NV^0 to NV^- . A photon which is resonant with NV^- has insufficient energy to excite NV^0 . If NV^0 is excited resonantly (yellow arrow) an additional electron can be excited from the valence band and convert NV^0 back to NV^- .

Importantly, the energies of the a_1 and e orbitals lie well within the bandgap of the diamond resulting in trapped-ion like electronic properties. There is a certain probability, however, that an electron in one of the e orbitals is excited to the continuum of the diamond conduction band, which results in an ionization of the NV center and a corresponding conversion of the charge state from NV^- to NV^0 [85, 86] (Fig. 2.3(a)).

The energetic splitting of ground and excited state is larger for the neutral charge state NV^0 (2.156 eV, 575 nm) compared to the negatively charged state NV^- (1.945 eV, 637 nm) and both charge states exhibit distinct fluorescence spectra [86]. Hence, the photon energy of the resonant NV^- transitions is insufficient to excite NV^0 . The signal intensity for resonant excitation of the NV^- decays with a power-dependent ionization rate due to this charge state conversion [80] (Fig. 2.3(b)).

There is a similar mechanism to convert the NV^0 back to NV^- (Fig. 2.3(c)). If NV^0 is excited resonantly there is a certain probability that an electron from the valence band is excited into the a_1 orbital before the excitation has decayed which results in converting NV^0 back to NV^- .

As the photon energy required for resonant spectroscopy of NV^- is not sufficient to recharge the NV after ionization, it is required to apply a “repump” optical field that excites NV^0 and hence resets the charge state. Repumping is a two-photon process requiring relatively high powers which typically also leads to a reconfiguration of the charge environment of the NV center. This charge reconfiguration results in a spectral

shift of the resonant transition. Since there are many possible configurations of the charge environment spectral fluctuations are induced. The aforementioned electric field tunability of the NV allows for compensating these fluctuations to a certain degree via a fast feedback loop [87].

As it is described in the next section, the NV center can also be excited efficiently with energies above its resonant energy via a phonon-mediated process (Fig. 2.4(a)). Therefore, a stable emission of photons from the negative charge state can be obtained for example by exciting the NV center with a “conventional” green laser at 532 nm, which allows for both exciting NV^- and converting the charge state from NV^0 to NV^- in case of an ionization event.

The aforementioned charge repumping required for resonant spectroscopy is typically performed with a green laser. Off-resonant excitation of NV^0 , however, requires higher laser powers than necessary under resonant NV^0 excitation, which exacerbate charge fluctuations. It was shown that resonantly repumping the charge state requires only moderate laser powers which mitigates spectral fluctuations [22].

2.1.3 Vibronic structure

The interactions of electronic and vibrational degrees of freedom give rise to the vibronic structure of the optical transition spectrum of the NV center. Besides the direct electronic transition between ground and excited state, called zero-phonon line (ZPL), the additional creation of phonons facilitates the NV center to be excited efficiently with light which is blue-shifted with respect to the ZPL. On the other hand, when the NV center decays from the excited state to the ground state the creation of a phonon results in red-shifted PL. Theoretical calculations predict that 99 % of transitions contributing to the PSB is caused by interaction with quasi-localized vibrational modes, which are confined to the vicinity of the NV center [88].

The influence of a vibrational mode on electronic transitions can be described by the Huang-Rhys model [78]. Here, the normal coordinate of the vibrational mode pointing along the NV axis corresponds to the relative displacement, q , of the nuclei with respect to their equilibrium coordinates. Importantly, the equilibrium coordinates of the vibrational levels in the electronic ground and excited state correspond to different q , where their relative shift is denoted as δq .

Fig. 2.4(b) depicts the energy of the electronic states, within the Huang-Rhys model, as a function of q considering a single vibrational mode. Local lattice vibrations shift the electronic energy of the NV center since the vibrations influence the Coulomb interaction of the NV electrons with the surrounding nuclei. The vibrational modes for ground

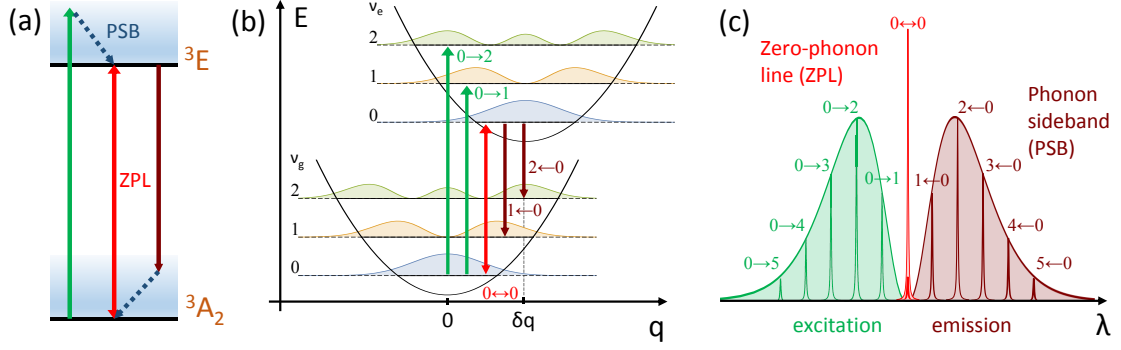


Fig. 2.4. **(a)** Level scheme of the NV center including the phonon sidebands (PSBs). Direct transitions from the ground to the excited state and vice versa correspond to the zero-phonon line (ZPL). In addition, the NV can be excited with energies above the ZPL transition involving the creation of phonons. Similarly, radiative decay involving the creation of phonons is red-shifted with respect to the ZPL. **(b)** Huang-Rhys model for a single vibrational mode explaining the transition probabilities between ground and excited state involving phonons. The nuclear equilibrium position of vibrational levels in the electronic excited state has an effective nuclear displacement coordinate, which is shifted by δq with respect to the electronic ground state (for details see text). **(c)** Optical transitions for a single vibrational mode involving different vibronic transitions $\nu_g \equiv \nu_e$ (individual peaks). PSBs and ZPL for excitation and emission arising from integrating the contributions to the transition spectrum of all vibrational modes (envelope).

(ν_g) and excited state (ν_e) are described by quantum harmonic oscillators resulting in parabolic potential wells. In addition, linear coupling is assumed which means that the interaction of both electronic states with the vibrational modes are the same.

Within the Born-Oppenheimer approximation [89] the motion of the lattice is much slower than the electronic transition between ground and excited state. Hence, the nuclear positions of both states need to be instantaneously compatible during an electronic transition, which entails that in this picture only vertical transitions, i.e. at a fixed q , are allowed. Based on the Franck-Condon principle [89] the overlap of the probability densities of the vibrational wavefunctions of ground and excited state for vertical transitions determines the strength of the optical transition at the corresponding frequency difference.

At room temperature, the NV center is in its vibrational ground state ($\nu_g = 0$) owing to a low phonon occupancy as a result of the high Debye temperature of diamond ($T_D \approx 1900$ K [90]). Transitions from the excited state to the ground state also occur only from the lowest vibrational level ($\nu_e = 0$), since the relaxation of vibrational modes is fast compared to the electronic transition. The fast relaxation of the quasi-localized vibrations of the NV center is caused by an efficient coupling to vibrational modes of

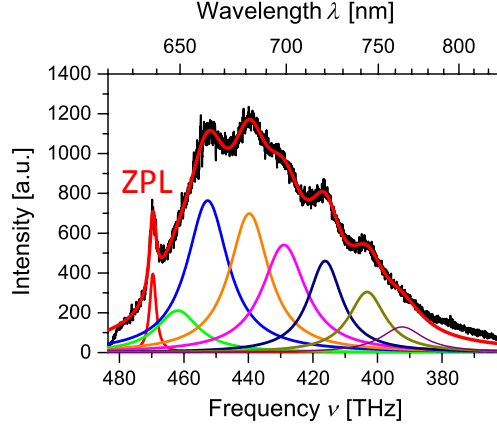


Fig. 2.5. Room-temperature emission spectrum of a single NV center in a nanodiamond on a plane mirror. The spectrum has been fitted with 8 Lorentzian lines. Adapted from Ref. [91].

the diamond lattice. Due to the different nuclear equilibrium coordinates of ground and excited state the maximum overlap occurs for different vibrational modes ν_g , ν_e . Exemplarily, for the mode displayed in Fig. 2.4 the overlap for the transitions $\nu_g = 2 \rightarrow \nu_e = 0$ and $\nu_g = 0 \leftarrow \nu_e = 2$ is maximal.

In general, the overall transition spectrum arises from the superposition of all phonon modes, which all exhibit different vibrational energies (Fig. 2.4(c)). The transitions involving the creation of phonons give rise to the continuous phonon sidebands (PSBs) for excitation and emission. Every mode contributes to the strength of the overall ZPL by their respective $\nu_g = 0 \rightarrow \nu_e = 0$ transitions which are always separated by the energetic difference of the direct electronic transition.

Fig. 2.5 displays a typical room temperature PL spectrum obtained from an NV center in a nanodiamond [91]. The PSB is well fitted by several Lorentzian lines corresponding to the contribution of the dominant vibronic mode. The ZPL is broadened by temperature-induced pure dephasing. In addition, the PSB transitions are significantly broadened due to the fast relaxation of the involved vibronic excitations to their ground state.

It turns out that for the NV center the Debye-Waller factor ξ_{ZPL} , which describes the overall fraction of emission within the ZPL is only $\sim 3\%$ [38]. This low fraction of phonon-free emission particularly limits applications where coherent photons are required.

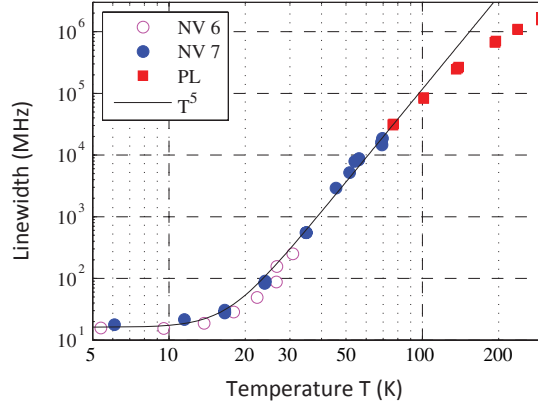


Fig. 2.6. Log-log plot showing linewidth measurements on different NV centers versus temperature: corrected PLE linewidths from NV6 and NV7, PL linewidths from NV3-5 and T^5 fit. Adapted from Ref. [93].

2.1.4 Temperature effects

As it was described in the previous section the creation of phonons plays an important role for the optical transitions of the NV center. The thermal occupation of optical phonon modes of the diamond lattice, with sufficient energy to interact with the molecular vibrations of the NV center, is very low at cryogenic temperatures due to the high Debye temperature of diamond. With increasing temperature, however, a two-phonon process mixes the excited state spin triplet states of the same spin projections since the orbital doublet states of the 3E state couple to the lattice vibrations [92]. For this reason, at room temperature it is not possible any more to resonantly address individual excited states [93]. At elevated temperatures, the excited state can be considered as a spin triplet in a similar fashion as the ground state [94, 93], which was measured directly by driving excited state spin transitions [95].

The quality of the ZPL transition is also affected by temperature. An inhomogeneous broadening of the linewidth with increasing temperature ($\propto T^5$) was observed (Fig. 2.6) which is suspected to be caused by a two-phonon Raman scattering process [93]. This temperature-dependent linewidth broadening has the important implication that highly indistinguishable photon emission can only be attained at cryogenic temperatures.

2.1.5 Optical spin pumping and readout

As indicated by the blue arrows in Fig. 2.7(a), at room temperature each NV spin projection of the ground state triplet 3A_2 is linked to corresponding spin projections of

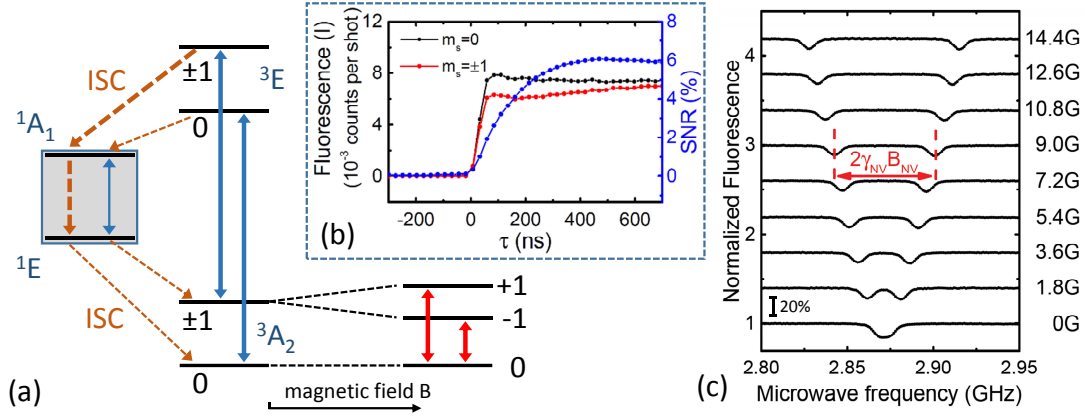


Fig. 2.7. (a) Left: Optical pumping scheme of the NV center. The radiative transitions between the ground state triplet (3A_2) and excited state triplet (3E) are spin-conserving (blue arrows). There is an additional weak non-radiative decay channel (dashed orange arrows) between the triplet states and the metastable singlet states 1A_1 and 1E mediated by spin-orbit coupling. Population from 3E decays to metastable singlet states with a significantly higher probability if the NV is in one of the $m_s = \pm 1$ states compared to $m_s = 0$. Transitions between 1A_1 and 1E can occur both radiatively and non-radiatively before repopulating the ground state triplet via an additional ISC transition. Bottom right: Zeeman splitting of the $m_s = \pm 1$ states due to the coupling with an external magnetic field. (b) Fluorescence transient for continuous laser illumination switched on at $t = 0$ if the NV center is prepared in $m_s = 0$ (black) and the $m_s = \pm 1$ (red). The signal to noise ratio increases with readout time and approaches 6% after 500 ns. Adapted from Ref. [96] (c) ODMR spectra of the NV center for various external magnetic fields. The spin transitions shift with the magnitude of the magnetic field projection along the NV defect quantization axis due to the Zeeman effect. Spectra for different magnetic fields are shifted vertically for clarity. Adapted from Ref. [50]

the excited state triplet 3E via a spin conserving optical transition (compare Sec. 2.1.2). After the NV center is excited, radiative relaxation can occur either resonantly into the ZPL or involving the creation of phonons into the PSB. In addition, there is a non-negligible probability for a strongly spin-selective non-radiative transition to metastable spin singlet states via an inter-system crossing (ISC), which is promoted by spin-orbit interaction [97].

The metastable state has the ground state electron configuration ($a_1^2 a_1^2 e^2$, Sec. 2.1.2). Since it is a spin singlet $|\uparrow\downarrow\rangle - |\downarrow\uparrow\rangle$ the orbital configuration must form an orbital triplet comprising the states $|e_x e_y + e_y e_x\rangle$ (1E_2), $|e_x e_x - e_y e_y\rangle$ (1E_1) and $|e_x e_x + e_y e_y\rangle$ (1A_1). Here, the orbital symmetry of the respective states is indicated in brackets. The energetic splitting of the 1A_1 and 1E states has been determined by the direct observation of a radiative infrared transition [98] and density functional theory calculations predict that 1A_1 is energetically above 1E [99].

It is still under debate what is the exact mechanism which leads to the strong spin-selectivity of the ISC [78, 75]. Measurements of the decay rates from the metastable state to the ground state spin projections $m_s = 0$ and $m_s = \pm 1$ show similar decay rates [100]. This suggests that the spin polarization is due to a larger probability for an ISC transition from the excited $m_s = \pm 1$ states compared to $m_s = 0$. Hence, under continuous optical excitation the NV center's spin state is initialized to $m_s = 0$.

Another consequence of these different relaxation pathways is that the fluorescence rate of the NV center strongly depends on its spin state. If initially the NV occupies one of the $m_s = \pm 1$ states it will decay into the metastable singlet state after a certain number of optical cycles and further photon emission in the visible stops. In contrary, if the NV starts out in $m_s = 0$, it continuously emits photons under optical excitation. The resulting difference in fluorescence emission rate can be harnessed to read out the spin state of the NV center. Fig. 2.7(b) shows a measurement of the transient photoluminescence intensity, if the NV is initialized in the $m_s = 0$ and $m_s = \pm 1$ states, respectively. After a certain transient time both initial configurations attain the steady state spin population resulting in a constant fluorescence level.

At low temperature individual transitions can be addressed in a spin-resolved way. As a result, this leads to a more efficient way to pump the spin into the $m_s = 0$ level [82]. Resonant transitions are driven between $m_s = \pm 1 \rightleftharpoons E_{1,2}/A_{1,2}$ and photons are collected from the PSB. Over time probabilistic spin flips $m_s = \pm 1 \rightleftharpoons 0$ occur via shelving to the singlet states. Since $m_s = 0$ remains unaffected by the laser the PL goes dark after some time indicating that all population is transferred to $m_s = 0$.

2.1.6 Optically detected magnetic resonance

As a direct consequence of the NV dynamics under optical excitation, introduced in the previous section, it is possible to perform optically detected magnetic resonance (ODMR). This technique is an alternative to the electron spin resonance technique where a spin transition is probed by measuring the frequency-dependent absorption of a microwave. In contrast, using ODMR, transitions between spin sublevels induced by a resonant microwave field can be inferred from measuring a change in fluorescence emission.

For ODMR, the NV center is polarized into $m_s = 0$ via continuous optical excitation. If additionally a microwave with frequency ω_{mw} is applied and tuned to resonance with either the $m_s = 0 \rightleftharpoons -1$ or $m_s = 0 \rightleftharpoons +1$ transition, population will be transferred between these states (see Sec. 2.1.8). This population transfer correspondingly leads to a reduction of the NV fluorescence rate.

The zero field splitting sets the quantization axis of the NV center's spin to be parallel to the NV symmetry axis. If in addition an external magnetic field B is applied the energies of the $m_s = \pm 1$ levels are split via the Zeeman effect (Fig. 2.7(a)). The ground state spin Hamiltonian can then be described via [101]:

$$H_0 = hDS_z^2 + g_e\mu_B\vec{B} \cdot \vec{S} \quad (2.1)$$

Here, $\vec{S} = [S_x, S_y, S_z]$ is the $S = 1$ spin matrix and $\gamma_e = 2.8 \text{ MHz/G}$ is the gyromagnetic ratio of the NV spin.

Fig. 2.7(c) shows ODMR measurements performed for different external magnetic fields. From the splitting between the two resonances, the magnitude of the projection of the magnetic field onto the NV axis B_{NV} can be inferred.

2.1.7 Spin readout

As mentioned before, at room temperature the spin state readout relies on the spin-state dependent fluorescence intensity. For continuous-wave excitation and continuous detection, the relative measurement contrast ϵ between the two spin states is even in the best case limited to $\sim 30 \%$. The readout time of the spin state is limited to timescales of the metastable singlet lifetime which is $\sim 250 \text{ ns}$ [102] at room temperature. If the NV spin is in $m_s = \pm 1$ there is a high probability that it decays via the singlet states, which facilitates a spin flip into $m_s = 0$. Typically after $\sim 500 \text{ ns}$ the spin flip occurred and an initial $m_s = \pm 1$ can not be distinguished from $m_s = 0$ any more [103]. Thus, the signal per readout pulse is limited by this optical polarization rate of the electron spin into the $m_s = 0$. In order to distinguish the spin states in a measurement, an experiment typically needs to be repeated several times before enough photons are averaged to determine the spin state. Currently achievable photon count rates $\sim 1 \text{ MHz}$ are not sufficient to resolve single passages through the singlet state.

If, however, the fluorescence photons could be detected at a rate exceeding the polarization rate $\gtrsim 4 \text{ MHz}$, in principle completely dark intervals in the fluorescence signal could be observed if a shelving event occurs [103]. In this ideal experiment, the spin state is read out correctly every time after it has been prepared and coherently manipulated, which is often referred to as “single-shot readout”.

In a realistic experiment classical readout noise needs to be considered. The requirement for single-shot readout is that classical readout noise ($\sigma_{\text{p,readout}}$) is small compared to the quantum projection noise ($\sigma_{\text{p,quantum}}$). For the optical readout of the NV center

the ratio R can be approximated by [10]:

$$R = \frac{\sigma_{\text{p,readout}}}{\sigma_{\text{p,quantum}}} = \frac{2\sqrt{x}}{|x_{|0\rangle} - x_{|1\rangle}|} = \frac{2\sqrt{1-\epsilon/2}}{\epsilon\sqrt{x_{|1\rangle}}} \quad (2.2)$$

Here $\epsilon = |1 - x_{|0\rangle}/x_{|1\rangle}|$ denotes the relative optical contrast between state $x_{|1\rangle}$ and state $x_{|0\rangle}$ and the standard error is assumed to be dominated by shot noise $\sqrt{x} \approx \sigma_x$. Assuming an average contrast $\epsilon = 0.3$ for a readout window of 500 ns, $R < 1$ would require $x_{|1\rangle} = 38$ photons, which corresponds to an average photon detection rate of 76 MHz during the readout window. This suggests that, without increasing the relative contrast ϵ of the two involved levels and prolonging the readout window by changing the dynamics of the optical cycle of the NV center, single-shot readout at room temperature is highly challenging and in all likelihood not in reach for the photonic structures discussed in this work.

At low temperature on the other hand, the NV spin can be read out by resonantly exciting the $m_s = 0 \rightleftharpoons E_{x,y}$ cycling transition and collecting photon emission into the PSB. The fact that NV is not excited by the laser if it is in the $m_s = \pm 1$ state results in a very strong PL spin readout contrast. Using this technique it has been shown that the spin state of the NV can be read out in a single shot achieving a fidelity of $\sim 93\%$ for a detection window of 40 μs [82].

Using Eq. 2.2, for a relative contrast of $\epsilon = 1$, two photons per detection window of 40 μs are required for $R < 1$. The corresponding required average photon detection rate of 50 kHz is readily exceeded in current experiments, where for a readout window of 10 μs on average 5.2 photons are detected if the spin is in the $m_s = 0$ state [104].

2.1.8 Coherent spin manipulation

Rabi oscillations

The population dynamics between the energy levels of the NV center allow for initializing the spin into the $m_s = 0$ state. The NV spin can then be manipulated coherently by driving resonant spin transitions between $m_s = 0 \rightleftharpoons -1$ or $m_s = 0 \rightleftharpoons +1$ using microwaves.

If the $m_s = \pm 1$ states are energetically split by applying a constant external field along the quantization axis, one of the transitions can be ignored while the remaining transition can be considered as a two-level system. Two involved basis states are given

by:

$$|m_s = 0\rangle = |0\rangle = \begin{pmatrix} 0 \\ 1 \end{pmatrix} \quad |m_s = \pm 1\rangle = |1\rangle = \begin{pmatrix} 1 \\ 0 \end{pmatrix} \quad (2.3)$$

The ground state Hamiltonian (Eq. 2.1) is then given by the following matrix representation:

$$H_0 = \hbar \begin{pmatrix} \omega_0 & 0 \\ 0 & 0 \end{pmatrix} \quad (2.4)$$

Here ω_0 corresponds to the energy difference between $|0\rangle$ and $|1\rangle$.

If an additional linearly-polarized microwave field is applied, which oscillates in a plane orthogonal to the quantization axis, transitions between the two spin states can be driven. Due to selection rules the $m_s = 0 \rightleftharpoons +1$ ($m_s = 0 \rightleftharpoons -1$) transition can only be excited by the right (left)-circularly polarized component of the microwave magnetic field B_{mw}^+ (B_{mw}^-) [96]. In the following the $m_s = 0 \rightleftharpoons +1$ transition is considered which interacts with a magnetic field oscillating at frequency ω_{mw} . The overall Hamiltonian of the system is then described by:

$$H = H_0 + H_{\text{int}} = \hbar \begin{pmatrix} \omega_0 & \Omega \cos(\omega_{\text{mw}} t) \\ \Omega \cos(\omega_{\text{mw}} t) & 0 \end{pmatrix} \quad (2.5)$$

where H_{int} is the interaction Hamiltonian and $\Omega = g\mu_B B_{\text{mw}}^+ / \hbar$ denotes the Rabi frequency. This Hamiltonian is considered in the interaction picture, i.e. a frame rotating at frequency ω_0 with respect to the laboratory coordinates:

$$\begin{aligned} H &= \hbar \begin{pmatrix} 0 & \frac{\Omega}{2}(e^{i\omega_{\text{mw}} t} + e^{-i\omega_{\text{mw}} t})e^{i\omega_0 t} \\ \frac{\Omega}{2}(e^{i\omega_{\text{mw}} t} + e^{-i\omega_{\text{mw}} t})e^{-i\omega_0 t} & 0 \end{pmatrix} \\ &= \hbar \begin{pmatrix} 0 & \frac{\Omega}{2}(e^{i(\omega_{\text{mw}} + \omega_0)t} + e^{-i(\omega_{\text{mw}} - \omega_0)t}) \\ \frac{\Omega}{2}(e^{i(\omega_{\text{mw}} - \omega_0)t} + e^{-i(\omega_{\text{mw}} + \omega_0)t}) & 0 \end{pmatrix} \end{aligned} \quad (2.6)$$

For weak driving, $\Omega < \omega_0$, and if the frequency of the magnetic field ω_{mw} is close to being resonant with ω_0 , the rotating wave approximation can be applied. Slowly varying terms at frequency $\omega_{\text{mw}} - \omega_0$ are considered while quickly oscillating terms at frequency $\omega_{\text{mw}} + \omega_0$ are neglected since they average out on the timescale of the interaction.

Now the system is considered in a frame rotating with frequency ω_{mw} about the

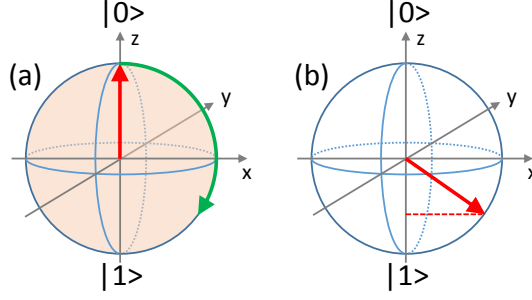


Fig. 2.8. Schematic of Rabi oscillations on the Bloch sphere. **(a)** The system is initially prepared in state $|0\rangle$. If a resonant microwave field is applied the spin rotates around the y -axis with the Rabi frequency Ω . **(b)** After a time t the microwave field is switched off leaving the spin in a superposition state of $|0\rangle$ and $|1\rangle$ depending on the rotation angle $\phi = \Omega t$. If the experiment is repeated several times under the same conditions, the average value of the readout of the spin state corresponds to the population difference of $|0\rangle$ and $|1\rangle$, which is given by z -component of the Bloch vector.

quantization axis where the Hamiltonian effectively becomes:

$$H = \hbar \begin{pmatrix} \Delta & \frac{\Omega}{2} \\ \frac{\Omega}{2} & 0 \end{pmatrix} \quad (2.7)$$

Here $\Delta = \omega_0 - \omega_{\text{mw}}$ is the relative detuning of the microwave field and the emitter transition. In general the state of the system in the rotating frame is described by the wavefunction:

$$|\Psi\rangle(t) = c_0 |0\rangle(t) + c_1(t) |1\rangle = \begin{pmatrix} c_1(t) \\ c_0(t) \end{pmatrix} \quad (2.8)$$

where $c_0(t)^2 + c_1(t)^2 = 1$. Solving the Schrödinger equation for zero detuning $\Delta = 0$ with the initial condition that the system is in state $|0\rangle$ ($c_0(0) = 1$, $c_1(0) = 0$) yields an oscillation of the occupation probabilities of the two states in time:

$$P_0(t) = |c_0(t)|^2 = \cos^2\left(\frac{\Omega}{2}t\right) = \frac{1}{2}(1 + \cos(\Omega t)) \quad (2.9)$$

$$P_1(t) = |c_1(t)|^2 = \sin^2\left(\frac{\Omega}{2}t\right) = \frac{1}{2}(1 - \cos(\Omega t)) \quad (2.10)$$

The cycling of population between the two states is denoted as “Rabi oscillation”. By controlling the duration of the interaction time t via gating of the microwave field, the spin state can be coherently driven into an arbitrary superposition. This coherent manipulation is an essential tool for various sensing schemes and allows the NV spin to be harnessed as a quantum bit for quantum information processing.

Bloch sphere

A useful concept to describe coherent spin rotations in the rotating frame constitutes the “Bloch vector”, whose entries can be defined with reference to the density matrix of the system $\rho = \sum_i p_i |\Psi_i\rangle \langle \Psi_i|$:

$$\rho = \begin{pmatrix} \rho_{00} & \rho_{01} \\ \rho_{10} & \rho_{11} \end{pmatrix} \quad (2.11)$$

The Bloch vector $\vec{a} = (x, y, z)$ is then given by:

$$\begin{aligned} x &= \rho_{10} - \rho_{01} \\ y &= i(\rho_{01} - \rho_{10}) \\ z &= \rho_{00} - \rho_{11} \end{aligned} \quad (2.12)$$

In this representation the z-axis gives the population difference, while the x- and y- axis are a measure for the coherences of the density matrix. Typically the Bloch vector is considered in the rotating frame of an external driving field ω_{mw} . At zero detuning of emitter and driving field $\Delta = \omega_0 - \omega_{mw} = 0$ the Bloch vector remains static in the rotating frame if the driving field is not switched on. If the emitter transition frequency is detuned from the driving frequency, $\Delta \neq 0$, on the other hand, the Bloch vector precesses about the z-axis with frequency Δ .

Using the concept of the Bloch sphere the Rabi oscillation between the populations of $|0\rangle$ and $|1\rangle$ under external driving (introduced in the previous section) can be interpreted as a rotation of the Bloch vector around the y-axis of the Bloch sphere, as illustrated in Fig. 2.8.

Decoherence

Decoherence describes the loss of information about the spin system due to interactions with the environment. If the system is initialized into one of its eigenstates the spin-lattice relaxation time T_1 gives the time scale on which the spin polarization decays to the thermal equilibrium. In the case of the NV center the main contribution to this decay is attributed to phonons, since the T_1 -time exhibits a strong temperature dependence ($T_1 \propto T^{-5}$ [105]). For the NV center T_1 approaches ~ 1 s in a cryogenic environment, where spin-flips due to lattice vibrations are strongly mitigated. The T_1 time is then limited by cross relaxation due to dipole-dipole interaction with other spin species [105]. The time scale on which a well-defined phase relation between the states of a coherent

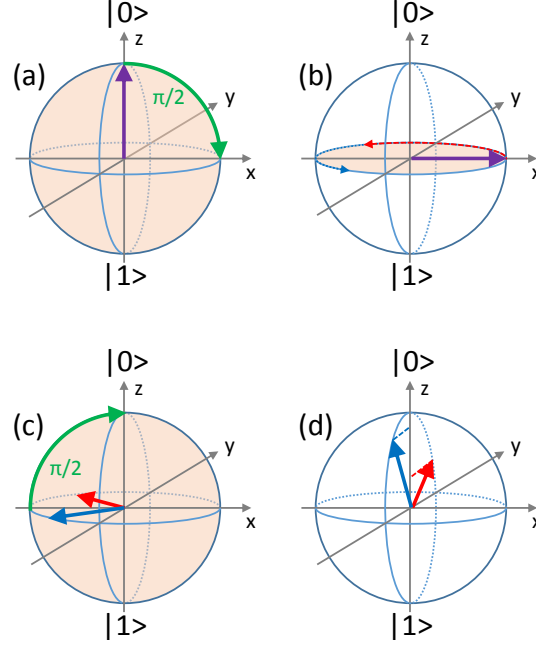


Fig. 2.9. Schematic of Ramsey interferometry for probing the coherence time of a spin superposition shown for two separate identically performed experiments (red and blue arrow). **(a)** The system is initially prepared in state $|0\rangle$. A resonant $\pi/2$ microwave pulse is applied that rotates about the y -axis into the equatorial plane of the Bloch sphere and creates a spin superposition. **(b)** The superposition state precesses for a time τ with a frequency given by the detuning Δ caused by an additional external magnetic field, which is different for the two separate experiments. **(c)** Using a further resonant $\pi/2$ microwave pulse the spins are rotated back into the yz -plane. **(d)** The expectation value of the measurement of the spin state corresponds to the z -component of the Bloch vector. The difference in precession angles results in different expectation values for the spin measurement in two identically prepared successive experiments, which deteriorates the signal averaged over several measurements. This process can be associated to decoherence due to magnetic fluctuations.

superposition is lost is given by the inhomogeneous dephasing time T_2^* . The coupling of the NV spin to the environment, specifically to fluctuating spins in the vicinity of the NV, limits T_2^* . By applying a “spin-echo” sequence low-frequency magnetic field noise can be overcome, which entails that the phase information is retained on a longer timescale T_2 - the homogeneous dephasing time.

T_2 measurements

The homogeneous spin coherence time T_2 of the NV center can be measured by creating a superposition of the two spin states $|0\rangle$ and $|1\rangle$, exploiting the technique of coherent spin manipulation (Sec. 2.1.8), and probing the temporal evolution of the superposition.

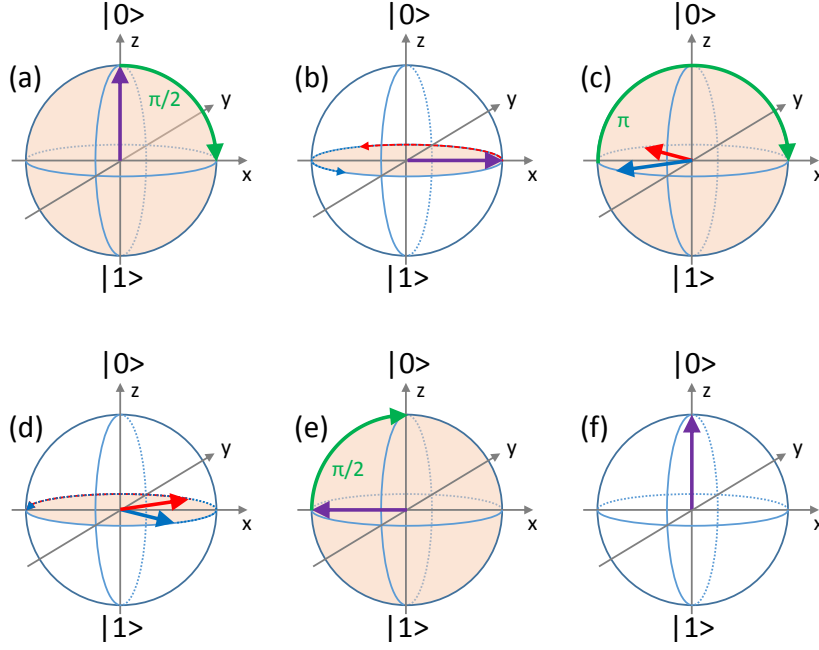


Fig. 2.10. Schematic of the Hahn-echo sequence for two separate identically performed experiments (red and blue arrow). **(a)** The system is initially prepared in state $|0\rangle$. A resonant $\pi/2$ microwave pulse is applied that rotates the Bloch vector about the y -axis into the equatorial plane of the Bloch sphere and creates a spin superposition. **(b)** The superposition state precesses for a given time $\tau/2$ with a frequency given by the detuning Δ , caused by an additional magnetic field from the environment. Due to fluctuations this detuning is typically different for the two successive experiments. **(c)** The spin superpositions are inverted in the equatorial plane using a π microwave pulse. **(d)** The Bloch vectors continue precessing in the equatorial plane. **(e)** After a further waiting time $\tau/2$ the vectors refocus on the negative x -axis if their respective detunings stay constant during the experiment time 2τ (for details see text). Using a further resonant $\pi/2$ microwave pulse the spins are rotated back into the yz -plane. **(f)** Reading out the population difference yields the same result for both experiments if the detuning stays constant over the time τ .

First, the Ramsey interferometry technique for probing the spin coherence is introduced (Fig. 2.9). If the system is prepared in the $|0\rangle$ state, the Bloch vector points to the north pole of the Bloch sphere. A microwave pulse of duration $t_{\pi/2}$ (i.e., $\Omega \cdot t_{\pi/2} = \pi/2$) creates a superposition of $|0\rangle$ and $|1\rangle$. This process corresponds to a $\pi/2$ -rotation of the Bloch vector about the y -axis onto the x -axis of the Bloch sphere.

Now the Bloch vector starts to precess in the equatorial plane about the quantization axis at the frequency of the detuning from resonance, Δ , caused by an additional magnetic field from the environment. After a delay time τ , another $\pi/2$ -microwave pulse is used to rotate the Bloch vector back to the yz -plane, after which the spin state ($|0\rangle/|1\rangle$) is read out. The average value of the spin state measurements obtain by several equiva-

lent experiments yields the population difference, which corresponds to the z-component of the Bloch vector. The experiment is then repeated for different waiting times τ . The magnitude of the z-component of the Bloch vector depends on the precession angle $\phi = \Delta\tau$, which results in the measurement of an oscillating population difference, which is often referred to as “Ramsey fringes”. If the detuning Δ is fluctuating, the expectation value for the spin state measurement between two successive experiments with the same waiting time τ is different. Since spectra in Ramsey interferometry are obtained by averaging several equivalent experiments, these fluctuations in the environment lead to a decay of the Ramsey oscillations on a time scale denoted as T_2^* .

Influences of the environment can be mitigated by applying a spin-echo technique (Fig. 2.10). The scheme is similar to Ramsey interferometry as introduced in the previous paragraph. First the spin is prepared $|0\rangle$ and a spin superposition is created by applying a $\pi/2$ microwave pulse. However in the spin-echo scheme, after the spin superposition has precessed for a certain waiting time $\tau/2$ and picked up a phase of $\phi = \Delta\tau/2$ the spin is inverted in the equatorial plane using a π microwave pulse, which changes the phase to $\phi = \pi - \Delta\tau/2$. If the detuning Δ is constant over τ , waiting for another time $\tau/2$ then results in an overall precession angle $\phi = \pi$, independent of the magnitude of Δ . Rotating the spin back into the yz -plane by a further $\pi/2$ microwave then leaves the Bloch vector pointing towards the north pole, which corresponds to always measuring the spin state $|0\rangle$ in identically performed experiments. Using the echo-scheme slow magnetic field fluctuations with frequencies $< 1/\tau$ are thereby compensated, since for slow fluctuations the detuning Δ is constant during the measurement time. The remaining decay of the spin coherence caused by rapid environmental fluctuations is then given by a timescale denoted as T_2 .

Sensitivity of magnetic field measurements

The NV center can be used as a magnetic sensor which allows highly sensitive probing of external magnetic fields at various frequencies. By evaluating the splitting of the peaks in an ODMR spectrum, constant magnetic fields can be determined. By driving the spin coherently inducing Rabi oscillations and by applying Ramsey interferometry or Spin Echo sequences alternating magnetic fields can be studied for different frequency regimes.

The major figure of merit of a sensor is the sensitivity η , which describes the smallest magnetic field δB which can be measured in a given measurement time t [96].

$$\eta = \delta B \sqrt{t} \quad (2.13)$$

The scaling of the sensitivity of all different NV sensing schemes can be described by a general formula [50]:

$$\eta \sim \frac{1}{\gamma_{\text{NV}}} \frac{1}{C\sqrt{I}} \frac{1}{T_{\text{coh}}} \quad (2.14)$$

Here, $\gamma_{\text{NV}} = g\mu_{\text{B}}/\hbar$ is the gyromagnetic ratio of the NV center, I is the detected fluorescence rate, C the fluorescence contrast between the spin levels and T_{coh} is the coherence time of the particular measurement.

Hence, there are several ways to improve the magnetic field sensitivity of the NV center. As mentioned in Sec. 2.1.1, the spin coherence time can be increased significantly by isotopically purifying the diamonds. For an NV in such a nuclear spin free environment coherence times of $T_2^* \sim 100 \mu\text{s}$ and $T_{2,\text{echo}} \sim 2 \text{ ms}$ have been reported [32, 106].

Furthermore, the sensitivity can be significantly boosted by increasing the NV PL intensity I . In order to avoid compromising the sensitivity due to power broadening I cannot be increased by simply using higher laser powers. One approach to obtain higher PL count rates is using ensembles of NV defects, where I is magnified by the number N of sensing spins. This improvement, however, comes at the cost of losing the potential atomic resolution of a single NV sensor.

A key problem for magnetic sensing with single NV centers is the low detection efficiency of the NV PL. Here, the essential limitation is the high refractive index of diamond ($n = 2.4$) which leads to total internal reflection at the diamond-air interface. Only photons emitted within the total internal reflection angle ($\theta = 22.6^\circ$) can be captured by the detection optics. Embedding the NV center into photonic structures like solid-immersion lenses, waveguides or antenna-structures mitigates the effect of total internal reflection. In fact, some of these structures even harness total internal reflection to guide a larger fraction of the PL towards the detection optics. In Ch. 4 our approach towards increasing the collection efficiency by embedding the NV center into a dielectric optical antenna is presented. The antenna channels 95 % of the NV PL into a solid angle corresponding to a numerical aperture (NA) of 0.8 [107].

2.1.9 Spin-photon and spin-spin entanglement

In order to be able to create long-distance entanglement between two NV centers, the method of entanglement swapping can be harnessed [108, 109, 110, 111]. To that end, the NV spin state needs to be entangled with a single emitted photon for both individual NV centers, where different degrees of freedom of the photonic state can be used like the polarization [17] or the temporal mode [26]. If the photons originating from the different NVs are indistinguishable and overlapped on a beamsplitter, the spins are projected on

a joint entangled state.

Recent experiments that demonstrated long-range spin-spin entanglement have shown that entangling the spin state with the photon using the temporal degree of freedom is technologically most feasible [26, 6]. Particularly, the Barret and Kok protocol [4] has been used which solely requires a spin-selective cycling transition between one of the ground states and an excited state. The description presented in Ref. [104] is followed:

First, two NV centers labeled A and B are initialized into the $m_s = 0$ ground state by optical spin pumping (Sec. 2.1.5) and a superposition of $m_s = 0$ ($|\uparrow\rangle$) and $m_s = -1$ ($|\downarrow\rangle$) is created using a resonant microwave $\pi/2$ -pulse (Sec. 2.1.8):

$$\frac{1}{\sqrt{2}}(|\uparrow\rangle + |\downarrow\rangle) \quad (2.15)$$

Second, a resonant optical excitation pulse affecting only $|\uparrow\rangle$ is applied. A successive resonant photon emission entangles the spin state of the NV with the presence of a photon:

$$\frac{1}{\sqrt{2}}(|\uparrow\rangle |1\rangle + |\downarrow\rangle |0\rangle) \quad (2.16)$$

where $|1\rangle/|0\rangle$ denotes the presence/absence of a photon.

Third, the spins are inverted coherently by applying a resonant microwave π -pulse:

$$\frac{1}{\sqrt{2}}(|\downarrow\rangle |1\rangle + |\uparrow\rangle |0\rangle) \quad (2.17)$$

Fourth, a further optical excitation pulse resonant with $|\uparrow\rangle$ entangles the spin state of the NV with the temporal mode of the photon:

$$\frac{1}{\sqrt{2}}(|\downarrow\rangle |L\rangle + |\uparrow\rangle |E\rangle) \quad (2.18)$$

If an early photon ($|E\rangle$) is detected the emitter was initially in the $|\uparrow\rangle$ while the detection of a late photon ($|L\rangle$) implies that the initial state was $|\downarrow\rangle$.

Finally, the photons originating from NV A and B are overlapped on a beamsplitter. The detection of one early and one late photon projects the spins of the two remote NV centers into a Bell state, in case the photons are otherwise indistinguishable:

$$\frac{1}{\sqrt{2}}(|\uparrow\rangle_A |\downarrow\rangle_B \pm |\downarrow\rangle_A |\uparrow\rangle_B) \quad (2.19)$$

Depending on whether the photons are detected in the same or two different output ports the joint state is either symmetric (+) or anti-symmetric (−). The detection of

the photons constitutes a herald for the spin entanglement, which allows, in principle, for entanglement preparation with unit fidelity. The success probability of this protocol is $\frac{1}{2}\eta^2$, where η denotes the overall detection probability of a photon emission triggered by resonant excitation from each side and the $\frac{1}{2}$ accounts for the need of detection two photons per entanglement.

The success probability η is given by the product of the probability of ZPL emission η_{ZPL} and the collection efficiency η_{coll} . In Ch. 3 our approach towards increasing the overall detection probability of ZPL emission by coupling the ZPL to a resonant cavity is reported. The cavity coupling results in an increase of the probability of ZPL η_{ZPL} emission from $\sim 3\%$ to $\sim 46\%$ [112]. With a further improvement of the collection efficiency η_{coll} a significant increase of the entanglement success probability is therefore anticipated.

2.2 Cavity quantum electrodynamics

The theory of quantum electrodynamics (QED) provides accurate predictions on how light and matter interact. If photons are confined in a reflective cavity the light-matter interaction is significantly enhanced and theoretically treated in the sub-field of cavity QED. The ideal case of confined photons interacting with a two-level system is described by the Jaynes-Cummings model (Sec. 2.2.1). In a realistic scenario the coupling of photons with matter is impaired by losses. These can either be due to photons leaking out of the cavity or material excitations decaying into non-resonant channels. For solid-state based single emitters, in particular NV centers, these losses typically exceed the emitter-photon coupling which results in the “weak coupling regime” for the system (Sec. 2.2.2). Hemispherical optical resonators have proven particularly well-suited system for the coupling with solid-state emitters due to their robustness to alignment errors and high finesse values [113, 114, 115].

2.2.1 Jaynes-Cummings model

The Jaynes-Cummings model treats the interaction of a two-level emitter exhibiting an energetic splitting of $\hbar\omega_e$ with the electromagnetic field of a single cavity mode at frequency ω_{cav} . The Hamiltonian describing this system comprises three different con-

tributions; the emitter, the cavity mode and their interaction:

$$\begin{aligned} H &= H_e + H_{\text{cav}} + H_{\text{int}} = \hbar\omega_e a^\dagger a + \hbar\omega_{\text{cav}} b^\dagger b + \hbar g \hat{E} \hat{S} \\ &= \hbar\omega_e a^\dagger a + \hbar\omega_{\text{cav}} b^\dagger b + \hbar g (a + a^\dagger) \cdot (b + b^\dagger) \end{aligned} \quad (2.20)$$

The interaction term consists of the electric field operator $\hat{E} = (a + a^\dagger)$, the emitter polarization operator $\hat{S} = (b + b^\dagger)$ and the emitter-photon coupling rate g . Here, a^\dagger/a and b^\dagger/b describe creation/annihilation of cavity photons and emitter excitations, respectively.

The time-dependence of the interaction Hamiltonian in a frame rotating with the frequency of the emitter transition ω_e is then given by:

$$\begin{aligned} H_{\text{int}}(t) &= \hbar g \left(a e^{i\omega_{\text{cav}} t} + a^\dagger e^{-i\omega_{\text{cav}} t} \right) \cdot \left(b e^{i\omega_e t} + b^\dagger e^{-i\omega_e t} \right) \\ &= \hbar g \left(a b e^{i(\omega_{\text{cav}} + \omega_e)t} + a b^\dagger e^{i(\omega_{\text{cav}} - \omega_e)t} + a^\dagger b e^{-i(\omega_{\text{cav}} - \omega_e)t} + a^\dagger b^\dagger e^{-i(\omega_{\text{cav}} + \omega_e)t} \right) \end{aligned} \quad (2.21)$$

If the frequency of the cavity mode ω_{cav} is close to being resonant with the emitter transition frequency ω_e and the interaction rate is small, $g < \omega_{\text{cav}}$, the rotating wave approximation can be applied. Slowly varying terms at frequency $\omega_{\text{cav}} - \omega_e$ are retained while quickly oscillating terms at frequency $\omega_{\text{cav}} + \omega_e$ are neglected as they average out on the relevant time scale. This approximation and transforming back into the Schrödinger picture yields the Jaynes-Cummings Hamiltonian [116]:

$$H_{\text{JC}} = \hbar\omega_{\text{cav}} a^\dagger a + \hbar\omega_e b^\dagger b + \hbar g (b^\dagger a + a^\dagger b) \quad (2.22)$$

Here ab^\dagger is replaced with $b^\dagger a$ taking advantage of the fact that creation and annihilation operators for the two different systems commute. This Hamiltonian couples only pairs of states where the emitter is either in the ground (g) or excited state (e), while there are either $n + 1$ or n photons present in the cavity mode:

$$|g, n + 1\rangle \xrightleftharpoons[a^\dagger b]{b^\dagger a} |e, n\rangle \quad (2.23)$$

The pairs of coupled states can then be considered as an effective two-level system with the basis states:

$$|g, n + 1\rangle = \begin{pmatrix} 0 \\ 1 \end{pmatrix} \quad |e, n\rangle = \begin{pmatrix} 1 \\ 0 \end{pmatrix} \quad (2.24)$$

which means that in this basis the Hamiltonian can be represented by the following

matrix [117]:

$$H_{JC} = \hbar \begin{pmatrix} \omega_e + n\omega_{\text{cav}} & g\sqrt{n+1}e^{-i\omega_{\text{cav}}t} \\ g\sqrt{n+1}e^{-i\omega_{\text{cav}}t} & (n+1)\omega_{\text{cav}} \end{pmatrix} \quad (2.25)$$

The corresponding normalized eigenstates of the Hamiltonian are the so-called dressed states:

$$|+, n\rangle = \frac{|e, n\rangle + |g, n+1\rangle}{\sqrt{2}} \quad (2.26)$$

$$|-, n\rangle = \frac{|e, n\rangle - |g, n+1\rangle}{\sqrt{2}} \quad (2.27)$$

The eigenenergies of these state are:

$$E_{\pm} = \frac{\hbar\omega_e}{2} + \omega_{\text{cav}} \left(n + \frac{1}{2} \right) \pm \frac{1}{2}\hbar\Omega_n \quad (2.28)$$

where $\Omega_n = \sqrt{4g^2(n+1) + \Delta^2}$ is the Rabi frequency of the system with $\Delta = \omega_e - \omega_{\text{cav}}$ being the detuning of cavity and emitter.

By shifting the energetic origin to $(n+1)\hbar\omega_{\text{cav}}$ and in a frame rotating with frequency ω_{cav} the system is described by the effective Hamiltonian:

$$H_{JC} = \hbar \begin{pmatrix} \Delta & g\sqrt{n+1} \\ g\sqrt{n+1} & 0 \end{pmatrix} \quad (2.29)$$

This Hamiltonian has the same structures as Eq. 2.7. At zero detuning $\Delta = 0$ in general a pure state of the system is described by the wavefunction

$$|\Psi\rangle = c_g(t) |g, n+1\rangle + c_e(t) |e, n\rangle = \begin{pmatrix} c_g(t) \\ c_e(t) \end{pmatrix} \quad (2.30)$$

where $c_e(t)^2 + c_g(t)^2 = 1$. For zero detuning and if the emitter is initially in the excited state at $t = 0$, $c_e(0) = 1$ and $c_g(0) = 0$, the solution of the Schrödinger equation describes an oscillation of the occupation probabilities of the two states in time:

$$P_e(t) = |c_e(t)|^2 = \cos^2((\sqrt{n+1})gt) = \frac{1}{2}(1 + \cos(\sqrt{n+1} \cdot 2gt)) \quad (2.31)$$

$$P_g(t) = |c_g(t)|^2 = \sin^2((\sqrt{n+1})gt) = \frac{1}{2}(1 - \cos(\sqrt{n+1} \cdot 2gt)) \quad (2.32)$$

If the system does not involve any external photons $|e, 0\rangle \rightleftharpoons |g, 1\rangle$, i.e. if the photon involved originates from a spontaneous emission process, $\Omega_{\text{vac}} = 2g$ is called the single-

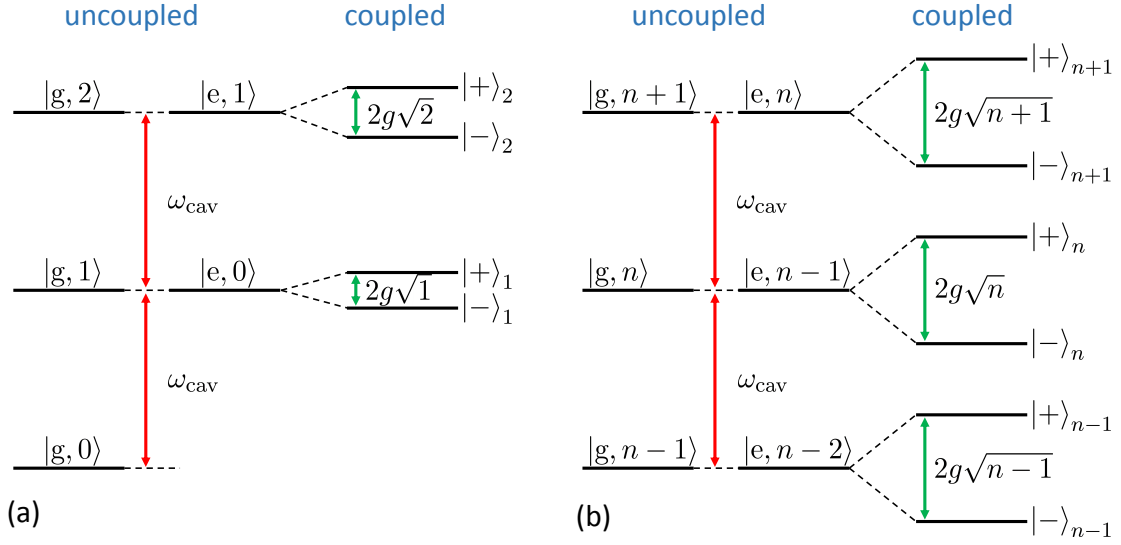


Fig. 2.11. Schematic of a two-level emitter coupled to a cavity by the emitter-cavity coupling rate g . In the uncoupled case the energies of the combined system of emitter being in the ground state (g) with $n + 1$ photons present in the cavity and emitter being in the excited state (e) with n photons present in the cavity are energetically degenerate. In the coupled case new Eigenstates form whose Eigenenergies are split by an energetic difference of $\hbar 2g\sqrt{n+1}$. **(a)** In the case of a single excitation ($|e, 0\rangle \rightleftharpoons |g, 1\rangle$) the coupling frequency is called the vacuum Rabi frequency $\Omega_{\text{vac}} = 2g$. **(b)** For a large number of photons n the Rabi splitting is almost constant $\approx 2g\sqrt{n}$, which allows for deriving the semi-classical limit for a coherent state $|\alpha\rangle$ with a large average photon number $\langle n \rangle \gg 1$ (for details see text)

photon or vacuum Rabi frequency (Fig. 2.11(a)). In this case an emitter initially emits a photon via spontaneous emission, which is then reversibly re-absorbed and re-emitted resulting in vacuum Rabi oscillations.

Note that, if the case of an external photon field in a coherent state $|\alpha\rangle$ is considered the interaction of the field and the emitter is obtained by summation of the Rabi oscillations between the coupled pairs $|g, n+1\rangle \rightleftharpoons |e, n\rangle$ for all involved Fock states $|n\rangle$. Considering a coherent state with a large average photon number $\langle n \rangle \gg 1$ and hence $\Delta n / \langle n \rangle \ll 1$ the Rabi frequencies of all involved Fock states are almost equal in magnitude ($\dots \approx 2g\sqrt{n-1} \approx 2g\sqrt{n} \approx 2g\sqrt{n+1} \approx \dots$) (Fig. 2.11(a)). In this case, the same result as in the semi-classical description is obtained (Eq. 2.9), where the Rabi frequency is given by $\Omega \approx 2g\sqrt{n}$.

To conclude this section, it is noted that the description of the interaction of an emitter with an electric field is conceptually equivalent to the interaction of a spin with a magnetic field as described in Sec. 2.1.8. Both cases constitute a two-level system coupled to a harmonic oscillator.

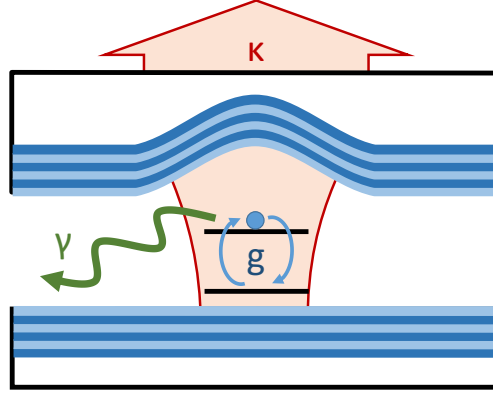


Fig. 2.12. Schematic of a two-level emitter coupled to a cavity by the emitter-cavity coupling rate g . Excitation from the system are caused by photon loss κ due to scattering, absorption or transmission through the mirrors and loss of emitter excitation γ due to decay via channels other than the cavity mode.

2.2.2 Emitter-cavity coupling including system losses

So far it has been assumed that no excitations are lost from the system. In a realistic scenario a photon loss rate κ out of the cavity due to scattering, absorption or transmission through the mirrors needs to be accounted for (Fig. 2.12). In addition, emitter excitations are lost from the system at rate γ due to decay via channels other than the cavity mode. In this case, the time evolution of the density matrix can be calculated using the Lindblad formalism. In the one-excitation limit, i.e. for the basis $|g, 0\rangle$, $|g, 1\rangle$ and $|e, 0\rangle$, the following solutions for the average photon and excitation numbers for an initial emitter excitation, $\langle a^\dagger a \rangle(0) = 0$ and $\langle b^\dagger b \rangle(0) = 1$, are obtained (for derivation see Sec. B):

$$\langle a^\dagger a \rangle(t) = e^{-\frac{\kappa+\gamma}{2}t} \left(\frac{g}{\eta} \sinh(\eta t) \right)^2 \quad (2.33)$$

$$\langle b^\dagger b \rangle(t) = e^{-\frac{\kappa+\gamma}{2}t} \left(\cosh(\eta t) + \frac{\kappa - \gamma}{4\eta} \sinh(\eta t) \right)^2 \quad (2.34)$$

where $\eta = \sqrt{((\kappa - \gamma)/4)^2 - g^2}$. Depending on the ratio of g , κ and γ the two different regimes of strong and weak coupling can be distinguished.

Strong coupling ($g \gg \kappa, \gamma$)

In the strong coupling regime the coupling rate of photon and emitter g is large compared to the losses κ and γ . For $\eta \approx ig$ and using the identities $\sinh(x) = -i \sin(ix)$ and

$\cosh(x) = \cos(ix)$ the average photon and excitation numbers are described by damped Rabi oscillations at the vacuum Rabi frequency $\Omega_{\text{vac}} = 2g$ (compare Eq. 2.9). The initial conditions $\langle a^\dagger a \rangle(0) = 0$ and $\langle b^\dagger b \rangle(0) = 1$ result in:

$$\langle a^\dagger a \rangle(t) = e^{-\frac{\kappa+\gamma}{2}t} \sin^2(gt) = e^{-\frac{\kappa+\gamma}{2}t} \frac{1}{2}(1 - \cos(2gt)) \quad (2.35)$$

$$\langle b^\dagger b \rangle(t) = e^{-\frac{\kappa+\gamma}{2}t} \cos^2(gt) = e^{-\frac{\kappa+\gamma}{2}t} \frac{1}{2}(1 + \cos(2gt)) \quad (2.36)$$

Weak coupling ($g \ll \kappa, \gamma$)

If the photon or excitation losses occur at a higher rate than the time it takes the emitter to re-absorb the photon the system is in the weak coupling regime. Here, the system decays with a rate increased above the decay rate in free space γ (for derivation see Sec. B):

$$\langle b^\dagger b \rangle(t) = e^{-F_P \gamma t} \quad (2.37)$$

The Purcell factor F_P is given by:

$$F_P = 1 + \frac{4g^2}{\kappa\gamma} \quad (2.38)$$

where the term $C = 4g^2/(\kappa\gamma)$ is denoted as cooperativity [114].

2.2.3 Spontaneous emission and Purcell enhancement

The transition rate in the weak coupling regime can alternatively be derived using Fermi's golden rule [37], which describes the transition rate between an initial state (i) and a set of final states (f) due to a perturbation:

$$\Gamma_{i \rightarrow f} = \frac{2\pi}{\hbar^2} |M_{i \rightarrow f}|^2 \rho \quad (2.39)$$

Here, ρ is the density of final states and $M_{i \rightarrow f} = \langle f | H_p | i \rangle$ is the transition matrix element between initial and final state for a perturbing Hamiltonian H_p . In the spontaneous emission process the coupling of the dipole moment of the emitter $\vec{\mu}_{eg}$ to the fluctuating vacuum field \vec{E}_{vac} perturbs the system causing a transition from the excited state (e) to the ground state (g).

$$\Gamma_{e \rightarrow g} = \frac{2\pi}{\hbar^2} |M_{e \rightarrow g}|^2 \rho = \frac{2\pi}{\hbar^2} |\vec{\mu}_{eg} \cdot \vec{E}_{\text{vac}}|^2 \rho \quad (2.40)$$

The dipole moment can be described by $\vec{\mu}_{eg} = q\langle g|\vec{d}|e\rangle$ where q is the electric charge and \vec{d} is the electric dipole operator. The electric field amplitude of the vacuum fluctuations at a specific frequency ω can be calculated via

$$|\vec{E}_{\text{vac}}| = \sqrt{\frac{\hbar\omega}{2\epsilon_0\epsilon_R V}} \quad (2.41)$$

where V is volume to which the field is confined.

Considering a homogeneous medium with refractive index n the density of states is given by [118]:

$$\rho_{\text{hom}}(\omega) = \frac{\omega^2 V}{\pi^2 (c/n)^3} \quad (2.42)$$

Vacuum fluctuations exhibit a random orientation with respect to the dipole moment of the emitter, hence an average over all angles is taken and $\vec{\mu}_{eg} \cdot \vec{E}_{\text{vac}} = \cos(\theta)\mu_{eg}E_{\text{vac}} = \frac{1}{3}\mu_{eg}E_{\text{vac}}$, where θ is the relative angle between $\vec{\mu}_{eg}$ and \vec{E}_{vac} . Using Eq. 2.40 gives the following expression for the decay rate of an emitter within a homogeneous medium:

$$\Gamma_{\text{hom}} = \frac{\mu_{ge}^2 \omega^3}{3\hbar\epsilon_0\epsilon_R\pi(c/n)^3} \quad (2.43)$$

Notably, the confinement volume V cancels out, which renders the need for defining to which volume the fluctuations are confined in a homogeneous medium unnecessary.

Determining Γ_{hom} in an experiment, allows the determination of the dipole moment of an emitter:

$$\mu_{ge} = \sqrt{\frac{3\hbar\epsilon_0\epsilon_R\pi(c/n)^3\Gamma_{\text{hom}}}{\omega^3}} \quad (2.44)$$

Here it is assumed that the emitter exhibits a quantum yield of 100 %, which means that there are no non-radiative decay channels.

If the vacuum fluctuations are confined with the aid of a cavity, V corresponds to the cavity mode volume. The frequency dependence of the density of final states in case of a cavity is given by the Lorentzian cavity resonance.

$$\rho_{\text{cav}}(\omega) = \frac{2}{\pi\delta\omega_{\text{cav}}} \frac{\delta\omega_{\text{cav}}^2}{4(\omega - \omega_{\text{cav}})^2 + \delta\omega_{\text{cav}}^2} = \frac{2Q}{\pi\omega_{\text{cav}}} \frac{\delta\omega_{\text{cav}}^2}{4(\omega - \omega_{\text{cav}})^2 + \delta\omega_{\text{cav}}^2} \quad (2.45)$$

where $Q = \omega_{\text{cav}}/\delta\omega_{\text{cav}}$ is the quality factor of the cavity (compare Eq. 2.70) and $\delta\omega_{\text{cav}}$ corresponds to the FWHM of the resonance. $\rho_{\text{cav}}(\omega)$ fulfills the normalization condition

$$\int_0^\infty \rho_{\text{cav}}(\omega) d\omega = 1 \quad (2.46)$$

Using Eq. 2.40 the emission rate of the emitter into the cavity mode is obtained:

$$\Gamma_{\text{cav}} = \frac{2Q\mu_{ge}^2}{\hbar\epsilon_0 V} \cos^2(\theta) \frac{\delta\omega_{\text{cav}}^2}{4(\omega - \omega_{\text{cav}})^2 + \delta\omega_{\text{cav}}^2} \quad (2.47)$$

The overall emission rate is then described by

$$\Gamma_{\text{tot}} = \Gamma_{\text{hom}} + \Gamma_{\text{cav}} = \left(1 + \frac{\Gamma_{\text{cav}}}{\Gamma_{\text{hom}}}\right) \Gamma_{\text{hom}} = F_{\text{P}} \Gamma_{\text{hom}} \quad (2.48)$$

Here, it is assumed that the presence of the cavity does not affect the recombination rate of the emitter, Γ_{hom} , for modes other than the cavity mode.*

The total recombination rate Γ_{tot} is then given by the sum of the accelerated emission in the cavity mode Γ_{cav} and Γ_{hom} . Using Eqs. 2.43 and 2.47 the Purcell factor F_{P} can be calculated:

$$\begin{aligned} F_{\text{P}} = 1 + \frac{\Gamma_{\text{cav}}}{\Gamma_{\text{hom}}} &= 1 + \frac{2Q\mu_{ge}^2}{\Gamma_{\text{hom}}\hbar\epsilon_0 V} \cos^2(\theta) \frac{\delta\omega_{\text{cav}}^2}{4(\omega - \omega_{\text{cav}})^2 + \delta\omega_{\text{cav}}^2} \\ &= 1 + \frac{3Q(\lambda_{\text{cav}}/n)^3}{4\pi^2 V} \cos^2(\theta) \frac{\delta\omega_{\text{cav}}^2}{4(\omega - \omega_{\text{cav}})^2 + \delta\omega_{\text{cav}}^2} \end{aligned} \quad (2.49)$$

Here c/ω_{cav} is replaced by $(\lambda_{\text{cav}}/2\pi)$.

On resonance $\omega = \omega_{\text{cav}}$ and if the emitter is aligned with the cavity field $\cos(\theta) = 1$ one obtains:

$$F_{\text{P}} = 1 + \frac{\Gamma_{\text{cav}}}{\Gamma_{\text{hom}}} = 1 + \frac{3Q(\lambda/n)^3}{4\pi^2 V} \quad (2.50)$$

Using Eq. 2.38 and performing the replacements

$$g = \frac{\mu_{ge} E_{\text{vac}}}{\hbar} \quad (2.51)$$

$$\kappa = \delta\omega = \frac{\omega}{Q} \quad (2.52)$$

$$\gamma = \Gamma_{\text{hom}} = \frac{\mu_{ge}^2 \omega^3}{3\hbar\epsilon_0 \epsilon_{\text{R}} \pi (c/n)^3} \quad (2.53)$$

*For certain type of cavities the spontaneous emission rate Γ_{hom} into modes other than the cavity mode can be strongly inhibited. Inhibition factors up to 70 were achieved using photonic crystal cavities, [119].

one obtains

$$\begin{aligned} F_P &= 1 + 4 \frac{\mu_{ge}^2 E_{\text{vac}}^2}{\hbar^2} \frac{Q}{\omega} \frac{3\hbar\epsilon_0\epsilon_R\pi(c/n)^3}{\mu_{ge}^2\omega^3} \\ &= 1 + \frac{24E_{\text{vac}}^2 Q\epsilon_0\epsilon_R\pi(c/n)^3}{\hbar\omega^4} \end{aligned} \quad (2.54)$$

It is noteworthy that here μ_{ge} cancels out, which means that the magnitude of the Purcell enhancement F_P is independent from the properties of the emitter given that it emits via a single dipole. By replacing E_{vac} (Eq. 2.41) the same expression for F_P as in Eq. 2.50 is found:

$$\begin{aligned} F_P &= 1 + \frac{24E_{\text{vac}}^2 Q\epsilon_0\epsilon_R\pi(c/n)^3}{\hbar\omega^4} \\ &= 1 + \frac{6\pi Q(c/n)^3}{V\omega^3} = 1 + \frac{3Q(\lambda/n)^3}{4\pi^2 V} \end{aligned} \quad (2.55)$$

Fermi's golden rule concerns an open system undergoing a weak interaction with its environment where an excited state decays into a continuum of modes described by the density of states. It is assumed that the photons emitted into these modes are “lost” meaning that they are not re-absorbed by the system.

This scenario corresponds to the weak coupling regime of cavity QED, where the coupling rate of a photon to the emitter is way smaller than the photon loss rate $g \ll \kappa$. This means that once the emitter has emitted a photon, this photon will not interact with the emitter before its “lost” from the system.

2.3 Plano-concave Fabry-Pérot cavities

In general, a Fabry-Pérot cavity comprises two curved mirrors that are arranged such that light bouncing back and forth between them forms a standing wave. The light in a curved-mirror cavity is well described via Gaussian optics within the paraxial approximation. The general set of solutions to the paraxial wave equation in Cartesian coordinates is given by [120]:

$$E(x, y, z)_{nm} = E_0 \frac{w_0}{w(z)} H_n \left(\sqrt{2} \frac{x}{w} \right) H_m \left(\sqrt{2} \frac{y}{w} \right) e^{-i(kz - \Phi_{nm}(z)) - i\frac{k}{4}(x^2 + y^2)} \quad (2.56)$$

where w_0 and $w(z)$ are the radius of the beam at the waist and at a distance z from the waist, respectively. The indices n and m are integers describing higher order transverse modes and H_n and H_m denote the Hermite polynomials. The term $\phi_{nm}(z) = (n +$

$m + 1) \arctan(z/z_R)$ is called the Gouy phase where $z_R = n\pi w_0^2/\lambda$ is the Rayleigh length. The Gouy phase describes the additional phase shift a Gaussian beam picks up at a distance z away from the focus in comparison to a planar wave with the same wavevector $k = 2\pi/\lambda$. The axial extent of the Gaussian beam depends on k and the integer q which describes the axial mode number.

Assuming perfect mirrors the cavity resonance condition is fulfilled when the Gaussian beam replicates itself after one round trip, which implies a round trip phase change of $\phi_{nm} = q \cdot 2\pi$:

$$\phi_{nm} = 2kL - 2(n + m + 1) \left(\arctan\left(\frac{z_2}{z_R}\right) - \arctan\left(\frac{z_1}{z_R}\right) \right) = q \cdot 2\pi \quad (2.57)$$

Here L is the spacing of the mirrors and z_1 and z_2 are the z -coordinates of the two mirrors with respect to the waist at $z = 0$.

The dimensionless parameters $g_1 = 1 - L/R_1$ and $g_2 = 1 - L/R_2$ are defined, where R_1 and R_2 are the respective radii of curvature of the two mirrors. The resonance frequencies of the cavity ν_{nmq} can be derived from Eq. 2.57 for $g_1, g_2 > 0$ implying $L < R_1, R_2$. “After a fair amount of algebra” the result is [120]:

$$\nu_{nmq} = \left(q + (n + m + 1) \frac{\arccos(\sqrt{g_1 g_2})}{\pi} \right) \frac{c}{2L} \quad (2.58)$$

This formula describing the cavity resonances sets constraints for possible stable cavity geometries: $0 \leq g_1 g_2 \leq 1$.

For our experiments (Ch.3), we opt for a plano-concave resonator comprising one plane and one curved mirror as in this geometry the mode waist is located at the plane mirror, where the NV center can be readily positioned. For the plane mirror $R_2 \rightarrow \infty$ ($g_2 = 1$) which effectively renders the stability criterion $0 \leq g_1 \leq 1$ or $L \leq R$ with $R = R_1$.

If the free spectral range $\Delta\nu_{\text{FSR}} = c/(2L)$ is introduced as the frequency spacing of two adjacent axial modes and the frequency spacing $\Delta\nu_{\text{trans}}$ of two adjacent higher order transverse modes is determined using Eq. 2.58 one obtains:

$$\begin{aligned} \Delta\nu_{\text{trans}} &= \frac{\Delta\nu_{\text{FSR}}}{\pi} \arccos\left(\sqrt{1 + \frac{R}{L}}\right), \text{ i.e.,} \\ R &= L \left[1 - \cos^2\left(\frac{\Delta\nu_{\text{trans}}}{\Delta\nu_{\text{FSR}}} \pi\right) \right]^{-1} \end{aligned} \quad (2.59)$$

This equation allows one to determine the radius of curvature of the top mirror by analyzing the frequency spacings of the different modes.

For a plano-concave resonator the radius of the beam waist at the plane mirror w_0 and the curved mirror w_1 can be calculated according to [120]:

$$w_0 = \sqrt{\frac{\lambda/n}{\pi}} (LR - L^2)^{\frac{1}{4}}, \quad (2.60)$$

$$w_1 = \sqrt{\frac{(\lambda/n)R}{\pi}} \left(\frac{R}{L} - 1 \right)^{-\frac{1}{4}} \quad (2.61)$$

In order to maximize the coupling strength of the cavity to an emitter located close to the planar surface the separation of the mirrors L has to be minimized.

Another approach is to operate the cavity in the near concentric regime $L \rightarrow R$ to minimize w_0 [121, 122]. In this regime, high coupling strengths can be achieved for non-microscopic mirror spacings. However, the larger beam waist at the curved mirror w_1 makes this geometry prone to high photon losses due to beam clipping.

Next, the standing wave within the cavity is described. An electromagnetic wave with amplitude E_0 is considered which is incident on a two-mirror cavity spaced by L . Given the reflection coefficients r_1, r_2 and transmission coefficients t_1, t_2 of the two mirrors, the electric field inside the cavity can be described by an infinite geometric series [120]:

$$E_{\text{cav}} = E_0 t_1 \sum_{j=1}^{\infty} \left(r_1 r_2 e^{-i\phi} \right)^j = \frac{E_0 t_1}{1 - r_1 r_2 e^{-i\phi}} \quad (2.62)$$

where ϕ is the round trip phase delay given by Eq. 2.57. The intensity of the field circulating inside the cavity can be calculated using $I_{\text{cav}} = |E_{\text{cav}}|^2$

$$I_{\text{cav}} = |E_{\text{cav}}|^2 = \left| \frac{E_0 t_1}{1 - r_1 r_2 e^{-i\phi}} \right|^2 = I_0 \frac{t_1^2}{(1 - r_1 r_2)^2 + 4r_1 r_2 \sin^2(\phi/2)} \quad (2.63)$$

which, to a good approximation, is a Lorentzian centered around $\phi = q \cdot 2\pi$. The full width at half maximum (FWHM) of this function is given by:

$$\text{FWHM} = 2\phi_{1/2} = \frac{2(1 - r_1 r_2)}{\sqrt{r_1 r_2}} \quad (2.64)$$

where $\phi_{1/2}$ is the phase at half the intensity. The ratio of the phase free spectral range of the cavity $\Delta\delta_{\text{FSR}} = 2\pi$ and the FWHM of the resonance is defined as the finesse of the cavity:

$$\mathcal{F} = \frac{\Delta\delta_{\text{FSR}}}{2\phi_{1/2}} = \frac{\pi\sqrt{r_1 r_2}}{(1 - r_1 r_2)} \quad (2.65)$$

Alternatively the finesse can also be defined in terms of cavity length L and frequency

of the electromagnetic field ν :

$$\mathcal{F} = \frac{\Delta L_{\text{FSR}}}{\delta L} = \frac{\lambda/n}{2\delta L} \quad (2.66)$$

$$\mathcal{F} = \frac{\Delta \nu_{\text{FSR}}}{\delta \nu} = \frac{c/n}{2L\delta \nu} \quad (2.67)$$

where δL and $\delta \nu$ are the resonance peak widths on detuning L and ν , respectively. For a cavity exhibiting a round-trip loss \mathcal{L}_{cav} and low mirror transmissions $\mathcal{T}_1 = |t_1|^2$ and $\mathcal{T}_2 = |t_2|^2$ with $|t_i|^2 = 1 - |r_i|^2$ the finesse can be approximated by [123]:

$$\mathcal{F} = \frac{2\pi}{\mathcal{L}_{\text{tot}}} \quad (2.68)$$

where $\mathcal{L}_{\text{tot}} = \mathcal{L}_{\text{cav}} + \mathcal{T}_1 + \mathcal{T}_2$ are the total cavity losses.

In general, the quality-factor (Q -factor) is a measure of the energy loss rate of a resonator relative to its stored energy and is given by:

$$Q = \omega \frac{2L}{(c/n)\mathcal{L}_{\text{tot}}} = \omega t_{\text{cav}} = \frac{2L\nu}{c/n} \mathcal{F} = \frac{2L}{\lambda/n} \mathcal{F} \quad (2.69)$$

where $t_{\text{cav}} = 2L/(c\mathcal{L}_{\text{tot}})$ is the photon lifetime inside the cavity and \mathcal{L}_{tot} is replaced using Eq. 2.68. This relationship can be interpreted such that the Q -factor equals the finesse times the number of half-waves between the mirrors in a standing wave cavity. Defining the round trip time as $\tau = 2L/c$ in Eq. 2.69 one obtains $Q = \nu\tau\mathcal{F}$ with which \mathcal{F} can be interpreted as relative round-trip energy loss of the cavity. Combining Eq. 2.69 and Eq. 2.66, it is verified that the Q -factor also gives the frequency resolution of the resonator:

$$Q = \frac{\nu}{\delta \nu} = \frac{\omega}{\delta \omega} = \frac{\omega}{\kappa} \quad (2.70)$$

Here $\kappa = 2\pi/(\tau\mathcal{F})$ is the photon loss rate of the cavity.

From Eq. 2.50 it can be inferred that in order to get a large Purcell enhancement factor F_P , the ratio Q/V needs to be optimized. Considering a short cavity $w_1 \approx w_0$ (Eq. 2.60) can be approximated and hence the mode volume can be described via [124]:

$$V = \pi \frac{w_0^2}{4} L \quad (2.71)$$

The beam waist w_0 increases with increasing cavity length L and larger radii of curvatures of the top mirror R ; V is thus minimized for as short as possible cavities and small R .

In a short plano-concave cavity there is an alternative way to describe the interaction

of an emitter with a cavity mode [125]. Using Eq. 2.50 and inserting $V = Lw_0^2\pi/4$ (Eq. 2.71) and $Q = \mathcal{F} \cdot 2L/(\lambda/n)$ (Eq. 2.69) yields

$$F_P = 1 + \frac{3\mathcal{F} \cdot 2L/(\lambda/n) \cdot (\lambda/n)^3}{4\pi^2 L w_0^2 \pi/4} = 1 + \underbrace{\frac{3(\lambda/n)^2}{2\pi}}_{\sigma_{\text{abs}}} \cdot \underbrace{\frac{\mathcal{F}}{\pi}}_{\substack{\# \text{ of} \\ \text{bounces}}} / \underbrace{\left(\frac{\pi}{4}w_0^2\right)}_{\text{beam area}} \quad (2.72)$$

The Purcell enhancement can be interpreted such that the absorption cross section of the emitter σ_{abs} is effectively increased by a factor \mathcal{F}/π , which corresponds to how many times the photon is bouncing back and forth between the mirrors.

While the geometrical description of the mode volume V is in many cases a good approximation it fails to predict the magnitude of the vacuum field E_{vac} (Eq. 2.41) for cavity systems which exhibit a more complex structure of the vacuum field distribution. For these systems $F_P \propto Q/V$ (Eq. 2.50) does not yield the correct value for the Purcell factor F_P .

For the cavity-coupling experiment presented in Ch. 3 a correct prediction of F_P is obtained by calculating the relevant magnitude of the vacuum field E_{vac} at the emitter position using a transfer-matrix approach (for more details see Sec. 3.3.4). For a given Q -factor F_P can then be calculated via Eq. 2.54. Furthermore, if E_{vac} is known using Eq. 2.41 an effective mode volume V_{eff} can be determined, for which $F_P \propto Q/V_{\text{eff}}$ using Eq. 2.50 yields the correct result.

According to Eq. 2.69 the Q -factor scales linearly with the cavity length L and the finesse \mathcal{F} . Increasing L , however, results in a super-linear increase of V (Eq. 2.71) due to the L -dependence of w_0 . The highest Q/V ratios can thus be achieved in short microcavities.

High finesse values require low mirror transmissions $\mathcal{T}_1, \mathcal{T}_2$ and a low round-trip loss \mathcal{L}_{cav} (Eq. 2.68). Metallic mirrors exhibit a reasonably high reflectivity ($\sim 98\%$), but suffer from high losses, which results in a low outcoupling efficiency. Hence, the mirrors typically used for cavity applications are low-loss distributed Bragg reflectors (DBRs), which are based on multiple layer pairs of two dielectric materials with different (high and low) refractive indices.

Each DBR layer has an optical thickness of $\lambda_{\text{DBR}}/4$, which results in extremely high reflectivities based on constructive interference of light reflected off the different interfaces, while the transmitted light destructively interferes accordingly, as illustrated in Fig. 2.13(a). The reflectivity spectrum of a specific DBR design can be calculated using the transfer-matrix approach (see Appx. A). A DBR coating exhibits a large reflectivity for a wide range of wavelengths around the design wavelength λ_{DBR} which is often

referred to as the “stopband” of the DBR mirror (Fig. 2.13(b)).

2.3.1 Effective cavity length

So far it was assumed that the length of the cavity is given by the mere spacing of the two mirrors, which is a good approximation for large mirror separations. For microcavities, however, the relative contribution of the Gouy-phase (Eq. 2.57) is significant, particularly if the cavity mode exhibits a short Rayleigh length z_R corresponding to a small beam waist w_0 .

In addition, if the mirrors are based on DBRs, the electromagnetic field experiences a phase delay τ upon reflection due to the distributed nature of a quarter-wave stack [126]. For the center frequency λ_{DBR} the reflection delay of a mirror with an infinite amount of layer pairs can be calculated analytically [127]:

$$\tau = \frac{\lambda_{\text{DBR}}}{2c} \frac{1}{n_H - n_L} \quad (2.73)$$

The corresponding effective phase penetration depth $L_{\text{DBR}} = c/(2\tau)$ increases the effective overall cavity length. At the stopband center λ_{DBR} this penetration depth can be calculated via:

$$L_{\text{DBR}} = \frac{c\tau}{2} = \frac{\lambda_{\text{DBR}}}{4} \frac{1}{n_H - n_L} \quad (2.74)$$

Here the n_H and n_L denote the refractive indices of the two dielectric materials employed in the DBR coating.

The overall effective cavity length L_{eff} is a combination of the mirror separation, the Gouy-phase contribution and the penetration depth into the mirrors.

$$L_{\text{eff}} = L + L_{\text{Gouy}} + 2L_{\text{DBR}} \quad (2.75)$$

For wavelengths detuned from the design wavelength λ_{DBR} , the reflectivity based on constructive interference due to the $\lambda/4$ design is impaired (Fig. 2.13(b)). This effect has the other important implication that the phase delay τ and hence the penetration depth L_{DBR} increase. A wave impinging on the DBR has a certain probability to be reflected back and forth within the coating before exiting the DBR due to the imperfect interference. The additional round-trips of the light increase (decrease) the probability that the light exits the DBR via transmission (reflection). The frequency-dependence of reflectivity and phase delay of a DBR coating can be calculated using a transfer matrix approach as introduced in Appx. A.

If an additional dielectric layer is added to the DBR, the interference condition is al-

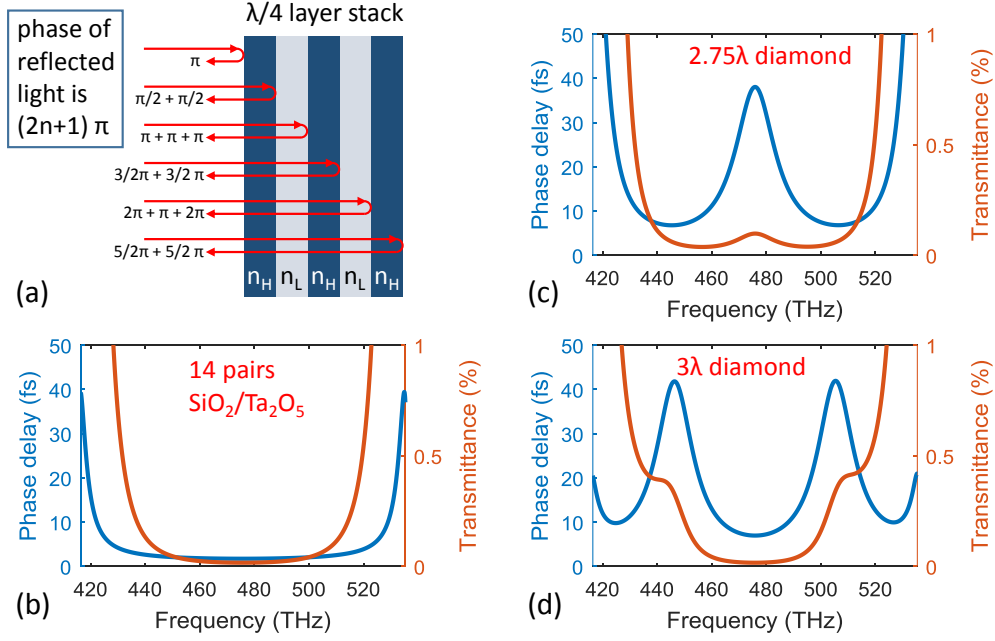


Fig. 2.13. **(a)** Operation principle of a distributed Bragg reflector. Extremely high reflectivities can be achieved due to constructive interference of light reflected off a stack of dielectric layers with an optical thickness of $\lambda_{\text{DBR}}/4$ and alternating high (n_H) and low (n_L) refractive indices. The phase shift for the reflection of an incoming beam off any interface is $(2n+1)\pi$ which results in constructive interference. Note that for a reflection off a layer with n_H an additional phase shift of π is introduced. For an analytical calculation including multiple interlayer reflections see Ref. [127]. **(b)** Transmittance and phase delay of a DBR comprising 14 layer pairs of at a design wavelength of $\lambda_{\text{DBR}} = 630 \text{ nm}$ (476 THz). For large detunings from the center frequency the transmittance strongly reduces, while the phase delay increases, respectively. **(c)** DBR with an additional diamond layer of optical thickness $2.75\lambda_{\text{DBR}}$. The joint diamond-Ta₂O₅ layer with an overall optical thickness of $3\lambda_{\text{DBR}}$ forms a weak cavity which impairs the constructive interference for the reflected beams and leads to an increased transmittance and phase delay. **(d)** DBR with an additional diamond layer of optical thickness $3\lambda_{\text{DBR}}$. The last Ta₂O₅ layer of the DBR and the diamond constitute an effective $3.25\lambda_{\text{DBR}}$ -layer, which maintains the constructive interference condition at λ_{DBR} . If the wavelength is detuned from λ_{DBR} weak cavities form which impair the interference of the reflected beams and lead to increased transmittance and phase delay.

tered and the frequency dependence of reflectivity and phase delay gets more pronounced, particularly if the layer exhibits a relatively large optical thickness $n \cdot d$.

In our experiments, we attach a diamond layer of thickness t_d to the plane mirror. The mirror terminates with a layer of high refractive index, i.e. Ta₂O₅. If the optical thickness of the joint diamond-Ta₂O₅ layer is an integer multiple $(2j-1)$ of $\lambda_{\text{DBR}}/4$ the constructive interference condition is maintained for light of wavelength λ_{DBR} and the reflectivity of the system remains unaltered. On the other hand however, if the

optical thickness of the joint diamond-Ta₂O₅ layer is an integer multiple j of $\lambda_{\text{DBR}}/2$ the layer features an interference with a phase opposing the constructive interference of the remainder of the DBR which results in a decrease of the overall reflectance of the system at the wavelength λ_{DBR} . The emergence of an increased transmission at λ_{DBR} can be explained by the formation of a weak cavity, where the diamond air-interface acts as a second mirror with low reflectivity. Due to the fact that the light circulates within the diamond layer there is an increased probability that it will be transmitted through the DBR compared to the DBR without additional diamond layer.

A transfer-matrix based commercial program designed for analyzing optical coatings (Essential MacLeod) is used to calculate the reflectance spectrum and group delay for an optical thickness of the diamond $n_d t_d = 2.75\lambda_{\text{DBR}}$ (Fig. 2.13(c)). As described previously, the formation of a weak cavity increases the transmittance of the system and its phase delay at λ_{DBR} . For wavelengths detuned from λ_{DBR} the system exhibits a similar behavior as the DBR without additional diamond layer (Fig. 2.13(b)).

If the DBR is combined with a $n_d t_d = 3\lambda_{\text{DBR}}$ diamond layer the interference condition for λ_{DBR} is maintained (Fig. 2.13(d)). In this system, however, weak cavities form for wavelengths detuned off the design wavelength resulting in a strong increase of the phase delay and an increased transmission as described in the previous paragraph.

Due to the occurrence of additional interference effects an optical cavity comprising a mirror with an additional diamond layer of thickness t_d can not be well described any more by considering two separate mirrors spaced by a distance L . A coupling of the mode confined within the air gap and the mode confined within the diamond layer gives rise to a non-linear relationship between detuning of L and the resonance frequency of the cavity.

2.3.2 Coupled diamond-air cavity

A method to qualitatively obtain the mode-structure of a coupled diamond-air cavity is to consider a one-dimensional model where an anticrossing between air-confined and diamond-confined modes emerges. In this model a layer of diamond with thickness t_d and refractive index n_d and a layer of air with thickness $L - t_d$ are surrounded by two perfectly reflecting mirrors (Fig. 2.14). For this structure the resonant wavelengths are given by the transcendental equations [128]:

$$(1 + n_d) \sin \left(\frac{2\pi}{\lambda} [L + t_d(n_d - 1)] \right) = (1 - n_d) \sin \left(\frac{2\pi}{\lambda} [L - t_d(n_d + 1)] \right) \quad (2.76)$$

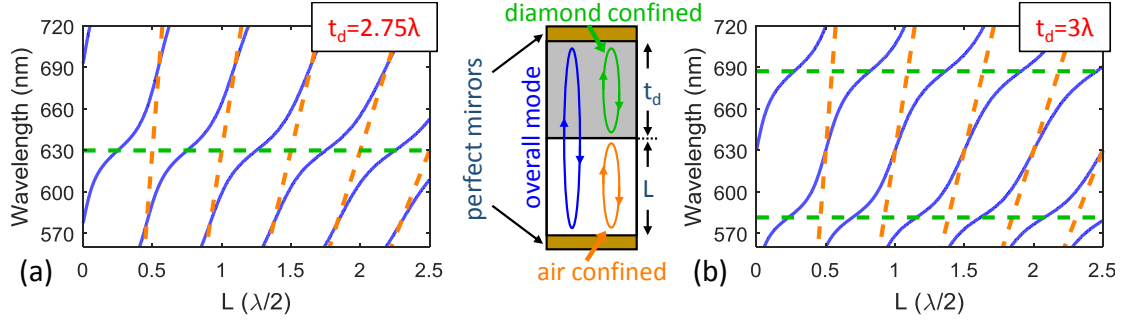


Fig. 2.14. Overall mode structure (blue) of a coupled diamond-air cavity on detuning the width of the air layer L for diamond layer thicknesses of (a) $t_d = 2.75\lambda$ and (b) $t_d = 3\lambda$, where $\lambda = 630$ nm. The coupling between air-confined (orange) and diamond-confined (green) modes results in the emergence of anti-crossings. (for more details see text)

Fig. 2.14 displays the L -dependent overall mode structure for a coupled diamond-air cavity with diamond layer thicknesses of $t_d = 2.75\lambda/n_d$ (a) and $t_d = 3\lambda/n_d$ (b) for $\lambda = 630$ nm. Resonances occur if the overall optical length of the cavity is an integer multiple of $\lambda/2$: $t_d n_d + L = j\lambda/2$.

For $t_d = 2.75\lambda/n_d$ and if $L = (2j - 1)\lambda/4$ the cavity is resonant with λ . In this case the overall cavity mode is “diamond-like”, which means that a variation of L will only have a relatively small impact on the resonance wavelength and that a large fraction of the electric field is confined within the diamond. On the other hand, for $t_d = 3\lambda/n_d$ and if $L = j\lambda/2$ the cavity is resonant with λ . In this case the overall cavity mode is “air-like”, which means that a variation of L will have a relatively strong impact on the resonance wavelength and that a large fraction of the electric field is confined within the air gap.

While this model provides a good qualitative insight into the overall mode structure of a coupled diamond-air resonator system, the aforementioned penetration depth into the DBR mirrors is not captured. The effective cavity length L_{eff} for a coupled diamond-air cavity deviates strongly from the geometric length of the cavity for certain frequencies. Hence, describing the mode volume using the geometry of the cavity does not yield the correct value for vacuum electric field E_{vac} (Eq. 2.41) and the corresponding atom-photon coupling rate g (Eq. 2.51).

Therefore, the mode structure and the vacuum electric field distribution of our cavity system are calculated using a transfer-matrix based commercial program designed for analyzing optical coatings (Essential MacLeod).

Chapter 3

Deterministic enhancement of coherent photon generation from a nitrogen-vacancy center in ultrapure diamond

The content of this chapter is partially adapted from:

Daniel Riedel, Immo Söllner, Brendan J. Shields, Sebastian Starosielec, Patrick Appel, Elke Neu, Patrick Maletinsky and Richard J. Warburton,

“Deterministic enhancement of coherent photon generation from a nitrogen-vacancy center in ultrapure diamond”, Physical Review X **7**, 031040 (2017).

The generation rate of coherent photons is of paramount importance for many quantum applications employing NV centers. For example, advances in spin-photon entanglement [17] and two-photon quantum interference protocols [129, 130] pave the way for the implementation of quantum teleportation [5] and long-distance spin-spin entanglement [6]. However, the success rate of these protocols and the scaling up to extended networks are both limited by the very small generation rate of indistinguishable photons from individual NV centers [28].

There are at least four factors which limit the generation rate of indistinguishable photons. First, the lifetime of NV centers is relatively long, ~ 12 ns. Secondly, only a small fraction, $\sim 3 - 4\%$, of the NV emission goes into ZPL [131, 132]. Only ZPL emission is useful for photon-based entanglement-swapping protocols as the phonon involved in non-ZPL emission dephases very rapidly. Thirdly, the photon extraction efficiency out of the diamond is hindered by the large refractive index of diamond itself. Finally, there are random spectral fluctuations in the exact frequency of the NV emission caused by charge noise in the diamond host [129].

Coupling the NV center to a high quality-factor, low mode volume optical microcavity offers a potential remedy to the first three factors thereby dramatically improving the

rate of coherent photon generation. These improvements depend on the weak coupling regime of cavity quantum electro-dynamics in which the emitter couples irreversibly to a single microcavity mode. The microcavity increases the total emission rate, the Purcell effect, and on resonance with the ZPL, the fraction of emission into the ZPL is likewise increased. The same coupling also enhances the ZPL extraction efficiency: photons leaking out of the cavity are channeled into a single propagating mode. A notable feature is that, as compared to the strong coupling regime of cavity quantum electrodynamics, modest cavity performance is all that is required [133].

Implementing these concepts for emitters in diamond has proved difficult so far. Nevertheless, coupling of NVs to photonic crystal cavities was shown to convey significant improvements on account of the particularly small mode volume V [134, 73, 39, 40, 135]. However, fabricating such structures exhibiting high quality-factors (Q -factors) in diamond is challenging: diamond is a very hard and chemically inert material. Achieving a spatial and spectral resonance with a single emitter is difficult and the device yield is low. Furthermore, efficient outcoupling is hard to engineer and the invasive processing causes a worsening of the spectral fluctuations, particularly for NV centers, the fourth problem mentioned above.

In comparison, a miniaturized Fabry-Pérot microcavity has the advantage of *in situ* spatial and spectral tuning, along with high Q -factors and good mode-matching to a propagating Gaussian beam, at the expense of an increased mode volume [113, 126, 114]. The feasibility of this approach has been demonstrated by enhancing the emission rate of emitters in nanocrystals [91, 136, 124, 137]. However, as in photonic crystal cavities, NVs in nanocrystals typically suffer from significant line broadening due to their close proximity to fluctuating charges at the surface [138, 139]. These spectral fluctuations are so severe that schemes involving photon-based entanglement swapping have only been successfully implemented using high-purity single-crystalline diamond material [26, 6].

3.1 Fully tunable open-access Fabry-Pérot microcavity

Our miniaturized Fabry-Pérot cavity consists of a diamond microplatelet attached to a plane bottom mirror and a concave top mirror (Fig. 3.1(a)). Both bottom and top mirrors are coated with distributed Bragg reflectors (DBRs) with reflectivity $> 99.99\%$ (Evaporated Coatings, Inc.) corresponding to a finesse $\mathcal{F} \gtrsim 10\,000$ (Eq. 2.65). Our state-of-the-art fabrication technologies enable us to create devices which exhibit very small loss rates; Q -factors of 50 000 are readily exceeded. The microcavity can be tuned *in situ* by moving the lower mirror with a set of three-axis nanopositioners. The top-mirror is

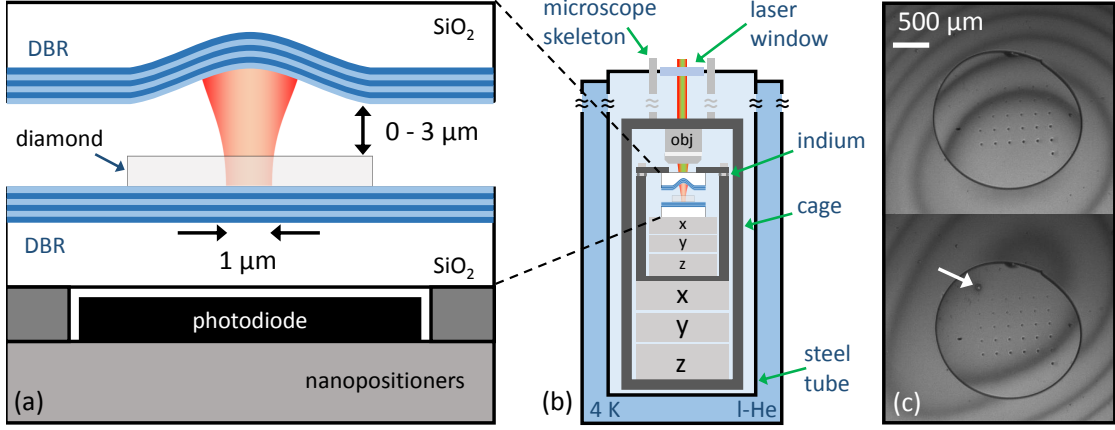


Fig. 3.1. (a) Schematic of the tunable microcavity containing a thin diamond membrane. Both the antinode location and resonance frequency of the microcavity mode can be tuned *in situ*. (b) Schematic drawing of the helium bath cryostat. The top-mirror of the cavity is glued to a titanium frame and fixed onto a homebuilt titanium cage. A thin layer of indium between the frame and the cage facilitates an adjustment of the angle between the two mirrors. The microcavity is mounted onto a set of three-axis piezo steppers allowing for adjusting its relative position with respect to the objective. All these components are housed in a sample cage which is attached to a long steel skeleton. The skeleton is inserted into a steel tube, which is sealed with a laser window enabling optical access. The tube is filled with helium exchange gas and immersed into liquid helium. (c) Images of the microcavity recorded with LED illumination outside the DBR stopband ($\lambda = 850$ nm). A round mesa structure is etched into the silica substrate before the fabrication of an array of micromirror templates and the application of the mirror coating. The two panels illustrate the close contact of the two mirrors for different alignment angles resulting in distinct patterns of Newton fringes arising from interference effects. The arrow in the lower panel highlights a small Newton fringe, which results from the contact of a diamond platelet attached to the bottom mirror with the top mirror.

glued to a titanium frame and fixed onto a homebuilt titanium cage (Fig. 3.1(b)). A thin layer of indium between the frame and the cage facilitates an adjustment of the angle between the two mirrors. Fig. 3.1(c) displays the *in situ* tuning of the angle between the two mirrors indicated by a change in the Newton fringe patterns. The mirrors can be made parallel to an extent that the diamond microplatelet bonded to the bottom mirror is the contact point when approaching the mirrors, which corresponds to a relative angle of $\lesssim 0.04^\circ$. The microscopic mirror separation in combination with the small radius of curvature of the concave top mirror facilitates a sub- μm cavity mode waist and hence a microscopic mode volume.

The entire microcavity can be moved *in situ* with respect to a fixed objective lens using a set of three-axes piezo nanopositioners (attocube, ANPx101 and ANPz101), which allows for mode-matching between the external excitation/detection mode and the

microcavity mode [113, 126, 114] (Fig. 3.1(b)). The compact cavity design facilitates low temperature experiments in a liquid-helium bath cryostat (Precision Cryogenic Systems, PVS-6.0/46.0). In order to perform our experiments at low temperature we fix the titanium cage to a long non-magnetic steel skeleton, insert it into a steel tube and immerse it in liquid helium. By evacuating the steel tube and filling it with a helium exchange gas ($p \approx 10$ mbar) we both avoid the buildup of ice upon cooling and ensure thermal contact of the sample with the helium bath. We attain optical access to the sample objective by sealing the top of the steel tube with a laser window (Thorlabs, WL11050-C13, thickness 5 mm).

Nanophotonic applications require state-of-the-art nano-fabrication techniques. To harness the full potential of miniaturization, the nanostructures need to be as small as possible without impairing their performance. In addition, high-quality materials which exhibit a low density of defects are required in order to minimize losses due to absorption and scattering. For our device, curved mirror microtemplates are fabricated by creating a concave depression in a silica substrate with laser ablation (Sec. 3.1.1) [140, 113, 126]. Furthermore, we fabricate thin microplatelets from ultrapure diamond material hosting individual NV centers and attach it to the plane mirror using a micromanipulation system (Sec. 3.1.2).

3.1.1 Concave micromirror template fabrication

The key enabling technology for the miniaturization of a Fabry-Pérot cavity constitutes the micromachining of curved mirror templates. In order to exploit the full potential of cavity coupling, the beam waist of the cavity, and hence the radius of curvature of the micromirror template, needs to be minimized (see Eq. 2.60). However, it is challenging to fabricate features with a micrometer-sized radius without compromising the mode volume. The fabrication of small radii of curvature requires a higher laser power which leads to deep indentations into the substrate. Only the combination of short cavity length and small beam waist yields a small mode volume.

At the same time, the mirror templates need to exhibit a low surface roughness in order to avoid significant scattering losses. Over the past years, CO₂ laser ablation and focused ion beam milling have been established as the main fabrication techniques, with complementary strengths and weaknesses. The former enables ultrahigh cavity Q -factors due to the atomic smoothness of the processed surface [141], while the latter allows for full shape control and hence the fabrication of smaller feature sizes [142, 143].

For the experiment presented in this thesis, we opt for CO₂ laser ablation, which is a well-established in our labs. This technique relies on the strong absorption of a single

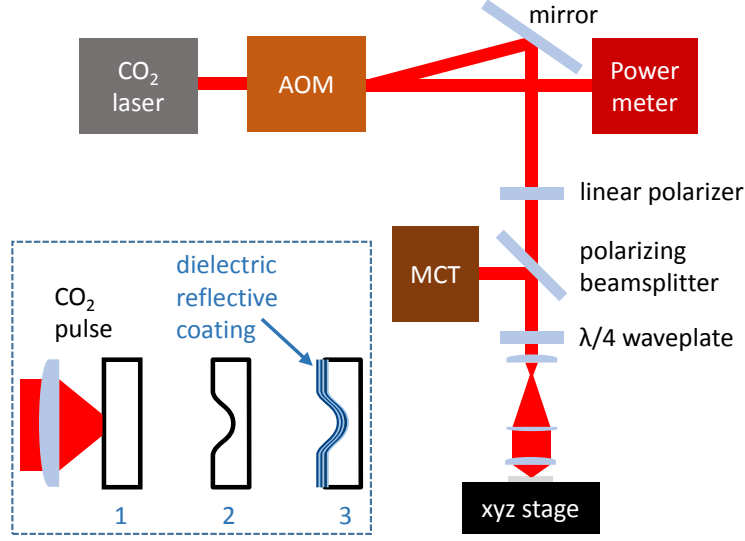


Fig. 3.2. Schematic of the CO₂ laser ablation setup. An acousto-optic modulator enables the creation of CO₂ laser pulses with defined power and length. The laser pulses are focused onto a silica chip where they create small parabolic indentations upon absorption [140]. The micromirror templates are subsequently coated with a dielectric reflective coating.

CO₂ laser pulse train by a fused silica surface (SiO₂) within the first few micrometers. Identifying the right parameter regime enables precise micromachining of an indentation via controlled thermal evaporation of material combined with melting of the surface. A key feature of this technique is that upon resolidification of the molten silica any surface roughness is smoothened due to surface tension.

In our setup (Fig. 3.2), we employ an RF-pumped CO₂ laser, which is pulsed at 20 kHz (Synrad Inc. Firestar v30, $\lambda_{\text{CO}_2} = 10.6 \mu\text{m}$), and set the pulse length to 20 μs . Since the heat transfer rate within the silica is much slower than the repetition rate, the radiation can be considered as continuous wave emission in context of the ablation process. In order to avoid unwanted back reflections of laser-light, which might lead to laser instabilities, we insert a quarter-wave plate (II-VI infrared, WPM-10.6-.35-90-U) and a linear polarizer (Thorlabs Inc., PHB-7) into the beam path. As a substrate we use 0.525 mm thick UV grade fused silica wafers which exhibit a roughness of $< 1.5 \text{ nm}$ (Plan Optik) diced into $5 \times 5 \text{ mm}^2$ chips.

Single pulses of variable duration and power are created using a water-cooled acousto-optic modulator (AOM) based on germanium (Brimrose Corporation, GEM-40-1-10.6). An AOM exploits the acousto-optic effect where a sound wave is used to diffract light. The sound wave leads to a periodic index modulation which effectively acts like a grat-

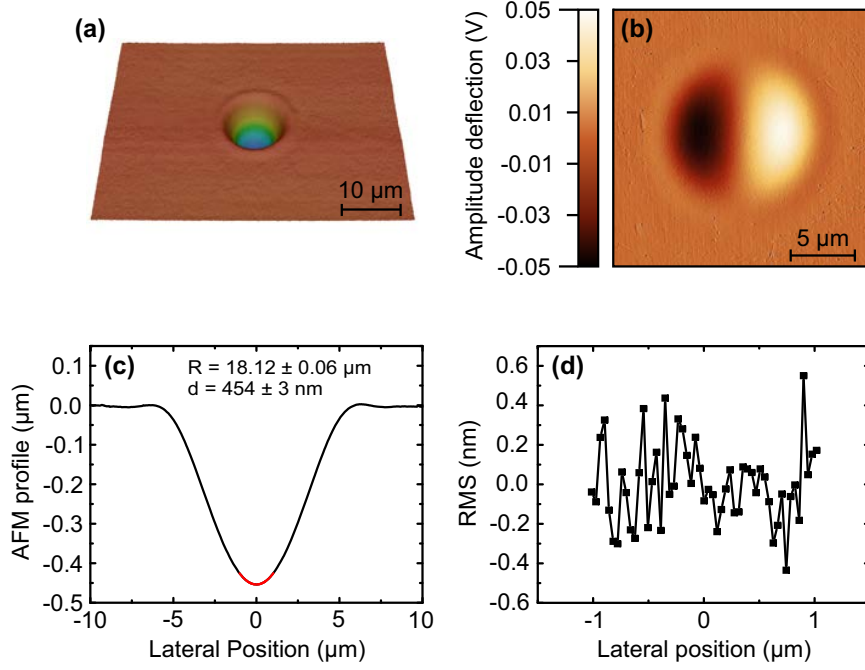


Fig. 3.3. Ablated crater fabricated with a power of 250 mW and pulse length of 58 ms. (a) Height image obtained by a confocal scanning laser microscope. (b) AFM amplitude deflection image of the crater qualitatively showing a low surface roughness. (c) AFM height profile. The red line represents a parabolic fit in the vicinity of the center of the crater. (d) Measured height subtracted by the fit and allowing for deducing a rms surface roughness of 0.2 nm. Adapted from reference [117].

ing structure. By controlling the piezo-electric transducer generating the sound waves, the intensity and the duration of the diffracted light can be set. The diffracted laser pulse is then focused onto a silica substrate via a zinc selenide lens (10ZAL25.4, ULO Optics Ltd.) with a focal length of 25.4 mm. The initial intensity waist diameter of the CO₂ laser (2.5 mm) is expanded with a telescope and then focused with an effective numerical aperture of 0.17 resulting in an FWHM beam diameter of 20 μm. The silica substrate is moved with respect to the laser focus via an xyz stepper motor stage (Physik Instrumente GmbH, M-112.12S). Analyzing the back reflection from the sample at low power using a nitrogen cooled mercury-cadmium-telluride detector (Hamamatsu Photonics K.K., P9697-01) allows for adjusting the focus.

A typical microtemplate fabricated with this process is shown in Fig. 3.3. By applying a pulse with a power of $P = 250 \text{ mW}$ for a duration of $\tau = 58 \text{ ms}$, we obtain a shallow (depth 0.45 μm) smooth concave feature (rms roughness 0.2 nm) exhibiting a radius of curvature of 18 μm. By varying the pulse power and duration the radius of curvature can be decreased. However, this decrease comes along with an increase of the depth of

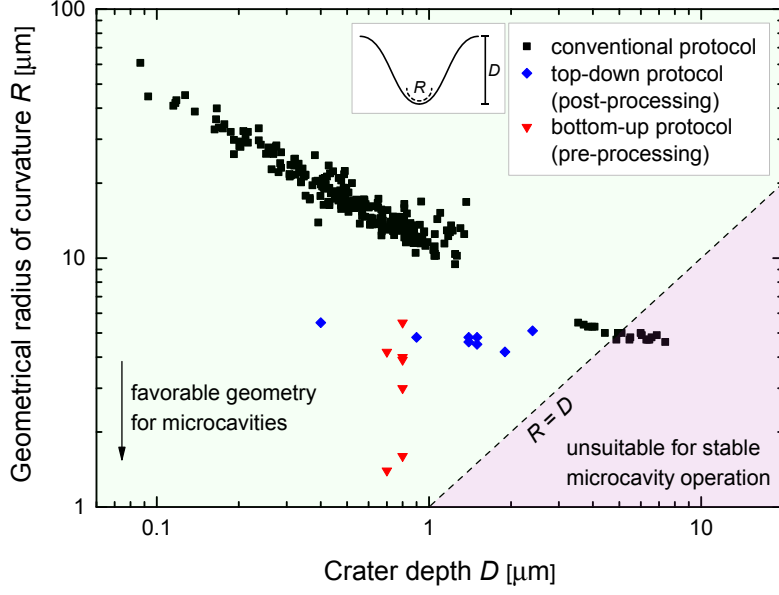


Fig. 3.4. Geometry parameters of craters produced by different fabrication methods. Conventional CO_2 laser ablation on polished fused silica substrates (black squares) shows a strong correlation between geometrical radius of curvature R and depth D . In our recent work, the favorable regime of low R at shallow D becomes accessible by both post-processing (“top-down”, blue diamonds) and pre-processing (“bottom-up”, red triangles) methods with a minimum radius of curvature $R = 1.2 \pm 0.1 \mu\text{m}$. Adapted from reference [144].

the indentation. For a wide range of fabrication parameters ($P = 240 \text{ mW} \dots 900 \text{ mW}$, $\tau = 50 \mu\text{s} \dots 120 \text{ ms}$) an inverse proportionality was found empirically, as indicated by the black dots in Fig. 3.4.

For our microcavity mirror we prepare the silica substrate by etching a round mesa using hydrofluoric acid (Fig. 3.1(b)), which allows the two mirrors to be approached as closely as possible. We fabricate a matrix of several microtemplates using varying pulse parameters resulting in a wide range of depths and radii of curvature. The ablated structures are then smoothed by an additional short pulse which melts any nanoparticles that may have been created during the ablation process of the template matrix.

Recently, we have shown different techniques that can help overcoming the inverse link between feature depth and radius by additional processing steps [144]. In a post-processing scheme we reduce the depth of indentations created by laser ablation via reactive ion etching. Another approach is to first define rectangular step-like templates with well-controlled height and width via photolithography and then to apply successive optical polishing [145]. The improved geometries are highlighted in Fig. 3.4 by blue diamonds and red triangles, respectively. For future applications, it might be interesting

to define the templates with focused ion beam rather than photolithography in order to combine the benefits of full shape control and atomic smoothness.

3.1.2 Diamond fabrication

In order to attain miniature mode volumes for our NV coupling experiments we fabricate thin microplatelets from high-quality single-crystalline synthetic diamond. The microplatelets adhere strongly to the plane mirror via van der Waals bonding. On account of a small bonding interface, the probability that the bonding is inhibited by the presence of nanoparticles [146] is strongly diminished. In the following the fabrication process of these microplatelets and their transfer to a planar mirror substrate are described.

Sample details

As starting material, we employ commercially available single-crystalline diamond of the highest quality grown via chemical vapor deposition (Element 6, (100)-orientation, “electronic grade” $4 \times 2 \times 0.5 \text{ mm}^3$). The material exhibits very low impurity concentrations $[\text{N}] < 1 \text{ ppb}$ and $[\text{B}] < 1 \text{ ppb}$, which implies a very low abundance of native NV centers. The defect concentration in these diamonds is so low that lifetime-limited emission linewidths of single NV centers could be observed [41]. The diamond is laser-cut and polished to a thickness of $\approx 40 \mu\text{m}$ (Delaware Diamond Knives). Prior to processing, the sample is cleaned in boiling acids (sulphuric acid, nitric acid and perchloric acid, mixed to 1:1:1) and then rinsed in de-ionized water and solvents (acetone, ethanol, isopropanol) to remove any residual contamination from the polishing.

The polishing process is known to strain and damage the diamond, which is why we remove the first few micrometers of the diamond sample using inductively coupled reactive ion etching (ICP-RIE, Sentech SI 500). During the etching process we mask off one corner of the diamond with a quartz mask in order to easily identify the etched surface (Fig 3.5 upper left). We employ an alternating plasma sequence with 5 min of Ar/Cl₂ plasma (ICP power 400 W, bias power 100 W, reactor pressure 1 Pa, 40 standard cubic centimeter per minute (sccm) Cl₂, 25 sccm Ar) followed by two times 5 min of O₂ plasma (ICP power 700 W, bias power 50 W, reactor pressure 1.3 Pa, 60 sccm O₂). Between the etching steps we cool the sample under Ar (100 sccm, 13.2 Pa). The Ar/Cl₂ plasma aids in maintaining a smooth surface [147, 148, 149]. The O₂ plasma has a higher etch selectivity between the oxide-based mask and the diamond and prevents a potential Cl₂ contamination of the surface [150, 149].

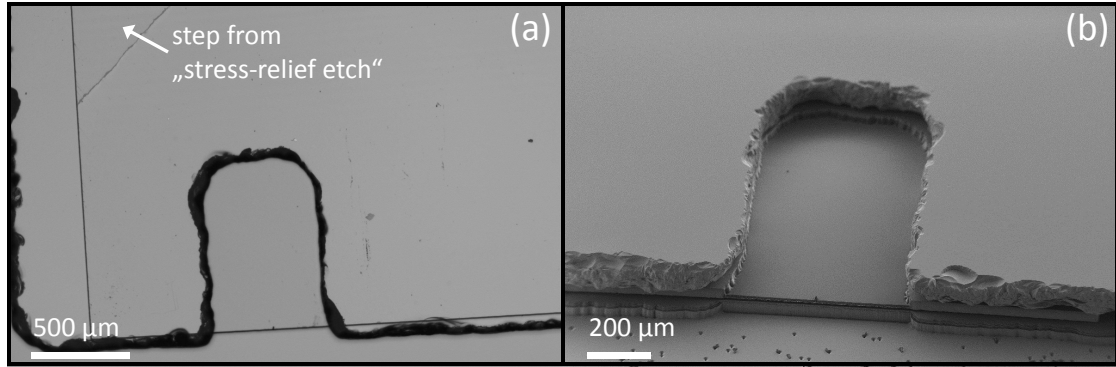


Fig. 3.5. (a) Diamond sample sandwiched between a silicon carrier chip and a quartz cover slip. The quartz mask exhibits a narrow slit in order to thin down only a small region of the diamond during the etching process. In the top left corner the etch mark stemming from the stress-relief etch can be seen. (b) Scanning electron microscope (SEM) image of the same structure after etching to a thickness of $\sim 5 \mu\text{m}$.

Creation of NV centers

Efficient cavity coupling demands the NV centers to be at the right distance ($\lambda_{\text{ZPL}}/4$) from the surface (Sec. 3.3.4). After the removal of the strained diamond surface, we therefore introduce nitrogen by ion beam implantation (Ion beam services, ^{14}N , 55 keV, $5 \cdot 10^8 \text{ ions/cm}^2$). The stopping range of the nitrogen ions is estimated to be at a target depth of 75 nm with a HWHM straggle 16 nm using the software SRIM. NV centers with close to lifetime-limited emission linewidths are created during a multi-step annealing process under vacuum ($\sim 10^{-7} \text{ mbar}$) [22]. We perform a tri-acid and solvent clean in order to remove potential surface graphitization caused by the annealing process. From initial confocal scans we infer a density of NV centers of $5 \times 10^7 / \text{cm}^2$ corresponding to a creation efficiency of 2.5 % per ^{14}N ion which is comparable to previously reported values [70].

Fabrication of thin diamond layer

To ease sample handling, the diamond is thinned down only in a small region via plasma etching. For protection of the NV centers and to avoid roughening, we cover the implanted surface with a chromium-gold layer (5 nm Cr, 10 nm Au) using an electron beam evaporator (Sharon). We clean the sample and mask off a region of approximately $500 \times 800 \mu\text{m}^2$ with a quartz mask (SPI supplies) exhibiting a slot of $500 \mu\text{m}$ width which was cut with a water jet (Microwater Jet). The diamond, with the uncoated surface facing up, is held between the quartz mask and a silicon chip, which are attached to each

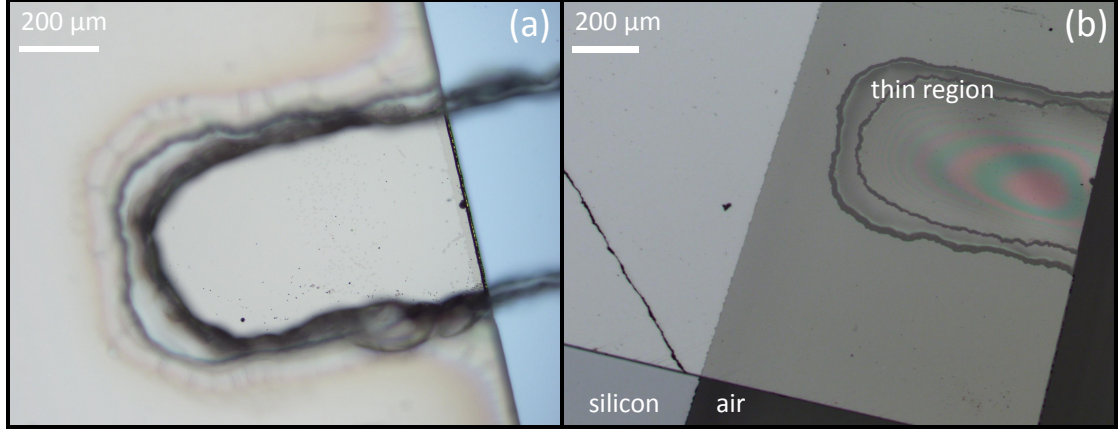


Fig. 3.6. (a) Replacement of the quartz mask for the second etching step. Focusing of the plasma in proximity of the sidewalls of the mask causes a trenching effect. Hence, we switch to a quartz mask exhibiting a narrower slot in order to avoid breaking the membrane. (b) Membrane thinned down to a thickness of $\sim 1 \mu\text{m}$. The optical interference fringes indicate the thickness variation throughout the membrane. Here, the sample is prepared for the electron beam lithography by mounting the diamond with the implanted surface facing upwards and the thinned-down region overhanging on a silicon carrier chip.

other with vacuum grease (Fig. 3.5(a)). We then thin the diamond down to a thickness of $\approx 5 \mu\text{m}$ using an alternating sequence of Ar/Cl_2 and O_2 plasmas as described previously (Fig. 3.5(b)). The etch rates are determined to be $\sim 8.4 \mu\text{m}/\text{h}$ for the O_2 plasma and $\sim 2.9 \mu\text{m}/\text{h}$ for the Ar/Cl_2 . During the long etching process a trench forms at the edge of the unmasked region of the diamond [149]. To avoid damaging the final device we therefore switch to a quartz mask with a narrower slot of $400 \mu\text{m}$ (Fig. 3.6(a)).

The diamond is then etched down to a final thickness of $\sim 1 \mu\text{m}$ exhibiting local thickness variations inherent to the etching/masking process. The thickness at the edge of the membrane is measured using SEM and found to be $\sim 850 \text{ nm}$ at the thinnest point. The interference fringes visible in Fig. 3.6(b) indicate that the thinnest part of the membrane is in the center with a thickness of $\sim 720 \text{ nm}$. The surface roughness of the diamond after the fabrication process is typically $\lesssim 0.3 \text{ nm}$ [149]. After etching, first the Cr/Au layer is removed with commercially available etchants (Sigma-Aldrich 651826 and 651818), then the sample is immersed in a buffered oxide etch (BOE) solution and again cleaned in boiling tri-acid and solvents as described before. SEM images reveal no resolvable roughness throughout the thinned region of the diamond. The diamond sample is then prepared for micro-structuring. We mount the sample on a silicon chip (using Crystalbond 509 as adhesive agent, SPI supplies) with the thinned down part overhanging and the implanted surface facing upwards.

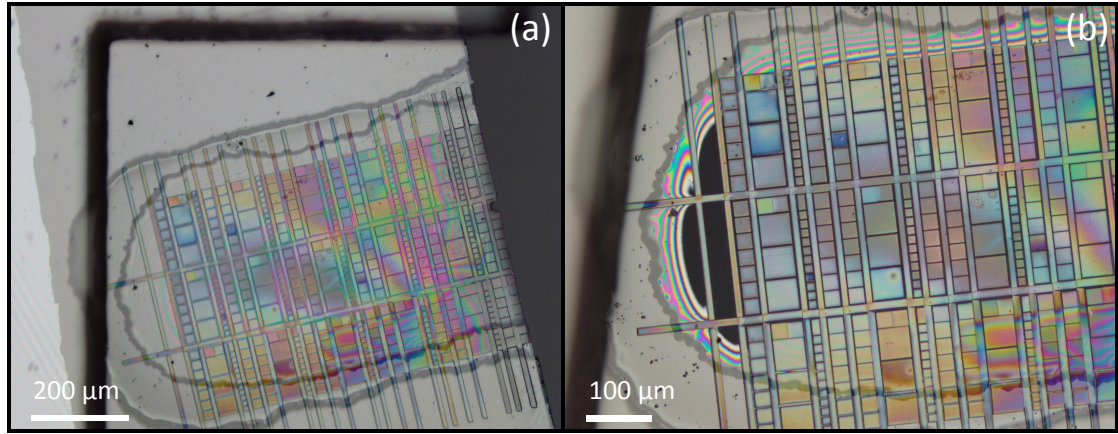


Fig. 3.7. (a) Patterned and developed electron beam resist on the implanted diamond surface. The pattern comprises small squares attached to a holding structure via a small connection. The unstructured part of the diamond is covered with a quartz-mask in order to maintain the layer of implanted NV centers. (b) Transfer of the mask pattern into the diamond using plasma etching.

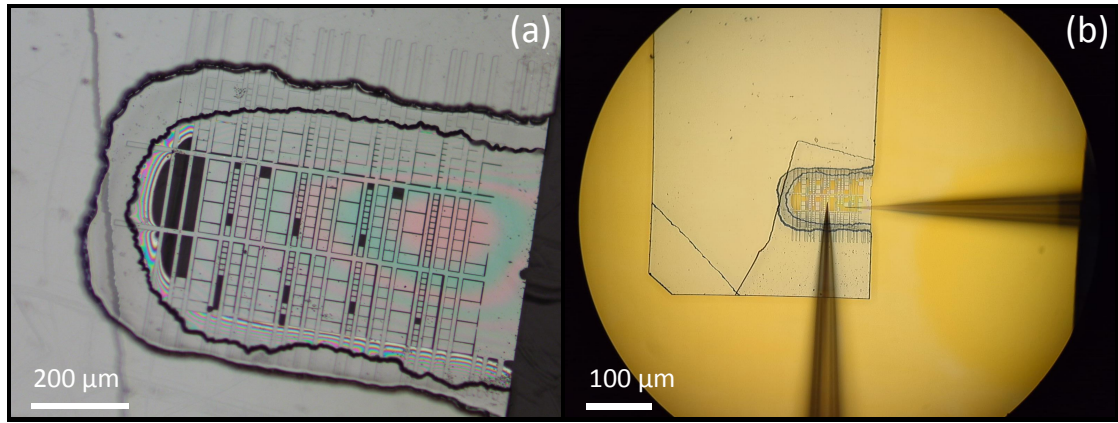


Fig. 3.8. (a) Structured diamond membrane after removal of the electron beam resist. Some diamond platelets broke out during the cleaning process. (b) Transfer of diamond platelets to a planar mirror substrate using a micromanipulation system. The mirror substrate is placed underneath the patterned diamond and platelets are removed with the aid of sharply tipped glass needles.

Fabrication of diamond microplatelets and transfer to mirror substrate

The thin region of the diamond is structured via electron beam lithography using a hydrogen silsesquioxane negative electron beam resist (FOX-16, Dow Corning). In order to improve the adhesion of the resist to the diamond we deposit a 2 nm thick titanium layer via electron beam evaporation before we spin coat and bake the sample on a

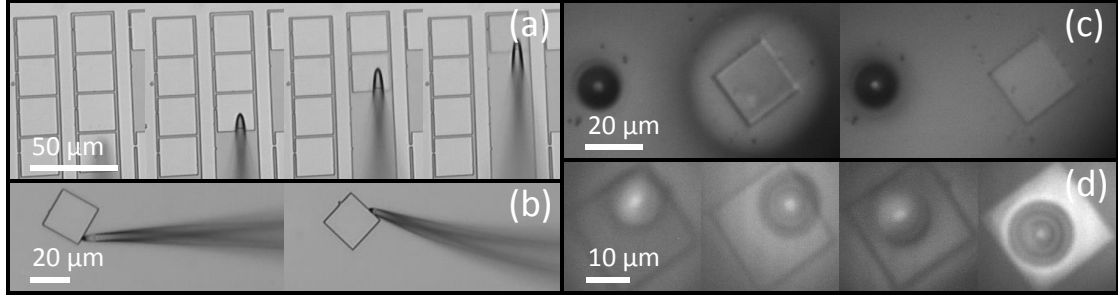


Fig. 3.9. **(a)** Removal of several diamond microplatelets (dimensions $20 \times 20 \mu\text{m}^2$) from the patterned diamond membrane. **(b)** Strong van der Waals bonding between plane mirror and microplatelets. The macroscopic micromanipulator needle bends when a force is applied. **(c)** Images of a diamond platelet inside the assembled cavity recorded with an LED whose wavelength ($\lambda = 850 \text{ nm}$) is outside the DBR stopband ($565 \dots 725 \text{ nm}$). The round structure on the left corresponds to a microindentation fabricated on the top mirror. The distance of the two mirrors can be tuned *in situ*. The Newton fringe forming around the diamond platelet in the left pictures suggests contact of the two mirrors. **(d)** Demonstration of *in situ* control of the relative lateral position of concave top mirror and diamond platelet. The variation of the brightness of the platelets originates from a slight change in reflectivity of the cavity system which is present even for wavelengths outside the DBR stopband.

hotplate (90°C , 10 min). The goal of the patterning is to obtain small diamond platelets (sizes between $10 \times 10 \mu\text{m}^2$ and $50 \times 50 \mu\text{m}^2$), which, due to a small bonding, interface adhere firmly to other materials. To that end, a pattern consisting of a large supporting structure with small squares of different sizes is exposed by electron beam lithography (30 keV). We then develop the samples using TMAH (25 %) for 20 s and remove the Ti layer in heated HCl (37 %, 70°C). Before transferring the mask pattern into the diamond via plasma etching, we protect the NV layer of the rest of the diamond with a quartz mask (Fig. 3.7(a)). We then first use a 60 s Ar/ Cl_2 plasma etching step followed by two steps of pure O_2 plasma (300 s and 600 s) to decrease mask erosion and etch through the diamond to yield free standing membranes. The relieved pattern can be seen in Fig. 3.7(b). After the etching, the FOX mask is removed in BOE and the sample is acid cleaned again. An image of the final device is shown in Fig. 3.8(a). Next, we place the structured part of the diamond atop the planar mirror substrate and use the sharply tipped glass needles of a micromanipulator to break out the platelets (Fig. 3.8(b)). Fig. 3.9(a) illustrates how we successively break out several platelets with a dimension of $20 \times 20 \mu\text{m}^2$. The platelets adhere very strongly to the planar mirror substrate. Due to the fact that both the mirror surface and the diamond surface exhibit very smooth surfaces, a strong van-der-Waals interaction is promoted. The small dimension of the platelets enables a very clean bonding interface without any nanoparticles inhibiting the bonding [146] (Fig. 3.9(b)).

After the successful transfer of the diamond microplatelet to the planar mirror substrate, the microcavity is assembled. If the mirrors exhibit a high degree of parallelism they can be approached to the point where the mirrors are in contact as the formation of a Newton fringe around the microplatelet under illumination with an infrared illumination suggests (Fig. 3.9(c)). As indicated in Fig. 3.9(d) our design allows for full *in situ* tuning of the relative position of the concave top mirror and the diamond microplatelet. Hence, we are able to couple different individual NV centers within the diamond to the microcavity mode.

3.2 Linewidth measurements

In order to characterize the quality of the NV centers we created via nitrogen implantation, we perform photoluminescence excitation (PLE) scans at a temperature of $T = 4$ K. To that end, we excite the NV center resonantly using an external cavity diode laser (Toptica, DL-pro 635, $\lambda = 631\ldots 640$ nm) providing tunable, narrow-linewidth laser light ($\delta\nu \lesssim 500$ kHz). The linewidth of the optical transition is determined by sweeping the frequency of the laser while recording the photons emitted in the phonon sideband (PSB).

In order to perform PLE measurements the optics need to allow for both detection and excitation of the ZPL transition. Hence, we employ a non-polarizing 10:90 beamsplitter (Thorlabs, BS025) in combination with different longpass and shortpass filters (see Fig. 3.10). A second 10:90 beamsplitter allows for imaging the sample and the reflected laser light via a CMOS camera (Allied Vision, Guppy Pro F-503). We align the microscope by overlapping the beams via a combination of a tilt stage for angular displacement and a laser window, which can be tilted with respect to the incoming beam by a gimbal mount (Thorlabs, KC45D), resulting in a lateral translation of the beam. Fig. 3.11(a) displays a typical confocal scan on a diamond microplatelet obtained at room temperature using a high-NA objective (Olympus, MPLFLN100X, NA=0.9). Here we excite the NV centers with a green laser (Laser Quantum, VENTUS, $\lambda = 532$ nm) with a power of $P = 580 \mu\text{W}$. We filter the laser using a 633 nm longpass filter (Semrock, LP02-633RU-25) and detect the PL photons with a single-photon avalanche diode (SPAD, Excelitas, SPCM-AQRH-15-FC). Microscope optics other than the sample objective all remain at room temperature.

We conduct our low-temperature measurements using a liquid-helium bath cryostat (compare Sec. 3.1). A titanium cage houses the sample which is mounted onto scanning nanopositioners (attocube, ANSxyz100) and another set of three-axes piezo nanoposi-

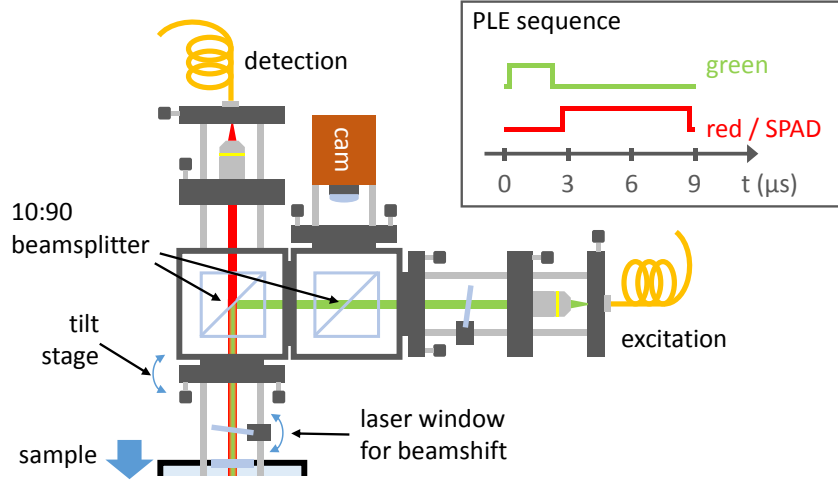


Fig. 3.10. Schematic drawing of the fiber-based confocal setup for resonant excitation of single NV centers. Opto-mechanical components are used to overlap the excitation and detection paths which are separated via 10:90 beamsplitters and a combination of longpass and shortpass filters (for more details see text). A green laser is tightly focused on the sample via a low-temperature compatible high numerical aperture objective. Fluorescence originating from a diffraction limited sample volume is collected with the same objective and coupled into the detection fiber. The fluorescence is either analyzed with a spectrometer or detected using a SPAD (not depicted). By changing the optical filters an additional laser can be coupled through the excitation fiber which is resonant with the ZPL of the NV center. By detecting the phonon sideband emission while sweeping the laser frequency the spectral linewidth of the transition can be determined. In the top right the PLE sequence, for which the maximum signal was obtained, is shown.

tioners for long-range displacements. We use a low-temperature compatible high-NA objective (Partec, 50x0.82, working distance 0.4 mm) for excitation and detection of the PL. As a first step, we perform confocal scans at low temperature. We excite NV centers with a green laser filtered by a combination of a laserline filter (Semrock, LL01-532-25) and a shortpass filter (Semrock, FF01-650/SP-25) and detect the PL via a SPAD using a longpass filter (Semrock, BLP01-594R-25). Next, we measure wavelength-resolved PL spectra with a spectrometer (Acton SP2500, 300 grooves/mm grating). The interference fringes within the PL spectrum allow us to determine the thickness of the diamond layer at the very location of the NV (Fig. 3.11(b)). The spacing of two adjacent maxima is given by the optical path length for a round trip of light between the two diamond-air interfaces. Furthermore, by detecting the PL emitted within the ZPL using a high-resolution grating (2160 grooves/mm) we obtain a good estimate for its transition frequency. We can approximately set the scan range required for resonant excitation by coupling a small fraction of the diode laser onto the spectrometer simultaneously. We

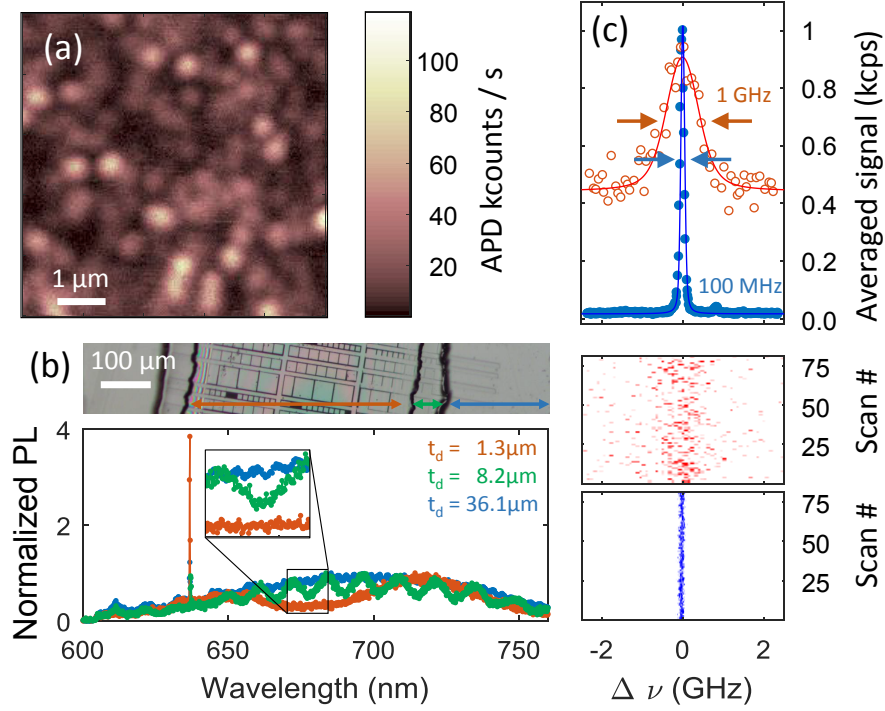


Fig. 3.11. **(a)** Confocal scan of NV centers within a diamond microplatelet bonded to a plane mirror. The PL is excited by a green laser (532 nm, 580 μW) and collected with an objective with NA=0.9. After passing a 633 nm longpass filter the PL is detected with a SPAD. **(b)** PL spectra of NV centers in the processed diamond sample. The PL spectra of an NV center in unprocessed (blue symbols, thickness $d \approx 36.1 \mu\text{m}$), etched (green symbols, $d \approx 8.2 \mu\text{m}$) and microstructured (red symbols, $d \approx 1.3 \mu\text{m}$) diamond is normalized to the maximum of the PSB. From the oscillations caused by interference within the diamond layer its thickness can be determined. **(c)** Photoluminescence excitation (PLE) scans of near-surface (68 nm) NV centers in unprocessed diamond (blue symbols; lower panel: resonant laser power 3 nW, scan speed 340 MHz/s) and in microstructured ($t_d \leq 1 \mu\text{m}$) diamond (red symbols; central panel: resonant laser power 10 nW, scan speed 7.8 GHz/s) yielding averaged ZPL linewidths of $\sim 100 \text{ MHz}$ and $\sim 1 \text{ GHz}$, respectively (upper panel).

then tune the frequency of the laser such that it overlaps with the ZPL signal.

Next, we use the diode laser to excite the ZPL transition resonantly. We collect the PL emitted via the PSB using a shortpass filter for excitation (Semrock, FF01-650/SP-25) and a longpass filter for detection (Semrock, BLP01-635R-25). In order to assess the linewidth of the transition we tune the red laser and record its frequency with a high-precision wavelength meter (HF-ANGSTROM, WS/U-30U). As mentioned in Sec. 2.1.2 two photon absorption leads to ionization of the NV center. Hence, in our experiment we repump the NV center to its negative charge state by applying a green laser pulse. Since we are only interested in detecting photons stemming from resonant excitation

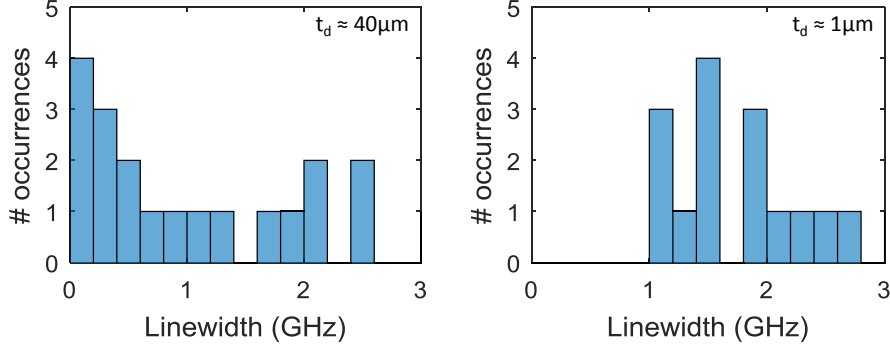


Fig. 3.12. Histogram of linewidths obtained by PL measurements for the unprocessed (left) and the etched (right) region of the diamond.

we employ a pulse sequence of alternating red and green excitation where the relative pulse times are optimized for maximum signal intensity. (see Fig. 3.10). We repump the charge state for a period of $2 \mu\text{s}$ alternated with a $6 \mu\text{s}$ window for the resonant excitation and detection of the photons via a SPAD. The two pulses are separated by 500 ns wait times, which minimizes the background of the measurement. The green and red lasers are coupled into the excitation arm via a wavelength combiner (Thorlabs, RGB46HA). Both lasers are gated via AOMs (Crystal Technology, 3200-146) based on TeO_2 (compare Sec. 3.1.1). The detection of PL photons with a SPAD is synchronized with the resonant excitation using a dual channel arbitrary waveform generator (Agilent 33522A).

PLE excitation measurements of NV centers in the unprocessed region of the diamond ($t_d \sim 40 \mu\text{m}$) yield long-term ZPL linewidths of $\lesssim 100 \text{ MHz}$. The linewidth measurement displayed in Fig. 3.11(c) is averaged over 80 individual linescans and is fitted well by a Lorentzian with a linewidth of 92.1 MHz. The absolute position of the peak varies between individual frequency scans due to slow fluctuations. Accounting for these shifts by aligning the center frequency of the different scans we retrieve a linewidth of 81.4 MHz. Individual linescans are performed in steps of $\sim 17 \text{ MHz/pixel}$ with an integration time of 50 ms. We note that the green repump pulse in our PLE pulse sequence is applied several thousand times for every step of the resonant laser, which randomizes the charge environment for every pixel in the linescan. Thus, we capture all spectral shifts arising from the charge fluctuations. For a single linescan, however, we find a minimum linewidth of 30.9 MHz, which is reasonably close to the transform limit $\delta\nu = \gamma_{\text{NV}}/(2\pi) = 12.6 \text{ MHz}$, which could be achieved in bulk material of the same quality [41]. Here $\gamma_{\text{NV}} = 1/\tau_{\text{R}}^0 = 79.4 \cdot 10^6 \text{ s}^{-1}$ is the excited state recombination rate inferred from a lifetime measurement with $\tau_{\text{R}}^0 = 12.6 \text{ ns}$ (see Sec. 3.3.3). We anticipate that the lifetime limit could be achieved

in these measurements by sweeping the frequency of the resonant laser and then applying a repump pulse at the end of every frequency sweep using a resonant charge repump [22, 151] (compare Sec. 2.1.2). Slow drifts could readily be compensated by applying external electric fields [87].

Individual NV centers in the membrane ($d \sim 1 \mu\text{m}$) have PLE linewidths of $\sim 1 \text{ GHz}$ increased above the linewidths in the starting material, but still much lower than typical linewidths in diamond nanocrystals [138] or nanofabricated diamond structures [39]. We note that for these measurements it is not possible to determine a single scan linewidth as the transition frequency exhibits significant spectral jumps during the measurement time (Fig. 3.11(c)). We speculate, however, that the linewidth would be significantly reduced if the aforementioned resonant charge repump was applied only at the end of each linescan.

Fig. 3.12 shows the distribution of several linewidth measurements in the unprocessed region of the diamond and the membrane. We find that several NV centers in the thicker region of the diamond ($t_d \sim 40 \mu\text{m}$) exhibit linewidths which are $\lesssim 100 \text{ MHz}$. Notably, the linewidths for several NV centers in the membrane are smaller than the ground state spin triplet splitting of 2.87 GHz , an essential feature for quantum information applications [39].

3.3 Cavity coupling experiment

For the cavity experiment we use a low-temperature compatible objective (Microthek, 20x/0.4) with a long working distance compared to the PLE experiments which is required by the geometry of the cavity cage. In order to attain high excitation powers needed due to the relatively low NA of the objective the green laser is reflected off a longpass dichroic mirror (cutoff 560 nm , Semrock, FF560-FDi01). A second dichroic mirror is inserted to image the reflected laser beam with a CMOS camera (see Fig. 3.13). An additional dichroic mirror (cutoff 644 nm , AHF, F48-644) allows for either separately detecting the ZPL and the PSB or to couple in an infrared LED (Harvathek, HT-P178IRPQ) to image the sample. We use pairs of mirrors (Thorlabs, BB1-E02) mounted in right-angled kinematic mounts (Thorlabs, KCB1C/M) to align the different microscope arms such that the beams enter the cryostat collinearly.

In order to reduce acoustic noise in our experiments we shield our cryostat (compare Sec. 3.1) from sound waves via a custom-built acoustic enclosure (Accurion). In addition, the cryostat is sitting on a compact dynamic antivibration systems (TableStable, TS-300). Highly sensitive piezoelectric sensors in combination with fast piezoelectric

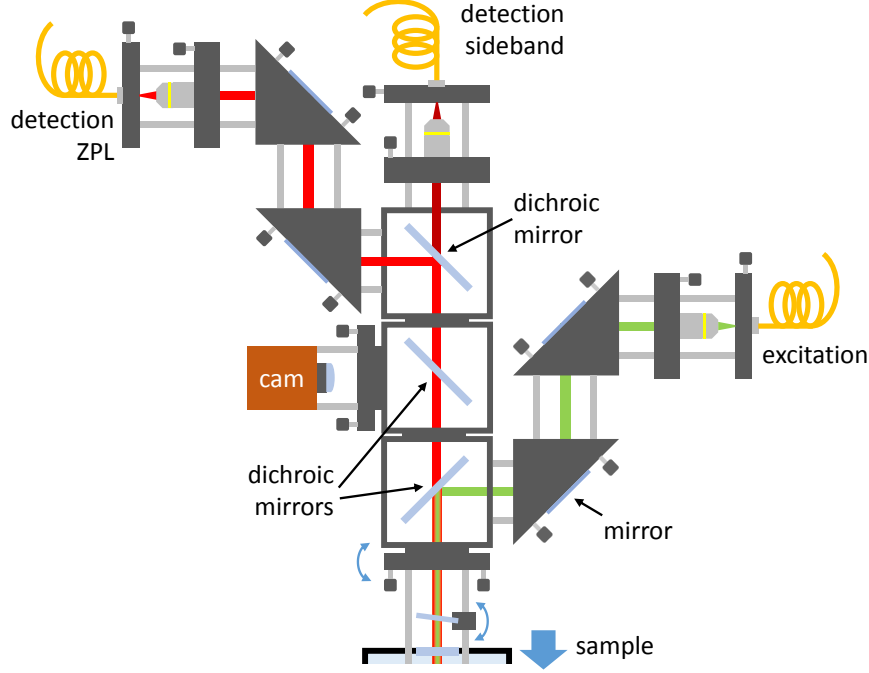


Fig. 3.13. Schematic drawing of the fiber-based confocal setup for the cavity coupling experiment. Opto-mechanical components are used to overlap the excitation and detection paths which are separated via a set of dichroic mirrors (for more details see text). A green laser is focused onto the cavity via a low-temperature objective. Fluorescence originating from the cavity is collected with the same objective and coupled into the detection fiber. The fluorescence is either analyzed with a spectrometer or detected using a SPAD (not depicted).

actuators offer isolation against translational and rotational vibrations stemming from the ground.

We characterize the acoustic noise of our system at low temperature using the cavity resonance as a sensitive probe by measuring the transmission of a narrow-linewidth diode laser ($\lambda = 637 \text{ nm}$) while tuning the cavity length. We optimize the mode matching of the external optics by moving the cavity cage with respect to the objective. We use the z-nanopositioner to set a large mirror separation which leads to a reduction of the cavity finesse due to clipping losses and coupling to lossy higher-order modes [152]. By applying a voltage to the z-positioner we can precisely adjust the mirror separation and find a transmission peak width of $\delta L = 664 \text{ pm}$ which corresponds to a finesse of $\mathcal{F} = 480$ (Fig. 3.14(a)). Here, the mirror separation is calibrated by determining the voltage required to tune the cavity length over a free spectral range $\Delta L_{\text{FSR}} = \lambda/2$. The relatively broad transmission peak allows the cavity length to be fixed on its flank

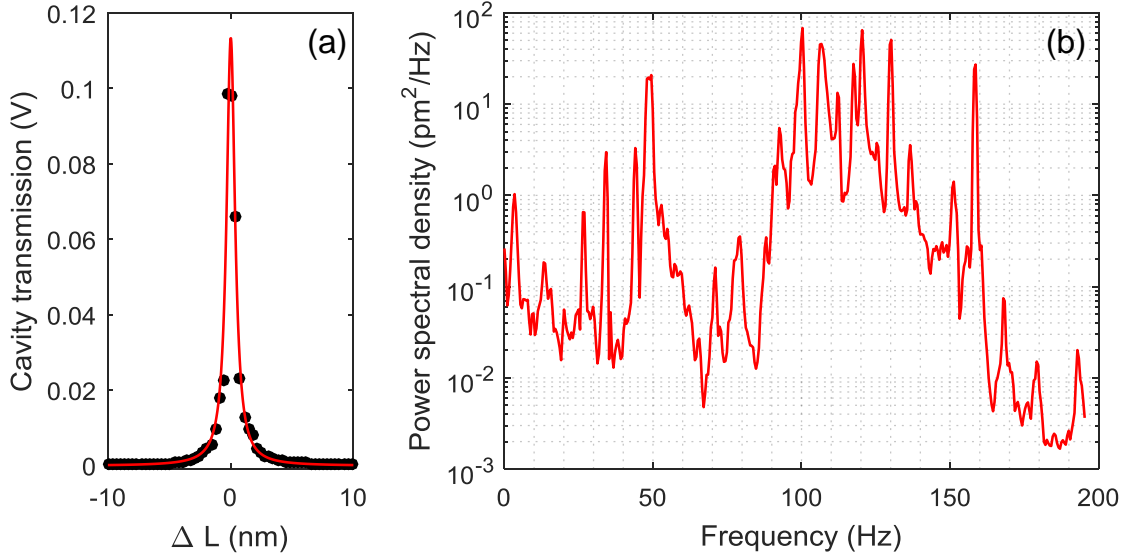


Fig. 3.14. **(a)** Resonant transmission for a large mirror separation exhibiting a linewidth of $\delta L = 664$ pm corresponding to $F = 480$. In order to be most sensitive to length changes, the mirror separation with the largest slope dV/dL is selected as working point. **(b)** Typical power spectral density spectrum of the cavity length fluctuations. The major contribution to the acoustic noise is found for frequencies < 200 Hz. The integration of the noise spectrum from 0 Hz to 200 Hz yields root-mean-square fluctuations of $\delta L_{\text{rms}} = 24$ pm.

where the signal exhibits the largest gradient dV/dL . Fluctuations in cavity length L are now transduced into fluctuations of the signal amplitude. We record the power spectral density of the fluctuations of the transmission signal using a fast Fourier transform (FFT) analyzer (Stanford SR760) and translate it into length fluctuations (Fig. 3.14(b)).

The detectable equivalent noise floor is limited by electrical mains pick-up noise (50 Hz and multiples) to $\approx 8 \cdot 10^{-4} \text{ pm}^2/\text{Hz}$, which we determine in a separate measurement. The acoustic noise power spectrum exhibits several resonances which are all $< 100 \text{ pm}^2/\text{Hz}$. Besides the electrical noise there are some additional major contributions due to resonances of unknown origin at 48 Hz, 107 Hz, 117 Hz, 120 Hz and 130 Hz while the noise amplitudes at other frequencies are $< 5 \text{ pm}^2/\text{Hz}$. We observe that no further significant contribution to the acoustic noise arises from frequencies $\gtrsim 200$ Hz. We retrieve the root-mean-square fluctuations of the cavity length via integration of the noise spectrum from 0 Hz to 200 Hz and find $\delta L_{\text{rms}} = 24$ pm. Considering this acoustic noise level the finesse in our cavity experiment is limited to values $\mathcal{F} = \frac{\lambda}{2\delta L_{\text{rms}}} \lesssim 13\,300$.

3.3.1 Cavity coupling of single NV centers

Figure 3.15(a) shows photoluminescence (PL), obtained at $T = 4$ K, from the diamond membrane-microcavity excited with a green laser at $\lambda = 560$ nm and a power of 20 mW while detuning the width of the air gap L . The spectra are recorded for the lowest attainable fundamental microcavity mode that comes into resonance with the different ZPL transitions. Notably here, no polarization splitting of the fundamental mode is observed, which points at a high symmetry of our concave micromirror [153]. This degeneracy in principle allows for full control over the light polarization. The mirrors are almost in physical contact such that L is dominated by the depth of the curved top mirror ($\sim 1 \mu\text{m}$). Spectra were recorded for detuning the microcavity by changing the membrane-top mirror separation L . Weak PL is observed at all L and arises from broadband emission from the diamond membrane. It allows the L -dependence of the microcavity mode to be characterized.

In addition to this weak broadband emission there are sharp features at specific L which we assign to individual ZPL transitions. The PL from ZPL2 which comes into resonance at an air-gap width $L = 1.96 \mu\text{m}$ is shown for different relative air-gap detunings ΔL in Fig. 3.15(b). We fit a Voigt profile to the resonance (the Gaussian component accounts for the low-frequency acoustic noise). The FWHM Lorentzian contribution of $\Gamma_L = 60.6$ pm yields a finesse of $\mathcal{F} = 5\,260$. We determine the Q -factor of the cavity according to $Q = \lambda/\Gamma_\lambda = \lambda/(\Gamma_L \cdot d\lambda/dL) = 2F/(d\lambda/dL) = 58\,500$ with $d\lambda/dL = 0.18$ (Eq. 2.69). For fixed L , for instance at ZPL2, the microcavity linewidth is $\Gamma_\nu = 8.0$ GHz.

We confirm that the observed resonances are associated with single quantum emitters by performing a photon autocorrelation ($g^{(2)}(t)$) measurement with a Hanbury Brown-Twiss setup. To that end, we excite the NV center with a pulsed supercontinuum source (NKT Photonics, SuperK Extreme EXW-12) operating at a pulse rate of 9.7 MHz and power of 1.3 mW. The PL signal is split up using a fiber beam splitter (Thorlabs, TW670R5A2) and sent to two SPADs. Using a picosecond event timing module (PicoQuant, PicoHarp 300) we record time-tagged time-resolved PL. We then postprocess the data and correlate the arrival times of the photons on each SPAD. The results on ZPL2 are shown in Fig. 3.15(c). The strong suppression of the peak at zero delay is a clear signature of single photon emission. The data are analyzed quantitatively by calculating the pulse area of each peak and normalizing the data to the averaged peak area at long delay times ($500 \mu\text{s}$). We find $g^{(2)}(0) = 0.24$, comfortably less than 0.5. Away from $t = 0$, $g^{(2)}(t)$ is initially larger than one with $g^{(2)}(103 \text{ ns}) = 3.93$, a bunching behavior. This bunching decays as t increases, signifying telegraph noise between bright and dark

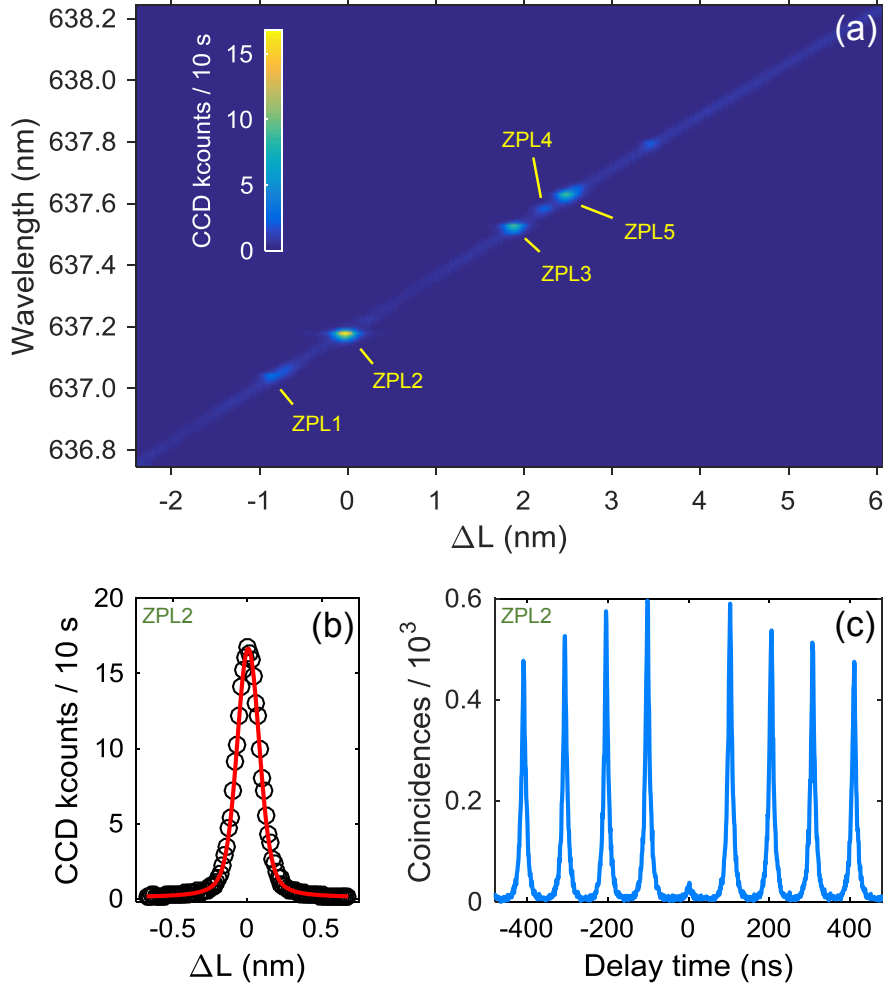


Fig. 3.15. (a) PL spectra around the typical ZPL transition wavelength for different relative air-gap detunings ΔL about $L = 1.96 \mu\text{m}$. Each resonance corresponds to the ZPL emission of a single NV center, as labeled. The PL is excited using a pulsed supercontinuum laser source. ($P \sim 10 \text{ mW}$, $\lambda = 560 \pm 20 \text{ nm}$) and detected by a grating spectrometer. (b) Integrated PL versus L for ZPL2 along with a Voigt fit (FWHM Lorentzian contribution $\Gamma_L = 60.6 \text{ pm}$). Together with the cavity dispersion in (a), Γ_L determines the cavity Q -factor, $Q = \lambda/\Gamma_\lambda = \lambda/(\Gamma_L \cdot d\lambda/dL) = 58\,500$. (c) Photon autocorrelation ($g^{(2)}(t)$) measurement on ZPL2 exhibiting a clear single photon emission $g^{(2)}(0) = 0.27$. The ZPL emission is filtered ($637 \pm 7 \text{ nm}$) and analyzed via a Hanbury Brown-Twiss setup (integration time: 45 000 s).

states. The dark states are the singlet shelving states and the neutral charge state [42]. In the bright state, the important quantity is g , the ratio of the probability of generating two photons in the same pulse to the probability of generating one photon in each of two successive pulses. We find here a small value, $g^{(2)}(0)/g^{(2)}(103 \text{ ns}) = 0.06$.

3.3.2 Observation of lifetime modification

The spectral analysis shows that the microcavity acts as a narrow spectral filter. It is crucial however to demonstrate that the microcavity modifies the behavior of the emitter itself. The key parameter in the weak coupling regime is the emitter decay rate (Eq. 2.48). We therefore turn to excited state lifetime measurements of individual NV centers and tune both the resonance frequency (via an *in situ* change of the air-gap width L) and the lateral position of the cavity anti-node (via an *in situ* change in (x, y)). We excite the NV PL with a short pulse from our supercontinuum source and monitor the relative arrival times of the PL photons using the same hardware as for the $g^{(2)}(t)$ -measurement. Figure 3.16(a) shows decay curves for ZPL2 for several different relative detunings of the air-gap width ΔL , showing a clear change in lifetime. To extract the lifetime quantitatively, we note that for large detunings ΔL the weak background emission represents a significant part of the signal. However, the background emission decays very rapidly: the slower decay process arises from the decay of the NV center. We therefore only consider data for delays larger than 3 ns, which are fitted to a single-exponential convolved with the instrumental response function [38]. The lifetime decreases on detuning ΔL from 10.4 ns to 7.06 ns, a clear evidence of a Purcell effect.

This assertion is backed up by recording the decay time over a larger range of ΔL (Fig. 3.16(b)). Five ZPLs come into resonance with the microcavity at different values of ΔL and each shows a clear Purcell effect, an enhanced decay rate γ_R when in spectral resonance with the microcavity. Each resonance is well described with a Lorentzian function of ΔL . Figure 3.16(c) shows the results of the alternative experiment, detuning in lateral position Δx while maintaining the spectral resonance ($\Delta L = 0$), on ZPL6, an NV located at a different location in the diamond membrane. These results also show a Purcell effect, a resonance in γ_R as a function of Δx . The γ_R versus Δx data are well fitted by a Gaussian function with FWHM $\Gamma_x = 1.33 \mu\text{m}$, which represents the lateral extent of the mode in the microcavity. ZPL6 exhibits the largest decay rate on resonance, $\gamma_R^{\text{on}} = 158 \cdot 10^6 \text{ s}^{-1}$ ($\tau_R^{\text{on}} = 6.33 \text{ ns}$); this suggests that this NV is positioned close to the optimal depth in the diamond membrane.

3.3.3 Analysis of the Purcell enhancement

We interpret the results in terms of a Purcell enhancement factor F_P . Without the top mirror the decay time is consistently $\tau_R^0 = 12.6 \text{ ns}$ for all NVs corresponding to a decay rate $\gamma_R^0 = 79.4 \cdot 10^6 \text{ s}^{-1}$. In terms of the total decay rates, $F_P = \gamma_R^{\text{on}}/\gamma_R^0 = 2.0$. We note that, in the microcavity, the decay rate in the limit of large ΔL -detunings is slightly

larger than the bulk decay rate (Fig. 3.16(b)). We attribute this to non-ZPL emission which is Purcell-enhanced not just at the fundamental microcavity mode but also at higher modes.

This modest Purcell enhancement of the total decay rate, $F_P = 2.0$, corresponds to large changes to the ZPL emission rate. Without the microcavity, radiative decay occurs predominantly into laterally-propagating modes, which are defined by the membrane itself. With the microcavity, these lateral modes still exist, and the decay rate into these modes is unchanged. Instead, the microcavity boosts the radiative decay rate into a single, vertically-propagating mode. Even a small overall Purcell factor therefore implies that the decay rate into the single microcavity mode dominates over the decay rate into all the lateral modes, i.e. a large change to the ZPL fraction.

We analyze the data to determine the ZPL Purcell factor and the ZPL fraction when the microcavity is tuned into resonance with the ZPL, the “on” state. For the “on” state, the total NV decay rate is

$$\gamma_R^{\text{on}} = \gamma_0^{\text{on}} + \gamma_1^{\text{on}} \quad (3.1)$$

where γ_0^{on} is the ZPL emission rate and γ_1^{on} the non-ZPL decay rate. When the microcavity is tuned far out of resonance with the ZPL line, the “off” state,

$$\gamma_R^{\text{off}} = \gamma_0^{\text{off}} + \gamma_1^{\text{off}} \quad (3.2)$$

The experiment determines γ_R^{on} and, by fitting γ_R as a function of either ΔL or Δx (Fig. 3.16), $\gamma_R^{\text{off}} = 88.2 \cdot 10^6 \text{ s}^{-1}$. To proceed, we note, first, that the non-ZPL emission is so broadband that the small frequency shift of the microcavity mode between the “on” and “off” states makes no change to the non-ZPL decay rate, i.e. $\gamma_1^{\text{on}} = \gamma_1^{\text{off}}$. Secondly, in the “off” state, ZPL emission takes place predominantly into laterally-propagating modes. This is also the case in a bare membrane such that $\gamma_0^{\text{off}} \approx \gamma_0$ where γ_0 is the ZPL emission rate in the bare membrane. Hence, we can rewrite Eq. 3.2

$$\gamma_R^{\text{off}} \approx \gamma_0 + \gamma_1^{\text{on}} \quad (3.3)$$

By combining Eq. 3.1 and Eq. 3.3 we obtain:

$$\gamma_0^{\text{on}} = \gamma_R^{\text{on}} - \gamma_R^{\text{off}} + \gamma_0 = F_P^{\text{ZPL}} \gamma_0 \quad (3.4)$$

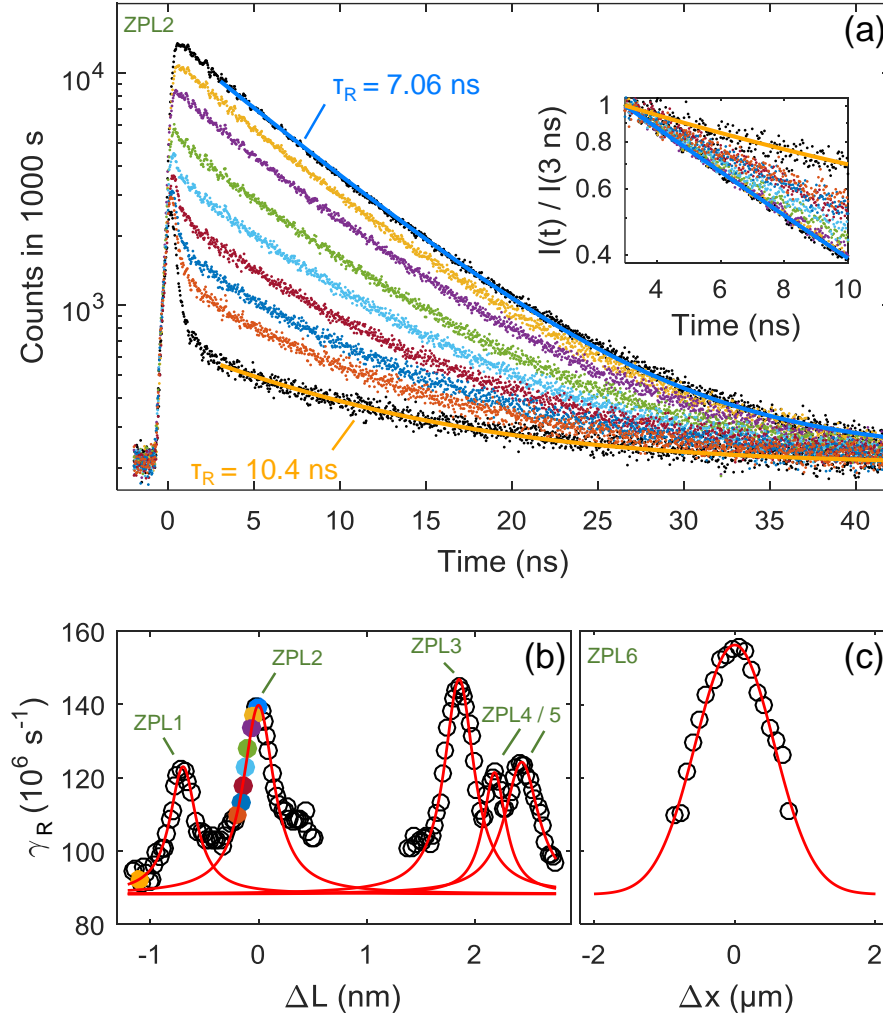


Fig. 3.16. **(a)** PL decay curves of ZPL2 following pulsed excitation as a function of the relative detuning of the air-gap width ΔL for an acquisition time of 1000 s. The data for delays larger than 3 ns are fitted to a single-exponential convolved with the instrumental response. The inset shows the normalized decay curves highlighting the clear change of the decay rate with changing ΔL . **(b)** Recombination rate γ_R versus ΔL for fixed lateral position. For each ZPL resonance, γ_R exhibits a Purcell effect. The experimental data are fitted to Lorentzian curves with FWHM $\Gamma_L = (0.32 \pm 0.05)$ nm. The color of the symbols match the decay curves in (a). **(c)** Recombination rate versus relative lateral position detuning Δx on ZPL6 for zero spectral detuning. The experimental data are fitted to a Gaussian with FWHM $1.33 \mu\text{m}$ corresponding to a radius of the intensity beam waist of $w_{I,\text{exp}} = 0.80 \mu\text{m}$.

This allows us to determine the Purcell factor for the ZPL alone

$$F_P^{\text{ZPL}} = \frac{\gamma_0^{\text{on}}}{\gamma_0} = \frac{\gamma_R^{\text{on}} - \gamma_R^{\text{off}}}{\gamma_0} + 1 \quad (3.5)$$

Taking $\gamma_0 = \xi_{\text{ZPL}}\gamma_R^0$ and using the range of reported NV Debye-Waller factors $\xi_{\text{ZPL}} = 2.4\%$ (5%) [38, 88] leads to $\gamma_0 = 1.91 \cdot 10^6 \text{ s}^{-1}$ ($3.97 \cdot 10^6 \text{ s}^{-1}$) and hence $F_P^{\text{ZPL}} = 37.7$ (18.6) (using the experimentally determined values for ZPL6: $\gamma_R^{\text{off}} = 88.2 \cdot 10^6 \text{ s}^{-1}$, $\gamma_R^{\text{on}} = 158 \cdot 10^6 \text{ s}^{-1}$). The fraction of photons emitted into the ZPL in the “on” state is:

$$\eta_{\text{ZPL}} = \frac{\gamma_0^{\text{on}}}{\gamma_R^{\text{on}}} = \frac{\gamma_0^{\text{on}}}{\gamma_R^{\text{off}} - \gamma_0 + \gamma_0^{\text{on}}} = \frac{F_P^{\text{ZPL}}\gamma_0}{\gamma_R^{\text{off}} - \gamma_0 + F_P^{\text{ZPL}}\gamma_0} \quad (3.6)$$

For ZPL6, $\eta_{\text{ZPL}} = 45.4\%$ (46.7%). We note that η_{ZPL} , a more important parameter for quantum photonics than F_P^{ZPL} , depends very weakly on ξ_{ZPL} which is not known precisely.

3.3.4 Theoretical description

Here, we attempt to account quantitatively for the experimental value of F_P^{ZPL} . The key parameter is the vacuum electric field in the microcavity at the location of the NV center. The vacuum field is a sensitive function of the microcavity geometry which in turn determines the mode structure. In particular, the separation of the fundamental microcavity modes depends on the width of the air gap L . Conversely, the frequency separation between the fundamental modes and the higher order modes depends on the radius of curvature of the top mirror. In addition, the mode structure on making large changes to L depends sensitively on the diamond membrane thickness.

To measure the mode structure, we excite the diamond-microcavity with a continuous-wave green laser at 532 nm with a power of 30 mW and use the weak broadband emission from the diamond as an internal light source. Fig. 3.17(a) shows the microcavity resonances as a function of wavelength and cavity length spanning several free spectral ranges. The fundamental microcavity modes along with the associated higher order modes are clearly observed.

We calculate the mode structure of our cavity by describing the longitudinal standing waves with a commercial software for one-dimensional transfer-matrix calculation (see Appx. A). To that end, we measure the transmission spectrum of a white light source through the individual mirrors and determine the structure of our DBR coatings by comparing the spectrum with the transfer-matrix calculation. We find that the top mirror, which features the concave indentation, is coated with 14 pairs of $\text{SiO}_2/\text{TaO}_2$,

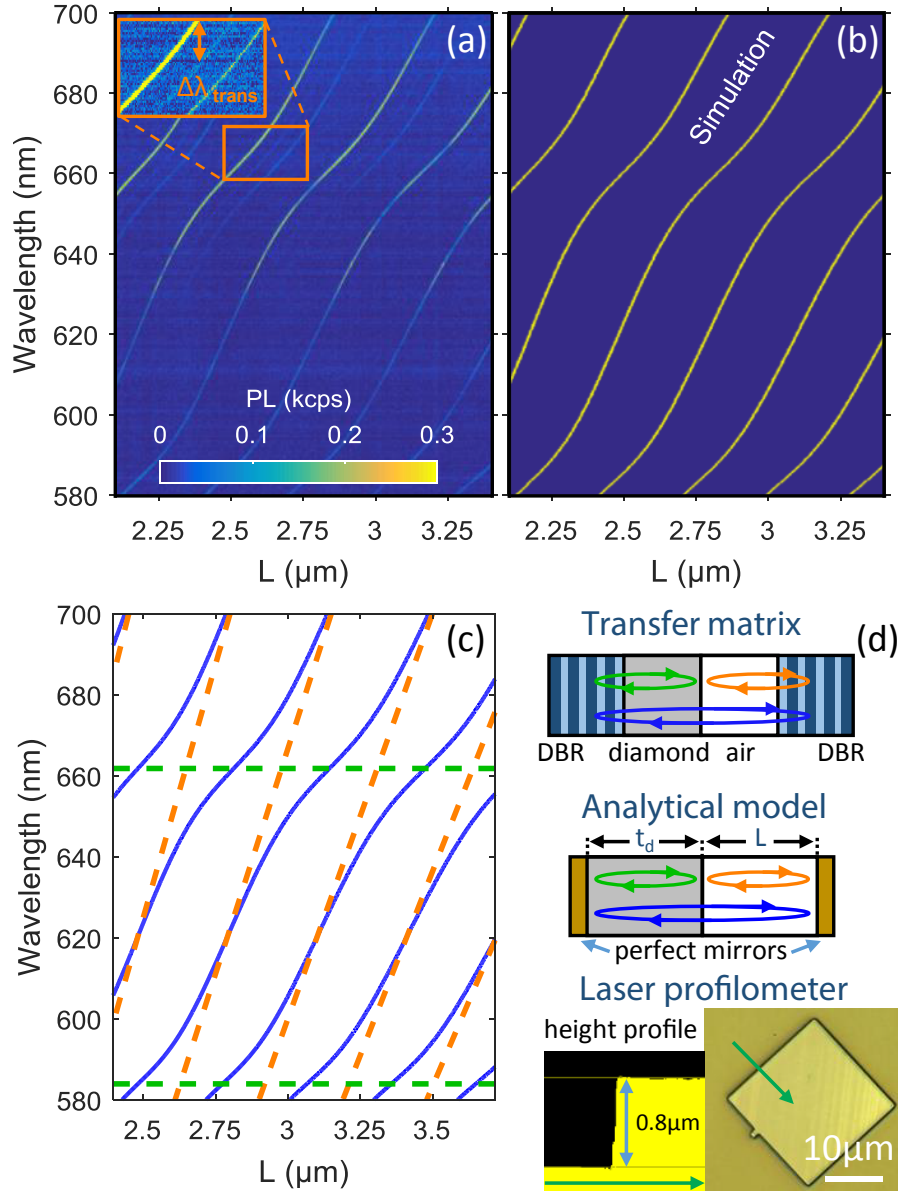


Fig. 3.17. **(a)** Experimentally determined PL spectra on tuning the width of the air gap L over several free spectral ranges. The inset highlights the higher order lateral modes. **(b)** Mode dispersion calculated using a transfer matrix simulation. **(c)** Analytical model highlighting the anti-crossing of dispersion of air-cavity and diamond-cavity. Since the penetration depth of the mirrors is not considered in this model, L is overestimated compared to (a) and (b). **(d)** Cavity schemes for transfer matrix simulation and analytical model. The transfer matrix calculation includes the penetration of the mode in the DBR. Analyzing the diamond with a laser profilometer yields a thickness of $\sim 0.8\mu\text{m}$.

while the bottom mirror exhibits 15 pairs, respectively (Sec. A). Using the transfer matrix formalism we can describe the system matrix of the whole cavity (Eq. A.6):

$$T_{\text{sub}}^{-1}(M_{\text{SiO}_2}M_{\text{Ta}_2\text{O}_5})^{14}M_{\text{air}}M_{\text{dia}}(M_{\text{Ta}_2\text{O}_5}M_{\text{SiO}_2})^{15}T_{\text{sub}} \quad (3.7)$$

We calculate the wavelength-dependent transmittance of the cavity while varying the width of the air gap L . The result of the calculations displayed in Fig. 3.17(b) is in excellent agreement with the experimentally determined mode structure for a diamond thickness of $t_d = 0.77 \mu\text{m}$ and a DBR design wavelength of $\lambda_{\text{DBR}} = 625 \text{ nm}$ (Appx. A). The diamond thickness used in our model corresponds closely to the physical thickness determined with a scanning confocal microscope (Keyence, VK-X200K), Fig. 3.17(d). We note that our 1D calculation does not include the Gouy phase of the Gaussian cavity mode, which leads to a small overestimate of L . The mode structure does not depend on the exact number of DBR layer pairs since the penetration depth of the electric field into the mirror stack is small compared to its overall thickness.

As displayed in Fig. 3.17(c), the shape of the experimentally determined mode structure can be reproduced very well with a simple analytical one-dimensional model, as described in Sec. 2.3.1 (Eq. 2.76) [128]. However, the parameters in this model overestimate both $t_d = 1.03 \mu\text{m}$ and L (see x-axis Fig. 3.17(c)) since the penetration of the field inside the mirrors is neglected ($L_{\text{DBR}} = 265 \text{ nm}$ at $\lambda = 637 \text{ nm}$, Eq. 2.74). Hence, finding t_d via the spacing of the two diamond-confined mode resonances at 583.9 nm and 661.8 nm (green lines in Fig. 3.17(c)) overestimates the actual diamond thickness.

The splitting of the higher-order TEM modes $\Delta\lambda_{\text{trans}}$ (Fig. 3.17(a)) allows to estimate the effective radius of curvature of the concave top mirror (Eq. 2.59). The length of the cavity L can in principle be inferred from the free spectral range of the cavity, $\nu_{\text{FSR}} = c/(2L)$. However, in order to account for the non-linear relationship between λ and L we determine the free spectral range via $\Delta\lambda_{\text{FSR}} = d\lambda/dL \cdot \Delta L_{\text{FSR}} = d\lambda/dL \cdot \lambda/2$. From this and Eq. 2.59 we obtain $R = 16 \mu\text{m}$, which matches the physical curvature of the mirror we expect for the ablation parameters employed (as determined by measurements using a different micromirror template). We note that for this cavity geometry the description of the cavity with Gaussian beam theory is a very good approximation due to the relatively small beam divergence $\theta = \lambda/(\pi w_{0,E}) = 0.18$, where $w_{0,E} = w_{\text{I,exp}} \cdot \sqrt{2}$ (Fig. 3.16).

After having determined the geometry of our microcavity we now turn to quantifying the vacuum field within the diamond. Using a commercial program for the analysis of thin films based on the transfer matrix approach (Thin Film Center Inc., Essential Macleod) we obtain the same mode structure as calculated analytically. We are able

to model very well the mode dispersion displayed in Fig. 3.15(a) with an air-gap width $L = 1.96 \mu\text{m}$ for the given diamond thickness of $t_d = 0.77 \mu\text{m}$. The model predicts the same wavelengths of the fundamental ($\lambda = 637.2 \text{ nm}$) and adjacent fundamental mode ($\lambda = 670.3 \text{ nm}$) as determined in the experiment. Furthermore, it reproduces the slope $d\lambda/dL$ correctly. In addition, the thin-film analysis program calculates the relative spatial distribution of the standing electric field within the cavity along its symmetry axis z . Now, we need to correctly normalize the field amplitudes in order to retrieve the electric vacuum field distribution. By integrating the electromagnetic field over the mode volume we obtain the energy of the vacuum fluctuation:

$$2 \cdot \int_V \frac{1}{2} \epsilon(\vec{r}) |\vec{E}(\vec{r})|^2 d^3r = \hbar\omega/2 \quad (3.8)$$

Here $\epsilon(\vec{r}) = \epsilon_0 \epsilon_r(\vec{r}) = \epsilon_0 n^2(\vec{r}) / \mu_r(\vec{r}) \approx \epsilon_0 n^2(\vec{r})$. The factor 2 arises from the fact that for an electromagnetic field half of the energy is stored in the electric field and the other half in the magnetic field.

For a finite mirror transmission the electric field leaks out of the cavity into propagating modes. Hence, the integral of the energy density diverges due to the normalization problem in open systems [154]. We avoid this problem by setting the integration boundaries of the quantization volume at the last layer of each DBR stack. Using $R = 16 \mu\text{m}$ we determine the radius of the intensity beam waist to be $w_{I,\text{theo}} = 0.83 \mu\text{m}$ via Gaussian optics (corresponding to the value $w_{I,\text{exp}} = 0.80 \mu\text{m}$ determined *in situ* on ZPL6, Fig. 3.17(b)). We use the experimentally determined beam waist to set the lateral confinement of the cavity mode. Since the length of the cavity is short compared to the radius of curvature of the concave mirror we can approximate the beam waist radius to be constant $w_1 \approx w_0$ (compare Eq. 2.60). So, we can rewrite Eq. 3.8:

$$\begin{aligned} \hbar\omega/2 &= \int_{-d_{\text{DBR}}}^{d_{\text{DBR}}} \epsilon_0 n^2(z) |\vec{E}_{\text{vac}}(z)|^2 dz \int_0^{2\pi} d\phi \int_0^\infty e^{-r^2/w_I^2} dr \\ &= 2\pi \cdot \frac{1}{4} w_I^2 \int_{-d_{\text{DBR}}}^{d_{\text{DBR}}} \epsilon_0 n^2(z) |\vec{E}_{\text{vac}}(z)|^2 dz \end{aligned} \quad (3.9)$$

With this normalization we obtain the properly normalized electric field distribution of the vacuum field fluctuations shown in Fig. 3.18. For an NV center located at the optimal position $\lambda_{\text{ZPL}}/(4n_{\text{diamond}}) = 66 \text{ nm}$ away from the Ta_2O_5 -diamond interface we find a maximum electric vacuum field “per photon” of $E_{\text{vac}} = |\vec{E}(\vec{r}_{\text{NV}})| = 36.2 \text{ kV/m}$ where \vec{r}_{NV} is the position of the NV. The optical dipoles of the NV centers are randomly oriented in a plane orthogonal to the NV axis [155, 107]. For NV centers that are coupled

maximally to the cavity mode, we assume that the optical dipole of the ZPL is parallel to the diamond surface and hence couples maximally to the vacuum field. The vacuum field strength at the location of the NV center then corresponds to an effective mode volume which is commonly defined as [133]:

$$V = \frac{\int \epsilon_0 n^2(\vec{r}) |\vec{E}_{\text{vac}}(\vec{r})|^2 d^3r}{\epsilon_0 n^2(\vec{r}_{\text{NV}}) |\vec{E}_{\text{vac}}(\vec{r}_{\text{NV}})|^2} = \frac{\hbar\omega/2}{\epsilon_0 n^2(\vec{r}_{\text{NV}}) |\vec{E}_{\text{vac}}(\vec{r}_{\text{NV}})|^2} \approx 125 (\lambda/n_{\text{diamond}})^3 \quad (3.10)$$

Using Eq. 2.50 we determine a theoretical Purcell factor of $F_P = 1 + \frac{3Q(\lambda/n)^3}{4\pi^2 V} = 36.5$ given $Q = 58\,000$ (Fig. 3.15).

We note that the experimentally determined value of F_P^{ZPL} (Eq. 3.5) is associated with a systematic error due to the uncertainty of the Debye-Waller factor ξ_{ZPL} , the fraction of photons emitted into the ZPL. In fact, the argument can be turned around. The properties of the microcavity are so well understood (Fig. 3.17(a,b)) that using the theoretical value of F_P allows the ZPL emission rate for the NV the bare diamond $\gamma_0 = 2.02 \cdot 10^6 \text{ s}^{-1}$ and hence $\xi_{\text{ZPL}} = \gamma_0/\gamma_R^0$ to be determined. We find $\xi_{\text{ZPL}} = 2.55\%$, which lies within the range of previous estimates [38].

Knowing γ_0 the effective optical dipole moment of the ZPL can be determined, $\mu_{\text{ZPL}} = 0.017 \text{ e}\cdot\text{nm}$ (Eq. 2.44), which agrees remarkably well with previously determined values (0.8 Debye [79]). We determine a coupling rate of the ZPL to the vacuum field of $g_{\text{ZPL}} = \mu_{\text{ZPL}} \cdot E_{\text{vac}}/\hbar = 953 \cdot 10^6 \text{ s}^{-1}$. Here we assume a unity internal quantum efficiency of the NV in accordance with a recent extrapolation of measured quantum efficiencies for shallow NVs into the bulk [156]. The measured Q -factor determines the photon decay rate out of the microcavity, $\kappa = 2\pi\Gamma_\nu = 5.06 \cdot 10^{10} \text{ s}^{-1}$. In the case that emission into “leaky” lateral modes is unchanged by the microcavity, the Purcell factor (Eq. 2.38 and [119]) is $F_P^{\text{ZPL}} = 4g_{\text{ZPL}}^2/(\kappa\gamma_0) + 1 = 36.5$. This value obviously agrees with the Purcell factor determined by Eq. 2.50 via introducing an effective mode volume (Eq. 3.10).

3.3.5 Estimation of the outcoupling efficiency

The analysis of our lifetime measurements shows that we achieve a strong increase of η_{ZPL} , the fraction of photons emitted into the ZPL, from 2.55 % to 46.2 %. The photon flux, however is limited by losses (absorption or scattering) in the dielectric mirror and the diamond. From the analysis of the mode structure, we could infer the geometry of our cavity. Without any losses, we simulate the finesse of our system (given by Eq. 3.7) to be $\mathcal{F}_{\text{theo}} = 15\,800$, where $\mathcal{T}_{\text{top}} = 215 \text{ ppm}$ and $\mathcal{T}_{\text{bottom}} = 183 \text{ ppm}$ are the respective

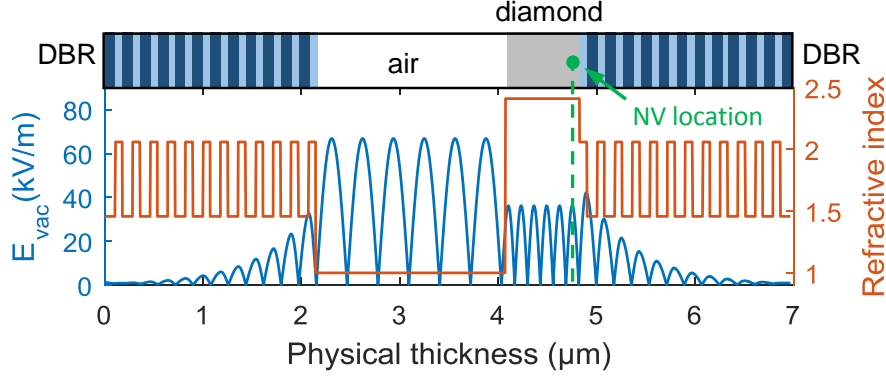


Fig. 3.18. The layer structure of the microcavity along with the refractive index dependence on z . The vacuum electric field E_{vac} is plotted against z for $(x, y) = (0, 0)$ for the lowest attainable fundamental microcavity mode. Parameters: diamond thickness $t_d = 0.77 \mu\text{m}$, air-gap width $L = 1.96 \mu\text{m}$, diamond refractive index $n_d = 2.41$, refractive indices of Bragg mirror $(n_H, n_L) = (2.06, 1.46)$, radius of curvature of top mirror $R = 16 \mu\text{m}$.

transmissions of top and bottom mirror.

Comparing this value with the experimentally determined finesse $\mathcal{F}_{\text{exp}} = 5260$ allows to calculate the round trip loss of our system: $\mathcal{L} = 2\pi/F_{\text{exp}} - 2\pi/\mathcal{F}_{\text{theo}} = 796 \text{ ppm}$. With $Q_{\text{exp}} = 58500$ we can calculate the effective cavity round trip time $\tau = Q_{\text{exp}}/(\nu\mathcal{F}_{\text{exp}}) = 23.6 \text{ fs}$ which enables us to derive the cavity loss rates $\kappa_{\text{top}} = \mathcal{T}_{\text{top}}/\tau = 9.09 \cdot 10^9 \text{ s}^{-1}$, $\kappa_{\text{bottom}} = \mathcal{T}_{\text{bottom}}/\tau = 7.75 \cdot 10^9 \text{ s}^{-1}$ and $\kappa_{\text{loss}} = \mathcal{L}/\tau = 33.69 \cdot 10^9 \text{ s}^{-1}$, where $\kappa_{\text{top}} + \kappa_{\text{bottom}} + \kappa_{\text{loss}} = \kappa_m + \kappa_{\text{loss}} = \kappa = \omega/Q_{\text{exp}} = 5.06 \cdot 10^{10} \text{ s}^{-1}$. Here, $\kappa_m = \kappa_{\text{top}} + \kappa_{\text{bottom}}$ is the total mirror loss rate.

We estimate the probabilities through which channel an initial excitation ($\langle b^\dagger b \rangle(0) = 1$) of the NV center leaks out of the system using the model introduced in Appx. B. For the parameters of our experiment, $g = g_{\text{ZPL}} = 953 \cdot 10^6 \text{ s}^{-1}$ (implying $\xi_{\text{ZPL}} = 2.55 \%$), $\kappa = \omega/Q_{\text{exp}} = 5.06 \cdot 10^{10} \text{ s}^{-1}$ and $\gamma = \gamma_{\text{R}}^0 = 79.4 \cdot 10^6 \text{ s}^{-1}$ the probability for a non-resonant decay of the NV is given by (Eq. B.27):

$$\eta_\gamma = \gamma \int_0^\infty \langle b^\dagger b \rangle dt = \frac{4g^2\gamma + \kappa\gamma^2 + \kappa^2\gamma}{(\kappa + \gamma)(4g^2 + \kappa\gamma)} = 52.5 \% \quad (3.11)$$

On the other hand, the probability for the NV center to decay via the ZPL and exit the system through one of the photonic channels can be calculated via (Eq. B.26):

$$\eta_j = \kappa_j \int_0^\infty \langle a^\dagger a \rangle dt = \frac{\kappa_j}{\kappa + \gamma} \frac{g^2}{g^2 + \kappa\gamma/4} \quad (3.12)$$

Using the cavity loss rates $\kappa_{\text{top}} = 9.09 \cdot 10^9 \text{ s}^{-1}$, $\kappa_{\text{bottom}} = 7.75 \cdot 10^9 \text{ s}^{-1}$ and $\kappa_{\text{loss}} = 33.69 \cdot 10^9 \text{ s}^{-1}$ we find $\eta_{\text{top}} = 8.5 \%$, $\eta_{\text{bottom}} = 7.3 \%$ and $\eta_{\text{loss}} = 31.6 \%$, respectively.*

The single-photon count rates in our experiment of $\sim 10 \text{ kcps}$ suggest, however, that the main fraction of the photons exiting the system via transmission through the top mirror does not reach the detector. Assuming that the NV center is excited by every pulse of the supercontinuum laser source with repetition rate of 78 MHz , we find $10 \text{ kHz}/78 \text{ MHz} = 0.013 \%$, which corresponds to a setup detection efficiency of $\eta_{\text{setup}} \approx 0.15 \%$.

We attempt to estimate the setup detection efficiency by accounting for the known losses, where we neglect transmission losses through anti-reflection coated laser windows and reflection losses off the dichroic and dielectric mirrors in our setup - transmission interface DBR substrate-air $\mathcal{T}_{\text{sub}} = 97.5 \%$, transmission objective $\mathcal{T}_{\text{obj}} = 80 \%$, single-mode fiber coupling efficiency $\eta_{\text{fiber}} = 70 \%$ and SPAD detection efficiency $\eta_{\text{SPAD}} = 70 \%$ - and obtain $\eta_{\text{setup}} \lesssim 38.2 \%$.

It is not clear where the majority of the photons is lost. The strong discrepancy between the estimated and measured value of η_{top} can be partially attributed to the fact that the NV is not excited in every pulse of the excitation laser. In addition, blinking of the NV center caused by shelving into the singlet state and the neutral charge state reduce the PL intensity (as indicated by the bunching in the autocorrelation measurement - see Sec. 3.3.1). Furthermore, the fiber coupling efficiency might be significantly lower due to poor mode-matching. Nevertheless, further systematic experiments are required to identify and mitigate sources of photon loss in our system.

3.4 Conclusions and potential improvements

Based on the work presented here, we suggest that a miniaturized Fabry-Pérot micro-cavity using a thin diamond membrane constitutes a potential key building block for quantum technology applications. We report a massive improvement in the photonics of NV centers by significantly enhancing their phonon-free photon emission. We demonstrate a step-change in NV ZPL fraction from 3% to close to 50% , while minimizing the effects of nano-fabrication on spectral purity. We demonstrate that our device enables us to deterministically couple several NV centers individually based on its *in situ* spectral and spatial tuning capability.

The ultimate goal for such a device is to obtain a high flux of indistinguishable coherent photon emission from the NV center, as it is required for many quantum information

* $\eta_{\gamma} + \eta_{\text{top}} + \eta_{\text{bottom}} + \eta_{\text{loss}} = 99.9 \% \neq 100 \%$ due to rounding errors.

applications. In order to collect as many of the ZPL photons as possible it is required to mitigate photon loss and maximize the outcoupling efficiency through the top mirror η_{top} . Furthermore, the fraction of ZPL emission η_{ZPL} can be increased towards 100 % by improving the performance of the cavity (i.e. the Purcell enhancement).

We estimate the potential of our approach by calculating the figure of merit η_{top} for various designs using the model introduced in Eq. 3.12 and Appx. B. For all the calculations we fix the decay rate $\gamma = 79.4 \cdot 10^6 \text{ s}^{-1}$ and the Debye-Waller factor $\xi_{\text{ZPL}} = 2.55 \%$. We infer the ZPL-cavity coupling rate g and the cavity round-trip time τ from the cavity geometry.

For our experiment we find that an initial emitter excitation results in a ZPL photon coupled out through the top mirror with a probability of $\eta_{\text{top}} = 8.5 \%$ (Eq. 3.12). For an ideal cavity, all photon losses due to transmission κ_{m} correspond to photon channeling towards the detection optics (perfectly reflecting bottom mirror: $\kappa_{\text{bottom}} \rightarrow 0$, $\kappa_{\text{top}} = \kappa_{\text{m}}$). In this case, the photon outcoupling efficiency is limited by the non-resonant decay rate of the NV center γ and losses \mathcal{L} . Keeping all other experimental parameters the same, $\mathcal{L} = 796 \text{ ppm}$, $\tau = 23.6 \text{ fs}$, $g = 953 \cdot 10^6 \text{ s}^{-1}$, the ZPL outcoupling probability for $\kappa_{\text{top}} = \kappa_{\text{m}} = 16.8 \cdot 10^9 \text{ s}^{-1}$ would increase to $\eta_{\text{top}} = 15.8 \%$ (Tab. 3.1(a)), a factor of two improvement compared to our experiment.

Our model suggests that if we adapt κ_{m} for the given losses in our experiment we can improve η_{top} . If the mirror reflectivities are reduced such that $\kappa_{\text{m}} = 5.18 \cdot 10^{10} \text{ s}^{-1}$ we find $\eta_{\text{top}} = 21.1 \%$ (Tab. 3.1(b)). Notably, a higher ZPL outcoupling probability can be achieved for a reduced value of the Purcell enhancement $F_{\text{P}}^{\text{ZPL}} = 22.0$, since the ratio of losses \mathcal{L} and transmission κ_{m} becomes more favorable in this case. Importantly, the resulting maximum in η_{top} as a function κ_{m} of is broad (Fig. 3.19), implying robustness against mirror imperfections. Assuming perfect reflection for the bottom mirror this κ_{m} corresponds to a top mirror transmission of $\mathcal{T}_{\text{top}} = 0.122 \%$.

Further improvements can be achieved if the losses of the system are mitigated. Fabry-Pérot microcavities with overall losses $\lesssim 100 \text{ ppm}$ have been demonstrated operating at $\lambda = 780 \text{ nm}$ [141]. The loss within the mirror coatings can be strongly reduced; $\sim 2 \text{ ppm}$ loss dielectric mirrors have been reported for $\lambda = 852 \text{ nm}$ [123]. Furthermore, losses originating from absorption and scattering within the diamond membrane and its surface can be decreased by optimizing the fabrication process. We guess that it is realistic that the overall round-trip losses can be reduced to $\mathcal{L} \lesssim 200 \text{ ppm}$. Hence, if for the current device geometry we adapt the optimized value for κ_{m} , $\kappa_{\text{m}} = 2.15 \cdot 10^{10} \text{ s}^{-1}$ ($Q = 98\,590$), we obtain an overall extraction efficiency of $\eta_{\text{top}} = 43.3 \%$ (Tab. 3.1(b)). In the limit of a loss-less cavity $\mathcal{L} = 0 \text{ ppm}$, κ_{m} can be strongly reduced to optimize

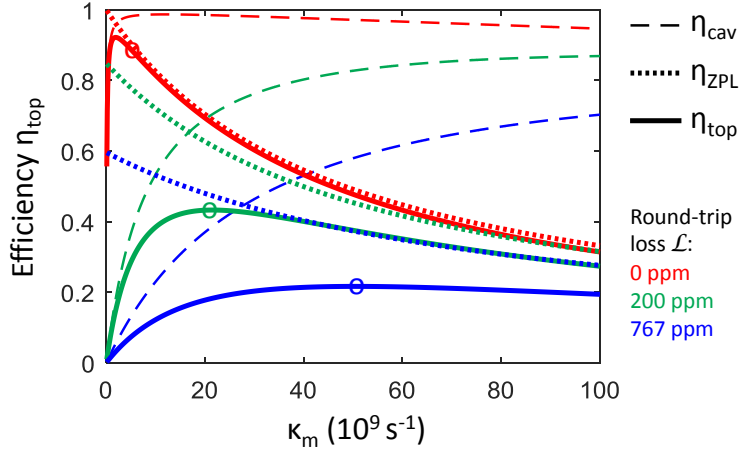


Fig. 3.19. Outcoupling efficiency η_{top} versus mirror transmission rate κ_m for different for different round-trip losses \mathcal{L} : 0 ppm (red), 200 ppm (green) and 767 ppm (blue). The total outcoupling efficiency is a product of the ZPL fraction η_{ZPL} and the outcoupling efficiency of the cavity in case of an ideal two-level emitter η_{cav} . The circles indicate the values of κ_m stated in Tab 3.1.

η_{top} . The value of κ_m for which η_{top} is maximized can be analytically determined from Eq. 3.12, $\kappa_m = 2g$, which results in $\eta_{\text{top}} = 92.2\%$. If κ_m is reduced further the system will enter the strong coupling regime (Sec. 2.2.2), where the photon outcoupling efficiency is limited by reabsorption of the photon by the emitter and an increased probability that the excitation is lost via non-resonant decay depending on γ . To reach the condition $\kappa_m = 2g$, the finesse would need to be increased to $\mathcal{F} = 139\,000$, which corresponds to a mirror transmission of $\mathcal{T}_{\text{top}} = 45$ ppm assuming a perfectly reflecting bottom mirror.

Fig. 3.19 displays the dependence of the outcoupling efficiency η_{top} on the mirror transmission rate κ_m for three different round-trip losses \mathcal{L} : 0 ppm, 200 ppm and 767 ppm. We note that Eq. 3.12 can be equivalently described as the product of the photon outcoupling efficiency for an ideal two-level system η_{cav} and the fraction of ZPL emission η_{ZPL} . It is apparent that increasing the value of κ_m above the optimum value may reduce η_{ZPL} , but still results in very high efficiencies.

We acknowledge that a cavity exhibiting the ideal finesse value for the lossless case $\mathcal{F} = 139\,000$ is not operable in a cryogenic environment due to vibrations. We estimate, however, that by implementing an active stabilization of our cavity via a fast feedback loop, finesse values of $\mathcal{F} = 50\,000$ are realistic. This value corresponds to $\kappa_m = 5.97 \cdot 10^{10} \text{ s}^{-1}$, which entails an extraction efficiency of $\eta_{\text{top}} = 88.3\%$ (Tab. 3.1(c)).

The present cavity design (Fig. 3.17(b)) results in a low vacuum electric field amplitude at the diamond–vacuum interface in order to minimize the scattering losses. For the

optimal diamond thickness, the vacuum field exhibits a node at the interface which would reduce the scattering losses further.

In addition to reducing losses and adapting the mirror reflectivities, changes of the cavity geometry provide a significant improvement to the ZPL fraction η_{ZPL} . By reducing the mode volume, the emitter-photon coupling rate g is enhanced. Calculations predict that by decreasing the diamond membrane thickness t_d and radius of curvature of the top mirror R the maximum vacuum field E_{vac} in the diamond is boosted significantly. Employing state-of-the-art laser ablation techniques, shallow depressions with a depth of about 400 nm and $R \sim 5.5 \mu\text{m}$ can be fabricated [144].

For instance, decreasing $t_d = \lambda_{\text{ZPL}}/2 = 132 \text{ nm}$, in combination with the aforementioned improved concave mirrors allowing for $L = \lambda_{\text{ZPL}} = 637 \text{ nm}$, increases the maximum vacuum field from $E_{\text{vac}} = 36.2 \text{ kV/m}$ to $E_{\text{vac}} = 85.7 \text{ kV/m}$ ($g = 2.25 \cdot 10^9 \text{ s}^{-1}$) (Fig. 3.20(a)). By simulating the Q -factor and finesse of this cavity geometry we find a round-trip time of $\tau = Q/(\nu\mathcal{F}) = 7.43 \text{ fs}$. (Note that the simulated τ does not depend on the exact number of DBR layer pairs if more than 10 pairs are considered.)

Again, accounting for round-trip losses of $\mathcal{L} = 200 \text{ ppm}$ we estimate that we obtain a maximum $\eta_{\text{tot}} = 52.8 \%$ for $\kappa_m = 87.3 \cdot 10^{10} \text{ s}^{-1}$ corresponding to $\mathcal{F} = 7\,400$ (Tab. 3.1(d)). The reason why the optimum extraction efficiency η_{tot} is obtained for a relatively modest Q -factor (27 300) is due to fact that κ_m needs to significantly exceed \mathcal{L} in order to not compromise η_{cav} . In the ideal case of $\mathcal{L} = 0$, $\eta_{\text{top}} = 93.4 \%$ for $\mathcal{F} = 50\,000$ $\kappa_m = 16.9 \cdot 10^9 \text{ s}^{-1}$ (Tab. 3.1(e)).

If the diamond surface can be made sufficiently smooth it becomes possible to change the design such that there is an anti-node of the vacuum field at the diamond–vacuum interface without introducing larger scattering losses due to surface roughness. These losses can be estimated via $S \approx (4\pi\sigma_{\text{rms}}/\lambda)^2$ [140]. The typical diamond roughness we obtain after the current fabrication process is $\lesssim 0.3 \text{ nm}$ [149] which corresponds to scattering losses of $S = 35.0 \text{ ppm}$. Furthermore, potential absorption losses due to surface contaminations can be mitigated by passivating the surface using atomic layer deposition (ALD) [157]. In addition, surface roughness scattering is expected to be less prominent as it was reported that ALD results in smoothing of the surface [158].

The improved cavity design boosts the vacuum electric field at the anti-node in the diamond membrane: the global maximum of the vacuum field is now located in the diamond rather than in the air gap [113] (Fig. 3.20(b)). For instance, for $t_d = 3\lambda_{\text{ZPL}}/4 = 198 \text{ nm}$ and $L = 3\lambda_{\text{ZPL}}/4 = 477.8 \text{ nm}$, $E_{\text{vac}} = 127 \text{ kV/m}$ and $g = 3.34 \cdot 10^9 \text{ s}^{-1}$. Again considering losses of $\mathcal{L} = 200 \text{ ppm}$, $\kappa_m = 70.8 \cdot 10^{10} \text{ s}^{-1}$ results in $\eta_{\text{tot}} = 77.9 \%$ (Tab. 3.1(f)). Neglecting losses we find $\eta_{\text{tot}} = 97.7 \%$ for $\kappa_m = 2g = 6.68 \cdot 10^{10} \text{ s}^{-1}$ ($\mathcal{F} = 41\,000$)

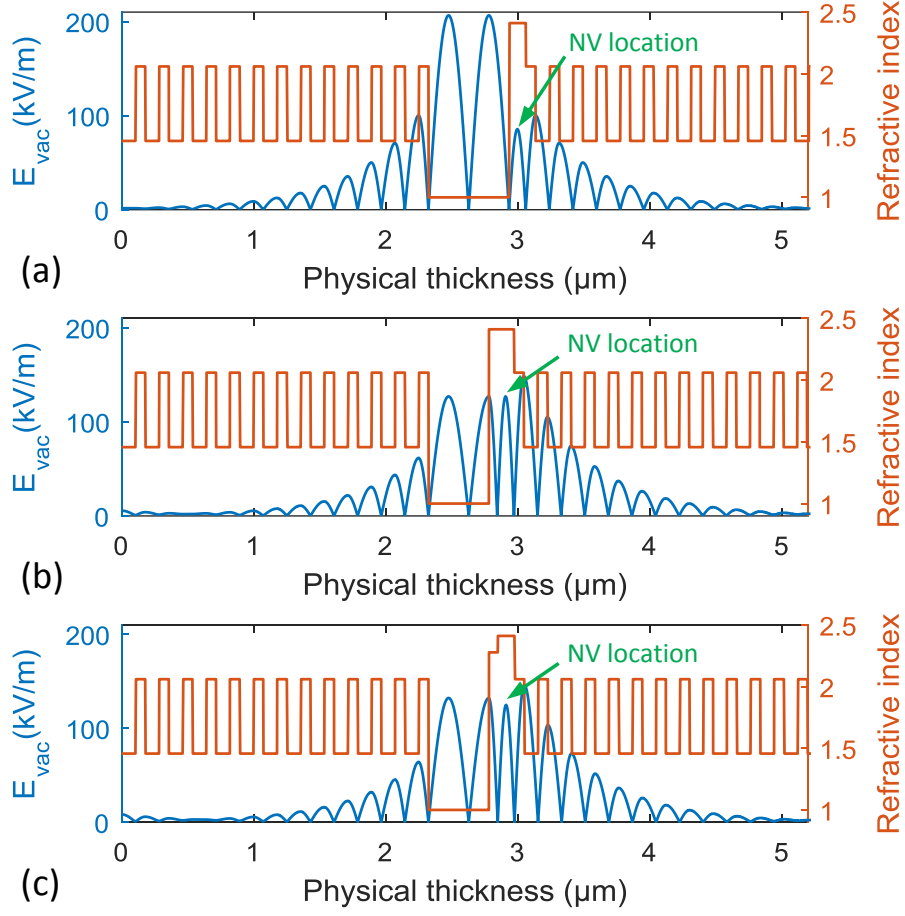


Fig. 3.20. Vacuum electric field E_{vac} for the best realistic microcavity structures along with the refractive index dependence plotted against z for $(x, y) = (0, 0)$: diamond refractive index $n_d = 2.41$, refractive indices of Bragg mirror $(n_H, n_L) = (2.06, 1.46)$, radius of curvature of top mirror $R = 5.5 \mu\text{m}$ (with depth of about 400 nm). **(a)** Best air-confined cavity: diamond thickness $t_d = \lambda/2 = 132 \text{ nm}$, width of air gap $L = \lambda = 637 \text{ nm}$. **(b)** Best diamond-confined cavity: diamond thickness $t_d = 3/4\lambda = 132 \text{ nm}$, width of air gap $L = 3/4\lambda = 477.8 \text{ nm}$. **(c)** Cavity with additional $\lambda/4$ -layer of TiO_2 : diamond thickness $t_d = \lambda/2 = 132 \text{ nm}$, width of air gap $L = 3/4\lambda = 477.8 \text{ nm}$.

(Tab. 3.1(g)).

Note that in this configuration round-trip losses of $\mathcal{L} = 200 \text{ ppm}$ are more difficult to obtain for two reasons. The aforementioned anti-node at the diamond–vacuum interface increases scattering losses due to surface roughness. Furthermore, in this design the round-trip time $\tau = Q/(\nu F) = 22.9 \text{ fs}$ is significantly increased which corresponds to an increased effective cavity length $L_{\text{eff}} = c\tau/2$. More losses are anticipated, since absorption losses typically scale with the effective cavity length.

Lastly, we suggest a different approach to strongly enhance the vacuum field while

	(a)	(b)	(c)	(d)	(e)	(f)	(g)	(h)
design	exp	exp	exp	A ⁴ D ²	A ⁴ D ²	A ³ D ³	A ³ D ³	A ³ TD ²
Fig.	3.18	3.18	3.18	3.20(a)	3.20(a)	3.20(b)	3.20(b)	3.20(c)
\mathcal{L} (ppm)	796	200	0	200	0	200	0	0
τ (fs)	23.6	23.6	23.6	7.43	7.43	22.9	22.9	21.3
E_{vac} (kV/m)	36.2	36.2	36.2	85.7	85.7	127	127	125
g (10^9 s^{-1})	0.953	0.953	0.953	2.25	2.25	3.34	3.34	3.23
κ_{m} (10^9 s^{-1})	51.8	21.5	5.32	87.3	16.9	70.8	6.68	6.58
\mathcal{F}	3 110	8 860	50 000	7 400	50 000	3 440	41 000	44 800
$F_{\text{P}}^{\text{ZPL}}$	22.0	60.9	339	88.7	593	278	3 300	3 250
η_{ZPL} (%)	36.5	61.4	89.9	69.9	93.9	87.9	98.9	98.8
η_{cav} (%)	51.8	70.4	98.2	75.5	99.4	88.6	98.8	98.8
η_{top} (%)	21.1	43.2	88.3	52.8	93.4	77.9	97.7	97.6

Table 3.1. Calculation of cavity parameters for various cavity designs. Here, a perfectly reflecting bottom mirror is assumed. Mirror losses occur only via transmission through the top mirror, $\kappa_{\text{top}} = \kappa_{\text{m}}$, which is optimized such that the figure of merit η_{top} is maximized. **(a),(b),(c)** Geometry from experiment with round-trip losses $\mathcal{L} = 796$ ppm, 200 ppm and 0 ppm (Fig. 3.18). **(d),(e)** Ideal air-confined geometry with round-trip losses $\mathcal{L} = 200$ ppm and 0 ppm comprising an air-gap width of $4\lambda/4$ (A⁴) and a diamond thickness of $2\lambda/4$ (D²) (Fig. 3.20(a)). **(f),(g)** Ideal diamond-confined geometry with round-trip losses $\mathcal{L} = 200$ ppm and 0 ppm comprising an air-gap width of $3\lambda/4$ (A³) and a diamond thickness of $3\lambda/4$ (D³) (Fig. 3.20(b)). **(h)** Optimized geometry without round-trip loss including a $\lambda/4$ TiO₂ layer, an air-gap width of $2\lambda/4$ (A²) and a diamond thickness of $2\lambda/4$ (D²) (Fig. 3.20(c))

keeping scattering losses at a minimum. Depositing a $\lambda/4$ layer of TiO₂ on a diamond with $\lambda/2$ thickness via ALD results in electric field nodes at both diamond interfaces (Fig. 3.20(c)). For an air-gap width of $3\lambda/4$ the electric field anti-node is shifted to the TiO₂-air interface where the surface roughness is significantly reduced by the aforementioned smoothing effect of the ALD process [158]. Compared to the previous case with the anti-node at the diamond-air interface the vacuum field is only slightly reduced, $E_{\text{vac}} = 125 \text{ kV/m}$ ($g = 2.07 \cdot 10^{10} \text{ s}^{-1}$). For $\mathcal{L} = 0$ ppm we predict $\eta_{\text{tot}} = 97.6\%$ for $\kappa_{\text{m}} = 6.58 \cdot 10^{10} \text{ s}^{-1}$ corresponding to $\mathcal{F} = 44 800$ (Tab. 3.1(h)).

In addition to providing a massive boost to the ZPL fraction a further advantage of a large Purcell enhancement is that the NV transform limit increases. In our experiment, for $F_{\text{P}}^{\text{ZPL}} = 36.5$, the transform limit of the ZPL linewidth is only slightly increased from $\Gamma_0 = \gamma_{\text{R}}^0/(2\pi) = 12.6 \text{ MHz}$ to $\Gamma_{\text{exp}} = \gamma_{\text{R}}^{\text{on}}/(2\pi) = 25.1 \text{ MHz}$. We predict a maximal Purcell enhancement of $F_{\text{P}}^{\text{ZPL}} = 527$ for the lossless diamond-confined cavity (Tab. 3.1(g)), which results in an increase of the natural linewidth to $\Gamma = (F_{\text{P}}^{\text{ZPL}} \xi_{\text{ZPL}} \gamma_{\text{R}}^0 + \gamma_{\text{R}}^0)/(2\pi) = 182 \text{ MHz}$. Implementing these improvements would therefore mitigate the constraints on the spectral stability of the NV ZPL transition. Only a slight reduction of the spectral

fluctuations of the NV centers in our current experiment would be required in order to create a high fraction of indistinguishable photons.

We attempt to estimate the potential improvement of the spin-spin entanglement rate due to cavity coupling. Typically in these experiments a hemispherical solid immersion lens (SIL) is etched into the surface of the diamond to hamper the effect of total internal reflection. These structures allow for collection efficiencies of $\sim 30\%$ [51]. Given $\xi_{\text{ZPL}} = 2.55\%$ the overall collection efficiency of the ZPL amounts to $\eta_{\text{tot,SIL}} = 0.8\%$. If the linewidth broadening can be overcome and in the case of an air-confined cavity with $\mathcal{L} = 200$ ppm, resulting in $\eta_{\text{tot,cav}} = 52.8\%$ (Tab. 3.1(d)), the spin-spin entanglement rate would be boosted by a factor of $(\eta_{\text{tot,cav}}/\eta_{\text{tot,SIL}})^2 \approx 4\,400$ compared to previous experiments [159].

If the losses can be strongly suppressed ($\mathcal{L} = 0$ ppm) for the current geometry of the experiment $\eta_{\text{tot,cav}} = 88.3\%$ (Tab. 3.1(c)) can be attained, which would lead to an enhancement factor of $\approx 12\,200$. For the improved geometry comprising a $\lambda/4$ layer of TiO_2 $\eta_{\text{tot,cav}} = 97.6\%$ (Tab. 3.1(i)) would result in an enhancement of $\approx 14\,900$.

Chapter 4

A low-loss, broadband antenna for efficient photon collection from a coherent spin in diamond

The content of this chapter is partially adapted from:

Daniel Riedel*, Dominik Rohner*, Marc Ganzhorn, Timo Kaldewey, Patrick Appel, Elke Neu, Richard J. Warburton and Patrick Maletinsky,

**equal contribution*

“A low-loss, broadband antenna for efficient photon collection from a coherent spin in diamond”, Physical Review Applied **2**, 064011 (2014).

For the majority of applications of NV center spins, the efficiency of collection and detection of the broadband NV PL is an essential figure of merit. For example, increased NV PL detection rates lead to improved sensitivities in magnetometry applications [50] and higher two-photon interference rates for entangling remote NV spins [26]. These collection efficiencies, however, are intrinsically limited by the non-directional emission of NV PL and total internal reflection at the interface of the high-index diamond host material and its low-index surrounding. Typically only $\sim 3\%$ of the photons can be collected using conventional microscope optics [55].

To overcome these obstacles and to improve the photon collection efficiency from NV spins, several approaches are currently being pursued. Total internal reflection can be rendered inefficient by placing NV centers inside nanocrystals [160] whose dimensions are smaller than the emission wavelength of the PL. Due to their small size nanodiamonds can also be integrated with photonic structures that enhance the collection [161]. The larger collection efficiency of the PL photons, however, is accompanied by an increased radiative lifetime due to the reduction of effective refractive index, which leads to a decrease of the density of final states for the spontaneous emission process (com-

pare Sec.2.2.2). Due to the proximity to fluctuating surface charges NV centers in nanodiamonds suffer from blinking [138]. Furthermore, the spin coherence times are orders of magnitude shorter and the emission lines broadened compared to NV centers in bulk [50, 138]. Another approach to reduce total internal reflection is to apply an anti-reflection coating onto the diamond [162]. This approach can be combined with the fabrication of solid immersion lenses (SIL) into the diamond via focused ion beam milling [51, 52]. If the NV center is located in the center of the SIL [53] its emission can be collected more efficiently for a wide range of angles as it is impinging the diamond-air interface orthogonally. In combination with an anti-reflection coating up to $\sim 15\%$ of the total emission can be collected [104]. However, anti-reflection coatings and SILs still do not address the directionality of the NV emission.

Conversely, the directionality of NV emission can be improved by optical waveguides [54], nanowires [55, 56, 57] and grating structures [58]. In these structures the total internal reflection at the diamond-air interface is harnessed to guide the light towards the detection optics. Nanowires and grating structures are monolithic structures fabricated by reactive ion etching. Although these devices enable high photon detection rates the collection efficiencies are limited. For symmetry reasons maximally half of the photons are emitted from the nanowire's top facet. The guiding via total internal reflection facilitates narrowband collection efficiencies of $\sim 50\%$ [56], while collection capabilities integrated over the whole NV emission spectrum is reduced to $\sim 30\%$ [55] using a conventional high-NA objective with a high acceptance angles ($\text{NA} = 0.95$). Theoretical predictions suggest that grating structures on the other hand can be engineered such that the collection efficiency for narrowband applications can be optimized to $\gtrsim 90\%$ for collection optics with an $\text{NA} = 1.5$ with an average efficiency of $\sim 70\%$ over the broadband NV PL. This high NA, however, significantly limits the realm of potential applications. Particularly, for low-temperature spin-photon entanglement applications, a high collection efficiency with low-NA emission is required. Simulations predict that 13% of the broadband emission occurs within an NA of 0.7, while the grating structure can be optimized for collecting 30% of the narrowband emission around the NV ZPL within an NA of 0.5.

Furthermore, metal-based broadband enhancement approaches [163, 161] have been realized, which are however plagued by high intrinsic optical losses. Optical resonators on the other hand typically only operate in a narrow wavelength range and are therefore ill-suited for broadband enhancement leading to high count rates. Nevertheless, specially engineered cavities with low quality factors and minimized mode volumes [124] were used for broadband enhancement of the PL from nanodiamonds. Note that as explained in

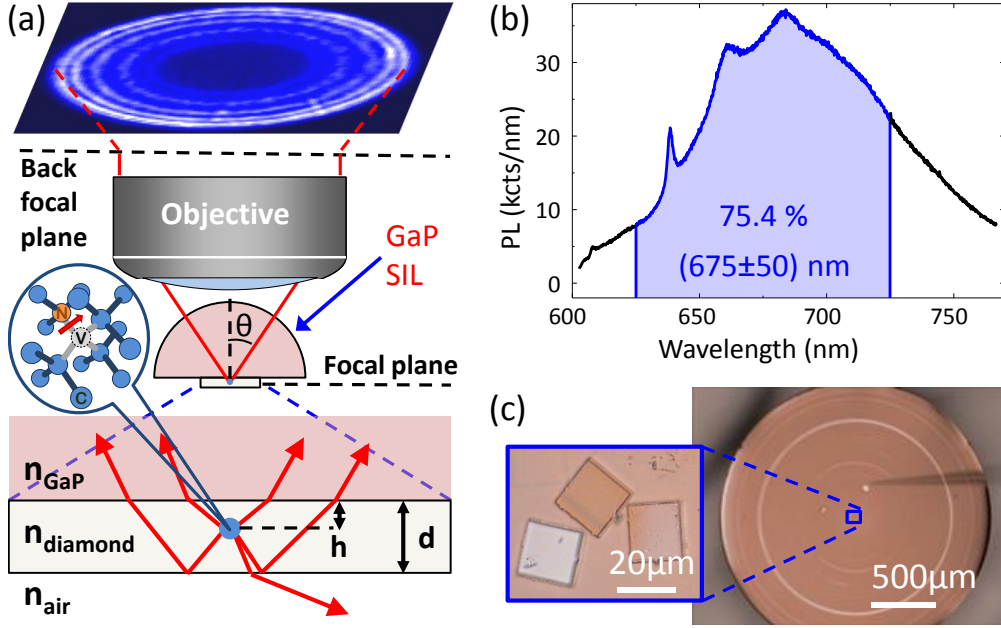


Fig. 4.1. (a) Schematic of the high-index dielectric optical antenna structure: a thin diamond membrane containing nitrogen-vacancy (NV) centers is bonded to a gallium phosphide solid immersion lens (GaP SIL). The majority of the NV photoluminescence (PL) is emitted within the critical angle $\theta \sim 47^\circ$ of the GaP-diamond interface (corresponding to emission within an NA ~ 0.73). (b) Room temperature PL spectrum of a single NV center collected through the dielectric antenna. PL studied in this work passes through a (675 ± 50) nm bandpass filter to improve the signal-to-background ratio. (c) Positioning of the transferred diamond membranes onto the GaP SIL using a micromanipulator.

Ch. 3 narrowband cavities are of paramount importance for the enhancement of the pure ZPL photon emission rates.

A new, alternative approach for broadband enhancement based on a layered, dielectric optical antenna was proposed and demonstrated for individual molecules in a low-index polymer matrix [164]. Such a “dielectric optical antenna” stands out due to its broadband and almost loss-less operation, which can in principle yield near-unity collection efficiencies for single emitters [165, 166]. By significantly boosting the collection efficiency the antenna allows for the creation of an extremely regular stream of photons from organic molecules leading to intensity squeezing of the emitted PL [167]. However, despite their attractiveness, dielectric optical antennas have never been realized for NV centers in diamond, where they would be particularly well-suited to collect the broadband PL. In addition to their excellent performance, such antennas can be engineered employing high-quality nano-fabricated single-crystalline material which exhibit a high degree of spin coherence.

4.1 Antenna design and implementation

Our antenna is based on a thin, single-crystalline diamond membrane directly bonded to the center of a high-index SIL, as illustrated in Fig. 4.1(a). The three layers consisting of air (refractive index $n_1 = 1.0$), the diamond film ($n_0 \sim 2.4$) and the gallium phosphide (GaP, $n_2 \sim 3.3$) SIL together form the antenna and lead to the highly directional NV emission.

Crucial to the operation of our antenna is the use of a SIL material which is transparent for the NV PL and whose refractive index exceeds the one of diamond. This index contrast and the thin diamond membrane are at the heart of the operation of the antenna as they lead to preferential photon emission into the high-index material [168] (Fig. 4.1(b)). The only readily available SIL material with refractive index significantly exceeding diamond and exhibiting transparency over the NV emission spectrum is GaP [169].

Efficient outcoupling of the photons from the GaP can be achieved with a hemispherical shape [170]: over a wide range of angles photons originating from the antenna have normal incidence at the GaP-air interface which prevents total internal reflection. If an optical beam is focused onto the lens, it will have an effectively shorter wavelength and the spot size at the focus reduced by a factor of $1/n_{\text{GaP}}$ resulting in an enhanced resolution [171]. Similarly, the system magnification is increased by a factor of n_{GaP} and the diameter of the field of view is decreased by a factor $1/n_{\text{GaP}}$ compared to the field of view without the SIL. Light originating from the outer regions of the field of view will experience aberration due to refraction at the surface.

Rays originating from the focal area off axis at a distance Δx will only make small angles with the surface normal and will not be strongly aberrated. These angles scale with the ratio of the distance from the SIL's center Δx to the radius of the SIL (Fig. 4.2). For a GaP SIL with a radius of 1 mm the region of the focal plane from which PL can be collected without introducing significant aberrations has a diameter of $\sim 20 \mu\text{m}$ [170]. The SIL was fabricated from bulk material by mechanical polishing of a sphere and successive laser cutting (A.W.I. Industries). The characterization of the optical properties of the employed GaP material is described in Appx. C.

The planar interfaces air-diamond-GaP form the dielectric antenna. In order to understand how this dielectric layer system channels the NV emission into a narrow solid angle, we first consider the far-field angular radiation pattern of a dipole in a homogeneous diamond medium (Fig. 4.3(a)) which exhibits the typical $\sim \cos^2(\theta)$ dependence.

If the dipole on the other hand is located close to an interface with GaP the emission pattern changes drastically. Using Fresnel equations and the Lorentz reciprocity

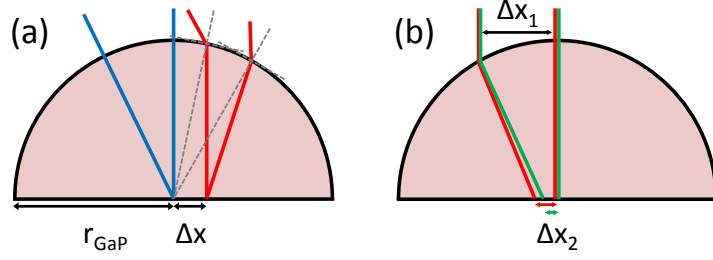


Fig. 4.2. (a) Off-axis aberration of SILs. Beams origination from the center of the focal plane (blue) pass the GaP surface orthogonally. Off center-beams (red) on the other hand are refracted leading to spherical aberration. The severity of aberration scales with the ratio $\Delta x/r_{\text{GaP}}$ (b) Chromatic aberration in the GaP SIL. Beams impinging the surface at the center of the SIL and are not refracted. Off-axis beams of different color experience different degrees of refraction due to the refractive dispersion of GaP ($n_{\text{GaP},560\text{ nm}} = 3.43$, $n_{\text{GaP},680\text{ nm}} = 3.27$).

theorem [172] this emission pattern can be calculated (for details see Appx. D). Radiation impinging the diamond-GaP interface under an angle will be refracted resulting in a distortion of the upward angular dipole emission. Fig. 4.3(b) illustrates the emission pattern of an orthogonal dipole located at a distance $z = 300\text{ nm}$ from the GaP-diamond interface. Since refraction is a non-linear phenomenon the angular emission density close to the critical angle of the two materials, $\alpha_{\text{crit},1} = \arcsin(n_1/n_0) = 47.5^\circ$, is strongly increased. In addition, partial reflection occurs which alters the downward radiation.

Adding a further interface with air below on the other side of a thin diamond results in reflecting the major contribution of the downward radiation up.* Light emitted within an angle below the critical angle of diamond and air $\alpha_{\text{crit},2} = \arcsin(n_0/n_2) = 24.5^\circ$, however, directly exits the antenna structure. In addition, the emission at certain angles is enhanced due to interference effects depending on the location of the dipole with respect to both surfaces and the diamond thickness. In Fig. 4.3(c) exemplarily the emission pattern for an orthogonal dipole located in the middle of a 600 nm thick diamond layer is shown. Notably, $\gtrsim 95\%$ of the radiation is emitted into an angle corresponding to an $\text{NA}=0.8$ (compare Appx. D).

4.2 Diamond fabrication

The diamond fabrication process described in this section is in principle very similar to the one introduced in the previous chapter (Ch. 3). In order to obtain a diamond film of suitable thickness for our antenna, we fabricate diamond membranes (with typical di-

*This effect is mainly responsible for the low photon extraction efficiency from an NV center in bulk diamond exhibiting a planar surface and an interface with air.

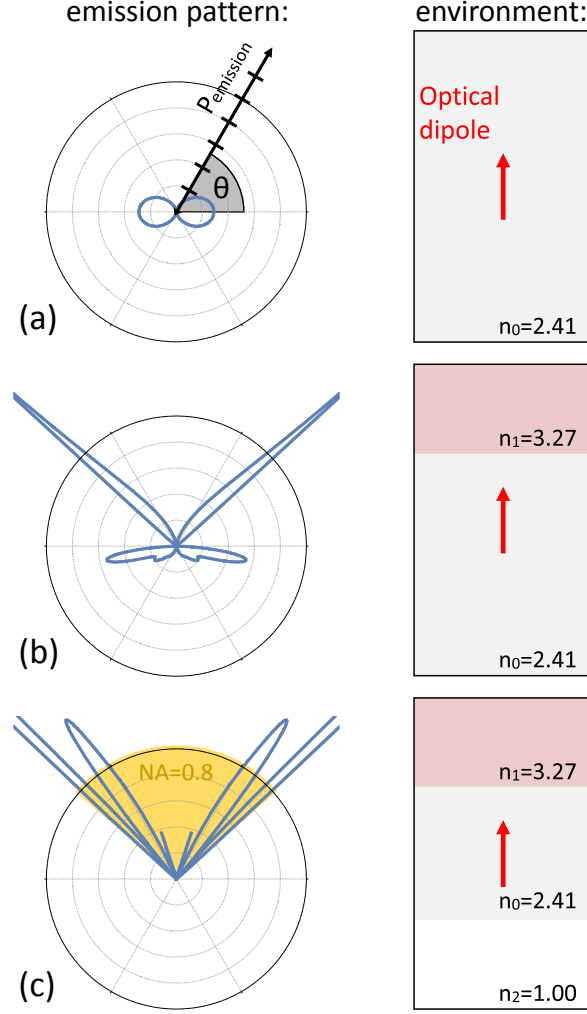


Fig. 4.3. Far-field angular radiation patterns of an optical dipole ($\lambda = 680$ nm) in different dielectric environments. (a) Typical dipole emission pattern in a homogeneous diamond medium with refractive index $n_0 = 2.41$. (b) Emission pattern of an orthogonal dipole at a distance of $z = 300$ nm from an interface between diamond and GaP ($n_1 = 3.27$). (c) Emission pattern of an orthogonal dipole located in the center of a diamond membrane of thickness $l = 600$ nm interfacing GaP on one side and air on the other side. $\gtrsim 95\%$ of the radiation is emitted into an angle corresponding to an $NA=0.8$.

mensions: $\approx 20 \mu\text{m} \times 20 \mu\text{m} \times 4 \mu\text{m}$) from commercially available diamond (Element Six, “optical grade”, impurity content of $[\text{N}_s]^0 < 1$ ppm and $[\text{B}] < 5$ ppb). We use a single-crystalline, chemical vapor deposition diamond sample which is laser-cut and double-side polished to a thickness of $21.4 - 21.9 \mu\text{m}$ (determined by scanning electron microscope (SEM) measurements). Prior to any processing, the sample is cleaned in boiling mixture of acids (sulphuric acid, nitric acid and perchloric acid, mixed to 1:1:1) and rinsed

in deionized water and solvents (acetone, ethanol, isopropanol) to remove any residual contamination from the polishing.

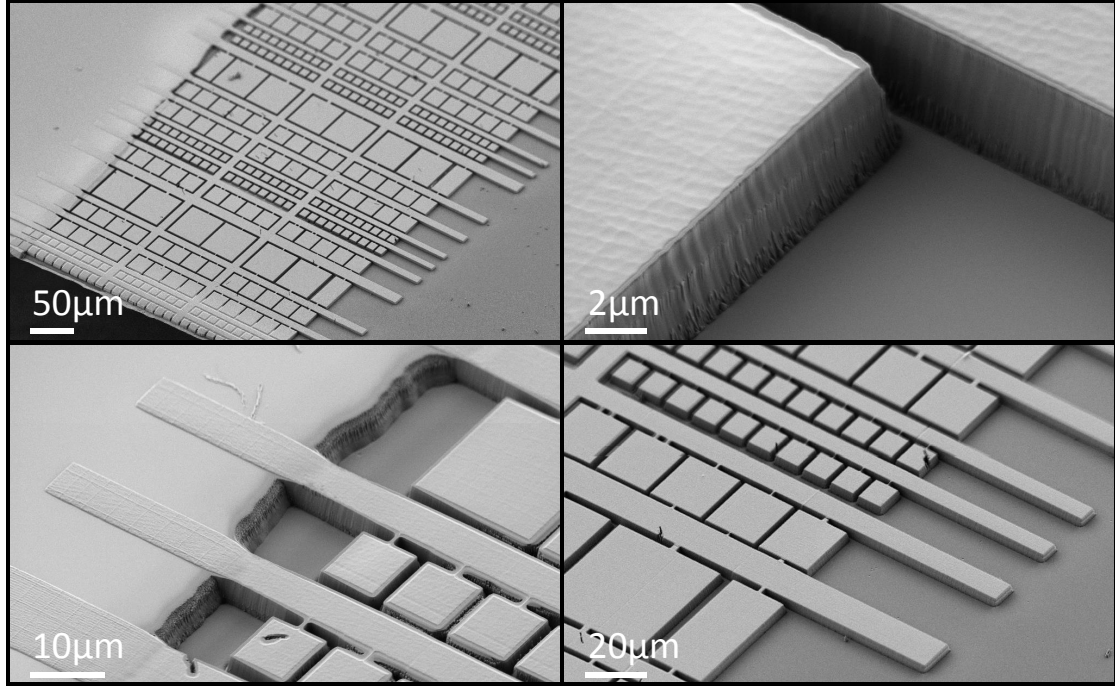


Fig. 4.4. Scanning electron microscope (SEM) image of the lithography pattern transferred into the diamond. Note the membranes with different sizes as well as the holding structures. The exposure pattern of the electron beam is imprinted into the etching mask.

Fabrication of thin diamond layer

To ease sample handling, the diamond is thinned down only in a small region of approximately $300 \times 600 \mu\text{m}^2$ using inductively coupled plasma reactive ion etching (ICP-RIE). For this, we cover the diamond with a quartz mask exhibiting a slit of the corresponding size. Then, we employ an alternating plasma sequence with 10 mins of Ar/Cl₂ plasma (ICP power 400 W, bias power 250 W, reactor pressure 1 Pa, 40 sccm Cl₂, 25 sccm Ar) followed by 20 mins of O₂ plasma (ICP power 700 W, bias power 100 W, reactor pressure 1.3 Pa, 60 sccm O₂). The Ar/Cl₂ plasma has the purpose of maintaining the diamond surface quality throughout the long etching process[173]. We estimate etch rates of $2.9 \mu\text{m/h}$ and $8.4 \mu\text{m/h}$ for the Ar/Cl₂ and the O₂ plasma, respectively. The diamond is etched down to a final thickness of $5.9 - 3.7 \mu\text{m}$ (number indicate local thickness variation inherent to etching/masking process). After etching, the sample is immersed in buffered oxide etch (BOE) solution and again cleaned as described in the previous

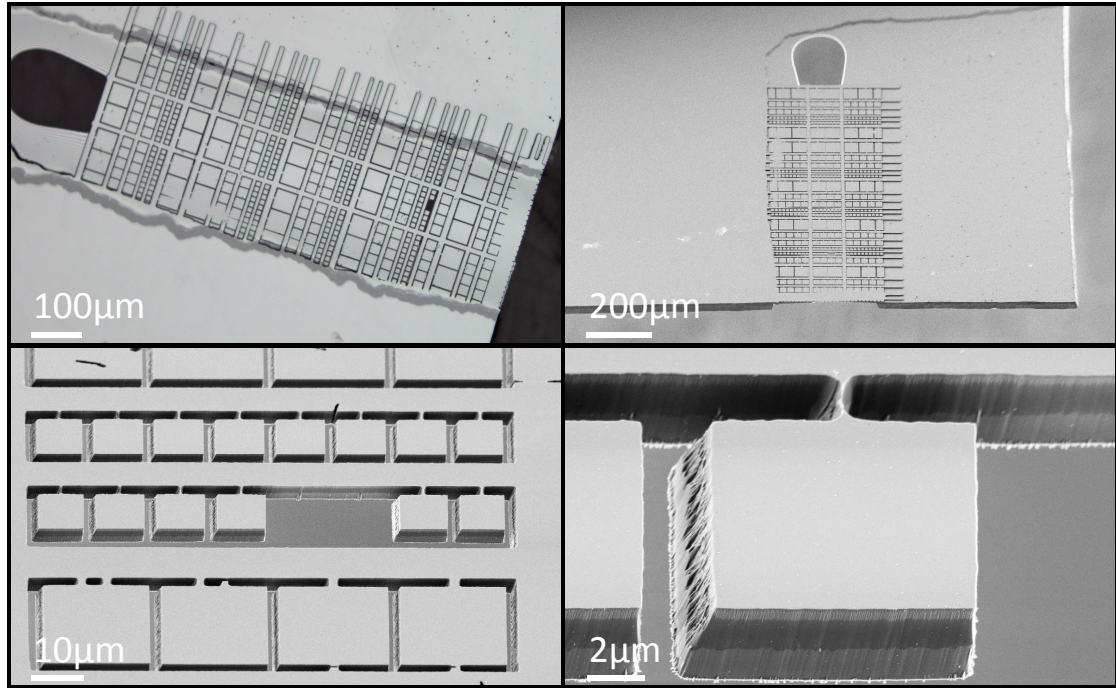


Fig. 4.5. Optical and SEM images of free standing membranes after mask removal and cleaning. In the bottom right panel the influence of the different etching steps on the sidewall topology of the structure can be seen.

paragraph. SEM images reveal no resolvable roughness throughout the thinned region of the diamond (Fig. 4.5).

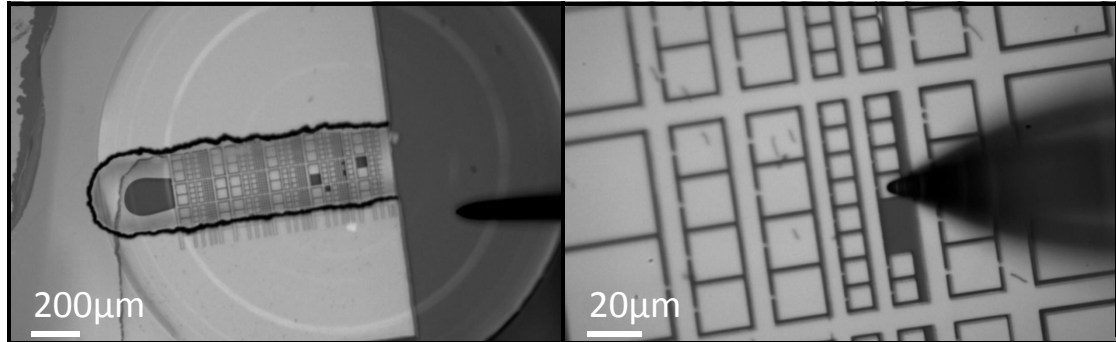


Fig. 4.6. Micromanipulator detaching of diamond membranes. The structured diamond is placed atop of a GaP SIL which is mounted with the planar surface facing up. We then break out membranes where the smallest have a size around $10 \times 10 \mu\text{m}^2$.

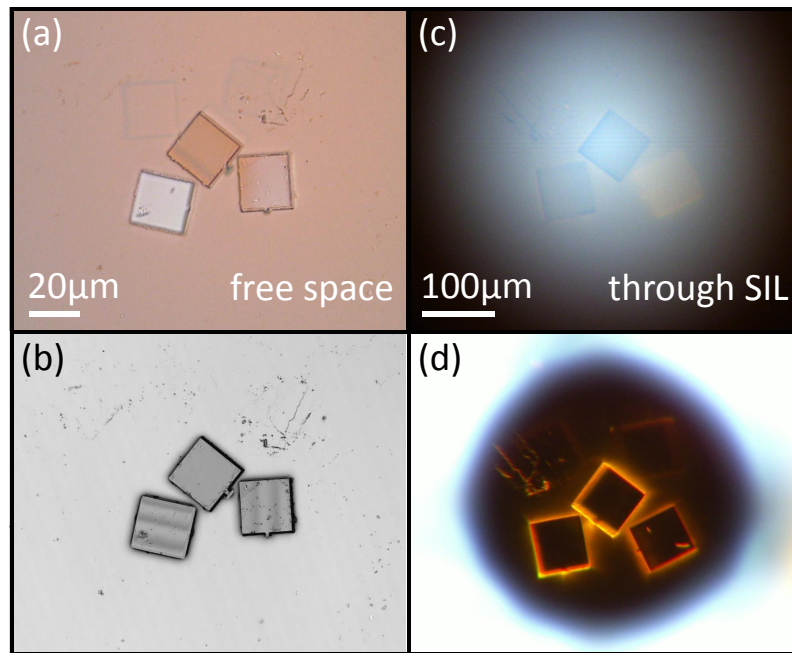


Fig. 4.7. Three $20 \times 20 \mu\text{m}^2$ diamond membranes with a thickness of $\sim 3 \mu\text{m}$ bonded on a GaP SIL. (a) Optical microscope and (b) laser scanning image of the membranes on the GaP surface. The interference fringes indicate that only the top membrane exhibits proper bonding. Optical microscope images in (c) brightfield and (d) darkfield mode through the SIL. The SIL provides a magnification factor of the refractive index of GaP, $n = 3.3$.

Fabrication of micro-structured diamond membranes

To ease placement and bonding of the diamond on the GaP SIL, the thin region of the diamond is structured to yield smaller diamond membranes (sizes between $10 \times 10 \mu\text{m}^2$ and $50 \times 50 \mu\text{m}^2$). To this end, we pattern the sample from the as yet non-etched side. We use electron beam lithography to expose a layer of spin-on-glass negative electron beam resist on a 2 nm Ti adhesion layer. For details of the mask fabrication see Sec. 3.1.2. To transfer the pattern into the diamond, we first use a 50 s Ar sputtering process in our ICP-RIE to remove the Ti adhesion layer (plasma parameters: 0.4 Pa, 50 sccm Ar, 500 W ICP, 300 W bias power). Diamond etching starts with a plasma containing 50% Ar and O₂ respectively (gas flow 50 sccm each, 0.5 Pa, ICP power 500 W, bias power 200 W). This plasma yields steep sidewalls and smooth surfaces in the non-masked areas [56]. However, the plasma also introduces a significant amount of mask erosion. After the first 8 mins of etching we thus examine the structure using a scanning electron microscope (Fig. 4.4). We then continue etching with a pure O₂ plasma (ICP power 700 W, bias power 100 W, reactor pressure 1.3 Pa, 60 sccm O₂) to decrease mask erosion

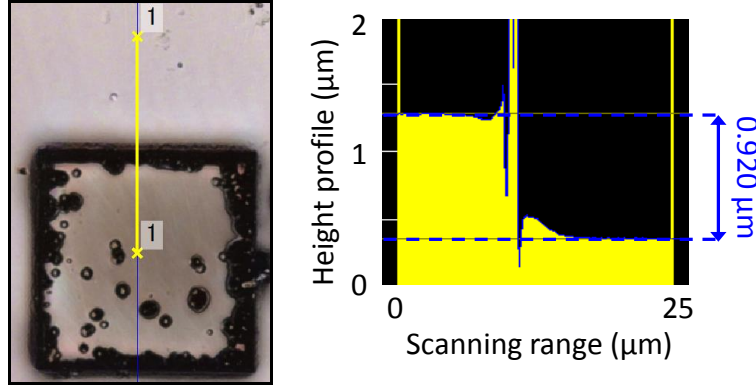


Fig. 4.8. Scanning laser confocal image of a thinned diamond membrane on GaP SIL. Note the blackened edges of the membrane and the occurrence of some needles. By measuring the step between the GaP and the diamond membrane's upper surface, we determine a thickness for the diamond membrane of $\approx 0.920 \mu\text{m}$.

and etch through the diamond to yield free standing-membranes. After the etching, the FOX mask is removed in BOE and the sample is acid cleaned again. Examples of free standing membranes are shown in Fig. 4.5.

Transfer of membranes and thickness tuning

The pre-defined membranes are detached from the sample using the sharp glass tip of a micromanipulator, see Fig. 4.6. They are placed at the center of the SIL using the micromanipulator tip and bonded to the SIL by van der Waals forces. Fig. 4.7 displays three $20 \times 20 \mu\text{m}^2$ diamond membranes with a thickness of $\sim 3 \mu\text{m}$ bonded close to the center of a GaP SIL. In the brightfield optical images (Fig. 4.7(a,b)), well-bonded membranes appear darker. The diamond layer acts like an anti-reflection coating since its refractive index lies between the one of GaP and air. The interference fringes in the confocal laser scanning image (Keyence, VK-X200K) indicate that only one of the three membranes exhibits proper bonding (Fig. 4.7(b)). If the membranes are observed through the GaP SIL (Fig. 4.7(a,b)) the additional magnification provided by the SIL becomes apparent. In the darkfield image obtained through the SIL chromatic aberration can be observed close to the edge of the field of view.

To ensure optimal performance of the dielectric antenna devices and to investigate the antenna performance in detail, the transferred membranes are thinned using ICP-RIE while attached to the SIL leading to thin membranes with well controlled thickness. This is feasible as the O_2 plasmas introduced above attack the GaP SIL only weakly (estimated

etch rate pure O₂ plasma 2.5 nm/min). To ensure the optimal thickness of the diamond, short etch steps are performed and the thickness of the fabricated diamond membrane is measured *ex situ* using a laser-scanning confocal-microscope. Fig. 4.8 shows an optical image of a diamond membrane on the SIL and the corresponding thickness measurement. During the successive etching steps masking of parts of the diamond membrane by small particules due to contamination lead to the formation of small needles on top of the membrane.

4.3 Experimental setup

For our room-temperature measurements we use a homebuilt confocal microscope relying on a cage system to excite and collect the NV PL. Two dichroic mirrors (Chroma, zt 594 RDC and Semrock, LM01-552-25) separate the excitation and detection arms of the microscope (Fig. 4.9). A mounting angle of 45° in opposite directions compensates for the lateral beam shift that is introduced by the finite thickness of the dichroic mirrors. For excitation we employ a fiber-coupled tunable pulsed supercontinuum laser source (NKT Photonics, SuperK Extreme EXW-12) operating at a pulse rate of 78 MHz. The supercontinuum radiation exits a high-damage threshold single mode fiber and is collimated via an objective (Olympus, RMS10x, NA=0.25). We block red shifted radiation created by nonlinear processes inside the fiber with a shortpass filter (Thorlabs FES0600). A high-NA objective (Olympus, MPLFLN100X, NA=0.8, working distance of 3.4 mm) facilitates tight focusing of the excitation laser. Samples are mounted onto scanning nanopositioners (attocube, ANSxyz100) and positioned with respect to the objective via a precision mechanical translational stage (Newport, M-562-XYZ). We image the reflection from the sample surface onto a camera (Watec Wat-120N+) which allows us to image and adjust the laser focus.

By collecting the PL via the same objective we achieve a high collection efficiency and spatial resolution. We filter out the residual excitation and light created via Raman processes with a bandpass filter (Delta Optical, BP 675/100) in order to improve the signal-to-background ratio. An objective (Olympus, RMS10x, NA=0.25) focuses the PL on the core of a single mode fiber, which acts as the pinhole in the confocal setup. The fiber guides the light to either a spectrometer (Acton SP2500, 300 grooves/mm grating) or a single-photon avalanche diode (SPAD, Laser Components, Count-250C). A Hanbury Brown-Twiss setup allows to perform second order autocorrelation measurements ($g(2)$) of the PL by splitting the signal up onto two separate SPADs via a 50:50 pellicle beamsplitter. A photon detected on one of the SPADs serves as a trigger for recording

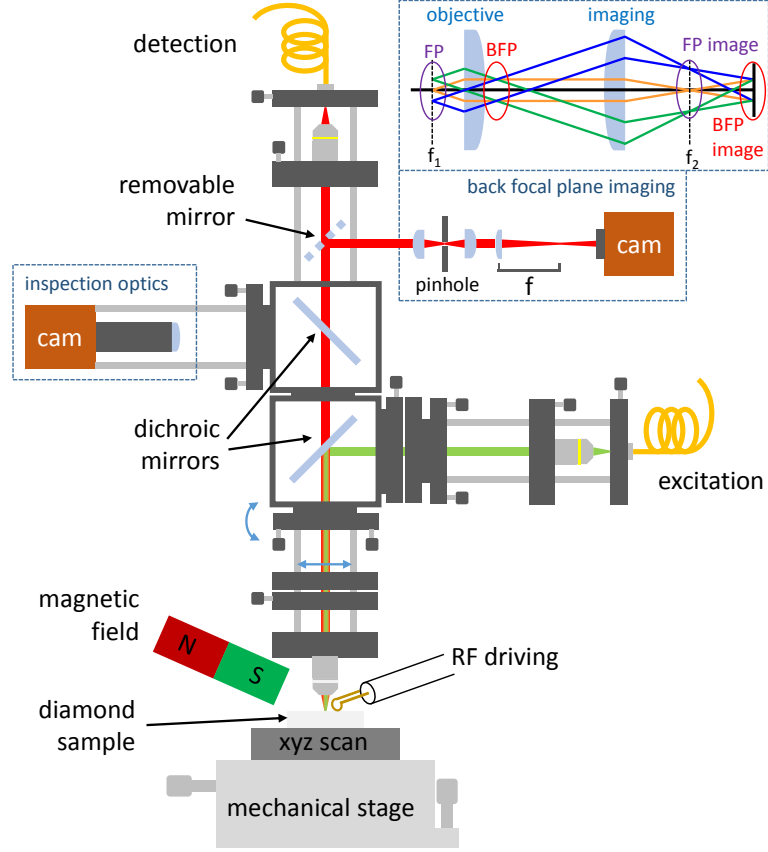


Fig. 4.9. Schematic drawing of the fiber-based confocal setup for detection and spin manipulation of single NV centers. Opto-mechanical components are used to overlap the excitation and detection paths which are separated via dichroic mirrors (for more details see text). A green laser is tightly focused on the sample via a high numerical aperture objective. Fluorescence originating from a diffraction limited sample volume is collected with the same objective and coupled to into the detection fiber. The fluorescence is either analyzed with a spectrometer or detected using an single photon avalanche diode (not depicted). By inserting an additional mirror into the detection path we can map the angular distribution of the fluorescence on a camera via back focal plane (BFP) imaging. A magnet and a home-built loop antenna in proximity of the sample allow for spin state manipulation of the NV center.

the time-tagged time-resolved signal of the other SPAD which is facilitated by fast correlation electronics (Fast ComTec, P7889). The absence of photon counting events at zero delay indicates that photons are emitted one after another indicating the presence of a single emitter.

While the detection arm serves as the optical axis, the overlap between excitation and detection is facilitated by inserting two alignment degrees of freedom into the excitation arm - a tilt stage (Thorlabs, KC1/M) and a lateral displacement stage (Thorlabs, ST1XY-D/M). In addition, the overlapped detection and excitation beams can be moved

with respect to the objective by another set of tilt and displacement stages in order to obtain an aberration-free diffraction-limited laser spot. As an additional feature, we employ a highly sensitive CCD camera (Watec WAT-910HX) on which we map the back focal plane (BFP) of the sample objective, which corresponds the angular distribution of the far-field emission of the PL [174]. To that end, we insert a mirror into the detection path, which reflects the PL towards the CCD. Before focusing the PL onto the CCD via an imaging lens, we spatially filter our signal by using a telescope comprising a pinhole. Here, the size of the pinhole determines the effective volume from which PL is collected. If the CCD is placed into the focus of the imaging lens a real space image of the focal plane is obtained. If the CCD is shifted further the lens system effectively images light emerging from the backfocal plane onto the CCD chip, which then allows to infer the angular distribution of the PL (Fig. 4.9, top right).

We place a home-built loop antenna between the sample and the large working distance objective which allows us to perform ODMR (optically detected magnetic resonance) measurements on the NV spins in the antennas. The microwaves driving the spin rotations are generated by an amplified RF generator (Rohde & Schwarz, SMB100A). We are able to adjust the magnetic field by moving a permanent magnet with respect to the sample using a combination of a rotational stage and three axis translational stages. In order to be able to perform spin coherence measurements we gate a green continuous wave laser (Changchun New Industries, MGL-III-532nm-200mW) via an acousto-optic modulator (AOM, EQPhotonics, AOM 3200-146). Both the microwave and the AOM are switched by RF electronics and synchronized with the detection signal of the SPAD via a programmable TTL pulse generator (Spincore, PulseBlasterESR-PRO 500).

4.4 Results and discussion

4.4.1 Angular emission pattern

The PL emission from optical dipoles embedded in dielectric antennas exhibits characteristic radiation patterns [164], signatures of the antenna effects we wish to demonstrate and exploit. We record these radiation patterns for native NV centers in our antenna structures through BFP imaging. The NV PL is excited using a pulsed, tunable supercontinuum laser source ($\lambda = 560$ nm, repetition rate 78 MHz) and detected using a narrowband filter to isolate characteristic interference patterns in the antenna emission, which are strongly wavelength-dependent. As a first step, we image the PL of NV ensembles in antennas with two different thicknesses, Fig. 4.10(a),(c). We observe a radiation pattern consisting of multiple interference rings whose positions strongly vary

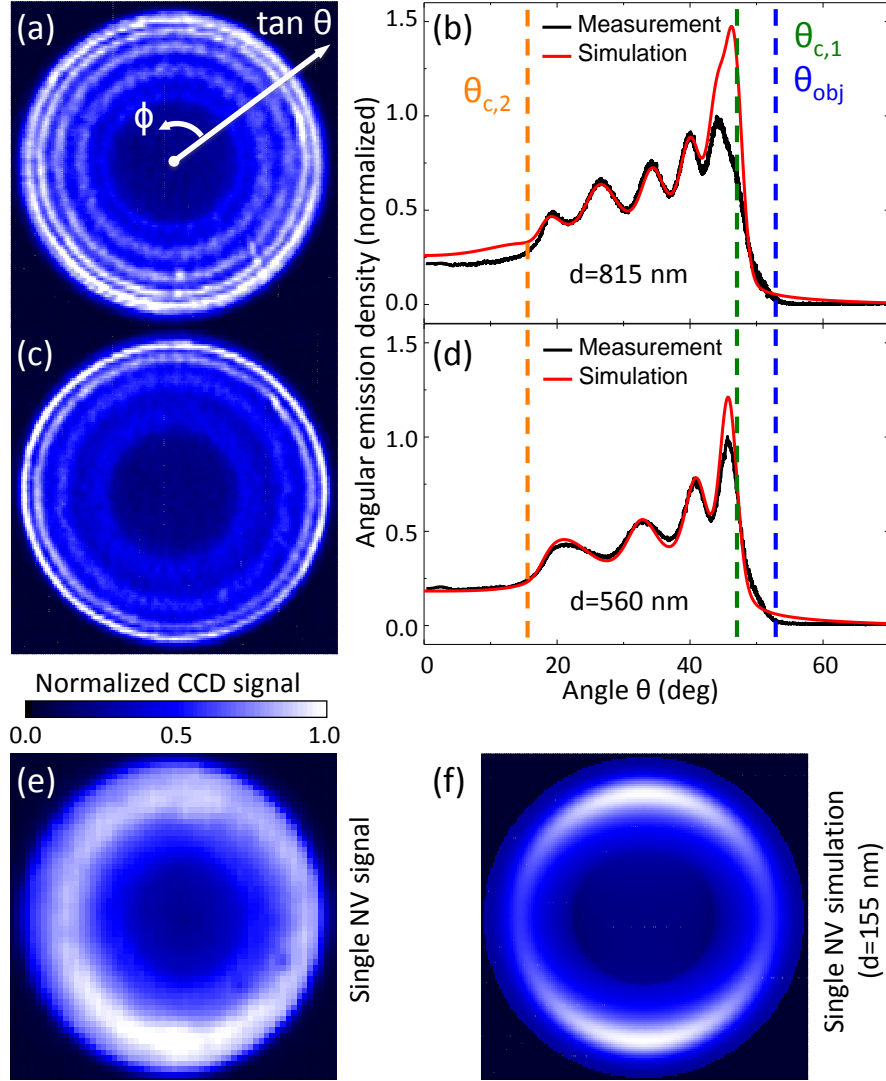


Fig. 4.10. Angular radiation patterns of NV ensembles in the dielectric antenna obtained by BFP imaging for (a) $d = 815$ nm and (c) $d = 560$ nm. (b),(d) Average of the measured BFP images over azimuthal angle ϕ and calculated emission patterns. (e) Broadband emission pattern of a single NV center. (f) Calculated BFP image for an NV center in a diamond membrane with $d = 155$ nm and $h = 140$ nm. The color-bar applies to all images in the figure. (a) - (d) use a (680 ± 5) nm bandpass filter, (e) a (675 ± 50) nm bandpass filter.

with d . The analysis of these patterns allows us to infer the associated layer thicknesses, $d = 815$ nm and $d = 560$ nm

For all our BFP images, the NV PL is confined to within a maximal emission angle $\theta_{c,1}$ which corresponds to the critical angle at the diamond-GaP interface $\alpha_{1,\text{crit}} = 47.5^\circ$ (Sec. 4.1). This observation demonstrates highly directional NV emission into a numer-

ical aperture $\text{NA} \sim 0.73$. Importantly, this value is significantly smaller than the NA of 0.8 of the microscope objective we employ.

In addition, we observe a region of relatively low PL intensity, bounded by an angle $\theta_{c,2}$, in the center of each BFP image. This region corresponds to PL light escaping the antenna through the diamond-air interface within the angle $\sin(\alpha_{\text{crit},2})$. Due to the collection through the GaP material, refraction at the diamond-GaP surface occurs, $\sin(\theta_{c,2}) = n_1/n_0 \sin(\alpha_{\text{crit},2}) = n_2/n_0 \cdot n_0/n_1 = n_2/n_0$. This angle is equivalent to the critical angle between GaP and air, $\theta_{c,2} = \arcsin(n_2/n_0) \sim 18^\circ$.

For a detailed analysis of the radiation patterns, we average the measured BFP images over the azimuthal angle ϕ and compare the resulting emission profile to an analytical calculation, Fig. 4.10(b),(d). These calculations rely on established procedures for the analysis of the far-field emission from layered, dielectric structures [172, 174, 175] (for details see Appx. D). Here we apply the Lorentz reciprocity theorem, which states that the strength of an electromagnetic field caused by an oscillating dipole at a certain distance remains unaltered if the location of the dipole and the point where the field is measured are interchanged. We harness this principle to calculate the angular far-field emission of the dipole within the dielectric layer structure by placing a dipole at infinity and calculating the field strength within the dielectric structure at the point where the dipole is located originally. We determine this field strength by considering plane waves (caused by the dipole at infinity) impinging the structure under different angles and account for the various interfaces using Fresnel equations.

We use tabulated values for refractive indices of diamond and GaP [176] and account for the NV PL spectrum by introducing wavelength-dependent weighting factors for the emission profile discretized in steps of 5 nm. For both values of d , we detect PL from a large ensemble of NVs in the diamond membrane and we assume these NVs to be homogeneously distributed and their emission dipoles to be randomly oriented. This assumption is based on the fact that the NV PL is emitted via two orthogonal dipoles located in a plane perpendicular to the NV's axis [155]. Assuming an equal oscillator strength, the alignment of the dipoles within this plane can be chosen arbitrarily (see Appx. D), which in combination with the four possible NV orientation enables the dipole to point in an arbitrary direction.

The resolution of the BFP images is limited by the pixel size of the CCD and can thus not capture very sharp features expected in the interference pattern (Sec. 4.1). We account for this by convolving our theoretical curves with a Gaussian point-spread function. With the exception of the highest emission angles $\theta \sim \theta_{\text{obj}}$, our experimental results show excellent agreement with the theoretical expectations. In particular, the

characteristic oscillations we observe in Fig. 4.10(b),(d) (and which persist despite our ensemble-average over dipole-orientation and position) allow us to determine precisely the only free parameter in our fit, the thickness d of the diamond layer. We believe that the deviation of experiment and theory at large angles is caused by imperfections in our experimental antenna implementation. For large angles effects like scattering due to surface roughness are strongly enhanced.

4.4.2 Coupling of single NV centers

Upon further thinning of the diamond membrane, the areal density of NV centers gradually decreases until eventually for a thickness of $d \lesssim 150$ nm, we are able to observe NV emission from isolated spots, Fig. 4.11(a). Figure 4.10(e) displays the angular radiation pattern of the broadband PL of such a spot. This emission pattern agrees well with the calculated BFP image for a single NV center, Fig. 4.10(f), for which we take into account the two optical dipoles responsible for NV emission [177] and use d and h (the distance between NV center and diamond-GaP interface) as fit parameters. Since, as mentioned before, the NV emits via two orthogonal dipoles lying in a plane perpendicular to the NV axis, we expect only weakly polarized antenna emission and therefore perform unpolarized detection of our BFP images.

To substantiate further that our observed isolated emission spots indeed stem from single NVs, we determined the photon autocorrelation function $g^{(2)}(t)$ of the detected PL (compare Sec. 3.3.1). Figure 4.11(b) shows $g^{(2)}(t)$ measured on NV #1. The data exhibits strong photon antibunching with $g^{(2)}(0) \lesssim 0.1$ and a decay of the pulsed PL on a timescale $\tau = (15.4 \pm 0.2)$ ns. The decay time is a typical NV center fluorescence lifetime [78]: this value therefore shows that our antenna fabrication process did not induce unwanted non-radiative decay channels for the NV and that the effective refractive index at the NV's surrounding remained unchanged.

To study the directionality η of single-photon emission from our antenna, we compare PL emission rates detected through the SIL and through the backside of the antenna, upper and lower panel in Fig. 4.11(a), respectively. Our confocal scans reveal several single NVs (labeled #1 – #5 in the figure) scattered throughout the diamond membrane. The random positioning of the native NVs in our structure allows us to observe the effect of varying vertical positions h on antenna performance: NVs which are well-coupled to the antenna (#1, 3, 4) appear bright when observed through the SIL and dark through the backside, while less well coupled NVs (#5) exhibit the opposite behavior.

For a more quantitative analysis of the antenna directionality, we compare the saturated PL count rate I_∞ of the well-coupled NV #1, measured through the GaP SIL and

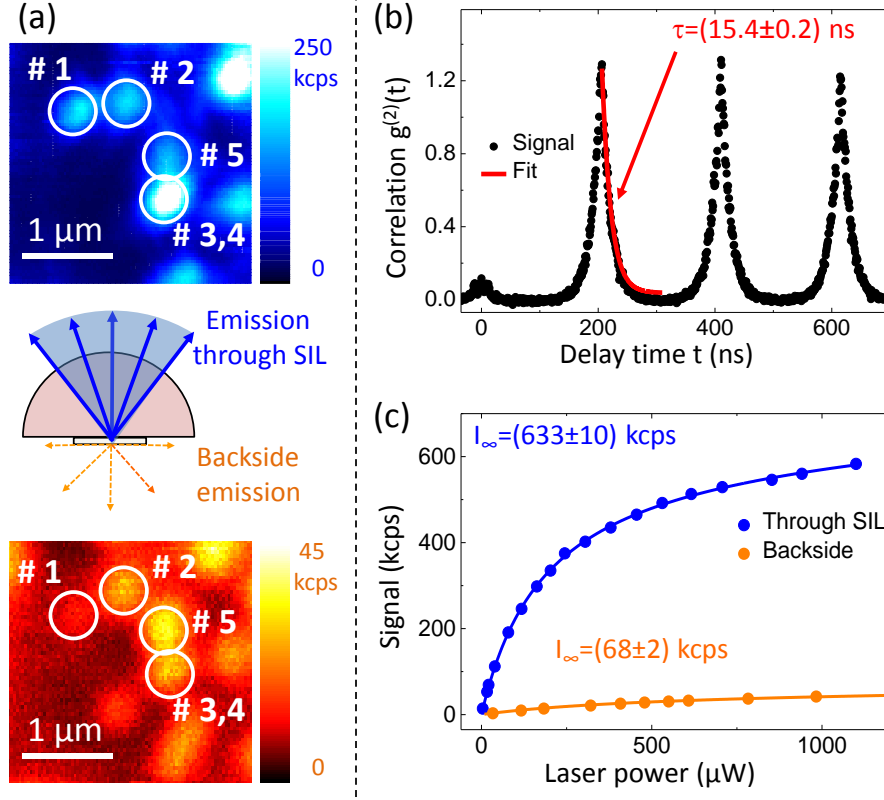


Fig. 4.11. (a) PL images of individual NV centers recorded through the SIL and through the backside of the antenna. (b) Photon autocorrelation measurement $g^{(2)}(t)$ of NV center #1 using pulsed excitation. The data shows $g^{(2)}(0) \lesssim 0.1$ and an exponential PL decay with a lifetime $\tau = (15.4 \pm 0.2)$ ns. (c) Comparison of PL saturation of a single NV in the dielectric antenna when detecting photons through the GaP SIL and through the backside of the antenna. NV PL is detected using a (675 ± 50) nm bandpass filter.

from the antenna backside. We obtain I_{∞} by fitting the measured PL saturation curves, Fig. 4.11(c), with $I(P) = I_{\infty} (1 + P/P_{\text{sat}})^{-1} + b \cdot P$ [42], where P is the laser power, P_{sat} the saturation power and $b \cdot P$ accounts for background fluorescence. For PL detection through the SIL, we find $I_{\infty, \text{SIL}} = (633 \pm 10)$ kcps, while we obtain $I_{\infty, \text{bs}} = (68 \pm 2)$ kcps for backside detection*. This corresponds to an enhancement of the detection rate by the antenna which we directly relate to the directionality of our antenna, i.e. we find $\eta = 9.3$.

We note that the directionality we determine in this way is an underestimate of the actual directionality of the dielectric antenna. Indeed, $\sim 37\%$ of the NV emission is

*We note that this value of I_{∞} is similar, but slightly smaller, to the value we find for single NVs measured in unstructured bulk diamond in our setup.

lost on outcoupling, where $\sim 10\%$ of the photons are absorbed in the GaP material (Appx. C) and $\sim 30\%$ of the remaining photons are reflected at the GaP-air interface (a consequence of the abrupt change in reflective index). We also note that a possible source of systematic error is the fact that the current realization of our antenna demands slightly different experimental conditions for top- and bottom-side collection. Specifically, top-side collection was performed in a non-confocal imaging mode since the emission pattern of our antenna has poor overlap with the Gaussian mode of the single mode fiber which represents the pinhole in our microscope (Sec. 4.3). Backside collection, however, was performed with confocal detection via a single mode fiber since the high density of NVs in our antenna did not allow us to isolate single NVs otherwise. However, we expect backside confocal detection to be very efficient (Appx. D) such that this systematic error is small. We emphasize that $\eta = 9.3$ represents the performance of the entire antenna device without correcting for known losses at the GaP-air interface. For d and h as determined from the radiation pattern for NV #1, the NA of the objective lens, and including reflection losses at the GaP-air interface, we calculate a directionality of $\eta = 13.9$, slightly higher than the measured value.

4.4.3 Optically detected magnetic resonance and coherent spin manipulation

With single NV centers isolated in our dielectric antenna, we now turn our attention to their electronic spin properties. To that end we perform ODMR [64] on individual NVs in our antenna (Sec. 2.1.6). The ODMR resonance frequencies are determined by the strength of an external magnetic field \vec{B} and the orientation between the NV axis and \vec{B} . We apply \vec{B} in an oblique direction with respect to the four possible NV axes such that ODMR allows us to differentiate NVs with different orientations. Fig. 4.12(a) shows ODMR for NVs #1-4 in a static magnetic field. The ODMR traces enable us to probe the spin dependence of the BFP image in Fig. 4.10(c). We record the difference of PL in the BFP when driving the NV on and off spin resonance. The corresponding, spin-resolved BFP image is shown in Fig. 4.12(b) and is, up to a constant scaling factor, identical to Fig. 4.10(c) and thereby clearly prove that the antenna emission originates from NV spins. In particular, the ODMR contrast is constant throughout the BFP and no ODMR contrast is detected in the BFP when we drive the spin resonance of one of the NV #1's neighbors (all of which have orientations different from NV #1).

Finally, we use coherent manipulation of the NVs' electronic spins to probe their homogeneous decay times (T_2) (Sec. 2.1.8). We perform the experiment on NV #4 with an external magnetic field aligned with the NV axis and set to $|\vec{B}| \sim 11.5$ mT. First,

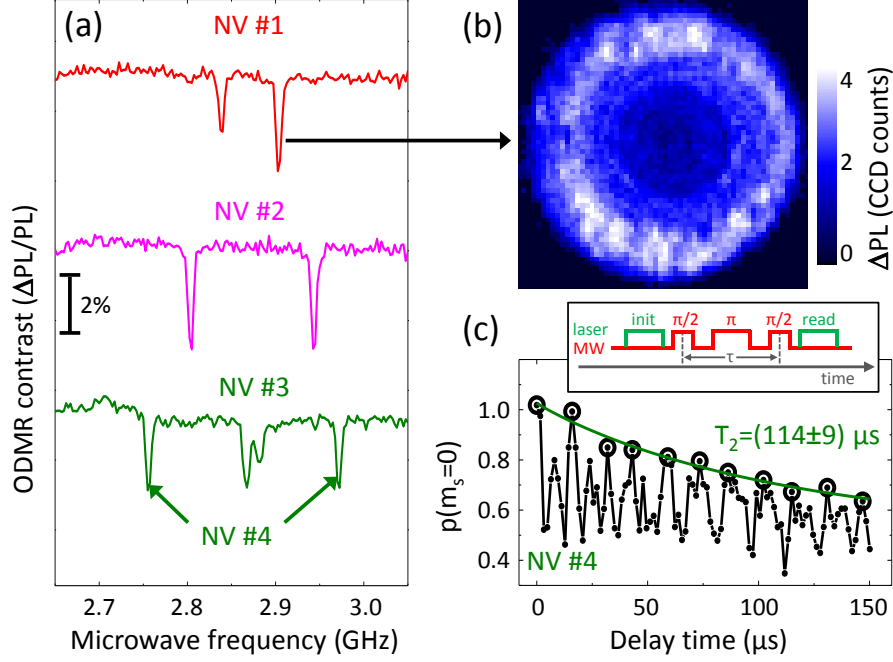


Fig. 4.12. (a) Optically detected magnetic resonance (ODMR) of the NVs highlighted in Fig. 4.11(a) ($|\vec{B}| \sim 4$ mT, along the NV axis), each exhibiting a different orientation within the diamond lattice. The moderate ODMR contrast results from the low microwave power at the NV location. (b) ODMR amplitude of NV #1 resolved in the back focal plane. (c) Hahn spin-echo measurement on NV #4 yielding $T_2 = (114 \pm 9) \mu s$ ($|\vec{B}| \sim 11.5$ mT). For details see text.

we find the microwave spin transition frequency by performing an ODMR experiment. Next, we determine the microwave parameters that are required to create $\pi/2$ - and π pulses. We initialize the NV into the $m_s = 0$ state via a green laser pulse. We then apply microwave pulses with different pulse lengths t at a fixed microwave power to drive Rabi oscillations between the two spin states $m_s = 0$ and $m_s = 1$. Reading out the population difference of the two states for different t we find the typical oscillations $\propto \sin^2(\Omega_R t/2)$ (compare Sec. 2.1.8). We set the microwave power to obtain a Rabi-frequency of $\Omega_R = 10.8$ MHz.

Next, we perform a Hahn-echo experiment, as described in Sec. 2.1.8. We initialize the NV into the $m_s = 0$ state and apply a $\pi/2$ -pulse which facilitates the creation of a superposition of $m_s = 0$ and $m_s = 1$. After a free precession interval $\tau/2$ we apply a π pulse, which leads to refocusing of the precession phase after another $\tau/2$ waiting time. Using a further $\pi/2$ -pulse the spin is projected back onto $m_s = 0$ state and the spin population is read out subsequently.

Fig. 4.12(c) shows the result of the spin coherence measurement. We find an initial fast

decay of the signal, which experiences several revivals with increasing τ . This behavior can be explained by the fact that the NV spin is influenced by adjacent electron and nuclear spins. If the evolution time of the NV spin matches the inverse Larmor frequency of these spins, a revival occurs [178]. In our experiment, the main contribution to these revivals stems from ^{13}C spins. From the external magnetic field we determined via an ESR measurement we retrieve $|\vec{B}| \sim 11.5 \text{ mT}$, which allows us to calculate the time delay at which we expect a revival due to ^{13}C , $\tau_{\text{rev}} = 2/(\gamma_{^{13}\text{C}} \cdot B) = 14.5 \mu\text{s}$. Fitting the decay of the envelope of the signal we can determine the actual homogeneous decay time T_2 . We find $T_2 = (114 \pm 9) \mu\text{s}$, which is typical for the CVD diamond material we employ here. This demonstrates that fabrication of the dielectric membrane preserves the long NV electronic spin coherence times.

4.5 Conclusions and outlook

In summary, we have for the first time applied the powerful concept of a dielectric optical antenna [164] to single quantum-emitters in the solid state. We have demonstrated successful antenna operation and the addressing of single NV spins in the antenna. The antenna has broadband operation and preserves the advantageous optical and spin properties of the single-crystalline diamond starting material. With the high antenna-directionality, photon collection efficiency and spin coherence times we were able to demonstrate simultaneously. Our results present significant advances over previous approaches in the field of diamond nanophotonics [52, 53, 161, 55, 56, 179, 38, 163]. In particular, the dielectric antenna constitutes the only demonstrated approach which in principle allows for near-unity collection efficiency [165] for NVs.

The radical change in the radiation patterns and the highly directed PL emission from single NVs demonstrate proper operation of the dielectric antenna. Still, several factors could be improved in future implementations. The losses at the GaP-air interface could be avoided primarily by an anti-reflection coating, but also by smoother surfaces; the losses at large angles need to be investigated and mitigated. The emission mode of the antenna could be further improved by using (111)-oriented diamond where the NV emission dipoles show an orientation better suited for our antenna [56]. Lastly, a slight improvement could be gained by optimization of d and h (by creating NVs at well-defined depths through ion-implantation or delta-doping [69]): according to our calculations, the fraction of PL coupled into the GaP-SIL could be increased from currently 95% ($d = 155 \text{ nm}$, $h = 140 \text{ nm}$) to above 97.5% (Appx. D). We note also that using an optimized background filter would readily reduce the losses in our setup which are presently $\gtrsim 25\%$,

Fig. 4.1(c). Further improvements to our structure should therefore allow for record-high single NV count rates approaching 10 MHz.

Chapter 5

Summary and future directions

The efficient optical addressing and readout of the spins of single NV centers is a central aspect of NV-related research. However, there are several factors impairing the photon flux which limit NV-based applications. Due to its weak oscillator strength the radiative recombination rate of the NV is relatively long compared to other solid-state emitters [35]. In addition, only a small fraction of the emitted photon can be detected on account of non-directional NV emission and total internal reflection at the diamond-air interface. Applications relying on coherent NV photons are limited additionally by the low fraction of ZPL emission ($\sim 3\%$).

In this thesis, two complementary approaches to increasing the PL photon detection rates of single NV centers were presented, which both rely on the engineering of the NV's photonic environment. On one hand, by embedding single NV centers into a dielectric optical antenna, it was demonstrated that the main fraction ($> 95\%$) of the broadband NV PL emission is channeled into a narrow solid angle. On the other hand, by coupling single NV centers to a miniaturized Fabry-Pérot microcavity, it was found that the generation rate of coherent ZPL photons is significantly boosted which results in a twofold reduction of the NV radiative lifetime and an increase of the fraction of ZPL emission by more than an order of magnitude from $\sim 3\%$ to almost 50% .

At the heart of these devices are diamond micromembranes fabricated from high-quality single-crystalline diamond material. The small dimensions of these membranes result in a strong bond to the flat surface of the GaP SIL and the DBR mirror, respectively. This strong bonding ensures a seamless integration of the membranes into the presented photonic structures, which is key to their proper operation. Improving the directionality of the emission via the dielectric antenna and enhancing the radiative recombination rate via cavity coupling confers general benefits to solid-state emitters. Due to the generic design of these devices it is an immediate possibility to integrate other color centers in diamond [180, 181, 182] and emitters in other solid-state hosts like SiC [183, 184, 185] and rare-earth doped crystals [186].

The high spin coherence of NV centers is preserved in the micromembranes ($T_2 \gtrsim 100 \mu\text{s}$). Hence, upon mitigation of known photon losses the antenna design will find applications in various emerging quantum-sensing applications ranging from wide-field magnetic imaging [187] to nanoscale nuclear spin detection [188] where in all cases it is poised to lead to a significant leap in performance.

The creation of the micromembranes keeps invasive plasma etching at a minimum which minimizes the effects of nano-fabrication on the spectral purity of the NV ZPL transition. While the averaged ZPL linewidths in the starting material before processing, $\lesssim 100 \text{ MHz}$, are approaching the transform limit ($\sim 13 \text{ MHz}$), the averaged linewidths in the micromembranes are inhomogeneously broadened to $\sim 1 \text{ GHz}$ due to spectral fluctuations. Nevertheless, these linewidths constitute an order of magnitude improvement over the best linewidths reported for NV centers coupled to monolithic diamond resonators [39]. Notably, the reported linewidths are smaller than the groundstate spin-triplet splitting of 2.87 GHz , which allows to resolve optical transitions associated to the different spin states of the NV. One of the next steps of the cavity coupling experiment will be to drive spin transitions within the ground state using microwaves and to perform spin-resolved cavity coupling measurements. The open geometry of the microcavity platform readily allows for patterning gold wires next to the diamond micromembranes using conventional lithography techniques without compromising the cavity performance [159].

In order to create a high fraction of indistinguishable photons an improvement of the linewidths reported in our experiment is required. A significant reduction can be achieved by applying resonant repump techniques [151] and slow drifts can be mitigated by electronic feedback stabilization via Stark effect tuning [87]. The PLE measurements of the starting material (thickness $\sim 40 \mu\text{m}$) show that NV centers implanted at the suitable depth for efficient cavity coupling exhibit narrow linewidths ($\lesssim 100 \text{ MHz}$). A systematic study that investigates the dependence of the ZPL linewidth on various parameters like the diamond thickness would help to understand and mitigate the mechanism of inhomogeneous broadening. Even though integrating thicker diamond layers into the cavity would compromise the Purcell enhancement, still a significant enhancement of η_{tot} over NV centers in bulk can be achieved.

Upon improving the microcavity design the ZPL detection rate can be significantly enhanced. First, the ZPL emission out of the microcavity suffers from scattering loss, which can be mitigated by using better mirror coatings. Secondly, the Purcell factor can be increased further if the mode volume of the microcavity is minimized by reducing the radius of curvature of the concave micromirror [144] and employing thinner diamond membranes. Thirdly, improving the fabrication process will result in the creation of

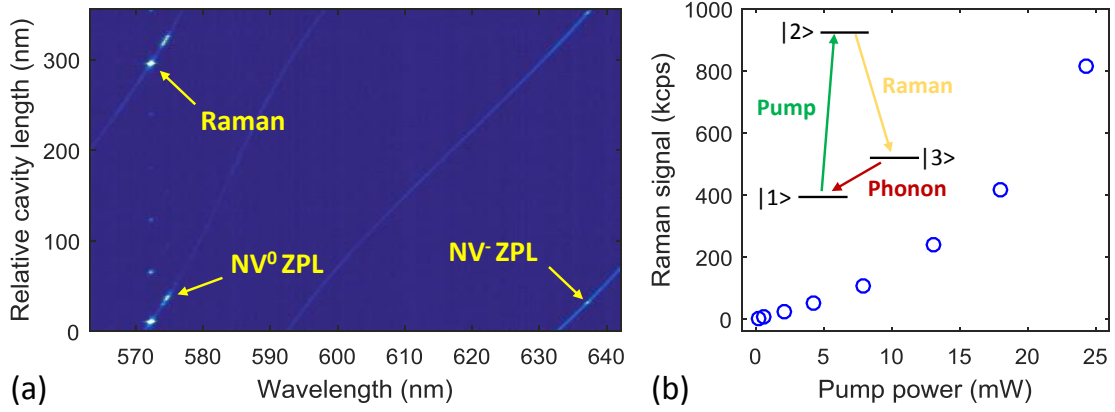


Fig. 5.1. (a) Mode-structure of the cavity from Fig. 3.17 for an extended wavelength region excited with a continuous-wave laser at 532 nm with a power of 30 mW. The sharp resonances correspond to the Raman transition (573 nm) and the resonant transitions of the two different charge states of the NV center (NV⁰: 575 nm, NV⁻: 637 nm). (b) Power dependence of the cavity-enhanced Raman signal pumped by a continuous-wave laser at 532 nm at room temperature using a low-NA objective (NA=0.3). Inset: Three-state scheme of the Raman transition. When ground state ($|1\rangle$) population is excited to a virtual state $|2\rangle$ it can de-excite via state $|3\rangle$ by emitting a red-shifted photon and a phonon at fixed energy $\Delta E = hc \cdot 1332 \text{ cm}^{-1}$. Changing the energy of the pump beam will hence involve a change of the energy of the Raman transition.

diamond membranes of higher quality which results in both lower background emission and lower optical linewidths.

It has been proposed that the creation of the first metropolitan-scale quantum internet consisting of several nodes based on NV centers is within reach [189]. The three main ingredients are entanglement distillation [190] to increase the entanglement fidelity, high-efficiency photon frequency conversion to the infrared [18] to mitigate fiber losses, and coupling NV centers to a photonic cavity to boost the photon flux. The proof-of-principle demonstration of the last point is presented in this thesis. Upon further improvement of the spectral stability of the NV ZPL and mitigation of photon loss our device paves the way for much enhanced spin-photon and spin-spin entanglement rates. As we point out in Sec. 3.3.5, we estimate that an enhancement of the entanglement rates by four orders of magnitude is within reach.

Besides their prospect to find applications in quantum information processing high-finesse microcavities can be used to enhance other optical processes like Raman scattering. Significant improvements of the Raman signal of carbon nanotubes [191] and atmospheric gases [192] have been reported.

In the cavity coupling experiment (Ch. 3) it was found that, in addition to enhancing

the ZPL of the NV^- , also the NV^0 ZPL and the Raman scattering signal caused by the laser excitation at 532 nm couple to the cavity (Fig. 5.1(a)). A systematic study of the effects of cavity coupling on these transitions has not been performed yet. A particularly interesting experiment would be to analyze the dynamics of the charge state conversion depending on the coupling strength of the cavity to the NV^0 and NV^- ZPLs.

Preliminary measurements at room temperature have shown that the Raman signal, generated by a continuous-wave laser at 532 nm, is strongly enhanced by coupling to the microcavity (Fig. 5.1(b)). Pumping and collecting the Raman signal with a low-NA objective (Olympus RMS10X-PF, NA=0.3) a superlinear power dependence of the Raman signal was measured, which indicates the emergence of self-stimulated Raman emission. For a pump laser power of 24.3 mW a Raman signal of 813 kcps was detected using a SPAD. This count rate corresponds to a ~ 35 -fold enhancement of the signal compared to previously reported values for diamond Raman signals created at 785 nm and collected with a high-NA objective (NA=0.9) [193]. Correcting for the higher Raman gain at shorter wavelengths ($42 \text{ cm GW}^{-1} \cdot I_0$ for 532 nm, $26 \text{ cm GW}^{-1} \cdot I_0$ for 800 nm, where I_0 is the intensity of the pump laser [194]) the enhancement is reduced to ~ 22 . Accounting for the smaller solid emission angle due to the lower NA we find an increase of the radiant intensity of the Raman signal by a factor of ~ 270 .

Correlated Stokes–anti-Stokes scattering [193] has been used for the remote entanglement of macroscopic diamonds [164] and the development of a macroscopic phonon-based quantum memory [195, 196, 197, 198]. Enhancing the intensity of the Raman scattering process in diamond via a cavity would improve the interaction rate in both applications significantly.

Diamond has emerged recently as a compelling material platform for nonlinear photonics outstanding for its high refractive index, large transmission window (from infrared to ultraviolet), low absorption losses and excellent thermal properties, which allow for efficient heat management in high-power applications [199]. Raman applications in diamond are particularly promising due to the large Raman shift (1332 cm^{-1}) and the high Raman gain coefficient ($7.6\text{...}78 \text{ cm GW}^{-1} \cdot I_0$ for 1280...355 nm [194]). Exploiting these properties a wide range of Raman-based lasers has been demonstrated including wavelengths from the ultraviolet [200] to the mid-infrared [201], temporal regimes from continuous wave [202, 203] to ultrashort pulses [204, 205], and average powers up to several hundreds of watts [206].

Since the Raman scattering probability is typically low ($\sim 10^{-7}$) compared to the elastic Rayleigh scattering process the Raman gain is generally low. Hence, high pump intensities are required to overcome the lasing threshold. The threshold powers of the

aforementioned applications are in the W to kW range. By using microcavities these high pump intensities are obtained for significantly lower laser powers due to the stronger lateral confinement of the pump beam compared to macroscopic cavities. In addition, the Raman gain coefficient is increased via Purcell enhancement. Furthermore, a cavity-enhancement of the pump laser by up to four orders of magnitude can be achieved via resonant recirculation [192].

Taking advantage of these effects low threshold-Raman lasers have been demonstrated using silica-based spherical ($P_{\text{threshold}} = 86 \mu\text{W}$ [207]) and whispering gallery microcavities ($P_{\text{threshold}} = 250 \mu\text{W}$ [208]). Recently, a diamond-based Raman laser has been implemented using a ring resonator geometry exhibiting a moderate threshold power ($\sim 85 \text{ mW}$ [209]). The ring resonator, however, operates in the infrared where the Raman gain is a factor of 20 lower than for visible light.

Tunable microcavities constitute a particularly suited platforms for the implementation of low-threshold diamond-based Raman lasers due to their *in situ* tuning capabilities. Using a slightly wedged diamond layer the diamond thickness can be tuned *in situ* via lateral displacement while the air-gap width can be tuned *in situ* by adjusting the separation of the mirrors. These two tuning mechanisms, in principle, allow for adjusting the free spectral range $\Delta\nu_{\text{FSR}}$ to match the Raman shift for an arbitrary combination of pump and Raman wavelengths.

A microcavity resonant simultaneously with a conventional green pump laser at 532 nm and the corresponding Raman transition at 573 nm enables the implementation of a yellow laser source. Lasers in the yellow wavelength regime are highly relevant for biomedical applications, like dermatologic and ophthalmic therapies, and have been very difficult to implement using robust solid-state based laser technologies [210].

Appendix A

Transfer-matrix calculations

Transfer-matrix formalism

The transfer-matrix formalism allows calculating the propagation of a planar electromagnetic wave through a dielectric multilayer stack comprising layers of different refractive indices [211]. In general, the reflection, refraction and absorption of a plane wave incident on a multilayer stack of different materials can be derived from the Fresnel equations.

The relationship between the forward (E^+) and backward (E^-) propagating waves in two different layers j and $j + 1$ can be described by a transfer matrix M :

$$\begin{pmatrix} E_{j+1}^+ \\ E_{j+1}^- \end{pmatrix} = M \begin{pmatrix} E_j^+ \\ E_j^- \end{pmatrix} \quad (\text{A.1})$$

If a plane wave exits from a material with refractive index n_j orthogonally its corresponding transfer matrix is given by:

$$T_j = \begin{pmatrix} 1 & 1 \\ n_j & -n_j \end{pmatrix} \quad (\text{A.2})$$

Since exiting and entering a material with the same refractive index does not have any effect, entering a material with refractive index n_j is described by the inverse matrix T_j^{-1} . The transfer from a layer j to a layer $j + 1$ is then given by:

$$T_{j+1}^{-1} T_j = \begin{pmatrix} \frac{n_j + n_{j+1}}{2n_j} & \frac{n_j - n_{j+1}}{2n_j} \\ \frac{n_j - n_{j+1}}{2n_j} & \frac{n_j + n_{j+1}}{2n_j} \end{pmatrix} = \frac{1}{t_{j \rightarrow j+1}} \begin{pmatrix} 1 & r_{j \rightarrow j+1} \\ r_{j \rightarrow j+1} & 1 \end{pmatrix} \quad (\text{A.3})$$

where $r_{j \rightarrow j+1}$ and $t_{j \rightarrow j+1}$ are the reflection and transmission coefficients given by the Fresnel equations.

The free propagation of the electromagnetic fields inside a material is represented by:

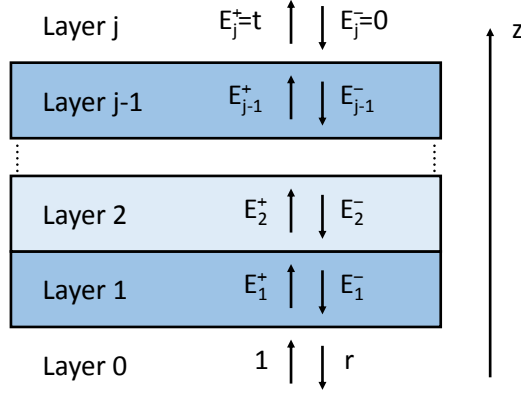


Fig. A.1. Model for calculating the propagation of plane waves through a layered system using the transfer matrix approach. The influence of interfaces and propagation within layers for forward (+) and backward (-) traveling plane waves is described by characteristic matrices. A forward propagating wave with normalized amplitude is partially transmitted (t) and partially reflected (r) by a layered system whose overall matrix can be calculated via matrix multiplication of the matrices of the individual components.

$$P_j = \begin{pmatrix} e^{ikn_j d_j} & 0 \\ 0 & e^{-ikn_j d_j} \end{pmatrix} \quad (\text{A.4})$$

where $k = 2\pi/\lambda$ is the free-space wave vector of the plane wave and d_j is the propagation length. Hence, the transfer of a plane wave through a layer j is represented by the transfer matrix M_j

$$M_j = T_j P_j T_j^{-1} = \begin{pmatrix} \cos(kn_j d_j) & i/n_j \cdot \sin(kn_j d_j) \\ in_j \cdot \sin(kn_j d_j) & \cos(kn_j d_j) \end{pmatrix} \quad (\text{A.5})$$

The total matrix of a layer system can be obtained by matrix multiplication of the consecutive layer matrices and considering the environment of the system, for example the substrate in case of a DBR

$$A = T_{\text{sub}}^{-1} \cdot \prod_j M_j \cdot T_{\text{sub}} \quad (\text{A.6})$$

The waves entering and exiting the structure can then be related via the following equation (see Fig. A.1):

$$\begin{pmatrix} 1 \\ r \end{pmatrix} = \begin{pmatrix} A_{11} & A_{12} \\ A_{21} & A_{22} \end{pmatrix} \begin{pmatrix} t \\ 0 \end{pmatrix} \quad (\text{A.7})$$

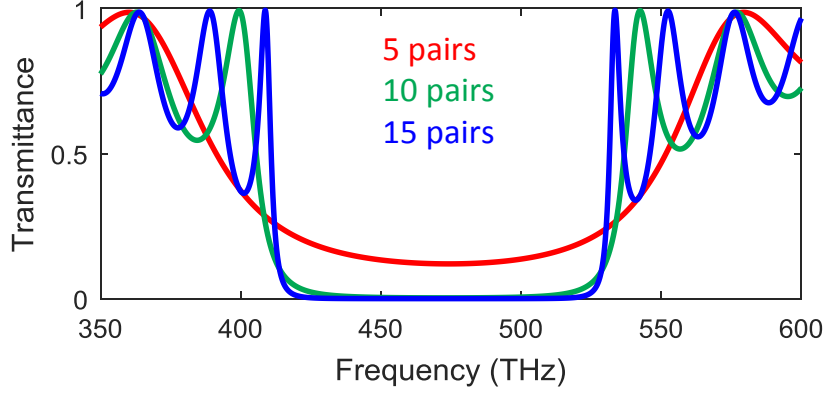


Fig. A.2. Calculations of the DBR mirror transmittance for different numbers of $\text{SiO}_2/\text{Ta}_2\text{O}_5$ layer pairs using the transfer matrix approach.

The reflectance and transmittance of the system are then given by

$$\mathcal{T} = |t|^2 = \left| \frac{1}{A_{11}} \right|^2 \quad (\text{A.8})$$

$$\mathcal{R} = |r|^2 = \left| \frac{A_{21}}{A_{11}} \right|^2 \quad (\text{A.9})$$

Using these equations the transmittance \mathcal{T} of a DBR mirror comprising different numbers of $\text{SiO}_2/\text{Ta}_2\text{O}_5$ layer pairs can be calculated. A DBR coating is described by the following system matrix (Eq. A.6) :

$$A_{\text{DBR}} = T_{\text{air}}^{-1} (M_{\text{Ta}_2\text{O}_5} M_{\text{SiO}_2})^x T_{\text{sub}} \quad (\text{A.10})$$

where x denotes the number of layer pairs and T_{sub} and T_{air}^{-1} are the matrices for exiting the substrate before the coating and entering air after the coating (Eq. A.2). Fig. A.2 shows the theoretical transmittance of 5, 10 and 15 pairs of $\text{SiO}_2/\text{Ta}_2\text{O}_5$ on a SiO_2 substrate for a design wavelength of $\lambda_{\text{DBR}} = 630 \text{ nm}$ (476 THz).

The spectrum exhibits a large reflectivity for a wide range of wavelengths around the design wavelength λ_{DBR} which is often referred to as the “stopband” of the DBR mirror. For wavelengths outside the stopband the reflectivity oscillates. The spacing of these oscillations depends on the number of DBR layer pairs. Notably, the DBR reflection is symmetric if plotted versus frequency rather than wavelength.

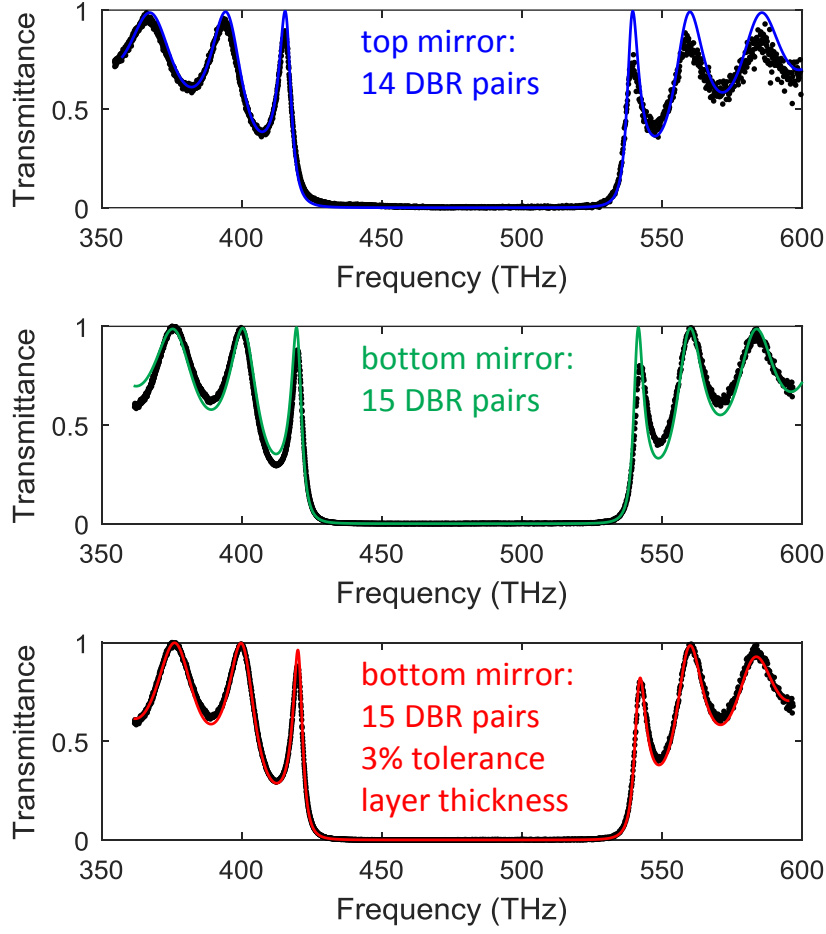


Fig. A.3. Modeling of the DBR mirror stopband of top and bottom mirror. The normalized transmission of the DBR mirrors is determined using a halogen white-light source (black dots). The shape of the stopband is reconstructed using a transfer matrix calculation with a center wavelength of 629 nm and 14 SiO₂/Ta₂O₅ layer pairs for the top mirror and a center wavelength of 625 nm and 15 SiO₂/Ta₂O₅ for the bottom mirror respectively. Allowing for 3% tolerance of the individual layer thicknesses an excellent agreement of experiment and theory is found.

Characterization of the mirror stopband

Distributed Bragg reflector coatings consist of alternating layers of SiO₂/Ta₂O₅ with an optical thickness of $n \cdot d = \lambda_{\text{DBR}}/4$ each. Their high reflectivities rely on constructive interference of light reflected off the interfaces of the individual dielectric layers. The exact design of the mirror coatings used in our experiment was not provided by the commercial supplier (ECI evapcoat), which necessitated the characterization of the coatings. Top and bottom mirror were fabricated in different coating runs where both

were specified to exhibit final reflectivities of $\mathcal{R} > 99.95\%$ at $\lambda = 635$ nm.

We determine the wavelength-dependent transmission of our DBR coatings using a halogen white-light source. First, we obtain a reference spectrum by measuring the transmission of white light through a quartz substrate of thickness $0.525\ \mu\text{m}$ using a grating spectrometer (Acton SP2500, 300 grooves/mm grating). Next, we insert a similar quartz substrate coated with a DBR and repeat the transmission measurement. Fig. A.3 shows the normalized transmission spectrum of our two different DBR coatings for the top and bottom mirror (black dots).

Since the transmission spectrum is symmetric if plotted versus frequency (Fig. A.2), taking the average of the frequencies of corresponding peaks outside the stopband allows to determine the center frequency of the stopband which corresponds to the design frequency for an ideal DBR. We were able to reproduce the characteristic shape of the transmission spectrum by considering 14 (15) layers pairs and using a center wavelength of $\lambda_c = 629$ nm (625 nm) for the bottom (top) mirror.

With the aid of a commercial program designed for analyzing optical coatings (Essential MacLeod) we are able to reproduce the exact shape of the transmission spectrum by optimizing the refractive indices of SiO_2 and Ta_2O_5 and in addition allowing for a 3 % tolerance of the individual layer thicknesses (Fig. A.3 bottom).

Simulation of the cavity mode structure

We model our cavity with alternating layers of high index (Ta_2O_5 , $n_H = 2.06$), and low index (SiO_2 , $n_L = 1.46$) dielectric layers with an optical thickness of $\lambda_{\text{DBR}}/4$. Using the transfer matrix formalism we can describe the system matrix of the whole cavity (Eq. A.6):

$$T_{\text{sub}}^{-1}(M_{\text{SiO}_2}M_{\text{Ta}_2\text{O}_5})^{14}M_{\text{air}}M_{\text{dia}}(M_{\text{Ta}_2\text{O}_5}M_{\text{SiO}_2})^{15}T_{\text{sub}} \quad (\text{A.11})$$

We calculate the transmission of the system and find a very good agreement with the measured mode dispersion displayed in Fig. 3.17(a) for a diamond thickness of $t_d = 0.77\ \mu\text{m}$ and a DBR design wavelength of $\lambda_{\text{DBR}} = 625$ nm.

Fig. A.4(a) displays the analytically calculated mode dispersion for various air-gap widths L and wavelengths λ . Each pixel corresponds to $\delta L = 1$ nm and $\delta \lambda = 0.1$ nm. Due to the discretized calculation and the high quality factors $Q \gtrsim 50\,000$, particularly close to the center of the stopband, the resonances are not captured. We overcome this limitation by plotting the logarithm of the transmission signal.* In Fig. A.4(b) we

*For Fig. 3.17(b) we only plotted the peak values of the resonances.

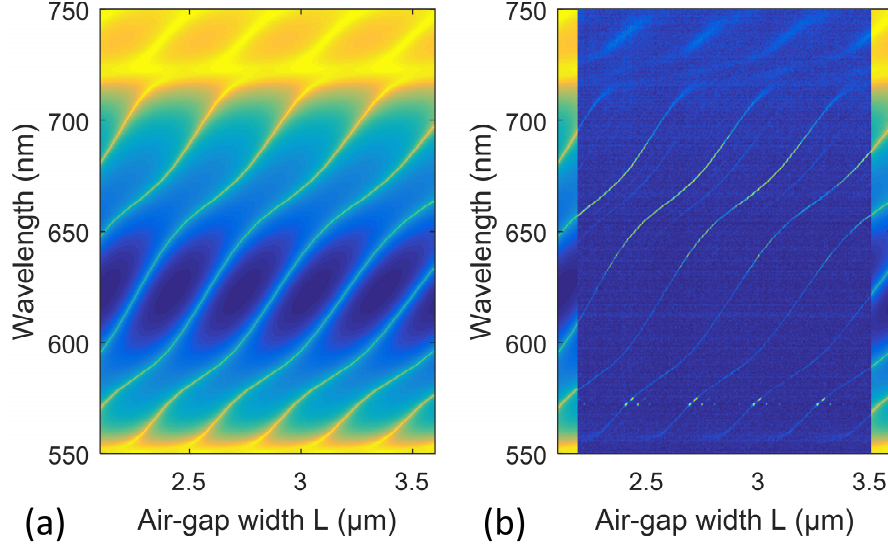


Fig. A.4. Modeling of the cavity mode structure for a diamond thickness of $t_d = 0.77 \mu\text{m}$ and a DBR design wavelength of $\lambda_{\text{DBR}} = 625 \text{ nm}$. **(a)** The logarithm of the transmission signal, calculated with the transfer matrix model, is displayed in order to capture the undersampled sharp resonance. **(b)** Overlay of the experimental data, which illustrates the very good agreement of experiment and calculations. The resonances around $\sim 575 \text{ nm}$ are discussed in Ch. 5.

overlay the experimental data of Fig. 3.17(a) for an extended wavelength range. An excellent agreement of the calculation and the experiment is attained. We highlight that even the mode-anticrossings at wavelengths outside the stopband at $\sim 725 \text{ nm}$ are well reproduced. The exact origin of these anticrossings has not been investigated. The two resonant signals close to 575 nm correspond to the Raman line generated by a green laser at 532 nm and the NV^0 ZPL (for more information see Ch. 5).

Appendix B

Dynamics of an emitter-cavity system in the one-excitation limit

We describe the dynamics of a two level emitter in a cavity under the assumption that at maximum only a single excitation is present at a time. Hence, the emitter is either in the ground (g) or excited state (e), while there is either a photon present in the cavity mode (1) or not (0). In a realistic scenario, excitations leak out of the system in which case the emitter is in its ground state, while there is no photon present in the cavity mode. Hence, the three joint states $|1\rangle = |g, 0\rangle = (1, 0, 0)^\top$, $|2\rangle = |g, 1\rangle = (0, 1, 0)^\top$ and $|3\rangle = |e, 0\rangle = (0, 0, 1)^\top$ form the basis of Hilbert space. In this basis the creation and annihilation operators can be represented by matrices.

$$\begin{aligned} a^\dagger &= \begin{pmatrix} 0 & 0 & 0 \\ 1 & 0 & 0 \\ 0 & 0 & 0 \end{pmatrix} & a &= \begin{pmatrix} 0 & 1 & 0 \\ 0 & 0 & 0 \\ 0 & 0 & 0 \end{pmatrix} \\ b^\dagger &= \begin{pmatrix} 0 & 0 & 0 \\ 0 & 0 & 0 \\ 1 & 0 & 0 \end{pmatrix} & b &= \begin{pmatrix} 0 & 0 & 1 \\ 0 & 0 & 0 \\ 0 & 0 & 0 \end{pmatrix} \end{aligned} \tag{B.1}$$

Note, that the matrix representation of the operators in the Hamiltonian can be readily obtained via Matrix multiplication:

$$\begin{aligned} a^\dagger a &= \begin{pmatrix} 0 & 0 & 0 \\ 0 & 1 & 0 \\ 0 & 0 & 0 \end{pmatrix} & b^\dagger b &= \begin{pmatrix} 0 & 0 & 0 \\ 0 & 0 & 0 \\ 0 & 0 & 1 \end{pmatrix} \\ b^\dagger a &= \begin{pmatrix} 0 & 0 & 0 \\ 0 & 0 & 0 \\ 0 & 1 & 0 \end{pmatrix} & a^\dagger b &= \begin{pmatrix} 0 & 0 & 0 \\ 0 & 0 & 1 \\ 0 & 0 & 0 \end{pmatrix} \end{aligned} \tag{B.2}$$

The Hamiltonian of the system in the rotation wave approximation is given by Eq. 2.22:

$$H_{JC} = \hbar\omega_{\text{cav}}a^\dagger a + \hbar\omega_e b^\dagger b + \hbar g (b^\dagger a + a^\dagger b) \quad (\text{B.3})$$

In order to describe the dynamics of the observables O of the system we need to calculate the time dependence of the expectation values of the operators. According to the Ehrenfest theorem these expectation values can be calculated via $\langle O \rangle(t) = \text{Tr}[\rho(t)O]$. The coherent time-evolution of the density matrix $\rho(t)$ is given by the Heisenberg equation

$$i\hbar \frac{\partial}{\partial t} \rho = [H, \rho] \quad (\text{B.4})$$

As mentioned before excitations leak out of the system via incoherent loss mechanisms. Cavity photons are lost at rate κ due to scattering, absorption or finite mirror reflectivity. Matter excitations decay non-radiatively or emit into modes other than the cavity mode at the rate γ . In this case, the temporal evolution of $\rho(t)$ is given by the Lindblad operator description:

$$\frac{\partial}{\partial t} \rho = \frac{i}{\hbar} [\rho, H] + \frac{\kappa}{2} (2a\rho a^\dagger - a^\dagger a \rho - \rho a^\dagger a) + \frac{\gamma}{2} (2b\rho b^\dagger - b^\dagger b \rho - \rho b^\dagger b) \quad (\text{B.5})$$

The matrix representation of the density operator is given by:

$$\rho = \begin{pmatrix} \rho_{11} & \rho_{12} & \rho_{13} \\ \rho_{21} & \rho_{22} & \rho_{23} \\ \rho_{31} & \rho_{32} & \rho_{33} \end{pmatrix} \quad (\text{B.6})$$

For zero detuning of emitter and cavity mode $\Delta = \omega_e - \omega_c = 0$ the dynamics of the system can be derived using Eq. B.5:

$$\frac{d}{dt} \begin{pmatrix} \rho_{22} \\ \rho_{33} \\ \rho_{32} \\ \rho_{23} \\ \rho_{12} \\ \rho_{13} \\ \rho_{21} \\ \rho_{31} \end{pmatrix} = \begin{pmatrix} -\kappa & 0 & -ig & ig & 0 & 0 & 0 & 0 \\ 0 & -\gamma & ig & -ig & 0 & 0 & 0 & 0 \\ -ig & ig & -\frac{\kappa+\gamma}{2} & ig & 0 & 0 & 0 & 0 \\ ig & -ig & 0 & -\frac{\kappa+\gamma}{2} & 0 & 0 & 0 & 0 \\ 0 & 0 & 0 & 0 & -\frac{\kappa}{2} & ig & 0 & 0 \\ 0 & 0 & 0 & 0 & ig & -\frac{\gamma}{2} & 0 & 0 \\ 0 & 0 & 0 & 0 & 0 & 0 & -\frac{\kappa}{2} & -ig \\ 0 & 0 & 0 & 0 & 0 & 0 & -ig & -\frac{\gamma}{2} \end{pmatrix} \begin{pmatrix} \rho_{22} \\ \rho_{33} \\ \rho_{32} \\ \rho_{23} \\ \rho_{12} \\ \rho_{13} \\ \rho_{21} \\ \rho_{31} \end{pmatrix} \quad (\text{B.7})$$

Using the Ehrenfest theorem, the elements of the density matrix can be identified to

be equivalent to the expectation values of the operators, e.g.

$$\langle b^\dagger a \rangle = \text{Tr}[\rho(t)b^\dagger a] = \text{Tr} \left[\begin{pmatrix} 0 & \rho_{13} & 0 \\ 0 & \rho_{23} & 0 \\ 0 & \rho_{33} & 0 \end{pmatrix} \right] = \rho_{23} \quad (\text{B.8})$$

Calculating the other elements in the same fashion and using the unity-probability property of the density matrix $\rho_{11} + \rho_{22} + \rho_{33} = 1$ yields:

$$\rho = \begin{pmatrix} 1 - \langle a^\dagger a \rangle - \langle b^\dagger b \rangle & \langle a^\dagger \rangle & \langle b^\dagger \rangle \\ \langle a \rangle & \langle a^\dagger a \rangle & \langle a^\dagger b \rangle \\ \langle b \rangle & \langle b^\dagger a \rangle & \langle b^\dagger b \rangle \end{pmatrix} \quad (\text{B.9})$$

This system of linear differential equations (Eq. B.7) can be decomposed into three subsystems. We can solve the subsystems for $(\langle a^\dagger \rangle, \langle b^\dagger \rangle)$ and $(\langle a \rangle, \langle b \rangle)$:

$$\frac{d}{dt} \begin{pmatrix} \langle a^\dagger \rangle \\ \langle b^\dagger \rangle \end{pmatrix} = \begin{pmatrix} -\frac{\kappa}{2} & ig \\ ig & -\frac{\gamma}{2} \end{pmatrix} \begin{pmatrix} \langle a^\dagger \rangle \\ \langle b^\dagger \rangle \end{pmatrix} \quad (\text{B.10})$$

$$\frac{d}{dt} \begin{pmatrix} \langle a \rangle \\ \langle b \rangle \end{pmatrix} = \begin{pmatrix} -\frac{\kappa}{2} & -ig \\ -ig & -\frac{\gamma}{2} \end{pmatrix} \begin{pmatrix} \langle a \rangle \\ \langle b \rangle \end{pmatrix} \quad (\text{B.11})$$

and obtain the following identical Eigenvalues:

$$\lambda_{\dagger 1,2} = -\frac{\kappa + \gamma}{4} \mp \sqrt{\left(\frac{\kappa - \gamma}{4}\right)^2 - g^2} \quad (\text{B.12})$$

$$\lambda_{1,2} = -\frac{\kappa + \gamma}{4} \mp \sqrt{\left(\frac{\kappa - \gamma}{4}\right)^2 - g^2} \quad (\text{B.13})$$

Derivation of Purcell enhancement

In the weak coupling regime ($g \ll \kappa, \gamma$, Sec.2.2.2) and for the typical experimental condition $\kappa > \gamma$ we can simplify Eq.B.13 using the condition $4g < |\kappa - \gamma|$:

$$\begin{aligned}\lambda_{1,2} = \lambda_{\mp 1,2} &= -\frac{\kappa + \gamma}{4} \mp \sqrt{\left(\frac{\kappa - \gamma}{4}\right)^2 - g^2} \\ &= -\frac{\kappa + \gamma}{4} \mp \frac{|\kappa - \gamma|}{4} \sqrt{1 - \left(\frac{4g}{\kappa - \gamma}\right)^2} \\ &\simeq -\frac{\kappa + \gamma}{4} \mp \frac{|\kappa - \gamma|}{4} \left(1 - \frac{1}{2} \left(\frac{4g}{\kappa - \gamma}\right)^2\right)\end{aligned}\quad (\text{B.14})$$

where in the last step we applied the Taylor expansion.

For $g \rightarrow 0$ there is a cavity-like branch (1) and an emitter-like branch (2). Due to the negligible photon contribution to (2) we can assume that λ_2 governs the dynamics of expectation values of the emitter annihilation and creation operators. In the case of the experiment presented in Ch. 3, $(g, \kappa, \gamma) = 2\pi(0.152, 8.04, 0.013)$ GHz, the normalized Eigenvectors Eqs. B.10 and B.11 of are given by:

$$v_{\mp 1} = i \cdot 0.999 |e_{\langle a^\dagger \rangle}\rangle + 0.038 |e_{\langle b^\dagger \rangle}\rangle \quad (\text{B.15})$$

$$v_{\mp 2} = i \cdot 0.038 |e_{\langle a^\dagger \rangle}\rangle + 0.999 |e_{\langle b^\dagger \rangle}\rangle \quad (\text{B.16})$$

$$v_1 = -i \cdot 0.999 |e_{\langle a \rangle}\rangle + 0.038 |e_{\langle b \rangle}\rangle \quad (\text{B.17})$$

$$v_2 = -i \cdot 0.038 |e_{\langle a \rangle}\rangle + 0.999 |e_{\langle b \rangle}\rangle \quad (\text{B.18})$$

We use the assumption that $\langle a^\dagger a \rangle = \langle a^\dagger \rangle \langle a \rangle$ and $\langle b^\dagger b \rangle = \langle b^\dagger \rangle \langle b \rangle$, which corresponds to neglecting quantum mechanical fluctuations. Hence, the radiative emitter decay rate $\langle b^\dagger b \rangle \propto e^{2\lambda_2 t}$ for $\kappa \gg \gamma$ can be calculated:

$$2\lambda_2 \simeq -\left(\gamma + \frac{4g^2}{|\kappa - \gamma|}\right) \approx -\gamma \left(1 + \frac{4g^2}{\kappa\gamma}\right) = -F_P \gamma \quad (\text{B.19})$$

Condition for maximal photon collection efficiency

We determine the temporal evolution of the expectation values of the photon and emitter creation operators by solving the system of linear differential equations given in Eq. B.10

for the initial conditions $\langle a^\dagger \rangle(0) = 0$ and $\langle b^\dagger \rangle(0) = 1$ and obtain:

$$\begin{aligned}\langle a^\dagger \rangle(t) &= ie^{-\frac{\kappa+\gamma}{4}t} \left(\frac{g}{2\eta} e^{\eta t} - \frac{g}{2\eta} e^{-\eta t} \right) \\ &= ie^{-\frac{\kappa+\gamma}{4}t} \cdot \frac{g}{\eta} \sinh(\eta t)\end{aligned}\tag{B.20}$$

$$\begin{aligned}\langle b^\dagger \rangle(t) &= e^{-\frac{\kappa+\gamma}{4}t} \left(\left(\frac{1}{2} + \frac{\kappa-\gamma}{8\eta} \right) e^{\eta t} + \left(\frac{1}{2} - \frac{\kappa-\gamma}{8\eta} \right) e^{-\eta t} \right) \\ &= e^{-\frac{\kappa+\gamma}{4}t} \left(\cosh(\eta t) + \frac{\kappa-\gamma}{4\eta} \sinh(\eta t) \right)\end{aligned}\tag{B.21}$$

where $\eta = \sqrt{((\kappa-\gamma)/4)^2 - g^2}$.

Similarly, for the photon and emitter annihilation operators we solve Eq. B.11 for the initial conditions $\langle a \rangle(0) = 0$ and $\langle b \rangle(0) = 1$:

$$\begin{aligned}\langle a \rangle(t) &= -ie^{-\frac{\kappa+\gamma}{4}t} \left(\frac{g}{2\eta} e^{\eta t} - \frac{g}{2\eta} e^{-\eta t} \right) \\ &= -ie^{-\frac{\kappa+\gamma}{4}t} \cdot \frac{g}{\eta} \sinh(\eta t)\end{aligned}\tag{B.22}$$

$$\begin{aligned}\langle b \rangle(t) &= e^{-\frac{\kappa+\gamma}{4}t} \left(\left(\frac{1}{2} + \frac{\kappa-\gamma}{8\eta} \right) e^{\eta t} + \left(\frac{1}{2} - \frac{\kappa-\gamma}{8\eta} \right) e^{-\eta t} \right) \\ &= e^{-\frac{\kappa+\gamma}{4}t} \left(\cosh(\eta t) + \frac{\kappa-\gamma}{4\eta} \sinh(\eta t) \right)\end{aligned}\tag{B.23}$$

With $\langle a^\dagger a \rangle = \langle a^\dagger \rangle \langle a \rangle$ and $\langle b^\dagger b \rangle = \langle b^\dagger \rangle \langle b \rangle$, the expectation value of the photon number and emitter excitation for the initial conditions $\langle a^\dagger a \rangle(0) = 0$ and $\langle b^\dagger b \rangle(0) = 1$ are then given by:

$$\langle a^\dagger a \rangle(t) = e^{-\frac{\kappa+\gamma}{2}t} \left(\frac{g}{\eta} \sinh(\eta t) \right)^2\tag{B.24}$$

$$\langle b^\dagger b \rangle(t) = e^{-\frac{\kappa+\gamma}{2}t} \left(\cosh(\eta t) + \frac{\kappa-\gamma}{4\eta} \sinh(\eta t) \right)^2\tag{B.25}$$

Now, the probability of a photon leaking out of the cavity can be calculated:

$$\eta_{\text{cav}} = \kappa \int_0^\infty \langle a^\dagger a \rangle dt = \frac{\kappa}{\kappa + \gamma} \frac{g^2}{g^2 + \kappa\gamma/4}\tag{B.26}$$

For fixed values of g and γ this probability is maximized under the condition $\kappa = 2g$.

Note, that the consistency of this model can be verified by checking whether the single

excitation quantum is conserved at all times. We first calculate

$$\gamma \int_0^\infty \langle b^\dagger b \rangle dt = \frac{4g^2\gamma + \kappa\gamma^2 + \kappa^2\gamma}{(\kappa + \gamma)(4g^2 + \kappa\gamma)} \quad (\text{B.27})$$

which allows us to perform the following checks:

$$\int_0^\infty (\kappa \langle a^\dagger a \rangle + \gamma \langle b^\dagger b \rangle) dt = 1 \quad (\text{B.28})$$

$$\int_0^T (\kappa \langle a^\dagger a \rangle + \gamma \langle b^\dagger b \rangle) dt + \left[\langle a^\dagger a \rangle + \langle b^\dagger b \rangle \right]_{t=T} = 1 \quad (\text{B.29})$$

Here, the first equation states that the probability that the excitation is lost from the system after an infinite amount of time is one. The second equation shows that the expected photon and emitter losses after a certain time T and the remaining expectation values for cavity and emitter excitation at time T add up to one.

Appendix C

Characterization of absorption losses in the employed GaP material

In order to estimate the absorption losses in the GaP material we measure the transmission of a $860\text{ }\mu\text{m}$ thick slab of the same material. The solid line in Fig.C.1 shows the normalized transmission spectrum of white light passing through the GaP slab. The spectrum reveals a strong increase of transmission at 550 nm (associated with the GaP band gap) while it is almost constant at $\sim 25\%$ for longer wavelengths. The oscillating behavior originates from interference effects within the GaP layer. Due to difficulties in collimating the white light source the measurement exhibits a significant systematic error in the absolute transmission. Therefore, we measure the transmission of coherent and collimated laser light ($\lambda = 926\text{ nm}$) and find a value of 38% . Without any scattering and without any absorption we calculate a transmission of 54% at this wavelength using the Fresnel equations. The additional losses are related either to absorption/scattering in the material or to scattering at the surfaces. To differentiate between the two possibilities, we also measure the transmission of the laser through a slab with $520\text{ }\mu\text{m}$ thickness which we determine to be 41% . The increased transmission implies a reduction of the layer-thickness-related losses which allows us to deduce a loss coefficient of the GaP material, 0.098 mm^{-1} , and a surface scattering loss of $\sim 4\%$ per GaP-air interface. We note that the surface of the SIL is smoother than that of the measured slabs. Hence, we assume that for the dielectric antenna structure, the main absorption/scattering loss arises from imperfections within the GaP material.

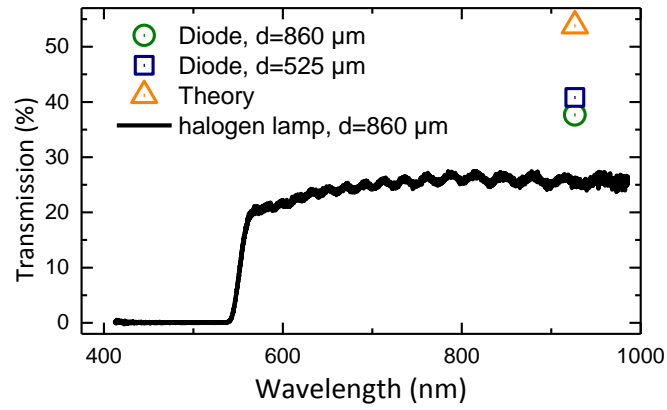


Fig. C.1. Normalized transmission measurement of a GaP slab (thickness d) performed using a halogen white-light source (solid line). Additionally, the transmission of a diode laser ($\lambda = 926 \text{ nm}$) is measured for two different slab thicknesses (green circles: $d = 860 \mu\text{m}$, black squares: $d = 520 \mu\text{m}$). Comparing these values with the theoretically calculated transmission for an ideal GaP layer allows to determine the loss coefficient of the material.

Appendix D

Calculations of the emission pattern of the dielectric optical antenna structure and estimation of collection efficiency

Description of calculations

The calculation of the emission pattern of our antenna structures relies on an asymptotic approach based on the Lorentz reciprocity theorem [172]. As a first step, we calculate the Fresnel coefficients for our 3 layer system consisting of a thin (100)-oriented diamond layer ($n \sim 2.4$) located between a GaP ($n \sim 3.3$) half-space and an air half-space ($n = 1$), Fig. D.1(a). We determine the angular distribution of the emission of a dipole embedded in a diamond layer of thickness d at distance h from the GaP-diamond interface for a given wavelength λ . To this end, we calculate the electric field amplitude of a plane wave approaching the structure from infinity for different polarizations. We obtain the basic angular dependence of the forward (+) and backward (−) propagating s/p-polarized electric fields $E_{s/p}^+(\theta)$ and $E_{s/p}^-(\theta)$ using Eqs. (1, 2) in Ref. [168], which are derived using a transfer matrix approach. Then, we derive the three basic quantities $E_s^\parallel(\theta)$, $E_p^\parallel(\theta)$ and $E_p^\perp(\theta)$, which describe the θ -dependence of the electric field of the three possible dipole orientations, Fig. D.1(a), for $\phi = 0$ [175]:

$$\begin{aligned} E_s^\parallel(\theta) &= E_s^+(\theta) + E_s^-(\theta) \\ E_p^\parallel(\theta) &= E_p^+(\theta) - E_p^-(\theta) \\ E_p^\perp(\theta) &= E_p^+(\theta) + E_p^-(\theta) \end{aligned} \tag{D.1}$$

While the radiation pattern is described by (θ, ϕ) , we introduce the spherical coordinates of the dipole orientation as (α, β) in order to describe the radiation pattern of a skewed dipole Fig. D.1(b). The p- and s- polarized components of the electric field are then

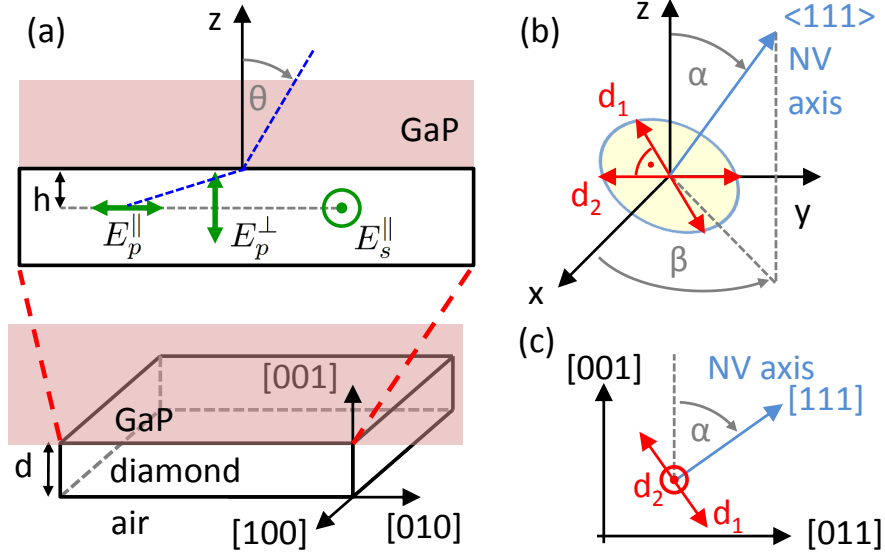


Fig. D.1. (a) Sketch of the dielectric antenna structure: a thin diamond membrane with thickness d ($n \sim 2.4$) containing a single NV center is bonded to gallium phosphide (GaP, $n \sim 3.3$). The NV center is located at distance h from the GaP-diamond interface. The dependence of the emission pattern on the polar angle θ can be described in terms of the three basic dipoles $E_p^{\parallel}(\theta)$, $E_p^{\perp}(\theta)$ and $E_s^{\parallel}(\theta)$. (b) Definition of the spherical coordinate system (α, β) used to describe the direction of the dipoles. (c) Particular orientation for the dipoles d_1 (in z - y plane, $\alpha = \arctan 1/\sqrt{2}$ tilted from the z -axis) and d_2 (aligned along the y -axis).

given by

$$\begin{aligned} E_p(\theta, \phi, \alpha, \beta) &= E_p^{\perp}(\theta) \cos \alpha \sin \theta \\ &\quad + E_p^{\parallel}(\theta) \sin \alpha \cos \theta \cos(\phi - \beta) \\ E_s(\theta, \phi, \alpha, \beta) &= E_s^{\parallel}(\theta) \sin \alpha \sin(\phi - \beta) \end{aligned} \quad (\text{D.2})$$

The emitted power density per solid angle $d\Omega$ is then calculated via

$$P(\theta, \phi, \alpha, \beta) \propto n(\theta) (E_p E_p^* + E_s E_s^*) \quad (\text{D.3})$$

where $n(\theta) = n_{\text{GaP}}$ for $0 < \theta, \pi/2$ and $n(\theta) = n_{\text{air}}$ for $\pi/2 < \theta, \pi$. In order to calculate the emission pattern in the back focal plane, the standard apodization factor $\cos^{-1} \theta$ is introduced [174]:

$$I(\theta, \phi, \alpha, \beta) \propto \frac{1}{\cos \theta} P(\theta, \phi, \alpha, \beta). \quad (\text{D.4})$$

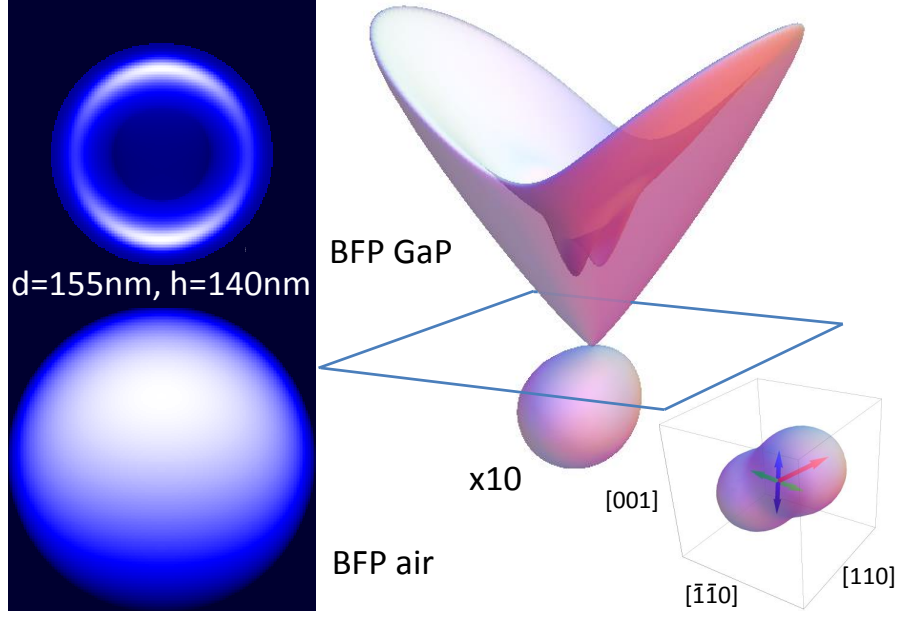


Fig. D.2. Simulated back focal plane images for an NV center with $d = 155$ nm and $h = 140$ nm for emission into air and GaP. On the right, the corresponding emission pattern along with the emission pattern of the two NV dipoles in vacuum are shown.

Calculation of the BFP for a single NV

Fig. D.1(c) displays the alignment of the optical dipoles in the plane normal to the NV axis. We note that, assuming an equal oscillator strength, the alignment of the dipoles within this plane can be chosen arbitrarily. We account for the NV PL spectrum by introducing a wavelength-dependent weighting factor for the emission profile and discretize the spectrum in 5 nm steps. We present the theoretical collection efficiencies $P_{obj}/(P_{GaP} + P_{air})$ for the two basic dipole orientations P_{\parallel} and P_{\perp} within the GaP-diamond dielectric antenna for different thicknesses d and relative positions h/d . We calculate the total power emitted by integrating the emission profile over the relevant solid angle:

$$\begin{aligned}
 P_{obj} &= \int_{\phi=0}^{2\pi} \int_{\theta=0}^{\arcsin 0.8} P(\theta, \phi, \alpha, \beta) \sin \theta d\theta d\phi, \\
 P_{GaP} &= \int_{\phi=0}^{2\pi} \int_{\theta=0}^{\pi/2} P(\theta, \phi, \alpha, \beta) \sin \theta d\theta d\phi, \\
 P_{air} &= \int_{\phi=0}^{2\pi} \int_{\theta=\pi/2}^{\pi} P(\theta, \phi, \alpha, \beta) \sin \theta d\theta d\phi.
 \end{aligned} \tag{D.5}$$

Integrating both emission patterns over their respective half-space ($\phi = 0 \dots 2\pi$, GaP:

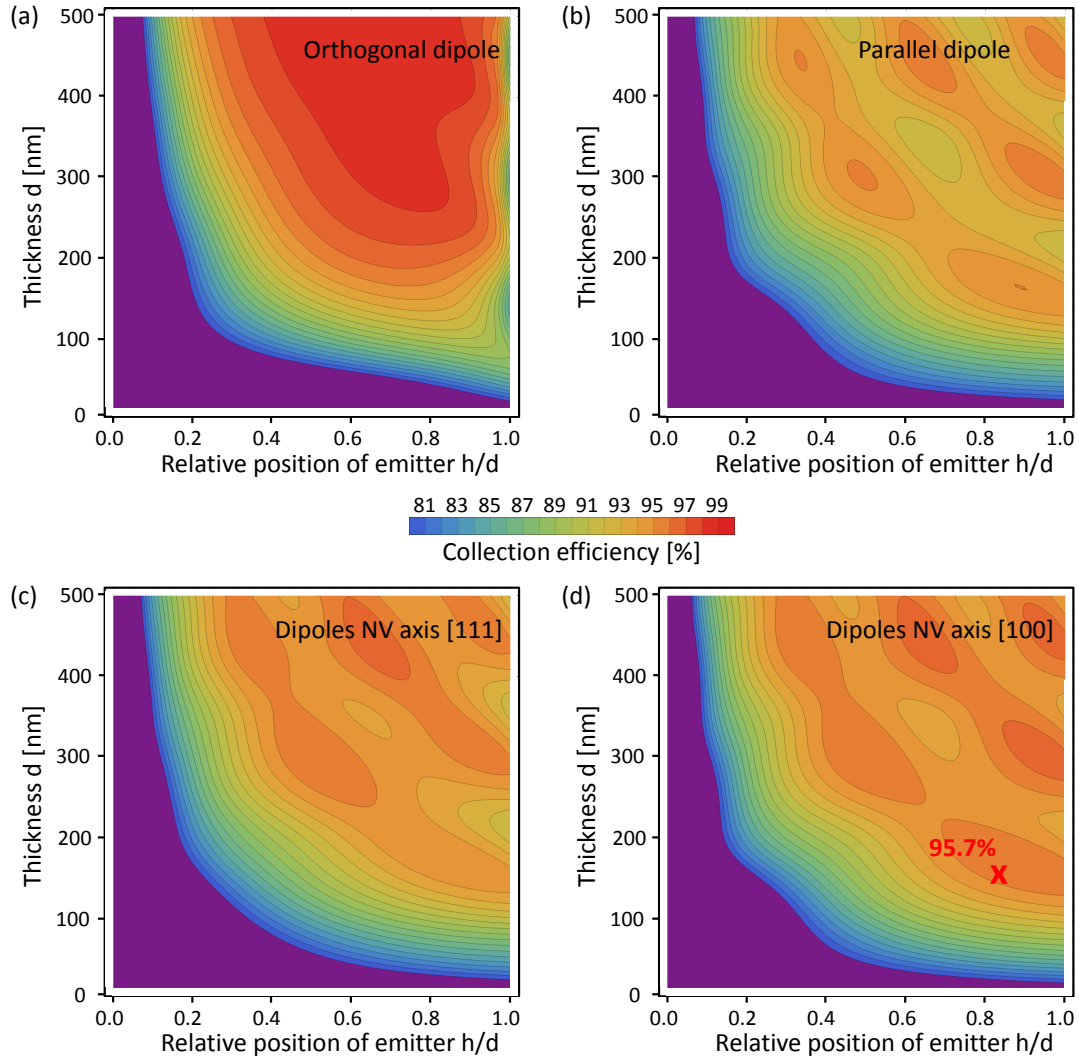


Fig. D.3. Collection efficiency at $\lambda = 675$ nm for different pairs of h and d for dipoles aligned (a) orthogonal, and (b) parallel to the GaP-diamond interface; and for NV emission in (c) [111] diamond, and (d) [100] diamond.

$\theta = 0 \dots \pi/2$, air: $\theta = \pi/2 \dots \pi$) yields the total emitted power. Comparison with the power emitted up to the maximum the angle which can be collected by the objective ($\phi = 0 \dots 2\pi$, $\theta = 0 \dots \arcsin(0.8)$) yields the collection efficiency. Fig.D.3 displays the calculated collection efficiencies as a function of d and h/d for a dipole aligned orthogonal (a) and parallel (b) to the surface and for the NV emission in [111] diamond (c) and [100] diamond (d). The efficiencies are calculated for a single wavelength $\lambda = 675$ nm. For an emitter close to the diamond-GaP interface the collection efficiency is reduced

drastically due to evanescent coupling into angles larger than the critical angle of the interface. For an NV center in [100] diamond with $d = 155$ nm and $h = 140$ nm the theoretical collection efficiency at 675 nm is 95.7%. Considering the entire broadband PL spectrum of an NV center, we calculate a collection efficiency of 95.0% for the same parameters.

References

- [1] V. Giovannetti, S. Lloyd, and L. Maccone, *Quantum-enhanced measurements: beating the standard quantum limit*, [Science](#) **306**, 1330 (2004).
- [2] V. Giovannetti, S. Lloyd, and L. Maccone, *Advances in quantum metrology*, [Nature Photonics](#) **5**, 222 (2011).
- [3] M. Riebe, H. Häffner, C. F. Roos, W. Hänsel, J. Benhelm, G. P. T. Lancaster, T. W. Körber, C. Becher, F. Schmidt-Kaler, D. F. V. James, and R. Blatt, *Deterministic quantum teleportation with atoms*, [Nature](#) **429**, 734 (2004).
- [4] S. D. Barrett and P. Kok, *Efficient high-fidelity quantum computation using matter qubits and linear optics*, [Physical Review A](#) **71**, 060310 (2005).
- [5] W. Pfaff, B. Hensen, H. Bernien, S. B. van Dam, M. S. Blok, T. H. Taminiau, M. J. Tiggelman, R. N. Schouten, M. Markham, D. J. Twitchen, and R. Hanson, *Unconditional quantum teleportation between distant solid-state qubits*, [Science](#) **345**, 532 (2014).
- [6] B. Hensen, H. Bernien, A. E. Dréau, A. Reiserer, N. Kalb, M. S. Blok, J. Ruitenberg, R. F. L. Vermeulen, R. N. Schouten, C. Abellán, W. Amaya, V. Pruneri, M. W. Mitchell, M. Markham, D. J. Twitchen, D. Elkouss, S. Wehner, T. H. Taminiau, and R. Hanson, *Experimental loophole-free violation of a Bell inequality using entangled electron spins separated by 1.3 km*, [Nature](#) **526**, 682 (2015).
- [7] M. Giustina, M. A. Versteegh, S. Wengerowsky, J. Handsteiner, A. Hochrainer, K. Phelan, F. Steinlechner, J. Kofler, J.-Å. Larsson, C. Abellán, W. Amaya, V. Pruneri, M. W. Mitchell, J. Beyer, T. Gerrits, A. E. Lita, L. K. Shalm, S. W. Nam, T. Scheidl, R. Ursin, B. Wittmann, and A. Zeilinger, *Significant-Loophole-Free Test of Bell's Theorem with Entangled Photons*, [Physical Review Letters](#) **115**, 250401 (2015).
- [8] L. K. Shalm, E. Meyer-Scott, B. G. Christensen, P. Bierhorst, M. A. Wayne, M. J. Stevens, T. Gerrits, S. Glancy, D. R. Hamel, M. S. Allman, K. J. Coakley, S. D.

- Dyer, C. Hodge, A. E. Lita, V. B. Verma, C. Lambrocco, E. Tortorici, A. L. Migdall, Y. Zhang, D. R. Kumor, W. H. Farr, F. Marsili, M. D. Shaw, J. A. Stern, C. Abellán, W. Amaya, V. Pruneri, T. Jennewein, M. W. Mitchell, P. G. Kwiat, J. C. Bienfang, R. P. Mirin, E. Knill, and S. W. Nam, *Strong Loophole-Free Test of Local Realism*, [Physical Review Letters](#) **115**, 250402 (2015).
- [9] W. Rosenfeld, D. Burchardt, R. Garthoff, K. Redeker, N. Ortegel, M. Rau, and H. Weinfurter, *Event-Ready Bell Test Using Entangled Atoms Simultaneously Closing Detection and Locality Loopholes*, [Physical Review Letters](#) **119**, 010402 (2017).
- [10] C. L. Degen, F. Reinhard, and P. Cappellaro, *Quantum sensing*, [Reviews of Modern Physics](#) **89**, 035002 (2017).
- [11] L. Pezzè, A. Smerzi, M. K. Oberthaler, R. Schmied, and P. Treutlein, *Non-classical states of atomic ensembles: fundamentals and applications in quantum metrology*, [arXiv: 1609.01609](#) (2016).
- [12] T. D. Ladd, F. Jelezko, R. Laflamme, Y. Nakamura, C. Monroe, and J. L. O'Brien, *Quantum computers*, [Nature](#) **464**, 45 (2010).
- [13] I. M. Georgescu, S. Ashhab, and F. Nori, *Quantum simulation*, [Reviews of Modern Physics](#) **86**, 153 (2014).
- [14] J. L. O'Brien, A. Furusawa, and J. Vučković, *Photonic quantum technologies*, [Nature Photonics](#) **3**, 687 (2009).
- [15] N. Gisin and R. Thew, *Quantum communication*, [Nature Photonics](#) **1**, 165 (2007).
- [16] H. J. Kimble, *The quantum internet*, [Nature](#) **453**, 1023 (2008).
- [17] E. Togan, Y. Chu, A. S. Trifonov, L. Jiang, J. Maze, L. Childress, M. V. G. Dutt, A. S. Sørensen, P. R. Hemmer, A. S. Zibrov, and M. D. Lukin, *Quantum entanglement between an optical photon and a solid-state spin qubit*, [Nature](#) **466**, 730 (2010).
- [18] K. De Greve, L. Yu, P. L. McMahon, J. S. Pelc, C. M. Natarajan, N. Y. Kim, E. Abe, S. Maier, C. Schneider, M. Kamp, S. Höfling, R. H. Hadfield, A. Forchel, M. M. Fejer, and Y. Yamamoto, *Quantum-dot spin-photon entanglement via frequency downconversion to telecom wavelength*, [Nature](#) **491**, 421 (2012).

- [19] W. B. Gao, P. Fallahi, E. Togan, J. Miguel-Sanchez, and A. Imamoglu, *Observation of entanglement between a quantum dot spin and a single photon*, [*Nature* **491**, 426](#) (2012).
- [20] J. R. Schaibley, A. P. Burgers, G. A. McCracken, L.-M. Duan, P. R. Berman, D. G. Steel, A. S. Bracker, D. Gammon, and L. J. Sham, *Demonstration of Quantum Entanglement between a Single Electron Spin Confined to an InAs Quantum Dot and a Photon*, [*Physical Review Letters* **110**, 167401](#) (2013).
- [21] A. Batalov, C. Zierl, T. Gaebel, P. Neumann, I.-Y. Chan, G. Balasubramanian, P. R. Hemmer, F. Jelezko, and J. Wrachtrup, *Temporal Coherence of Photons Emitted by Single Nitrogen-Vacancy Defect Centers in Diamond Using Optical Rabi-Oscillations*, [*Physical Review Letters* **100**, 077401](#) (2008).
- [22] Y. Chu, N. de Leon, B. Shields, B. Hausmann, R. Evans, E. Togan, M. J. Burek, M. Markham, A. Stacey, A. Zibrov, A. Yacoby, D. Twitchen, M. Loncar, H. Park, P. Maletinsky, and M. Lukin, *Coherent Optical Transitions in Implanted Nitrogen Vacancy Centers*, [*Nano Letters* **14**, 1982](#) (2014).
- [23] H. Wang, Z.-C. Duan, Y.-H. Li, S. Chen, J.-P. Li, Y.-M. He, M.-C. Chen, Y. He, X. Ding, C.-Z. Peng, C. Schneider, M. Kamp, S. Höfling, C.-Y. Lu, and J.-W. Pan, *Near-Transform-Limited Single Photons from an Efficient Solid-State Quantum Emitter*, [*Physical Review Letters* **116**, 213601](#) (2016).
- [24] A. V. Kuhlmann, J. H. Prechtel, J. Houel, A. Ludwig, D. Reuter, A. D. Wieck, and R. J. Warburton, *Transform-limited single photons from a single quantum dot*, [*Nature Communications* **6**, 8204](#) (2015).
- [25] J.-P. Jahn, M. Munsch, L. Béguin, A. V. Kuhlmann, M. Renggli, Y. Huo, F. Ding, R. Trotta, M. Reindl, O. G. Schmidt, A. Rastelli, P. Treutlein, and R. J. Warburton, *An artificial Rb atom in a semiconductor with lifetime-limited linewidth*, [*Physical Review B* **92**, 245439](#) (2015).
- [26] H. Bernien, B. Hensen, W. Pfaff, G. Koolstra, M. S. Blok, L. Robledo, T. H. Taminiau, M. Markham, D. J. Twitchen, L. Childress, and R. Hanson, *Heralded entanglement between solid-state qubits separated by three metres.*, [*Nature* **497**, 86](#) (2013).
- [27] A. Delteil, Z. Sun, W.-b. Gao, E. Togan, S. Faelt, and A. Imamoglu, *Generation of heralded entanglement between distant hole spins*, [*Nature Physics* **12**, 218](#) (2015).

- [28] W. B. Gao, A. Imamoglu, H. Bernien, and R. Hanson, *Coherent manipulation, measurement and entanglement of individual solid-state spins using optical fields*, [Nature Photonics](#) **9**, 363 (2015).
- [29] R. J. Warburton, *Single spins in self-assembled quantum dots*, [Nature Materials](#) **12**, 483 (2013).
- [30] A. V. Kuhlmann, J. Houel, A. Ludwig, L. Greuter, D. Reuter, A. D. Wieck, M. Poggio, and R. J. Warburton, *Charge noise and spin noise in a semiconductor quantum device*, [Nature Physics](#) **9**, 570 (2013).
- [31] F. Jelezko and J. Wrachtrup, *Single defect centres in diamond: A review*, [physica status solidi \(a\)](#) **203**, 3207 (2006).
- [32] G. Balasubramanian, P. Neumann, D. Twitchen, M. Markham, R. Kolesov, N. Mizuochi, J. Isoya, J. Achard, J. Beck, J. Tissler, V. Jacques, P. R. Hemmer, F. Jelezko, and J. Wrachtrup, *Ultralong spin coherence time in isotopically engineered diamond*, [Nature Materials](#) **8**, 383 (2009).
- [33] M. V. G. Dutt, L. Childress, L. Jiang, E. Togan, J. Maze, F. Jelezko, A. S. Zibrov, P. R. Hemmer, and M. D. Lukin, *Quantum Register Based on Individual Electronic and Nuclear Spin Qubits in Diamond*, [Science](#) **316**, 1312 (2007).
- [34] P. C. Maurer, G. Kucsko, C. Latta, L. Jiang, N. Y. Yao, S. D. Bennett, F. Pastawski, D. Hunger, N. Chisholm, M. Markham, D. J. Twitchen, J. I. Cirac, and M. D. Lukin, *Room-Temperature Quantum Bit Memory Exceeding One Second*, [Science](#) **336**, 1283 (2012).
- [35] I. Aharonovich, D. Englund, and M. Toth, *Solid-state single-photon emitters*, [Nature Photonics](#) **10**, 631 (2016).
- [36] E. M. Purcell, H. C. Torrey, and R. V. Pound, *Resonance Absorption by Nuclear Magnetic Moments in a Solid*, [Physical Review](#) **69**, 37 (1946).
- [37] P. A. M. Dirac, *The Quantum Theory of the Emission and Absorption of Radiation*, [Proceedings of the Royal Society A: Mathematical, Physical and Engineering Sciences](#) **114**, 243 (1927).
- [38] A. Faraon, P. E. Barclay, C. Santori, K.-M. C. Fu, and R. G. Beausoleil, *Resonant enhancement of the zero-phonon emission from a color center in a diamond cavity*, [Nature Photonics](#) **5**, 301 (2011).

- [39] A. Faraon, C. Santori, Z. Huang, V. M. Acosta, and R. G. Beausoleil, *Coupling of nitrogen-vacancy centers to photonic crystal cavities in monocrystalline diamond*, [*Physical Review Letters* **109**, 033604](#) (2012).
- [40] B. J. M. Hausmann, B. J. Shields, Q. Quan, Y. Chu, N. P. De Leon, R. Evans, M. J. Burek, A. S. Zibrov, M. Markham, D. J. Twitchen, H. Park, M. D. Lukin, and M. Loncar, *Coupling of NV centers to photonic crystal nanobeams in diamond*, [*Nano Letters* **13**, 5791](#) (2013).
- [41] P. Tamarat, T. Gaebel, J. R. Rabeau, M. Khan, A. D. Greentree, H. Wilson, L. C. L. Hollenberg, S. Prawer, P. Hemmer, F. Jelezko, and J. Wrachtrup, *Stark Shift Control of Single Optical Centers in Diamond*, [*Physical Review Letters* **97**, 083002](#) (2006).
- [42] C. Kurtsiefer, S. Mayer, P. Zarda, and H. Weinfurter, *Stable Solid-State Source of Single Photons*, [*Physical Review Letters* **85**, 290](#) (2000).
- [43] F. Jelezko, T. Gaebel, I. Popa, A. Gruber, and J. Wrachtrup, *Observation of Coherent Oscillations in a Single Electron Spin*, [*Physical Review Letters* **92**, 076401](#) (2004).
- [44] J. Teissier, A. Barfuss, P. Appel, E. Neu, and P. Maletinsky, *Strain Coupling of a Nitrogen-Vacancy Center Spin to a Diamond Mechanical Oscillator*, [*Physical Review Letters* **113**, 020503](#) (2014).
- [45] P. Ouartchaiyapong, K. W. Lee, B. A. Myers, and A. C. B. Jayich, *Dynamic strain-mediated coupling of a single diamond spin to a mechanical resonator*, [*Nature Communications* **5**, 4429](#) (2014).
- [46] G. Kucsko, P. C. Maurer, N. Y. Yao, M. Kubo, H. J. Noh, P. K. Lo, H. Park, and M. D. Lukin, *Nanometre-scale thermometry in a living cell*, [*Nature* **500**, 54](#) (2013).
- [47] P. Neumann, I. Jakobi, F. Dolde, C. Burk, R. Reuter, G. Waldherr, J. Honert, T. Wolf, A. Brunner, J. H. Shim, D. Suter, H. Sumiya, J. Isoya, and J. Wrachtrup, *High-Precision Nanoscale Temperature Sensing Using Single Defects in Diamond*, [*Nano Letters* **13**, 2738](#) (2013).
- [48] F. Dolde, H. Fedder, M. W. Doherty, T. Nöbauer, F. Rempp, G. Balasubramanian, T. Wolf, F. Reinhard, L. C. L. Hollenberg, F. Jelezko, and J. Wrachtrup, *Electric-field sensing using single diamond spins*, [*Nature Physics* **7**, 459](#) (2011).

- [49] G. Balasubramanian, I. Y. Chan, R. Kolesov, M. Al-Hmoud, J. Tisler, C. Shin, C. Kim, A. Wojcik, P. R. Hemmer, A. Krueger, T. Hanke, A. Leitenstorfer, R. Bratschitsch, F. Jelezko, and J. Wrachtrup, *Nanoscale imaging magnetometry with diamond spins under ambient conditions*, [Nature](#) **455**, 648 (2008).
- [50] L. Rondin, J.-P. Tetienne, T. Hingant, J.-F. Roch, P. Maletinsky, and V. Jacques, *Magnetometry with nitrogen-vacancy defects in diamond*, [Reports on Progress in Physics](#) **77**, 056503 (2014).
- [51] J. P. Hadden, J. P. Harrison, A. C. Stanley-Clarke, L. Marseglia, Y.-L. D. Ho, B. R. Patton, J. L. O'Brien, and J. G. Rarity, *Strongly enhanced photon collection from diamond defect centers under microfabricated integrated solid immersion lenses*, [Applied Physics Letters](#) **97**, 241901 (2010).
- [52] P. Siyushev, F. Kaiser, V. Jacques, I. Gerhardt, S. Bischof, H. Fedder, J. Dodson, M. Markham, D. Twitchen, F. Jelezko, and J. Wrachtrup, *Monolithic diamond optics for single photon detection*, [Applied Physics Letters](#) **97**, 241902 (2010).
- [53] L. Marseglia, J. P. Hadden, A. C. Stanley-Clarke, J. P. Harrison, B. Patton, Y.-L. D. Ho, B. Naydenov, F. Jelezko, J. Meijer, P. R. Dolan, J. M. Smith, J. G. Rarity, and J. L. O'Brien, *Nanofabricated solid immersion lenses registered to single emitters in diamond*, [Applied Physics Letters](#) **98**, 133107 (2011).
- [54] D. Le Sage, L. M. Pham, N. Bar-Gill, C. Belthangady, M. D. Lukin, A. Yacoby, and R. L. Walsworth, *Efficient photon detection from color centers in a diamond optical waveguide*, [Physical Review B](#) **85**, 121202 (2012).
- [55] T. M. Babinec, B. J. M. Hausmann, M. Khan, Y. Zhang, J. R. Maze, P. R. Hemmer, and M. Loncar, *A diamond nanowire single-photon source.*, [Nature Nanotechnology](#) **5**, 195 (2010).
- [56] E. Neu, P. Appel, M. Ganzhorn, J. Miguel-Sánchez, M. Lesik, V. Mille, V. Jacques, A. Tallaie, J. Achard, and P. Maletinsky, *Photonic nano-structures on (111)-oriented diamond*, [Applied Physics Letters](#) **104**, 153108 (2014).
- [57] S. A. Momenzadeh, R. J. Stöhr, F. F. de Oliveira, A. Brunner, A. Denisenko, S. Yang, F. Reinhard, and J. Wrachtrup, *Nanoengineered Diamond Waveguide as a Robust Bright Platform for Nanomagnetometry Using Shallow Nitrogen Vacancy Centers*, [Nano Letters](#) **15**, 165 (2015).

- [58] L. Li, E. H. Chen, J. Zheng, S. L. Mouradian, F. Dolde, T. Schröder, S. Karaveli, M. L. Markham, D. J. Twitchen, and D. Englund, *Efficient Photon Collection from a Nitrogen Vacancy Center in a Circular Bullseye Grating*, [Nano Letters](#) **15**, 1493 (2015).
- [59] J. R. Weber, W. F. Koehl, J. B. Varley, A. Janotti, B. B. Buckley, C. G. Van de Walle, and D. D. Awschalom, *Quantum computing with defects*, [Proceedings of the National Academy of Sciences](#) **107**, 8513 (2010).
- [60] Y. Doi, T. Makino, H. Kato, D. Takeuchi, M. Ogura, H. Okushi, H. Morishita, T. Tashima, S. Miwa, S. Yamasaki, P. Neumann, J. Wrachtrup, Y. Suzuki, and N. Mizuochi, *Deterministic Electrical Charge-State Initialization of Single Nitrogen-Vacancy Center in Diamond*, [Physical Review X](#) **4**, 011057 (2014).
- [61] B. Grotz, M. V. Hauf, M. Dankerl, B. Naydenov, S. Pezzagna, J. Meijer, F. Jelezko, J. Wrachtrup, M. Stutzmann, F. Reinhard, and J. A. Garrido, *Charge state manipulation of qubits in diamond*, [Nature Communications](#) **3**, 729 (2012).
- [62] M. V. Hauf, B. Grotz, B. Naydenov, M. Dankerl, S. Pezzagna, J. Meijer, F. Jelezko, J. Wrachtrup, M. Stutzmann, F. Reinhard, and J. A. Garrido, *Chemical control of the charge state of nitrogen-vacancy centers in diamond*, [Physical Review B](#) **83**, 081304 (2011).
- [63] W. Kaiser and W. L. Bond, *Nitrogen, a major impurity in common type I diamond*, [Physical Review](#) **115**, 857 (1959).
- [64] A. Gruber, A. Dräbenstedt, C. Tietz, L. Fleury, J. Wrachtrup, and C. von Borczyskowski, *Scanning Confocal Optical Microscopy and Magnetic Resonance on Single Defect Centers*, [Science](#) **276**, 2012 (1997).
- [65] R. Hanson, *Quantum information: Mother Nature outgrown*, [Nature Materials](#) **8**, 368 (2009).
- [66] J. Isberg, J. Hammersberg, E. Johansson, T. Wikstrom, D. J. Twitchen, A. J. Whitehead, S. E. Coe, and G. A. Scarsbrook, *High Carrier Mobility in Single-Crystal Plasma-Deposited Diamond*, [Science](#) **297**, 1670 (2002).
- [67] H. Kraus, D. Simin, C. Kasper, Y. Suda, S. Kawabata, W. Kada, T. Honda, Y. Hijikata, T. Ohshima, V. Dyakonov, and G. V. Astakhov, *Three-Dimensional Proton Beam Writing of Optically Active Coherent Vacancy Spins in Silicon Carbide*, [Nano Letters](#) **17**, 2865 (2017).

- [68] Y.-C. Chen, P. S. Salter, S. Knauer, L. Weng, A. C. Frangeskou, C. J. Stephen, S. N. Ishmael, P. R. Dolan, S. Johnson, B. L. Green, G. W. Morley, M. E. Newton, J. G. Rarity, M. J. Booth, and J. M. Smith, *Laser writing of coherent colour centres in diamond*, [Nature Photonics](#) **11**, 77 (2016).
- [69] K. Ohno, F. Joseph Heremans, L. C. Bassett, B. A. Myers, D. M. Toyli, A. C. Bleszynski Jayich, C. J. Palmstrøm, and D. D. Awschalom, *Engineering shallow spins in diamond with nitrogen delta-doping*, [Applied Physics Letters](#) **101**, 082413 (2012).
- [70] S. Pezzagna, B. Naydenov, F. Jelezko, J. Wrachtrup, and J. Meijer, *Creation efficiency of nitrogen-vacancy centres in diamond*, [New Journal of Physics](#) **12**, 065017 (2010).
- [71] J. Meijer, B. Burchard, M. Domhan, C. Wittmann, T. Gaebel, I. Popa, F. Jelezko, and J. Wrachtrup, *Generation of single color centers by focused nitrogen implantation*, [Applied Physics Letters](#) **87**, 261909 (2005).
- [72] P. Spinicelli, A. Dréau, L. Rondin, F. Silva, J. Achard, S. Xavier, S. Bansropun, T. Debuisschert, S. Pezzagna, J. Meijer, V. Jacques, and J.-F. Roch, *Engineered arrays of nitrogen-vacancy color centers in diamond based on implantation of CN-molecules through nanoapertures*, [New Journal of Physics](#) **13**, 025014 (2011).
- [73] J. Riedrich-Möller, S. Pezzagna, J. Meijer, C. Pauly, F. Mücklich, M. Markham, A. M. Edmonds, and C. Becher, *Nanoimplantation and Purcell enhancement of single nitrogen-vacancy centers in photonic crystal cavities in diamond*, [Applied Physics Letters](#) **106**, 221103 (2015).
- [74] A. Gali, M. Fyta, and E. Kaxiras, *Ab initio supercell calculations on nitrogen-vacancy center in diamond: Electronic structure and hyperfine tensors*, [Physical Review B](#) **77**, 155206 (2008).
- [75] J. R. Maze, A. Gali, E. Togan, Y. Chu, A. Trifonov, E. Kaxiras, and M. D. Lukin, *Properties of nitrogen-vacancy centers in diamond: the group theoretic approach*, [New Journal of Physics](#) **13**, 025025 (2011).
- [76] M. W. Doherty, N. B. Manson, P. Delaney, and L. C. L. Hollenberg, *The negatively charged nitrogen-vacancy centre in diamond: the electronic solution*, [New Journal of Physics](#) **13**, 025019 (2011).

- [77] J. P. Goss, R. Jones, S. J. Breuer, P. R. Briddon, and S. Öberg, *The Twelve-Line 1.682 eV Luminescence Center in Diamond and the Vacancy-Silicon Complex*, [Physical Review Letters](#) **77**, 3041 (1996).
- [78] M. W. Doherty, N. B. Manson, P. Delaney, F. Jelezko, J. Wrachtrup, and L. C. Hollenberg, *The nitrogen-vacancy colour centre in diamond*, [Physics Reports](#) **528**, 1 (2013).
- [79] Y. Chu and M. D. Lukin, *Quantum optics with nitrogen-vacancy centers in diamond*, [arXiv: 1504.05990](#) (2015).
- [80] L. Robledo, H. Bernien, I. van Weperen, and R. Hanson, *Control and Coherence of the Optical Transition of Single Nitrogen Vacancy Centers in Diamond*, [Physical Review Letters](#) **105**, 177403 (2010).
- [81] A. Batalov, V. Jacques, F. Kaiser, P. Siyushev, P. Neumann, L. J. Rogers, R. L. McMurtrie, N. B. Manson, F. Jelezko, and J. Wrachtrup, *Low Temperature Studies of the Excited-State Structure of Negatively Charged Nitrogen-Vacancy Color Centers in Diamond*, [Physical Review Letters](#) **102**, 195506 (2009).
- [82] L. Robledo, L. Childress, H. Bernien, B. Hensen, P. F. A. Alkemade, and R. Hanson, *High-fidelity projective read-out of a solid-state spin quantum register*, [Nature](#) **477**, 574 (2011).
- [83] L. C. Bassett, F. J. Heremans, C. G. Yale, B. B. Buckley, and D. D. Awschalom, *Electrical Tuning of Single Nitrogen-Vacancy Center Optical Transitions Enhanced by Photoinduced Fields*, [Physical Review Letters](#) **107**, 266403 (2011).
- [84] J. Wolters, N. Sadzak, A. W. Schell, T. Schröder, and O. Benson, *Measurement of the Ultrafast Spectral Diffusion of the Optical Transition of Nitrogen Vacancy Centers in Nano-Size Diamond Using Correlation Interferometry*, [Physical Review Letters](#) **110**, 027401 (2013).
- [85] K. Beha, A. Batalov, N. B. Manson, R. Bratschitsch, and A. Leitenstorfer, *Optimum Photoluminescence Excitation and Recharging Cycle of Single Nitrogen-Vacancy Centers in Ultrapure Diamond*, [Physical Review Letters](#) **109**, 097404 (2012).
- [86] N. Aslam, G. Waldherr, P. Neumann, F. Jelezko, and J. Wrachtrup, *Photo-induced ionization dynamics of the nitrogen vacancy defect in diamond investigated by single-shot charge state detection*, [New Journal of Physics](#) **15**, 013064 (2013).

- [87] V. M. Acosta, C. Santori, A. Faraon, Z. Huang, K. M. C. Fu, A. Stacey, D. A. Simpson, K. Ganesan, S. Tomljenovic-Hanic, A. D. Greentree, S. Prawer, and R. G. Beausoleil, *Dynamic stabilization of the optical resonances of single nitrogen-vacancy centers in diamond*, [Physical Review Letters](#) **108**, 206401 (2012).
- [88] A. Alkauskas, B. B. Buckley, D. D. Awschalom, and C. G. Van de Walle, *First-principles theory of the luminescence lineshape for the triplet transition in diamond NV centres*, [New Journal of Physics](#) **16**, 073026 (2014).
- [89] H. Haken and H. Wolf, *Molekülphysik und Quantenchemie* (Springer, Berlin) (2006).
- [90] V. Hizhnyakov, H. Kaasik, and I. Sildos, *Zero-Phonon Lines: The Effect of a Strong Softening of Elastic Springs in the Excited State*, [physica status solidi \(b\)](#) **234**, 644 (2002).
- [91] R. Albrecht, A. Bommer, C. Deutsch, J. Reichel, and C. Becher, *Coupling of a single nitrogen-vacancy center in diamond to a fiber-based microcavity*, [Physical Review Letters](#) **110**, 243602 (2013).
- [92] M. L. Goldman, M. W. Doherty, A. Sipahigil, N. Y. Yao, S. D. Bennett, N. B. Manson, A. Kubanek, and M. D. Lukin, *State-selective intersystem crossing in nitrogen-vacancy centers*, [Physical Review B](#) **91**, 165201 (2015).
- [93] K. M. C. Fu, C. Santori, P. E. Barclay, L. J. Rogers, N. B. Manson, and R. G. Beausoleil, *Observation of the dynamic Jahn-Teller effect in the excited states of nitrogen-vacancy centers in diamond*, [Physical Review Letters](#) **103**, 256404 (2009).
- [94] L. J. Rogers, R. L. McMurtrie, M. J. Sellars, and N. B. Manson, *Time-averaging within the excited state of the nitrogen-vacancy centre in diamond*, [New Journal of Physics](#) **11**, 063007 (2009).
- [95] P. Neumann, R. Kolesov, V. Jacques, J. Beck, J. Tisler, A. Batalov, L. Rogers, N. B. Manson, G. Balasubramanian, F. Jelezko, and J. Wrachtrup, *Excited-state spectroscopy of single NV defects in diamond using optically detected magnetic resonance*, [New Journal of Physics](#) **11**, 013017 (2009).
- [96] P. Appel, *Scanning Nanomagnetometry: Probing Magnetism with Single Spins in Diamond*, Ph.D. thesis, University of Basel (2017).

- [97] N. Manson, L. Rogers, M. Doherty, and L. Hollenberg, *Optically induced spin polarisation of the NV- centre in diamond: role of electron-vibration interaction*, [arXiv: 1011.2840](#) (2010).
- [98] L. J. Rogers, S. Armstrong, M. J. Sellars, and N. B. Manson, *Infrared emission of the NV centre in diamond: Zeeman and uniaxial stress studies*, [New Journal of Physics](#) **10**, 103024 (2008).
- [99] Y. Ma, M. Rohlfing, and A. Gali, *Excited states of the negatively charged nitrogen-vacancy color center in diamond*, [Physical Review B](#) **81**, 041204 (2010).
- [100] L. Robledo, H. Bernien, T. V. D. Sar, and R. Hanson, *Spin dynamics in the optical cycle of single nitrogen-vacancy centres in diamond*, [New Journal of Physics](#) **13**, 025013 (2011).
- [101] M. W. Doherty, F. Dolde, H. Fedder, F. Jelezko, J. Wrachtrup, N. B. Manson, and L. C. L. Hollenberg, *Theory of the ground-state spin of the NV⁻ center in diamond*, [Physical Review B](#) **85**, 205203 (2012).
- [102] R. Schirhagl, K. Chang, M. Loretz, and C. L. Degen, *Nitrogen-Vacancy Centers in Diamond: Nanoscale Sensors for Physics and Biology*, [Annual Review of Physical Chemistry](#) **65**, 83 (2014).
- [103] M. Steiner, P. Neumann, J. Beck, F. Jelezko, and J. Wrachtrup, *Universal enhancement of the optical readout fidelity of single electron spins at nitrogen-vacancy centers in diamond*, [Physical Review B](#) **81**, 035205 (2010).
- [104] B. Hensen, *Quantum Nonlocality with Spins in Diamond*, Ph.D. thesis, Technische Universiteit Delft (2016).
- [105] A. Jarmola, V. M. Acosta, K. Jensen, S. Chemerisov, and D. Budker, *Temperature- and Magnetic-Field-Dependent Longitudinal Spin Relaxation in Nitrogen-Vacancy Ensembles in Diamond*, [Physical Review Letters](#) **108**, 197601 (2012).
- [106] T. Ishikawa, K. M. C. Fu, C. Santori, V. M. Acosta, R. G. Beausoleil, H. Watanabe, S. Shikata, and K. M. Itoh, *Optical and spin coherence properties of nitrogen-vacancy centers placed in a 100 nm thick isotopically purified diamond layer*, [Nano Letters](#) **12**, 2083 (2012).
- [107] D. Riedel, D. Rohner, M. Ganzhorn, T. Kaldewey, P. Appel, E. Neu, R. J. Warburton, and P. Maletinsky, *Low-Loss Broadband Antenna for Efficient Photon*

- Collection from a Coherent Spin in Diamond*, [Physical Review Applied](#) **2**, 064011 (2014).
- [108] M. Żukowski, A. Zeilinger, M. A. Horne, and A. K. Ekert, "*Event-ready-detectors*" *Bell experiment via entanglement swapping*, [Physical Review Letters](#) **71**, 4287 (1993).
- [109] B. B. Blinov, D. L. Moehring, L.-M. Duan, and C. Monroe, *Observation of entanglement between a single trapped atom and a single photon*, [Nature](#) **432**, 81 (2004).
- [110] D. L. Moehring, P. Maunz, S. Olmschenk, K. C. Younge, D. N. Matsukevich, L.-M. Duan, and C. Monroe, *Entanglement of single-atom quantum bits at a distance*, [Nature](#) **449**, 68 (2007).
- [111] J. Hofmann, M. Krug, N. Ortegel, L. Gerard, M. Weber, W. Rosenfeld, and H. Weinfurter, *Heralded Entanglement Between Widely Separated Atoms*, [Science](#) **337**, 72 (2012).
- [112] D. Riedel, I. Söllner, B. J. Shields, S. Starosielec, P. Appel, E. Neu, P. Maletinsky, and R. J. Warburton, *Deterministic enhancement of coherent photon generation from a nitrogen-vacancy center in ultrapure diamond*, [Physical Review X](#) **7**, 031040 (2017).
- [113] R. J. Barbour, P. A. Dalgarno, A. Curran, K. M. Nowak, H. J. Baker, D. R. Hall, N. G. Stoltz, P. M. Petroff, and R. J. Warburton, *A tunable microcavity*, [Journal of Applied Physics](#) **110**, 053107 (2011).
- [114] L. Greuter, S. Starosielec, A. V. Kuhlmann, and R. J. Warburton, *Towards high-cooperativity strong coupling of a quantum dot in a tunable microcavity*, [Physical Review B](#) **92**, 045302 (2015).
- [115] L. Greuter, D. Najer, A. V. Kuhlmann, S. R. Valentin, A. Ludwig, A. D. Wieck, S. Starosielec, and R. J. Warburton, *Epitaxial lift-off for solid-state cavity quantum electrodynamics*, [Journal of Applied Physics](#) **118**, 075705 (2015).
- [116] E. del Valle, F. P. Laussy, and C. Tejedor, *Luminescence spectra of quantum dots in microcavities. II. Fermions*, [Physical Review B](#) **79**, 235326 (2009).
- [117] L. Greuter, *Self-assembled quantum dots in a fully tunable microcavity*, Phd thesis, University of Basel (2015).

- [118] M. Fox, *Quantum Optics: An Introduction* (Oxford University Press) (2006).
- [119] P. Lodahl, S. Mahmoodian, and S. Stobbe, *Interfacing single photons and single quantum dots with photonic nanostructures*, [Reviews of Modern Physics](#) **87**, 347 (2015).
- [120] W. Nagourney, *Quantum Electronics for Atomic Physics* (Oxford University Press) (2010).
- [121] C. H. Nguyen, A. N. Utama, N. Lewty, K. Durak, G. Maslennikov, S. Straupe, M. Steiner, and C. Kurtsiefer, *Single atoms coupled to a near-concentric cavity*, [Physical Review A](#) **96**, 031802 (2017).
- [122] K. Durak, C. H. Nguyen, V. Leong, S. Straupe, and C. Kurtsiefer, *Diffraction-limited Fabry-Perot cavity in the near concentric regime*, [New Journal of Physics](#) **16**, 103002 (2014).
- [123] C. J. Hood, H. J. Kimble, and J. Ye, *Characterization of high-finesse mirrors: Loss, phase shifts, and mode structure in an optical cavity*, [Physical Review A](#) **64**, 033804 (2001).
- [124] H. Kaupp, T. Hümmer, M. Mader, B. Schlederer, J. Benedikter, P. Haeusser, H. C. Chang, H. Fedder, T. W. Hänsch, and D. Hunger, *Purcell-Enhanced Single-Photon Emission from Nitrogen-Vacancy Centers Coupled to a Tunable Microcavity*, [Physical Review Applied](#) **6**, 054010 (2016).
- [125] A. Reiserer and G. Rempe, *Cavity-based quantum networks with single atoms and optical photons*, [Reviews of Modern Physics](#) **87**, 1379 (2015).
- [126] L. Greuter, S. Starosielec, D. Najer, A. Ludwig, L. Duempelmann, D. Rohner, and R. J. Warburton, *A small mode volume tunable microcavity: Development and characterization*, [Applied Physics Letters](#) **105**, 121105 (2014).
- [127] D. Babic and S. Corzine, *Analytic expressions for the reflection delay, penetration depth, and absorptance of quarter-wave dielectric mirrors*, [IEEE Journal of Quantum Electronics](#) **28**, 514 (1992).
- [128] E. Janitz, M. Ruf, M. Dimock, A. Bourassa, J. Sankey, and L. Childress, *Fabry-Perot microcavity for diamond-based photonics*, [Physical Review A](#) **92**, 043844 (2015).

- [129] H. Bernien, L. Childress, L. Robledo, M. Markham, D. Twitchen, and R. Hanson, *Two-photon quantum interference from separate nitrogen vacancy centers in diamond*, [Physical Review Letters](#) **108**, 043604 (2012).
- [130] A. Sipahigil, M. L. Goldman, E. Togan, Y. Chu, M. Markham, D. J. Twitchen, A. S. Zibrov, A. Kubanek, and M. D. Lukin, *Quantum interference of single photons from remote nitrogen-vacancy centers in diamond*, [Physical Review Letters](#) **108**, 143601 (2012).
- [131] P. E. Barclay, K. M. C. Fu, C. Santori, A. Faraon, and R. G. Beausoleil, *Hybrid nanocavity resonant enhancement of color center emission in diamond*, [Physical Review X](#) **1**, 011007 (2011).
- [132] H. Kaupp, C. Deutsch, H.-C. Chang, J. Reichel, T. W. Hänsch, and D. Hunger, *Scaling laws of the cavity enhancement for nitrogen-vacancy centers in diamond*, [Physical Review A](#) **88**, 053812 (2013).
- [133] G. Khitrova, H. M. Gibbs, M. Kira, S. W. Koch, and A. Scherer, *Vacuum Rabi splitting in semiconductors*, [Nature Physics](#) **2**, 81 (2006).
- [134] A. Sipahigil, R. E. Evans, D. D. Sukachev, M. J. Burek, J. Borregaard, M. K. Bhaskar, C. T. Nguyen, J. L. Pacheco, H. A. Atikian, C. Meuwly, R. M. Camacho, F. Jelezko, E. Bielejec, H. Park, M. Lončar, and M. D. Lukin, *An integrated diamond nanophotonics platform for quantum-optical networks*, [Science](#) **354**, 847 (2016).
- [135] L. Li, T. Schröder, E. H. Chen, M. Walsh, I. Bayn, J. Goldstein, O. Gaathon, M. E. Trusheim, M. Lu, J. Mower, M. Cotlet, M. L. Markham, D. J. Twitchen, and D. Englund, *Coherent spin control of a nanocavity-enhanced qubit in diamond*, [Nature Communications](#) **6**, 6173 (2015).
- [136] S. Johnson, P. R. Dolan, T. Grange, A. A. Trichet, G. Hornecker, Y. C. Chen, L. Weng, G. M. Hughes, A. A. Watt, A. Auffèves, and J. M. Smith, *Tunable cavity coupling of the zero phonon line of a nitrogen-vacancy defect in diamond*, [New Journal of Physics](#) **17**, 122003 (2015).
- [137] J. Benedikter, H. Kaupp, T. Hümmer, Y. Liang, A. Bommer, C. Becher, A. Krueger, J. M. Smith, T. W. Hänsch, and D. Hunger, *Cavity-Enhanced Single-Photon Source Based on the Silicon-Vacancy Center in Diamond*, [Physical Review Applied](#) **7**, 024031 (2017).

- [138] A. D. Greentree, P. Olivero, M. Draganski, E. Trajkov, J. R. Rabeau, P. Reichart, B. C. Gibson, S. Rubanov, S. T. Huntington, D. N. Jamieson, and S. Praver, *Critical components for diamond-based quantum coherent devices*, [Journal of Physics: Condensed Matter](#) **18**, S825 (2006).
- [139] T. Schröder, S. L. Mouradian, J. Zheng, M. E. Trusheim, M. Walsh, E. H. Chen, L. Li, I. Bayn, and D. Englund, *Quantum nanophotonics in diamond [Invited]*, [Journal of the Optical Society of America B](#) **33**, B65 (2016).
- [140] D. Hunger, C. Deutsch, R. J. Barbour, R. J. Warburton, and J. Reichel, *Laser micro-fabrication of concave, low-roughness features in silica*, [AIP Advances](#) **2**, 012119 (2012).
- [141] D. Hunger, T. Steinmetz, Y. Colombe, C. Deutsch, T. W. Hänsch, and J. Reichel, *A fiber Fabry-Perot cavity with high finesse*, [New Journal of Physics](#) **12**, 065038 (2010).
- [142] H. Kelkar, D. Wang, D. Martín-Cano, B. Hoffmann, S. Christiansen, S. Götzinger, and V. Sandoghdar, *Sensing nanoparticles with a cantilever-based scannable optical cavity of low finesse and sub- λ^3 volume*, [Physical Review Applied](#) **4**, 054010 (2015).
- [143] A. A. P. Trichet, P. R. Dolan, D. M. Coles, G. M. Hughes, and J. M. Smith, *Topographic control of open-access microcavities at the nanometer scale*, [Optics Express](#) **23**, 17205 (2015).
- [144] D. Najer, M. Renggli, D. Riedel, S. Starosielec, and R. J. Warburton, *Fabrication of mirror templates in silica with micron-sized radii of curvature*, [Applied Physics Letters](#) **110**, 011101 (2017).
- [145] K. M. Nowak, H. J. Baker, and D. R. Hall, *Efficient laser polishing of silica micro-optic components*, [Applied Optics](#) **45**, 162 (2006).
- [146] A. Plöchl and G. Kräuter, *Wafer direct bonding : tailoring adhesion between brittle materials*, [Materials Science and Engineering: R: Reports](#) **25**, 1 (1999).
- [147] I. Friel, S. Clewes, H. Dhillon, N. Perkins, D. Twitchen, and G. Scarsbrook, *Control of surface and bulk crystalline quality in single crystal diamond grown by chemical vapour deposition*, [Diamond and Related Materials](#) **18**, 808 (2009).

- [148] P. Maletinsky, S. Hong, M. S. Grinolds, B. Hausmann, M. D. Lukin, R. L. Walsworth, M. Loncar, and A. Yacoby, *A robust scanning diamond sensor for nanoscale imaging with single nitrogen-vacancy centres*, [Nature Nanotechnology](#) **7**, 320 (2012).
- [149] P. Appel, E. Neu, M. Ganzhorn, A. Barfuss, M. Batzer, M. Gratz, A. Tschöpe, and P. Maletinsky, *Fabrication of all diamond scanning probes for nanoscale magnetometry*, [Review of Scientific Instruments](#) **87**, 063703 (2016).
- [150] Y. Tao, J. M. Boss, B. A. Moores, and C. L. Degen, *Single-crystal diamond nanomechanical resonators with quality factors exceeding one million*, [Nature Communications](#) **5**, 3638 (2014).
- [151] P. Siyushev, H. Pinto, M. Vörös, A. Gali, F. Jelezko, and J. Wrachtrup, *Optically Controlled Switching of the Charge State of a Single Nitrogen-Vacancy Center in Diamond at Cryogenic Temperatures*, [Physical Review Letters](#) **110**, 167402 (2013).
- [152] J. Benedikter, T. Hümmer, M. Mader, B. Schlederer, J. Reichel, T. W. Hänsch, and D. Hunger, *Transverse-mode coupling and diffraction loss in tunable Fabry-Pérot microcavities*, [New Journal of Physics](#) **17**, 053051 (2015).
- [153] M. Uphoff, M. Brekenfeld, G. Rempe, and S. Ritter, *Frequency splitting of polarization eigenmodes in microscopic Fabry-Perot cavities*, [New Journal of Physics](#) **17**, 013053 (2015).
- [154] T. J. A. Kippenberg, *Nonlinear Optics in Ultra-high-Q Whispering-Gallery Optical Microcavities*, Ph.D. thesis, California Institute of Technology (2004).
- [155] P. R. Dolan, X. Li, J. Storteboom, and M. Gu, *Complete determination of the orientation of NV centers with radially polarized beams*, [Optics Express](#) **22**, 4379 (2014).
- [156] I. P. Radko, M. Boll, N. M. Israelsen, N. Raatz, J. Meijer, F. Jelezko, U. L. Andersen, and A. Huck, *Determining the internal quantum efficiency of shallow-implanted nitrogen-vacancy defects in bulk diamond*, [Optics Express](#) **24**, 27715 (2016).
- [157] B. Guha, F. Marsault, F. Cadiz, L. Morgenroth, V. Ulin, V. Berkovitz, A. Lemaître, C. Gomez, A. Amo, S. Combrié, B. Gérard, G. Leo, and I. Favero, *Surface-enhanced gallium arsenide photonic resonator with quality factor of 6×10^6* , [Optica](#) **4**, 218 (2017).

- [158] W. S. Lau, J. Zhang, X. Wan, J. K. Luo, Y. Xu, and H. Wong, *Surface smoothing effect of an amorphous thin film deposited by atomic layer deposition on a surface with nano-sized roughness*, [AIP Advances](#) **4**, 027120 (2014).
- [159] S. Bogdanović, S. B. Van Dam, C. Bonato, L. C. Coenen, A. M. J. Zwerver, B. Hensen, M. S. Liddy, T. Fink, A. Reiserer, M. Lončar, and R. Hanson, *Design and low-temperature characterization of a tunable microcavity for diamond-based quantum networks*, [Applied Physics Letters](#) **110**, 171103 (2017).
- [160] A. Beveratos, S. Kühn, R. Brouri, T. Gacoin, J. P. Poizat, and P. Grangier, *Room temperature stable single-photon source*, [European Physical Journal D](#) **18**, 191 (2002).
- [161] J. Wolters, G. Kewes, A. W. Schell, N. Nüsse, M. Schoengen, B. Löchel, T. Hanke, R. Bratschitsch, A. Leitenstorfer, T. Aichele, and O. Benson, *Coupling of single nitrogen-vacancy defect centers in diamond nanocrystals to optical antennas and photonic crystal cavities*, [physica status solidi \(b\)](#) **249**, 918 (2012).
- [162] T. K. Yeung, D. Le Sage, L. M. Pham, P. L. Stanwix, and R. L. Walsworth, *Anti-reflection coating for nitrogen-vacancy optical measurements in diamond*, [Applied Physics Letters](#) **100**, 251111 (2012).
- [163] J. T. Choy, B. J. M. Hausmann, T. M. Babinec, I. Bulu, M. Khan, P. Maletinsky, A. Yacoby, and M. Lončar, *Enhanced single-photon emission from a diamond-silver aperture*, [Nature Photonics](#) **5**, 738 (2011).
- [164] K. G. Lee, X. W. Chen, H. Eghlidi, P. Kukura, R. Lettow, A. Renn, V. Sandoghdar, S. Go, and S. Götzinger, *A planar dielectric antenna for directional single-photon emission and near-unity collection efficiency*, [Nature Photonics](#) **5**, 166 (2011).
- [165] X.-W. Chen, S. Götzinger, and V. Sandoghdar, *99% efficiency in collecting photons from a single emitter.*, [Optics Letters](#) **36**, 3545 (2011).
- [166] X.-L. Chu, T. J. K. Brenner, X.-W. Chen, Y. Ghosh, J. A. Hollingsworth, V. Sandoghdar, and S. Götzinger, *Experimental realization of an optical antenna designed for collecting 99% of photons from a quantum emitter*, [Optica](#) **1**, 203 (2014).
- [167] X.-L. Chu, S. Götzinger, and V. Sandoghdar, *A single molecule as a high-fidelity photon gun for producing intensity-squeezed light*, [Nature Photonics](#) **11**, 58 (2016).

- [168] L Luan and P R Sievert and J B Ketterson, *Near-field and far-field electric dipole radiation in the vicinity of a planar dielectric half space*, [New Journal of Physics](#) **8**, 264 (2006).
- [169] K. M. C. Fu, C. Santori, P. E. Barclay, I. Aharonovich, S. Prawer, N. Meyer, A. M. Holm, and R. G. Beausoleil, *Coupling of nitrogen-vacancy centers in diamond to a GaP waveguide*, [Applied Physics Letters](#) **93**, 234107 (2008).
- [170] Q. Wu, G. D. Feke, R. D. Grober, and L. P. Ghislain, *Realization of numerical aperture 2.0 using a gallium phosphide solid immersion lens*, [Applied Physics Letters](#) **75**, 4064 (1999).
- [171] S. M. Mansfield and G. S. Kino, *Solid immersion microscope*, [Applied Physics Letters](#) **57**, 2615 (1990).
- [172] J.-Y. Courtois, J.-M. Courty, and J. C. Mertz, *Internal dynamics of multilevel atoms near a vacuum-dielectric interface*, [Physical Review A](#) **53**, 1862 (1996).
- [173] C. Lee, E. Gu, M. Dawson, I. Friel, and G. Scarsbrook, *Etching and micro-optics fabrication in diamond using chlorine-based inductively-coupled plasma*, [Diamond and Related Materials](#) **17**, 1292 (2008).
- [174] M. A. Lieb, J. M. Zavislan, and L. Novotny, *Single-molecule orientations determined by direct emission pattern imaging*, [Journal of the Optical Society of America B](#) **21**, 1210 (2004).
- [175] L. Luan, P. R. Sievert, B. Watkins, W. Mu, Z. Hong, and J. B. Ketterson, *Angular radiation pattern of electric dipoles embedded in a thin film in the vicinity of a dielectric half space*, [Applied Physics Letters](#) **89**, 031119 (2006).
- [176] M. Bass, C. DeCusatis, J. M. Enoch, V. Lakshminarayanan, G. Li, C. MacDonald, V. N. Mahajan, and E. V. Stryland, *Handbook of Optics, Third Edition Volume IV*, (2009).
- [177] T. P. M. Alegre, C. Santori, G. Medeiros-Ribeiro, and R. G. Beausoleil, *Polarization-selective excitation of nitrogen vacancy centers in diamond*, [Physical Review B](#) **76**, 165205 (2007).
- [178] L. Childress, M. V. Gurudev Dutt, J. M. Taylor, A. S. Zibrov, F. Jelezko, J. Wrachtrup, P. R. Hemmer, and M. D. Lukin, *Coherent Dynamics of Coupled Electron and Nuclear Spin Qubits in Diamond*, [Science](#) **314**, 281 (2006).

- [179] B. J. M. Hausmann, B. Shields, Q. Quan, P. Maletinsky, M. McCutcheon, J. T. Choy, T. M. Babinec, A. Kubanek, A. Yacoby, M. D. Lukin, and M. Loncar, *Integrated Diamond Networks for Quantum Nanophotonics*, [Nano Letters](#) **12**, 1578 (2012).
- [180] I. Aharonovich and E. Neu, *Diamond Nanophotonics*, [Advanced Optical Materials](#) **2**, 911 (2014).
- [181] P. Siyushev, M. H. Metsch, A. Ijaz, J. M. Binder, M. K. Bhaskar, D. D. Sukachev, A. Sipahigil, R. E. Evans, C. T. Nguyen, M. D. Lukin, P. R. Hemmer, Y. N. Palyanov, I. N. Kupriyanov, Y. M. Borzdov, L. J. Rogers, and F. Jelezko, *Optical and microwave control of germanium-vacancy center spins in diamond*, [Physical Review B](#) **96**, 081201 (2017).
- [182] M. K. Bhaskar, D. D. Sukachev, A. Sipahigil, R. E. Evans, M. J. Burek, C. T. Nguyen, L. J. Rogers, P. Siyushev, M. H. Metsch, H. Park, F. Jelezko, M. Lončar, and M. D. Lukin, *Quantum Nonlinear Optics with a Germanium-Vacancy Color Center in a Nanoscale Diamond Waveguide*, [Physical Review Letters](#) **118**, 223603 (2017).
- [183] W. F. Koehl, B. B. Buckley, F. J. Heremans, G. Calusine, and D. D. Awschalom, *Room temperature coherent control of defect spin qubits in silicon carbide*, [Nature](#) **479**, 84 (2011).
- [184] S. Castelletto, B. C. Johnson, V. Ivády, N. Stavrias, T. Umeda, A. Gali, and T. Ohshima, *A silicon carbide room-temperature single-photon source*, [Nature Materials](#) **13**, 151 (2013).
- [185] D. Riedel, F. Fuchs, H. Kraus, S. Váth, A. Sperlich, V. Dyakonov, A. A. Solta-mova, P. G. Baranov, V. A. Ilyin, and G. V. Astakhov, *Resonant addressing and manipulation of silicon vacancy qubits in silicon carbide*, [Physical Review Letters](#) **109**, 226402 (2012).
- [186] T. Zhong, J. M. Kindem, J. G. Bartholomew, J. Rochman, I. Craiciu, E. Miyazono, M. Bettinelli, E. Cavalli, V. Verma, S. W. Nam, F. Marsili, M. D. Shaw, A. D. Beyer, and A. Faraon, *Nanophotonic rare-earth quantum memory with optically controlled retrieval*, [Science](#) **357**, 1392 (2017).
- [187] D. Le Sage, K. Arai, D. R. Glenn, S. J. DeVience, L. M. Pham, L. Rahn-Lee, M. D. Lukin, A. Yacoby, A. Komeili, and R. L. Walsworth, *Optical magnetic imaging of living cells.*, [Nature](#) **496**, 486 (2013).

- [188] T. Staudacher, F. Shi, S. Pezzagna, J. Meijer, J. Du, C. A. Meriles, F. Reinhard, and J. Wrachtrup, *Nuclear magnetic resonance spectroscopy on a (5-nanometer)³ sample volume.*, [*Science* **339**, 561](#) (2013).
- [189] S. B. van Dam, P. C. Humphreys, F. Rozpędek, S. Wehner, and R. Hanson, *Multiplexed entanglement generation over quantum networks using multi-qubit nodes*, [*Quantum Science and Technology* **2**, 034002](#) (2017).
- [190] N. Kalb, A. A. Reiserer, P. C. Humphreys, J. J. W. Bakermans, S. J. Kamerling, N. H. Nickerson, S. C. Benjamin, D. J. Twitchen, M. Markham, and R. Hanson, *Entanglement distillation between solid-state quantum network nodes*, [*Science* **356**, 928](#) (2017).
- [191] T. Hümmer, J. Noe, M. S. Hofmann, T. W. Hänsch, A. Högele, and D. Hunger, *Cavity-enhanced Raman Microscopy of Individual Carbon Nanotubes*, [*Nature Communications* **7**, 12155](#) (2016).
- [192] B. Petrak, N. Djeu, and A. Muller, *Purcell-enhanced Raman scattering from atmospheric gases in a high-finesse microcavity*, [*Physical Review A* **89**, 023811](#) (2014).
- [193] M. Kasperczyk, A. Jorio, E. Neu, P. Maletinsky, and L. Novotny, *Stokes–anti-Stokes correlations in diamond*, [*Optics Letters* **40**, 2393](#) (2015).
- [194] V. G. Savitski, S. Reilly, and A. J. Kemp, *Steady-State Raman Gain in Diamond as a Function of Pump Wavelength*, [*IEEE Journal of Quantum Electronics* **49**, 218](#) (2013).
- [195] C. Santori and R. G. Beausoleil, *Quantum memory: Phonons in diamond crystals*, [*Nature Photonics* **6**, 10](#) (2011).
- [196] K. C. Lee, B. J. Sussman, M. R. Sprague, P. Michelberger, K. F. Reim, J. Nunn, N. K. Langford, P. J. Bustard, D. Jaksch, and I. a. Walmsley, *Macroscopic non-classical states and terahertz quantum processing in room-temperature diamond*, [*Nature Photonics* **6**, 41](#) (2011).
- [197] D. G. England, P. J. Bustard, J. Nunn, R. Lausten, and B. J. Sussman, *From Photons to Phonons and Back: A THz Optical Memory in Diamond*, [*Physical Review Letters* **111**, 243601](#) (2013).
- [198] D. G. England, K. A. G. Fisher, J.-P. W. MacLean, P. J. Bustard, R. Lausten, K. J. Resch, and B. J. Sussman, *Storage and Retrieval of THz-Bandwidth Single*

- Photons Using a Room-Temperature Diamond Quantum Memory*, [Physical Review Letters](#) **114**, 053602 (2015).
- [199] B. J. M. Hausmann, I. Bulu, V. Venkataraman, P. Deotare, and M. Lončar, *Diamond nonlinear photonics*, [Nature Photonics](#) **8**, 369 (2014).
- [200] E. Granados, D. J. Spence, and R. P. Mildren, *Deep ultraviolet diamond Raman laser*, [Optics Express](#) **19**, 10857 (2011).
- [201] A. Sabella, J. A. Piper, and R. P. Mildren, *Diamond Raman laser with continuously tunable output from 338 to 380 μm* , [Optics Letters](#) **39**, 4037 (2014).
- [202] W. Lubeigt, G. M. Bonner, J. E. Hastie, M. D. Dawson, D. Burns, and A. J. Kemp, *Continuous-wave diamond Raman laser*, [Optics Letters](#) **35**, 2994 (2010).
- [203] O. Kitzler, A. McKay, and R. P. Mildren, *Continuous-wave wavelength conversion for high-power applications using an external cavity diamond Raman laser*, [Optics Letters](#) **37**, 2790 (2012).
- [204] D. J. Spence, E. Granados, and R. P. Mildren, *Mode-locked picosecond diamond Raman laser*, [Optics Letters](#) **35**, 556 (2010).
- [205] J. Lin and D. J. Spence, *255 fs dissipative soliton diamond Raman laser*, [Optics Letters](#) **41**, 1861 (2016).
- [206] R. J. Williams, J. Nold, M. Strecker, O. Kitzler, A. McKay, T. Schreiber, and R. P. Mildren, *Efficient Raman frequency conversion of high-power fiber lasers in diamond*, [Laser and Photonics Reviews](#) **9**, 405 (2015).
- [207] S. M. Spillane, T. J. Kippenberg, and K. J. Vahala, *Ultralow-threshold Raman laser using a spherical dielectric microcavity*, [Nature](#) **415**, 621 (2002).
- [208] T. J. Kippenberg, S. M. Spillane, D. K. Armani, and K. J. Vahala, *Ultralow-threshold microcavity Raman laser on a microelectronic chip*, [Optics Letters](#) **29**, 1224 (2004).
- [209] P. Latawiec, V. Venkataraman, M. J. Burek, B. J. M. Hausmann, I. Bulu, and M. Lončar, *On-chip diamond Raman laser*, [Optica](#) **2**, 924 (2015).
- [210] A. D. Greentree and S. Prawer, *Yellow lasers: A little diamond goes a long way*, [Nature Photonics](#) **4**, 202 (2010).
- [211] S. J. Byrnes, *Multilayer optical calculations*, [arXiv: 1603.02720](#) (2016).

Acknowledgements

The acknowledgments will be edited in the final version of the thesis.

Curriculum vitae

Daniel Riedel

Personal information

Mailing address: Metzerstrasse 7, 4056 Basel, Switzerland
Email address: daniel.riedel@outlook.com
Date of birth: 7th July 1987
Place of birth: Dinkelsbühl, Germany
Citizenship: German

Education

2013 – 2017	PhD in Experimental Physics University of Basel, Switzerland Thesis: <i>Engineering of the photonic environment of single nitrogen-vacancy centers in diamond</i> Advisors: Prof. Richard J. Warburton, Prof. Patrick Maletinsky
2006 – 2012	Diploma studies in Physics Julius-Maximilians University Würzburg, Germany Thesis: <i>Resonant optical addressing and multi-quantum spin resonances of silicon vacancy defects in silicon carbide</i> Advisor: Prof. Vladimir Dyakonov Grade: 1.0 (with distinction - “mit Auszeichnung”)
2009 – 2010	Exchange studies University of British Columbia, Vancouver, Canada
1997 – 2006	High school Gymnasium Dinkelsbühl, Germany Grade: 1.4 (excellent - “sehr gut”)

List of publications

1. [D. Riedel](#), I. Söllner, B. J. Shields, S. Starosielec, P. Appel, E. Neu, P. Maletinsky, and R. J. Warburton, *Deterministic enhancement of coherent photon generation from a nitrogen-vacancy center in ultrapure diamond*, [Physical Review X](#) **7**, 031040 (2017).
2. D. Najer, M. Renggli, [D. Riedel](#), S. Starosielec, and R. J. Warburton, *Fabrication of mirror templates in silica with micron-sized radii of curvature*, [Applied Physics Letters](#) **110**, 011101 (2017).
3. [D. Riedel](#)*, D. Rohner*, M. Ganzhorn, T. Kaldewey, P. Appel, E. Neu, R. J. Warburton, and P. Maletinsky, *Low-Loss Broadband Antenna for Efficient Photon Collection from a Coherent Spin in Diamond*, [Physical Review Applied](#) **2**, 064011 (2014).
*equal contribution
4. H. Kraus, V. A. Soltamov, [D. Riedel](#), S. Vāth, F. Fuchs, A. Sperlich, P. G. Baranov, V. Dyakonov, and G. V. Astakhov, *Room-temperature quantum microwave emitters based on spin defects in silicon carbide*, [Nature Physics](#) **10**, 157 (2013).
5. [D. Riedel](#), F. Fuchs, H. Kraus, S. Vāth, A. Sperlich, V. Dyakonov, A. A. Soltamova, P. G. Baranov, V. A. Ilyin, and G. V. Astakhov, *Resonant addressing and manipulation of silicon vacancy qubits in silicon carbide*, [Physical Review Letters](#) **109**, 226402 (2012).